The 27th Annual International RAPDASA Conference joined by AMI

RAPDASA

RAPID PRODUCT DEVELOPMENT ASSOCIATION OF SOUTH AFRICA

Annual CONFERENCE

www.rapdasa.org

27 - 30 OCTOBER 2026

Protea Hotel Polokwane Ranch Resort, South Africa

FROM PROTOTYPE TO PRODUCTION: TRANSLATING RESEARCH INTO REALITY

CONFERENCE BOOKLET

Co-hosted by MINTEK and the University of Limpopo

www.rapdasas.org

RAPDASA

RAPID PRODUCT DEVELOPMENT ASSOCIATION OF SOUTH AFRICA

The Hosts

MINTEK
https://mintek.co.za/

University of Limpopo
https://www.ul.ac.za/

Table of Contents

The Hosts 3

Conference Sponsors 6

Exhibitors 12

Exhibitors Profiles 14

Technical Committee 22

Reviewers 24

Foreword and Welcome 26

Submission for Review Process 30

Pre-Conference Keynote Speakers 32

Invited Speakers 37

Keynote Speakers 44

Seminar Programme:
Design & Additive Manufacturing of Sailplane and Jewellery Parts 68

Seminar Programme:
Computational & Data-driven Modelling seminar 72

Programme: RAPDASA Conference Day 1 78

Programme: RAPDASA Conference Day 2 79

Programme: RAPDASA Conference Day 3 84

Programme: RAPDASA Conference Day 4 89

ABSTRACTS

1. Design & AM of Sailplane & Jewellery Parts Seminar.....94
2. Computational & Data-driven Modelling Seminar.....113
3. Materials Engineering.....140
4. Additive Manufacturing Material and Part Characterisation..202
5. Computational & Data-driven Modelling.....241
6. Additive Manufacturing Post Processing and Qualification....267
7. Product Design and Development.....282
8. Process Development.....305
9. Rapid Casting.....327
10. Industry Presentations.....339
11. Poster Abstracts.....344

Conference Sponsors

A huge thank you to all of the Conference Sponsors!



PLATINUM SPONSORS	
Department of Science, Technology and Innovation (DSTI)	www.dsti.gov.za/
MINTEK	https://mintek.co.za/

GOLD SPONSORS	
Central Univrsity of Technology, Free State (CUT)	www.cut.ac.za/
University of Limpopo (UL)	www.ul.ac.za/

SILVER SPONSORS	
Anton Paar Southern Africa	www.anton-paar.com/za-en/
Advanced Materials initiative (AMI)	

BRONZE SPONSORS	
The Collaborative Programme for Additive Manufacturing (CPAM)	www.csir.co.za/
The South African Nuclear Energy Corporation (Necsa) SOC Ltd	www.necsa.co.za/

PLATINUM SPONSORS

Department of Science, Technology and Innovation (DSTI)
www.dsti.gov.za/



science, technology & innovation

Department:
Science, Technology and Innovation
REPUBLIC OF SOUTH AFRICA

MINTEK
https://mintek.co.za/

MINTEK
A global leader in mineral and metallurgical innovation

GOLD SPONSORS

University of Limpopo (UL)
www.ul.ac.za

Central University of Technology, Free State (CUT)
www.cut.ac.za

SILVER SPONSORS

Anton Paar
www.anton-paar.com/za-en/

Anton Paar

AMI
Advanced Materials Initiative

ami
advanced materials initiative

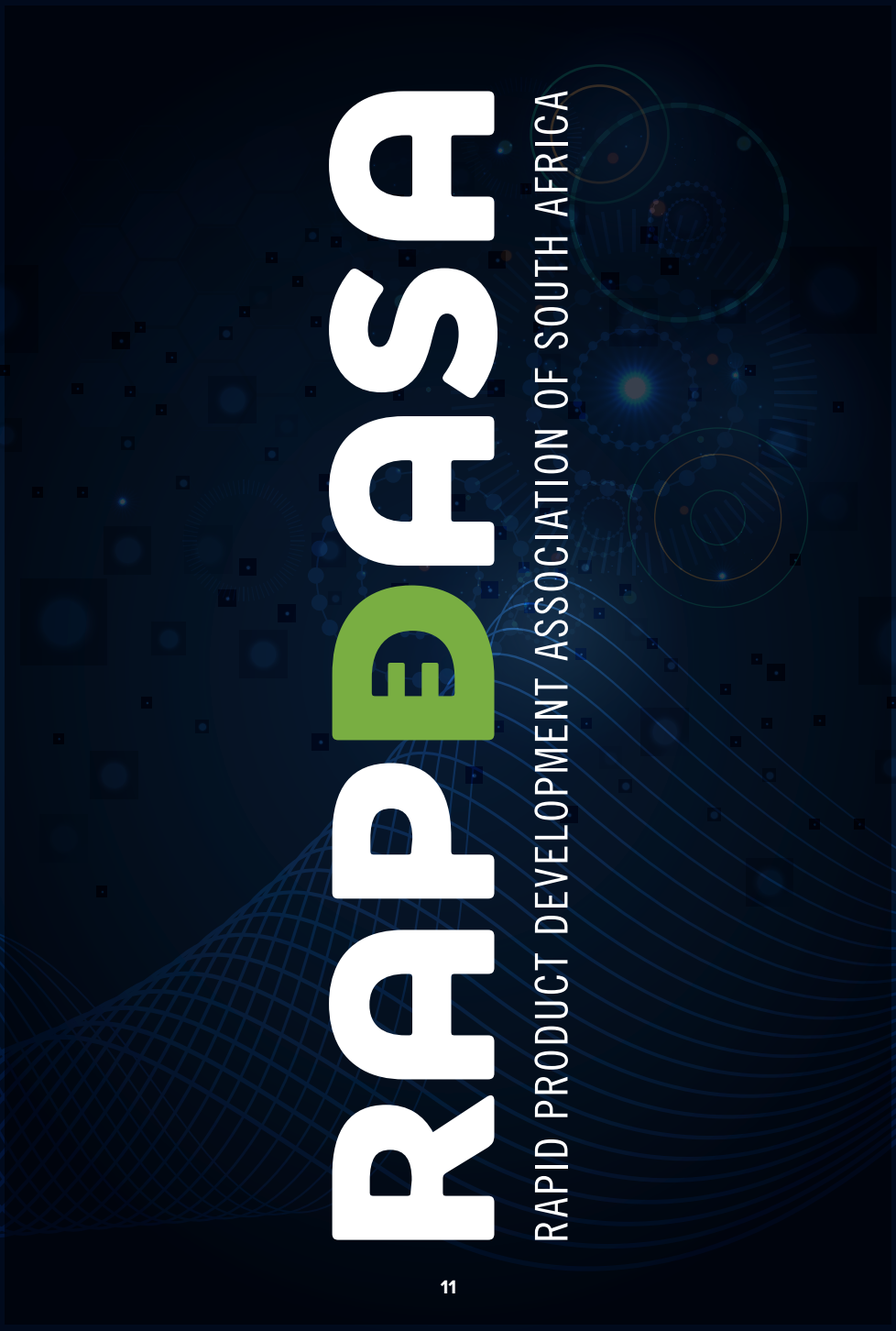
BRONZE SPONSORS

CPAM
The Collaborative Programme in Additive Manufacturing

NECSA
The South African Nuclear Energy Corporation (Necsa) SOC Ltd
www.necsa.co.za

necsa
We're in your world
South African Nuclear Energy Corporation SOC Limited

Co-hosted by **MINTEK** and the **University of Limpopo**



From Prototype to Production: Translating Research in to Reality

Exhibitors

Listed alphabetically, also featured on **https://site.rapdasa.org/exhibitors/**

Advanced Materials Initiative (AMI)
www.csir.co.za

Anton Paar
www.anton-paar.com/za-en/

Central University of Technology, Free State (CUT)
www.cut.ac.za/

MINTEK
www.mintek.co.za

The South African Nuclear Energy Corporation (Necsa) SOC Ltd
www.necsa.co.za

Univesity of Limpopo (UL)
www.ul.ac.za

Verder Scientific
www.verder-scientific.com/

Exhibitors


ami
advanced materials initiative


Anton Paar


CUT
CENTRAL UNIVERSITY OF TECHNOLOGY, FREE STATE


MINTEK
A global leader in mineral and metallurgical innovation


necsa
We're in your world
South African Nuclear Energy Corporation SOC Limited


UNIVERSITY OF LIMPOPO


VERDER

Exhibitors Profiles

Advanced Materials Initiative (AMI)

The Advanced Materials Initiative (AMI) is a strategic research and development program supported by South Africa's Department of Science, Technology and Innovation (DSTI) to add value to the country's mineral endowments and drive industrial competitiveness. The Advanced Materials Initiative contributes towards the beneficiation of light metals (including aluminium), precious metals, ferrous metals and nuclear metals.

www.csir.co.za

Exhibitors Profiles

Anton Paar

Anton Paar

Founded in 1922 in Graz, Austria, Anton Paar is a global technology leader in the measurement of density, concentration, rheometry, viscometry, and dissolved CO_2, with expanding expertise in Raman spectroscopy, X-ray diffraction (XRD), particle size, and surface analysis. Serving key sectors such as food and beverage, pharmaceuticals, chemicals, and petroleum, as well as leading academic institutions, Anton Paar continues to drive innovation through a strong commitment to research and development, investing over 14.5% of its annual turnover in R&D.

Anton Paar Southern Africa (Pty) Ltd, established in 2013, is a wholly owned subsidiary of Anton Paar GmbH. Headquartered in Johannesburg, the company also operates in its regional branches based in the Western Cape and KwaZulu-Natal, supported by dedicated staff based in Kenya, Tanzania, Ethiopia, Cameroon, and Côte d'Ivoire.

With a team of over 80 professionals, Anton Paar Southern Africa provides expert sales coverage across 45 countries in Sub-Saharan Africa, along with authorized servicing, technical support and application assistance. The company supports a wide range of industries and institutions with high-performance analytical solutions designed for both laboratory and process environments.

https://www.anton-paar.com/za-en/

Exhibitors Profiles

Central University of Technology, Free State (CUT)

Central University of Technology (CUT) is driven by a vision to be a leading University of Technology - changing lives, transforming society and shaping the future.

CUT delivers quality academic programmes and applied research while promoting access with success and meaningful engagement with communities.

Through strategic partnerships, the university continues to support innovation, entrepreneurship, social impact and inclusive development, helping strengthen the connection between education, industry and society.

www.cut.ac.za

Exhibitors Profiles

MINTEK

MINTEK
A global leader in mineral and metallurgical innovation

Mintek is South Africa's national mineral research organisation, dedicated to advancing the minerals industry through research, development and innovation. With over 90 years of research excellence, Mintek is a globally recognised leader in mineral processing, extractive metallurgy and mineral technology, delivering innovative solutions across the minerals value chain.

www.mintek.co.za

Exhibitors Profiles

South African Nuclear Energy Corporation (Necsa) SOC Ltd (NECSA)

The South African Nuclear Energy Corporation (Necsa) SOC Ltd. is a national facility dedicated to nuclear science, engineering, research, and innovation. As part of its research capabilities, Necsa provides access to advanced X-ray and neutron beamline facilities for the investigation of materials, structures, and processes across multiple length scales. These complementary techniques enable detailed characterisation of materials and components, supporting both fundamental research and industrial applications.

For the additive manufacturing (AM) community, Necsa's beamline facilities provide non-destructive approaches for characterising the structure, properties, and integrity of manufactured components. Diffraction and imaging techniques can be used to investigate residual stresses, phase transformations, crystallographic structure, porosity, density variations, internal features, and build-induced defects. The complementary penetration and sensitivity of X-rays and neutrons provide valuable insights into different aspects of AM materials and components, supporting process optimisation, performance assessment, and the qualification of advanced manufactured parts.

Ongoing upgrades and the planned Neutron Beam Line Centre (NBLC) at Necsa's future Multi-Purpose Reactor (MPR) will further expand the organisation's neutron-based research capabilities.

www.necsa.co.za

Exhibitors Profiles

University of Limpopo (UL)

The University of Limpopo (UL), which was established with a college status in 1959, has transformed into one of Africa's most innovative universities, offering highly competitive and industry-relevant qualifications. It has a vision to be a leading African University focused on the developmental needs of its communities and epitomising academic excellence and innovativeness. The university values Accountability, Transparency, Integrity, Academic Freedom, Excellence and Professionalism.

www.ul.ac.za

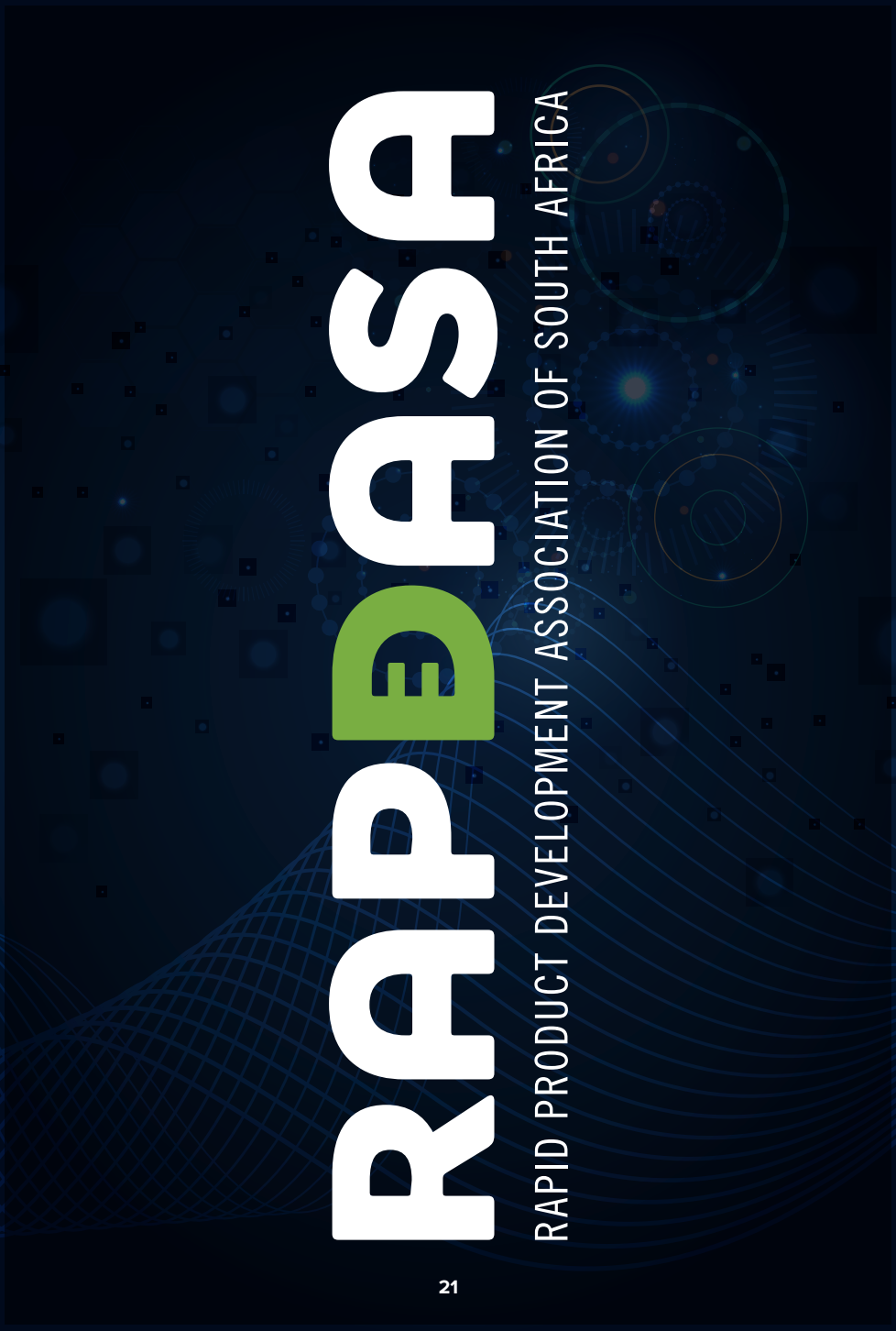
Exhibitors Profiles

Verder Scientific

Verder Scientific specialises in precise sample preparation and analytical solutions for laboratories worldwide. With innovative equipment and extensive expertise, we support our customers in performing reliable and reproducible analyses. Our technologies are used across a wide range of industries and research institutions — always with the goal of ensuring the highest standards of quality and efficiency.

https://www.verder-scientific.com/

Co-hosted by **MINTEK** and the **University of Limpopo**



2026 RAPDASA-AMI CONFERENCE

Technical Committee

CONFERENCE EDITOR:

Prof Willie du Preez (Visiting Professor, Central University of Technology, Free State)

GUEST EDITORS:

Design and Additive Manufacturing of Sailplane and Jewellery Parts

Dr Francis Monaheng (Central University of Technology, Free State)

Computational and data-driven modelling A

Prof Hasani Chauke (University of Limpopo)

Computational and data-driven modelling B

Dr Ramogohlo Diale-Boshielo (Mintek)

Materials engineering A

Prof Thywill Dzogbewu (Central University of Technology, Free State)

Materials engineering B

Dr Maria Mathabathe (University of the Witwatersrand)

Process development
Dr Jaco van der Walt (HyperTherm Technologies (Pty) Ltd)

Additive manufacturing material and part characterisation
Dr Hertzog Bissett (South African Nuclear Energy Corporation)

Additive manufacturing post processing and qualification
Mr James Dicks (University of Cape Town)

Product design and development
Mr Heinrich van der Merwe (Fabco Technologies (Pty) Ltd)

Rapid casting
Dr Joseph Moema (Mintek)

Robotics
Dr Daniel Kirkman (University of KwaZulu-Natal)

Posters
Dr Bathusile Masina (CSIR)

Reviewers
CONTRIBUTING TO THE 2026 RAPDASA-ROBMECH-PRASA-AMI CONFERENCE PROCEEDINGS

REVIEWERS 2026

Bernard Dreyer	Dr Ndivhuwo Nelwalani
Bradley Nemutudi	Dr Ntombi Mathe-Maleboho
Desmond Klenam	Dr Onyeka Ochonogor
Donald Hlungwani	Dr Ramogohlo Diale-Boshielo
Dr Charmaine Johnston	Dr Richard Klein
Dr CP Kloppers	Dr Samuel Oke
Dr David Tshwane	Dr Sigqibo Camagu
Dr Devon Hagedorn-Hansen	Dr Sylvester Bolokang
Dr Donald Mkhonto	Dr Winfred Mulwa
Dr Gonasagren Govender	Edwin Mapasha
Dr Hein Möller	Imdaadullah Adam
Dr Kalenda Mutombo	Jacob Wafula
Dr Lameck Mugwagwa	James Hepworth
Dr Lerato Raganya	Jean van Laar
Dr Maria Ntsoaki Mathabathe	Jurgens Taljaard
Dr Melody Neaves	Katlego Phoshoko
Dr Michael Bodunrin	Kelvin Mpofu
Dr Modupeola Dada	Khomotso Maenetja
Dr Mordecai Mashamaite	Lehlohonolo Lisema
Dr Moses Charles	Marné van Niekerk

REVIEWERS 2026 (continued)

Milton Makhofane	Prof Philip Crouse
Morena Xaba	Prof Philip Loveday
Muhammad Arshad	Prof Pieter Pistorius
Mulenga Bwalya	Prof Regina Maphanga
Nana Arthur	Prof Raesibe Sylvia Ledwaba
Nathaniel Oyedeji	Prof Riaan Stopforth
Ndanduleni Lethole	Prof Schalk Kok
Nicole Sibuyi	Prof Thorsten Becker
Nthape Mphasha	Prof Tom Vaneker
Paul Shangase	Ranwaha Tshifhiwa
Pandwe Lubamba	Rosinah Modiba
Pushetso Tema	Ryno van der Merwe
Prof Amos Muiruri	Sateesh Bandaru
Prof André van der Merwe	Stephen Masete
Prof Charles Siyasiya	Steven Magogodi
Prof Debby Blaine	Tebogo Ledwaba
Prof Natasha Sacks	Tshegofatso Phaahla
Prof Nthabiseng Maledi	Velile Vilane
Prof Olaf Diegel	William Shipman
Khathutshelo Nemavhola	

Foreword and Welcome

Foreword and Welcome by the 2026 RAPDASA Conference Chairperson:



Dr. Marandela Mulaudzi

Dear Colleagues,

On Behalf of the RAPDASA organizing committee, it is my sincere pleasure and honour to welcome you all to the 27th annual international RAPDASA 2026 conference, which is being held under the timely theme “From Prototype to Production: Translating Research into Reality”.

This conference is being co-hosted by Mintek (science council) and University of Limpopo (UL). It is my privilege to welcome local and international delegates, researchers, industry leaders and students to the RAPDASA 2026 conference in Polokwane.

This year’s RAPDASA conference began by hosting two pre-conference seminars, namely, Design and additive manufacturing of sailplane and jewellery parts, and Computational & data-driven modelling, and also hosted Industry day.

The conference then placed a key focus on the vital role that materials engineering, additive manufacturing, product design and process development, rapid casting and computational modelling play in promoting the technical exchanges, collaborations, career-building, as well as influencing global manufacturing industry.

As RAPDASA organizing committee, we would like to express our sincere gratitude to everyone who participated in the coordination and organisation of this conference, ensuring its success. Once again, RAPDASA has been reaffirmed as an association, which bridges the gap between manufacturing industries and academic institutions by creation of the much needed technical knowledge base from which research can be turned into products fit for industrial use.

Thank you.

Dr Marandela Mulaudzi

DIMITRI DIMITROV SCHOLARSHIP

In honour of Prof Dimitri Dimitrov

Enabling Student Participation

Financial aid for postgraduate students to attend and present at the annual RAPDASA conference

Make your donation to grow the number of students attending future conferences and ensure sustainability via the Snapscan QR code.





RAPDASA

For more information, visit
www.rapdasa.org

Submission for Review Process

A formal "Call for papers" for the 27th Annual International RAPDASA Conference joined by AMI, hosted by Mintek and the University of Limpopo, was issued in January 2026 to submit an extended abstract within the identified conference themes. Extended Abstract submissions were subjected to an internal reviewing process by the Track Chairs. The authors of successful submissions were notified and invited to submit a full paper, which was intended for publication in the conference proceedings. Both the extended abstracts and full papers were submitted online through the EasyChair conferencing system, whereafter acknowledgement of receipt was sent to authors through the system. Authors were informed that their submitted full papers would be subjected to a double-blind review process.

The following dates were set by the technical committee:

- First announcement and call for abstracts for 2026 conference: December 2025
- Deadline for submission of abstracts: 16 March 2026
- Notification of acceptance of abstracts: 30 March 2026
- Deadline for submission of full papers: 8 June 2026
- Feedback on paper reviews: 3 August 2026
- Submission deadline for e-posters: 31 August 2026
- Submission deadline for final revised papers: 31 August 2026
- Deadline for early-bird registration: 31 August 2026
- Conference dates: 27 – 30 October 2026

Extended Abstracts were required to comply with the Author Guidelines and template provided on the conference website and in EasyChair and be a maximum length of 2 to 3 pages. Full papers were required to comply with the Author Guidelines and template provided on the conference website and in EasyChair. A double-blind peer review process was used in the selection of full papers for publication in the conference proceedings. Throughout the review process the authors' identities were concealed from reviewers and the reviewers' identities were concealed from the authors. Each full

paper was sent to a minimum of two reviewers, with a third reviewer being requested in case of a lack of consensus between the first two reviewers. The reviews were performed by national and international academics and other experts in the respective field, listed on the Reviewers page under the Technical Committee heading.

Reviewers were asked to review submissions according to the following criteria and were encouraged to provide recommendations and suggestions.

- Does the title reflect the contents of the paper?
- Does the paper relate to what has already been written in the field?
- Do you deem the paper to be proof of thorough research and knowledge of the most recent literature in the field of study?
- Is the paper clearly structured, easy to read and with a logical flow of thought?
- Are the arguments employed valid and supported by the evidence presented?
- Are the conclusions clear and valid?
- Does the paper conform to accepted standards of language and style?
- Any other recommendation(s)?

Reviewer feedback was saved in the EasyChair submission system, from where emails together with the review reports were sent to the authors, requesting them to submit a revised paper with a rebuttal to the review reports added to the last page of the manuscript. The authors were given 2 to 3 weeks to prepare these documents, after which the revised document was reviewed by the Track Chair for adequate response to the review reports. If satisfactory, the revised paper was recommended to the Conference Editor for acceptance and publication in the conference proceedings.

Based on the outcome of the double-blind peer review process and the recommendations of the reviewers, five to ten papers of high quality that complied with the focus and scope of The South African Journal of Industrial Engineering (SAJIE), were selected from the papers submitted to the conference and were submitted to the journal to be considered for publication as journal articles. These papers were not included in the conference proceedings and were subjected to SAJIE's editorial process.

Pre-Conference Keynote Speakers

TUESDAY, 27 OCTOBER 2026

Prof A Jonker



From Composite Material Qualification to Additive Manufacturing: A Practical Certification Framework for CS-22 Aircraft.

Bio: Attie Jonker is an engineer, academic and co-founder of Jonker Sailplanes. Inspired by his father, who built the family's first glider, he decided at the age of 15 to pursue the development of high-performance sailplanes. He holds B.Sc. Mathematics, B.Eng., M.Eng. and PhD degrees.

Since 1998, he has been involved in the development and certification of the Jonker Sailplanes JS series, with experience spanning composite materials, structural design, manufacturing, testing and EASA CS-22 certification. His current work includes the qualification and certification challenges associated with introducing polymer, continuous-fibre and metal additive manufacturing into certified aircraft structures.

Abstract: The introduction of new materials and manufacturing processes into certified aircraft requires reliable material properties and evidence that these properties can be reproduced consistently in production. This paper presents experience gained by Jonker Sailplanes during the development and certification of composite sailplanes under EASA CS-22 and considers how the established composite-material qualification philosophy can be extended to additive manufacturing (AM).

Conventional composite qualification included statistically based tensile, compression and shear testing, together with control of manufacturing parameters such as fibre volume fraction and post-curing. The progressive introduction of AM, from polymer components to continuous-carbon-

fibre-reinforced polymers and laser powder bed fusion of stainless steel, introduces additional challenges associated with interlayer strength, build orientation, process variability and elevated-temperature behaviour.

Based on this experience, a practical framework comprising material qualification, process qualification and continued production conformity is proposed for the introduction of structural AM components into CS-22 aircraft.

Prof K Govender



The Digital Lab: Computational Chemistry and Materials Modelling.

Bio: Professor Krishna Govender is an Associate Professor and Deputy Head of Department in the Department of Chemical Sciences at the University of Johannesburg. As Principal Investigator of the E=c^2 m^2 Research Group, his research focuses on computational chemistry, quantum mechanical DFT calculations, molecular dynamics, and data-driven material discovery. His group develops automated Python workflows to optimize high-performance computing execution across complex systems, ranging from 2D energy storage heterostructures and functional nanocomposites to therapeutic drug targets.

Prof Govender plays a leading role in shaping South Africa's computational science landscape, serving as Chair of the Centre for High Performance Computing (CHPC) Special Interest Group for Computational Chemistry and Material Science, Chair of the South African Chemical Institute (SACI) Molecular Modelling Division, and an Associate of the National Institute for Theoretical and Computational Sciences (NITheCS). He is dedicated to integrating digital open-access tools and supercomputing infrastructure to solve pressing industrial and environmental challenges.

Abstract: The rapid evolution of High-Performance Computing (HPC) infrastructure and first-principles simulation tools has transformed materials discovery, positioning computational modeling as an essential pillar alongside theoretical and experimental research. This talk explores how density functional theory (DFT) and multiscale modeling serve as a "digital

laboratory" to predict, design, and optimize novel functional materials prior to physical synthesis.

Focusing on recent advances from our research group, this talk highlights the first-principles investigation of two-dimensional (2D) van der Waals heterostructures as high-capacity anode materials for next-generation lithium-ion batteries. By interrogating interfacial structural stability, electronic conductivity, and lithium-ion diffusion energy barriers at atomic precision, we demonstrate how computational modeling unravels critical charge-transfer kinetics and strain dynamics during energy storage cycles.

Invited Speakers

WEDNESDAY, 28 OCTOBER 2026

Dr Luyolo Mabhali, Executive Cluster Manager, CSIR Future Production: Manufacturing.

Venue: Rose Room



Built here, used here: Localising manufacturing technology from applied research.

Bio: Dr Luyolo Mabhali, Executive Cluster Manager for CSIR Future Production: Manufacturing, has over 15 years of expertise in driving innovation across manufacturing, and research. He holds two PhDs, one in Metallurgical Engineering and another in Innovation Management, as well as an MBA from the University of the Witwatersrand and Wits Business School.

In his former role as a Research Group Leader at the Photonics Centre, previously known as the CSIR National Laser Centre, Dr Mabhali showcased his extensive knowledge in laser applications. He steered research efforts in laser additive manufacturing and surface engineering, making significant contributions to the field. This expertise is reinforced by his experience as a Research and Development Manager at the South African Mint Company, where he drove forward materials and processes critical to the minting industry.

His background as a Senior Engineer at ArcelorMittal South Africa, where he specialised in process modelling and coke production, further speaks to his versatile skill set in manufacturing. Dr Mabhali merges academic insight with practical experience, cementing his role as a leader in driving manufacturing innovation.

As a member of the South African Institute of Mining and Metallurgy, Dr Mabhali remains engaged in the industry to ensure that he is at the forefront of advancements in metallurgy and manufacturing.

Abstract: South African manufacturers know the frustration well: a critical component fails, the replacement has to be imported, and production waits. Behind that frustration is an opportunity. Many of the parts, processes, and technologies we depend on can be repaired, made, or improved here if research addresses the problems industry faces. The CSIR, through its Future Production: Manufacturing Cluster, uses its capabilities in materials and process engineering, and manufacturing processes such as metal injection moulding, additive manufacturing, digital manufacturing, and testing and qualification, to turn applied research into locally available solutions. The talk reflects on what it takes to localise technology: starting with available capabilities for product development or qualifying processes, developing the skills to sustain them, and building partnerships that allow for co-creation with industry, as well as sharing risk and reward. It argues that localisation is not a single breakthrough but a deliberate, collaborative effort, and invites industry, the research community and other stakeholders on this RAPDASA (Rapid Product Development Association of South Africa) platform to forward challenges and exchange ideas on what solutions we should collectively address moving forward.

Website: https://www.csir.co.za/

Dr Ricardo Grau-Crespo



Venue: Safari Room

Modelling disordered alloys: density functional theory and machine learning.

Bio: Dr Ricardo Grau-Crespo leads a materials theory group at the School of Engineering and Materials Science of Queen Mary University of London, UK, using a combination of quantum chemistry and machine learning techniques to investigate and predict the properties of energy materials. He is also interested in developing new methodologies and software for materials modelling. He is originally from Cuba, where he studied Physics at the University of Havana. He completed a PhD at Birkbeck, University of London, followed by faculty positions at University College London and the University of Reading in the UK. He is a Fellow of the Royal Society of Chemistry, and Associate Editor for the Royal Society of Chemistry 's Journal of Materials Chemistry A and Materials Advances.

Abstract: This talk will present a perspective on our work modelling site-occupancy disorder in crystalline solids. I will first outline the methodological landscape for treating alloy disorder, from mean-field strategies to explicit configurational and ensemble-based approaches. I will then focus on symmetry-adapted ensemble models [1], which make it possible to combine statistical mechanics with atomistic calculations such as DFT in order to predict not only configurational thermodynamics, but also properties that are often difficult to capture with conventional cluster expansions, including cell parameters, effective physical properties and average spectra (such as NMR [2, 3]). Examples will be used to illustrate how ensemble models can

provide a realistic description of disordered materials when local geometry, long-range interactions, or property averaging are essential. Finally, I will discuss recent work on generative artificial intelligence (AI) for crystal structures through the CrystaLLM project [4], and a possible route to address its limitations in the treatment of alloy disorder.

[1] Site-Occupancy Disorder (SOD) repository: https://github.com/rgraucrespo/sod
[2] R Grau-Crespo, S Hamad, SRG Balestra, R Issa, TD Sparks, A Fernandes, BL Griffiths, R Moran, D McKay, SE Ashbrook. Capturing local compositional fluctuations in NMR modelling of solid solutions. Chemical Science 16 (2025) 19357-19369.
[3] RF Moran, D McKay, PC Tornstrom, A Aziz, A Fernandes, R Grau-Crespo, SE Ashbrook. Ensemble-Based Modeling of the NMR Spectra of Solid Solutions: Cation Disorder in Y2(Sn,Ti)2O7. Journal of the American Chemical Society 141 (2019) 17838-17846.
[4] LM Antunes, KT Butler, R Grau-Crespo. Crystal structure generation with autoregressive large language modeling. Nature Communications 15 (2024) 10570.

Website Link: https://www.linkedin.com/in/ricardo-grau-crespo-80757425/

Mr Mangalani Miyambo,
Research Group Leader (Applied Detonics, Ballistics and Explosives)



Venue: Day Lily Room

Integrated Material Characterisation and Computational Modelling Capability for Defence Protection Technologies.

Bio: Mangalani Miyambo is the Research Group Leader for Applied Detonics, Ballistics and Explosives at the Council for Scientific and Industrial Research (CSIR) in Pretoria. With over 15 years of experience at the CSIR, his expertise includes project management, blast and ballistics laboratory experiments, and landmine-protected vehicle validation testing against NATO and South African military standards. He holds a Bachelor of Technology in Mechanical Engineering and a master's degree in Mechanical Engineering, awarded cum laude, from the University of Johannesburg. His career combines mechanical engineering, experimental testing and research leadership.

Abstract: Landwards Sciences provides an integrated material characterization capability supporting the development and evaluation of protection technologies for military vehicles and personnel. The capability combines experimental testing, structural response measurements and computational modelling to investigate material behavior under loading conditions relevant to blast, ballistic impact and operational service.

The experimental programe incorporates quasi-static tensile testing and high strain rate compression, tension and shear testing using the Split Hopkinson Pressure Bar (SHPB) systems. Materials investigated include armour and structural steels, aluminum, titanium alloys, sintered iron and

metal matrix composites. Testing across different strain rates, temperatures and stress states enables characterization of strength, ductility, thermal softening and failure behavior. The LDERI material characterization programe consolidates experimental results into technical reports and an evolving material materials database, providing material parameters for constitutive and failure modelling.

The DIC complements conventional instrumentation by providing full field deformation measurements during blast loading. These measurements are coupled with numerical predictions.

The material characterisation capability is integrated with blast and ballistic testing, protection concept evaluation and vehicle validation activities. this enables assesment of hull deformation, shock attenation and structural performance, contributing to improved understanding of the soldier and crew survivability.

Ongoing capability development includes elevated temperature dynamic testing design and commissioning the Torsional modification to the SHPB systems. Through various collaborations with industry and academia the LS business unit strengthens the scientific basis for material selection, protection solutions designs and computational model validation as research capability for the SANDF.

Website: https://www.csir.co.za/

Keynote Speakers

WEDNESDAY, 28 OCTOBER 2026

KEYNOTE SPEAKER 1

Mr Vince Zhao
Mr Vince Zhao, Director of Business Development – AMEA
Farsoon Technologies, China



From Laboratory Research to Industrial-Scale up of Additive Manufacturing

Bio: Vince joined Farsoon in 2017 and leads business strategy and ecosystem development across Asia Pacific, Australia, Africa, South America and the Middle East. With over 10 years of dedicated experience in additive manufacturing, he has spearheaded the industrial adoption of polymer and metal additive technologies throughout the AMEA region. He maintains in-depth insights into industry trends, advanced applications and mass-production scenarios. Boasting nearly 20 years of cross-sector expertise covering construction machinery, medical devices and additive manufacturing in technical support, marketing and sales, Vince delivers end-to-end additive manufacturing solutions for industrial clients. He has supported numerous enterprises in their transformation from prototyping to serial production, establishing solid industry influence in the commercialization of additive manufacturing within the AMEA territory.

Abstract: Farsoon & Changsha facility at a glance. Farsoon's polymer & Metal machine portfolio. Benchmark Industry customers. Farsoon's open platform strategy. Latest Technology Innovation. Metal platforms & application.
olymer platforms & application.

Website: https://www.farsoon-gl.com/

KEYNOTE SPEAKER 2

Dr Ndanduleni Lethole
Sefako Makgatho Health Sciences University, South Africa



From Binary to Ternary Pt-Based Magnetic Alloys: First-Principles Insights into Structure, Magnetism and Materials Design

Bio: Dr Ndanduleni Lethole is a Senior Lecturer in the Department of Physics at Sefako Makgatho Health Sciences University. He obtained his PhD in Materials Science from the Materials Modelling Centre at the University of Limpopo. His research integrates both computational and experimental approaches, with a strong emphasis on density functional theory (DFT) and advanced characterisation techniques. His computational work focuses on the design and optimisation of cathode materials for rechargeable batteries, as well as the development of advanced alloys for magnetic data storage applications. Complementing this, his experimental research involves the solid-state synthesis and characterisation of phosphor-based luminescent materials for dye-sensitised solar cells (DSSC), as well as neutron diffraction studies of magnetic alloys. Dr Lethole has authored over 30 peer-reviewed publications in accredited journals and has presented his work at both national and international scientific conferences. In addition to his research contributions, he is actively involved in postgraduate supervision and mentorship, supporting the development of students in materials sciences. To date, he has successfully supervised one doctoral and four master's students to completion, with several others currently under supervision.

Abstract: The rapid growth of digital technologies, artificial intelligence and data-intensive computing continues to drive demand for magnetic materials with high thermal stability, strong magnetic anisotropy and controllable magnetisation. Pt-based alloys containing 3d transition metals are promising candidates for high-density magnetic recording and spintronic technologies because their properties can be tailored through composition and chemical ordering. The work presents a first-principles perspective on Pt-based magnetic alloys, progressing from binary M-Pt systems to Fe3Pt polymorphs and Mn-substituted FePt ternary alloys. DFT calculations demonstrate strong coupling between composition, structural stability, electronic structure and magnetism. Among Fe-Pt phases, ordered FePt exhibits pronounced MCA anisotropy, with [001] as the easy magnetisation direction. Extension to MnPt, CoPt and NiPt reveals substantial variation in magnetic moments and highlights the importance of thermodynamic, mechanical and dynamical stability in evaluating magnetic materials. The martensitic Fe3Pt structures further demonstrates the importance of structural polymorphism in controlling magnetic-material properties. Different Fe3Pt phases reveal that changes in crystal symmetry influence structural, mechanical, dynamical and magnetic behaviour, highlighting phase engineering as an additional pathway for tailoring Pt-based magnetic alloys.

The calculations extend this framework to ternary Mn-Fe-Pt where Mn substitution progressively modifies lattice tetragonality and produces strongly non-monotonic magnetic behaviour, reflecting competing magnetic interactions between the ferromagnetic FePt and antiferromagnetic MnPt limits. The results demonstrate how DFT modelling can evolve from property prediction towards composition-guided materials design, providing a foundation for data-driven discovery of magnetic alloys for high-density recording, heat-assisted magnetic recording and spintronics.

KEYNOTE SPEAKER 3

Dr Terry Wohlers
Distinguish Fellow of Advanced Manufacturing at Wohlers Associates, powered by ASTM International.



Evolution of AM and Trends Shaping its Future

Bio: Industry analyst, author, and speaker Terry Wohlers is Distinguish Fellow of Advanced Manufacturing at Wohlers Associates, powered by ASTM International. He founded Wohlers Associates 40 years ago and has provided consulting assistance to nearly 300 organizations in 27 countries. Wohlers has authored 450 books, articles, and technical papers, and given more than 200 keynote presentations on six continents. He has appeared on many television and radio news programs, including Australia's Sky News, Al Jazeera, Bloomberg TV, CNBC, CNN, Fox Business, and MSNBC. In 2012 and 2014, he was a featured speaker at the White House.

For 29 years, he served as a principal author of the Wohlers Report, the undisputed industry-leading report on additive manufacturing and 3D printing worldwide. After 35 years, Wohlers Associates was acquired by ASTM International, a non-profit organization. In 2004, Wohlers received an Honorary Doctoral Degree from Central University of Technology in Bloemfontein, South Africa. Wohlers was inducted into the TCT Hall of Fame in 2022.

Abstract: The AM industry has experienced peaks and valleys over its nearly 40-year history. Overall, revenue growth has been strong, averaging more than 24% annually, according to Wohlers Report 2026. However, it has

slowed to an average of nearly 14% annually over the past five years.

Recent trends are influencing AM and its future. Among them are streams of revenue currently funding research, development, and commercialization efforts. Others are developments in China and the impact of low-cost systems. Combined, these trends are making the AM industry much different and more challenging than in the past.

Website: https://wohlersassociates.com

Keynote Speakers

THURSDAY, 29 OCTOBER 2026

KEYNOTE SPEAKER 4

Prof Diego Rafael Nespeque Correa
Assistant Professor: Department of Physics and Meteorology,
Faculty of Sciences of UNESP, Brazil



Innovative design of biomedical high entropy alloys

Bio: Assistant Professor at the Department of Physics and Meteorology, School of Sciences, São Paulo State University (UNESP) Campus Bauru. Faculty member of the Graduate Program in Science and Technology of Materials (POSMAT) at UNESP and co-leader of the Laboratory of Anelasticity and Biomaterials. Associate researcher in the Center for Development of Assistive Technology (CMDTA) and the INCT-BIOCRON: Bone biology and chronic diseases. Holds a Bachelor's degree in Physics (2010) and a Direct Doctorate in Science and Technology of Materials (2015) from UNESP Campus Bauru, with postdoctoral research conducted at UNESP (Campus Bauru and Sorocaba) and at the Institute of Biomaterials and Bioengineering, Tokyo Medical and Dental University TMDU (Japan). Acted as a visiting professor at the Institute of Structure of Matter, National Research Council CNR (Italy), completed a technical training internship at Universidad Carlos III de Madrid UC3M (Spain), and carried out a technical visit at the Egypt-Japan University of Science and Technology E-JUST (Egypt) and at the Graduate School of Dentistry of the Tohoku University (Japan).

Experienced in Condensed Matter Physics, with emphasis on surfaces and interfaces, physical metallurgy, and biomaterials. Research focuses on the development of novel metallic biomaterials, particularly low-cost

titanium alloys and high-entropy alloys, surface modification of metals and alloys using plasma and electrochemical methods, and surface and bulk characterization techniques. Author of over 50 published articles, with more than 1,400 citations and an h-index of 20 (Google Scholar).

Abstract: Metallic implants play a critical role in orthopedics, dentistry, and cardiology, where they are used to replace or support damaged hard tissues. Although titanium and its alloys remain the benchmark materials for these applications, several challenges persist, including stress shielding caused by the mismatch between the elastic modulus of the implant and cortical bone, corrosion and wear resulting from long-term contact with physiological environments, and limited bioactivity associated with their intrinsically bioinert surfaces. In recent years, high-entropy alloys (HEAs) have emerged as promising candidates for biomedical applications due to their unique combination of mechanical strength, corrosion resistance, and wear resistance, which arise from their characteristic core effects.

Among them, the equiatomic TiNbTaZrMo alloy has been proposed as a representative biomedical HEA (Bio-HEA) because of its non-toxic, non-allergenic composition and relatively low elastic modulus. However, the incorporation of refractory elements such as Ta, Nb, and Mo significantly increases production costs, potentially limiting widespread clinical adoption, particularly in low-income countries. Consequently, the development of cost-effective implant materials is becoming increasingly important, not only from a commercial perspective but also in support of the United Nations 2030 Sustainable Development Goals (SDGs). This presentation will discuss current strategies for designing and producing low-cost Bio-HEAs through the incorporation of lightweight and economically attractive alloying elements, such as Fe and Al, and the resulting effects on the key properties required for biomedical applications. Furthermore, recent advances in surface biofunctionalization approaches aimed at improving bioactivity, osseointegration, and long-term implant performance will be highlighted.

Website: http://lattes.cnpq.br/2282008544774759

KEYNOTE SPEAKER 5

Prof Ulrich E. Klotz
Professor of Materials Science, HM Munich University of Applied Sciences.



From Phase Diagram to Digital Twin: An Integrated Approach to the Development of Precious Metal and Technical Alloys

Bio: Prof. Dr. Ulrich E. Klotz holds a Diploma in Physical Metallurgy from the University of Stuttgart, Germany, and a PhD in Materials Science from ETH Zurich, Switzerland. From 2007 to 2025 he was Head of the Department of Physical Metallurgy at the fem Research Institute for Precious Metals and Metals Chemistry in Schwäbisch Gmünd, Germany. Since 2025 he has been Professor of Materials Science at Munich University of Applied Sciences.

His research covers alloy development, the experimental determination and thermodynamic modelling of phase diagrams, investment casting and casting simulation, additive manufacturing, and microstructure characterisation, with a particular focus on precious metals.

Abstract: The development of new alloys and their manufacturing processes is a complex and labour-intensive task. The compositional space grows rapidly with the number of alloying elements, and for platinum group and other precious metals the high material value makes trial-and-error approaches particularly costly. This keynote presents an integrated development chain in which each step builds on the data of the previous one.

The chain starts with the experimental determination of phase equilibria in binary and ternary systems using equilibrated alloys, thermal analysis and microanalysis. These classical investigations remain the foundation on which all thermodynamic descriptions rest. Diffusion couples extend this approach to larger compositional ranges. A single specimen contains a continuous range of compositions and, combined with a subsequent heat treatment, also reveals process-related properties such as the age-hardening potential. On this experimental basis, CALPHAD calculations serve two purposes. They allow large numbers of compositions to be screened for promising new alloys, and they provide the temperature-dependent material parameters needed to simulate and assess manufacturing processes such as investment casting and laser powder bed fusion. Comparison with experiments in turn shows where existing databases need revision, so that the chain becomes an iterative loop.

Finally, the concept of the digital twin is discussed, in which experimental data, simulation results, processing parameters and their metadata are brought together along the entire process chain.

Each step is illustrated by examples from precious metal, titanium-containing or copper-based alloy systems. The talk concludes with an assessment of what is still required to implement the complete chain for a single material.

Website: https://sci.hm.edu/kontakte_de/phonebook_detailseite_103786.en.html

KEYNOTE SPEAKER 6

Prof Peace Mkhonto
Associate Professor : Materials Modelling Centre, University of Limpopo, South Africa



Application of Computational Modelling in Reagents Design for Separation of Minerals and Adaptation of Machine Learning Approach

Bio: Peace Mkhonto earned his doctor of philosophy (PhD) in Physics (Computational Modelling of Materials) focussed on pentlandite minerals simulations in 2017. In 2017-2018 he held a postdoctoral position at the University of Limpopo, Materials Modelling Centre. In addition he holds a postgraduate diploma in engineering (Metallurgy and Materials) from the University of the Witwatersrand. He is currently an associate professor at the University of Limpopo, Materials Modelling Centre. He is a National Research Foundation (NRF) Y1-Rated researcher. He is the coordinator of the minerals cluster at the University of Limpopo, Materials Modelling Centre and a group leader of the Minerals Modelling and Processing (MMP) Group. His niche area is on Computational Modelling and Processing of Minerals. He employs computational method to design reagents which are complemented by microflotation experiments. His minerals of interests are base metal sulphides (BMSs), platinum group minerals (PGMs), lithium bearing minerals (LBMs) and metal carbonate minerals (MCMs).

He has supervised 22 postgraduate students which include honours, masters and doctoral students to completion. He has also published articles in peer-reviewed journals and conference proceedings. He also has accolades for his

research presentations and also the University of Limpopo Vice-Chancellor excellence award for Second Best Researcher in the School of Physical and Mineral Sciences. He has held a number of funding that includes NRF Thuthuka grant, SAMMRI grant, the DSTI-Joint Research Centre (JRC) grant between South Africa and China and currently a Y-Rated researcher grant. He has collaborations with Qingdao University of Science and Technology (QUST) in China. In 2019 he participated in the Young Scientist Exchange Program between South Africa and China. He is currently a participant of the Future Professor Program (FPP) funded by the South African Department of Higher Education and Training (DHET).

Abstract: Reagents, in particular collectors are the current hot topic for both computational modelling and experimental mineral processing (flotation) research. This is due to the demand for novel and green reagents for recovery of critical minerals. The major minerals include copper, lead, manganese, lithium, zinc, nickel, platinum and chrome bearing minerals. The growing demand for critical elements for energy is driven by the electric vehicles and energy storage sector. To meet these demands, computational modelling and flotation experiments were conducted to recover and separated the platinum group minerals (PGMs), base metal sulphides (BMSs) and lithium bearing minerals (LBMs) from the gangue minerals.

The computational modelling was utilised as a tool to design highly selective and green reagents that can outperform or complement the currently used reagents. This was due to drawback of toxicity and selectivity of the currently well-known xanthate, dithiocarbamate and dithiophosphates used in flotation process. The computational simulation unravelled the fundamentals mechanisms on how these reagent bind on the minerals surfaces and their chemistry behaviour. It was established that complementary of the computational methods to the flotation experiments was pivotal in achieving well performing reagents and great separation of the minerals. Lastly, the machine learning approach such as machine learned force-fields (MLFF) within the ab-initio molecular dynamics (AIMD) was used to include temperature in the modelling of the surface-collector-water system, which also unravelled the technique capability and disadvantages.

Website: https://sites.google.com/view/minerals-modelling-and-process/home

Keynote Speakers

FRIDAY, 30 OCTOBER 2026

KEYNOTE SPEAKER 7

Professor Conrado Ramos Moreira Afonso
Federal University of São Carlos (UFSCar), Brazil



3D Printing by LPBF of Multiprincipal Equimassic β Ti-Nb-Zr(-Ta) alloys from Ultrasonic Atomized powder for Implant Applications

Bio: Recently received International Award from the JALCOM "Journal of Alloys and Compounds – Advanced Career Researcher 2023", for researchers more than 10 years after defending their doctorate, at the XXI-Brazilian MRS 2023, organized by SBPMat, held in October/2023.

Born in Boa Esperança do Sul – São Paulo state (SP), Brazil. He has a degree in Materials Engineering from the Federal University of São Carlos (1998), a Master's degree (2000) and a PhD in Materials Science and Engineering from the Federal University of São Carlos (2004). He did his Sandwich Doctorate for 6 months at the University of Florida (UF), FL - USA (2003), 1 year as a FAPESP postdoctoral fellow (2005) in "Beta Titanium Alloys" at the State University of Campinas (FEM/UNICAMP) and postdoctoral fellow in 2016 at the Polytechnic University of Valencia (UPV) – Valencia, Spain (BPE-FAPESP) and has been visiting professor at the UPV since 2011. He is currently the Head of Department (since May/2022) along the 50th anniversary of DEMa/UFSCar, the first course of Materials Engineering and celebrating 50 years of Materials Science and Engineering in Brazil and Latin America, he works nowadays as Associate Professor III (since 2023) and Professor since 2010 of the Department of Materials Engineering (DEMa/UFSCar).

CNPq Scholarship in Research Productivity PQ-1-E since 2011, advisor to Master's and Doctorate students as Full Professor enrolled in the PPG-CEM of UFSCar, grade 7 (maximum) of CAPES-Brazil in six consecutive evaluations. From 2006 to 2010 worked as a Materials Engineer at the Electron Microscopy Laboratory (LME) of the former National Synchrotron Light Laboratory (LNLS), current National Nanotechnology Laboratory (LNNano) of the National Center for Energy and Materials Research (CNPEM).

Member of the External Advisory Committee of Marie Sklodowska Curie actions - European Commission – MSCA, and Czech Science Foundation (GACR) projects reviewer.

Abstract: This work deals with production of spherical ultrasonic atomized powders of multiprincipal equimassic Beta Ti-33Nb-33Zr (TNZ-33) and Ti-25Nb-25Ta-25Zr (TNTZ-25) alloys. The TNZ33 and TNTZ-25 alloys were chosen for its ideal combination of mechanical (low modulus and high strength) and biological properties (corrosion resistance), compared with higher elastic modulus of cp-Ti (E=110 GPa) and Ti-6Al-4V (E=100 GPa). Ultrasonic atomized powders with high sphericity of 0.94 of TNZ-33 and TNTZ-25 alloys were obtained by ultrasonic atomization ATO Lab+ equipment and subsequent 3D printing by laser powder bed fusion of multiprincipal Beta TNZ-33 and TNTZ-25 alloys samples that were printed at laser speeds of 500, 750, and 1000 mm/s (VED of 167, 111 and 83 J/mm3, respectively), for a laser power of 200 W. The results indicate that LPBF samples printed at 500 mm/s exhibited larger grain size for TNZ-33 and TNTZ-25 alloys, characterized by a fine dendritic texture and minimal defects. For 750 and 1000 mm/s speeds grain size decreased due to higher cooling rates imposed by previous substrate printed layers. Microhardness remained constant for TNZ-33 and TNTZ-25 alloys regardless of laser speed (308 - 316 HV and 315 - 323 HV, respectively) and elastic modulus of E=75 and 70 GPa were obtained for TNZ-33 and TNTZ-25 alloys.

This study presents new powders produced by advanced ultrasonic atomization method and 3D Printing of multiprincipal equimassic Ti-33Nb-33Zr and Ti-25Nb-25Ta-25Zr alloys with lower elastic modulus suitable for special metallic biomaterials for implant applications. Keywords: β-Ti alloys; multiprincipal alloy, ultrasonic atomization, 3D printing; elastic modulus; mechanical properties; implants.

Website: https://www.biometcam.ufscar.br/

KEYNOTE SPEAKER 8

Prof Mohamed Abdel-Hady Gepreel
Egypt-Japan University of Science and Technology



Modeling the high temperature deformation of a novel TiNbTaMo alloy for biomedical applications

Bio: Prof. Gepreel is of metallurgical engineering background and got his PhD from Nagoya University, Japan in 2008. He worked in Nagoya University then Tohoku University, Japan, till 2010 when he moved to Egypt-Japan University of Science and Technology (E-JUST), Egypt. He is professor of advanced materials at E-JUST since 2019 and leading the Advanced Functional Metallic Materials Lab. His research is focusing on alloy design and microstructure control of advanced alloys. He worked in developing New generation of Ti-alloys for biomedical applications, Ultra-high strength Ti-alloys, Negative and zero thermal expansion alloys and recently developing new functional High entropy alloys. He received the State's Award (Egypt) in Engineering, 2014, beside more than 15 national and international awards. He was visiting professors to many well-known institutes, such as; Tohoku University, Japan, IIT-Madras, India, Michigan State University, USA, Korean Basic Science Institute, Korea, Joint Institute for Nuclear Research, Russia, Sao Paulo State University, Brazil. He supervised more than 30 M.Sc. and 20 PhD thesis. He shared in organizing 15 International conferences. He was invited as Keynote speaker /invited speaker for more than 30 international conferences worldwide. He had 20 funded research projects (national and international) and more than 210 publications [including filed 10 Patents, 10 Book chapters, 115 Journal papers, and 95 international conferences] with

total citation >5500.

Abstract: A novel biomedical β-Ti alloy Ti-13Nb-1.5Ta-3Mo (at%) was recently **designed** for biomedical applications. High temperature flow behaviour of this alloy was studied using isothermal hot compression tests across various strain rates (0.01 – 10s-1) in the temperatures rage of (800 – 9000C). To establish a relationship between flow stress and processing parameters, a strain-compensated Arrhenius constitutive model (SC Arrhenius) and a back-propagated artificial neural network model (BP-ANN) were developed.

Statistical analysis of the flow stress predictions revealed that the BP-ANN model outperformed the SC Arrhenius model, achieving a correlation coefficient (R) of 0.9997 and an average absolute relative error (AARE) of 0.5333%, compared to the SC Arrhenius model's R value of 0.9882 and AARE of 4.3855%. Additionally, hot processing maps were constructed based on the dynamic materials model (DMM), utilizing experimental flow stress values at true strains of 0.2, 0.4, and 0.55 to assess flow instability regimes and optimize processing parameters. The accuracy of these hot processing maps was corroborated through microstructural evolution studies. Overall, the findings indicate that the developed models can reliably predict the flow stress of the Ti-13Nb-1.5Ta-3Mo alloy across a wide range of experimental conditions, facilitating the evaluations of hot deformation mechanisms and microstructural changes.

* Mohamed.gepreel@ejust.edu.eg

KEYNOTE SPEAKER 9

Prof Alain Bernard
Honorary President of France Additive, Honorary Professor Centrale Nantes, Fellow of the Academy of Technologies of France



Ontological approach for a systemic improvement of AM value chains

Bio: Honorary Prof. Alain BERNARD, graduated in 1982, PhD in 1989, was associate-Professor, from 1990 to 1996 in Centrale Paris. From Sept. 1996 to Oct. 2001, he was Professor in CRAN, Nancy I, and leaded the "Integrated Design and Manufacturing" team. Since Oct. 2001, he has been Professor at Centrale Nantes and Dean for Research from 2007 to 2012. He retired in Sept. 2021 and became emeritus Professor for 2 years. Now, he is Honorary Professor of Centrale Nantes and emeritus researcher in LS2N laboratory (Laboratory of Digital Sciences in Nantes - UMR CNRS 6004), former head of the "Systems Engineering – Products – Processes -Performances" team. His research topics are KM, PLM, information system modeling, enterprise modeling, systems performance assessment, virtual engineering, additive manufacturing. He supervised 40 PhD students. He published more than 150 papers in refereed international journals and books. He is Honorary President of France Additive (French Association on Additive Manufacturing), former vice-chairman of WG5.1 of IFIP (Global Product Development for the whole product lifecycle) and Fellow emeritus of CIRP. In 2018, he has been elected as Fellow of the National Academy of Technologies of France.

Abstract: Despite the advantages of additive manufacturing (AM), many problems related to the management of its value chain must be solved to

get the highest benefits. Value chain management refers to various decision support processes such as: technical process selection supporting strategy, machine parameters configuration, cost estimation and prediction of potential part defects, etc.

This keynote, issued from the PhD Thesis of Dr. Qussay Jarrar (https://www.researchgate.net/profile/Qussay-Jarrar), deals with the above issues and aims of proposing a decision support and traceability Framework in the case of AM powder bed fusion technology.

To do so, knowledge engineering techniques are used to exploit the large amount of data generated throughout the FA process, but also to consider human expertise in the field.

The structure of the knowledge base is designed as domain ontology for AM and associated with a rule-based inference engine. The management of the value chain is focusing on the generation of process alternatives and the assistance to the realization of budget quotations for AM projects. The integration of knowledge base with decision aid allows the estimation of some parameters of the cost model for costing perspective. The history resulting from traceability process allows comparing the estimated cost with the real one, and to improve the estimation of influencing parameters by similarity based reasoning.

The proposed approach has been applied on three industrial cases provided by a partner of the SOFIA project. The interactions with industrial experts have allowing the consolidation of the proposed model regarding their real practices.

Website: https://research.ec-nantes.fr/fr/annuaire/m-alain-bernard

PLATINUM SPONSORS

Department of Science, Technology and Innovation (DSTI)
www.dsti.gov.za/

science, technology & innovation
Department:
Science, Technology and Innovation
REPUBLIC OF SOUTH AFRICA

MINTEK
https://mintek.co.za/

MINTEK
A global leader in mineral and metallurgical innovation

GOLD SPONSORS

University of Limpopo (UL)
www.ul.ac.za

Central University of Technology, Free State (CUT)
www.cut.ac.za

SILVER SPONSORS

Anton Paar
www.anton-paar.com/za-en/

AMI
Advanced Materials Initiative

BRONZE SPONSORS

CPAM
The Collaborative Programme in Additive Manufacturing

NECSA
The South African Nuclear Energy Corporation (Necsa) SOC Ltd
www.necsa.co.za

necsa
We're in your world
South African Nuclear Energy Corporation SOC Limited

PROGRAMME

TUESDAY, 27 OCTOBER 2026
8:30 TO 12:45

Venue: Day Lily, Protea Hotel Polokwane Ranch Resort, South Africa

PRE-CONFERENCE SEMINAR ON DESIGN AND ADDITIVE MANUFACTURING OF SAILPLANE AND JEWELLERY PARTS

Hosted by the Central University of Technology, Free State (CUT)
Sponsored by the Department of Science, Technology and Innovation

CUT
CENTRAL UNIVERSITY OF TECHNOLOGY, FREE STATE

science, technology & innovation
Department:
Science, Technology and Innovation
REPUBLIC OF SOUTH AFRICA

Programme Director: Dr LF Monaheng

08:30 – 09:00
Registration
09:00 – 09:05
Welcoming Address: **Dr LF Monaheng**, CUT
09:05 - 09:30
Opening Address: **Ms Wilna du Plessis**, CPAM
09:30 - 10:00
Certification of materials for aviation and additive manufacturing **Prof Attie Jonker, Jonker Sailplanes**
10:00 - 10:20
Redesign of a sailplane tailwheel fork using topology optimisation for laser powder bed fusion manufacturing in Ti6Al4V(ELI) **Tristan Strydom,** Lehlohonolo Francis Monaheng, Claudia Polese and Johan Bosman
10:20 - 10:40
Enhancing surface morphology of LPBF TI6Al4V(ELI) specimens through rotary and vibratory tumbling **Neo Moabi,** Lehlohonolo Francis Monaheng, Willie du Preez, and Attie Jonker

10:40 - 11:10 **TEA**

11:10 - 11:30
Conceptual and parametric design development of a modified reciprocating compressor cylinder head with integral cooling channels and a finned piston **Junior Makhubela,** Gys Jacobs and Annaléne Olwagen
11:30 - 11:50

Structural and elastic properties of two commercial binary Pt jewellery alloys – ab initio study **Maje Phasha,** Melita Lekganyane, Joseph Moema and Donald Mkhonto
11:50 - 12:10
A study into the laser powder bed fusion of customised pure platinum jewellery **Imdaadulah Adam,** Willie du Preez, Charmaine Johnston and Allan Ross
12:10 - 12:30
First-principles study of thermodynamic and mechanical enhancement in V and Cr alloyed FCC platinum for jewellery applications **Mawisha Mafifi,** Donald Mkhonto, Mwende Mbilo, Maje Phasha and Refilwe Mapasha
12:30 - 12:45
General Discussion
13:00 – 14:00 **LUNCH**

RAPDASA

RAPID PRODUCT DEVELOPMENT ASSOCIATION OF SOUTH AFRICA

PROGRAMME

TUESDAY, 27 OCTOBER 2026
09:00 TO 15:00

Venue: Rose Room,
Protea Hotel Polokwane Ranch Resort, South Africa

PRE-CONFERENCE SEMINAR ON COMPUTATIONAL & DATA-DRIVEN MODELLING

Hosted by MINTEK,
Supported by the Department of Science, Technology and Innovation

CoSAami
CONFERENCE OF THE SOUTH AFRICAN ADVANCED MATERIALS INITIATIVE

MINTEK
A global leader in mineral and metallurgical innovation

science, technology & innovation
Department:
Science, Technology and Innovation
REPUBLIC OF SOUTH AFRICA

Programme Director: Dr Ramogohlo Diale-Boshielo

08:30 – 09:00
Registration
09:00 – 09:10
Welcoming Address: **Dr Ramogohlo Diale-Boshielo**
09:10 - 09:40
Opening Address: **Prof Krishna Govender**
09:40 - 10:00
Effect of TiCl4 medium on Ti13 cluster: a molecular dynamics study **Andile Mazibuko** and Hasani Chauke
10:00 - 10:20
Computational mechanical behaviour in high entropy alloys **Abidemi Adeyoye**, Patricia Popoola, Olawale Popoola, Samson Adeosun and Modupeola Dada
10:20 - 10:40
Numerical simulation of Fano resonant electromagnetic split ring resonators **Realeboga Dikole** and Edwin Magidimisha

10:40 - 11:10 **TEA**

11:10 - 11:30
A comparison of classical machine learning and vision language models for TB diagnostics **Kelvin Mpofu**, Nkgaphe Tsebesebe and Sello Manoto
11:30 - 11:50
A comparative analysis of classical planning algorithms for MAV navigation in dynamic subterranean environments **Trymore Aloni**, Makhosazana Moyo and Turgay Celik
11:50 - 12:10

Design and characterization of Si-Ge compounds for enhanced silicon-based anodes in advanced battery applications
Samson Singo, Katlego Phoshoko, Tshidi Mogashoa, Phuti Ngoepe and Raesibe Ledwaba

12:10 - 12:30

Adsorption properties of Fe and Cr modified GaN monolayer for CH2O detection
Malesela Walter Makgoba, Mokete Abram Mahladisa, Malili Matshaba, Moshibudi Ramoshaba and Thuto Mosuang

12:30 - 12:50

Effect of Ta on the magnetic and mechanical properties of $Fe_{50}Co_{43.75}Ni_{6.25}$ alloy
Dineo Maepa, Tshegofatso Phaahla, Ramogohlo Diale-Boshielo, and Hasani Chauke

13:00 - 14:00
LUNCH

14:00 - 14:20

Gaussian process regression versus response surface methodology for laser powder bed fusion process qualification in dimensionless coordinates
Michael Thomson and Thorsten Becker

14:30

Closure

15:00
COFFEE

RAPDASA

RAPID PRODUCT DEVELOPMENT ASSOCIATION OF SOUTH AFRICA

Co-hosted by **MINTEK** and the **University of Limpopo**

Annual CONFERENCE

www.rapdasa.org

PROGRAMME

FROM PROTOTYPE TO PRODUCTION: TRANSLATING RESEARCH INTO REALITY

PROGRAMME

Venues

FOR BREAKAWAY SESSIONS

SAFARI

DAY LILY

ROSE ROOM

PROGRAMME

TUEDAY, 27 OCTOBER 2026

08:30

PRE-CONFERENCE SEMINAR

Design and Additive Manufacturing of Sailplane and Jewellery Parts.
Programme Director: Dr Francis Monaheng

VENUE: DAY LILY

08:30

PRE-CONFERENCE SEMINAR

Computational and Data-driven Modelling
Programme Director: Dr Ramogohlo Diale-Boshielo

VENUE: ROSE ROOM

09:00

INDUSTRY DAY

Programme Director: Mr David Mauchline
Venue: Makhulu

17:00

WELCOMING COCKTAIL & REGISTRATION

Venue: Lapa

PROGRAMME

WEDNESDAY, 28 OCTOBER 2026

07:30	Registration
PLENARY SESSIONS IN THE SAFARI ROOM	
08:00	Plenary Sessions: Chair: **Dr Marandela Mulaudzi**
08:10	Welcoming: Chairperson of RAPDASA - **Dr Washington Makoana**
08:30	Opening address: **Dr Jones Papo,** Group Executive: Mining, Materials and Automation, Mintek, South Africa
PLENARY SESSIONS IN THE SAFARI ROOM	
Keynote address K1:	
09:00	**Mr Vince Zhao,** Farsoon Technologies, China: From Laboratory Research to Industrial-Scale up of Additive Manufacturing
Keynote address K2:	
09:30	**Dr Ndanduleni Lethole,** Sefako Makgatho Health Sciences University, South Africa: From Binary to Ternary Pt-Based Magnetic Alloys: First-Principles Insights into Structure, Magnetism and Materials Design
10:00	**TEA/COFFEE BREAK**

BREAKAWAY SESSIONS

BREAKAWAY SESSIONS

SAFARI	DAY LILY	ROSE ROOM
Session Chair: Dr Maje Phasha	**Session Chair: Dr Hertzog Bissett**	**Session Chair: Prof Hasani Chauke**
Theme: Materials Engineering	**Theme: AM Material and Part Characterisation**	**Theme: Computational & Data-driven Modelling**
SAFARI	**DAY LILY**	**ROSE ROOM**
	10:30	
Modelling disordered alloys: density functional theory and machine learning. **Invited speaker: Dr Ricardo Grau-Crespo** (Online)	Integrated material characterisation and computational modelling capability for defence protection technologies. **Invited speaker: Mr Mangalani Miyambo**	Built here, used here: Localising manufacturing technology from applied research. **Invited speaker: Dr Luyolo Mabhali**
	11:00	
First principles study of the structural, magnetic and electronic properties of Fe50Pt50-xCux alloys. **Mashilo Matlala**	Characterisation of titanium metal powder produced by ultrasonic atomisation from scrap parts. **Kiyaasha Dyal Ukabhai**	Prediction of stable structures in Ti-V-Mn AB2-type alloys using a cluster expansion approach. **Vukosi Chauke**
	11:20	
β-constrained crystallographic evolution of B19′ TiNi: a DFT study with comparison to experimental XRD data. **Bongani Ngobe**	Correlation between microstructure and mechanical properties in A356 aluminum alloy. **Philisile Sekgata**	Comparative performance analysis of OpenCV and ArrayFire for computer vision systems. **Patrick Malatjie**
	11:40	
Coupled CFD–DQMOM modeling of titanium nanoparticle formation and size evolution during plasma-assisted vapor condensation. **Alex Seya (Online)**	Comparison of additively manufactured lattice structure types for sustainable basalt fibre reinforced sandwich panel composites. **James Dicks**	The structural, magnetic, and elastic properties of the Mn50Al50-xMgx alloys: a DFT study. **Thabang Mokwena**

12:00		
Benchmarking artificial neural networks against traditional regression models for the scalable prediction of Ti-6Al-4V powder spheroidization. **Justin Mbwebwe (Online)**	Simulation framework and thermal descriptor extraction for direct energy deposition of Ti-Nb-Zr alloys. **Tinashe Matyatya**	Unsupervised learning for biomedical data classification. **Kelvin Mpofu**

12:30 - 13:00

POSTER PRESENTATIONS IN MAKHULU
Chair: Dr. Bathusile Masina

13:00
LUNCH BREAK

PLENARY SESSIONS IN THE SAFARI ROOM

Keynote address K3: (Online)

14:00	**Dr Terry Wohlers,** Distinguished Fellow of Advanced Manufacturing at Wohlers Associates, powered by ASTM International, USA: Evolution of AM and Trends Shaping its Future.

BREAKAWAY SESSIONS

BREAKAWAY SESSIONS

SAFARI	DAY LILY	ROSE ROOM
Session Chair: Prof Thywill Dzogbewu	**Session Chair: Dr Nthabiseng Cholo**	**Session Chair: Dr Ramogohlo Diale-Boshielo**
Theme: Materials Engineering	**Theme: AM Material and Part Characterisation**	**Theme: Computational & Data-driven Modelling**
14:30		
A localised heat treatment process for hardenable steels . **Maxwell Vos**	Effect of alloying on microstructure and mechanical properties of high chromium white cast iron (HCWCI) for mill liner application. **Joseph Moema**	Automated micrograph feature extraction and machine learning surrogate benchmarking for bead geometry prediction in LMD repair of Al-Si alloys . **Laone Ronaldo Pilane**
14:50		
Effect of laser power on the microstructure and microhardness of CpTi/ TiC composites deposited on Ti6Al4V by laser metal deposition. **Xolile Michael Mdlalo (Online)**	Effect of surface preparation techniques on hybrid investment cast-additive manufactured Ti-6Al-4V components. **Kim du Preez**	Electronic charge-transfer dynamics of Zn-O co-adsorption on MO2 (M= Mn, Ti, V) (110) surfaces in Zn-air batteries. **Percy Ngobeni**
15:10		
The effect of heat treatment on microstructure and hardness of 9% Ni and 25% Mn cast steels. **Sibongile Mamonyane**	Mechanical and corrosion behaviour of TiC thin films deposited on brass substrate by RF magnetron sputtering. **Musibau Ogunlana**	First-principles study of the effect of Ni and Pt addition on the ductility of brittle FCC iridium: structural, mechanical, and electronic properties. **Thabo Nhlenyama**
15:30 TEA/COFFEE BREAK		

BREAKAWAY SESSIONS

SAFARI	DAY LILY	ROSE ROOM
Session Chair: Dr Washington Makoana	**Session Chair: Mr James Dicks**	**Session Chair: Dr Kemeridge Malatji**
Theme: Materials Engineering	**Theme: AM Post Processing and Qualification**	**Theme: Computational & Data-driven Modelling**
16:00		
The effect of Nb and V on the metallurgical properties of FeCo alloy. **Ramogohlo Diale-Boshielo**	Microstructure–hardness response to localised laser tempering of LMD 17-4 PH stainless steel. **Michael Femi Olabisi**	Atomistic simulation synthesis of LixTiO2 nanoporous as an anode electrode material for energy storage in lithium-ion batteries. **Blessing Rikhotso**
16:20		
Finite element analysis of weight-strength trade-offs in Ti6Al4V sternal implant design. **Eric Dlamini (online)**	Digital twin-based monitoring and data management in the laser powder bed fusion process chain using a learning integrated manufacturing system. **Kekeletso Thejane**	First principles study of electronic and thermoelectric properties of hexagonal tungsten disulphide (WS2). **Moshibudi Ramoshaba**
17:00 RAPDASA Annual General Meeting		

PROGRAMME

THURSDAY, 29 OCTOBER 2026

08:00	Welcoming: Dr Marandela Mulaudzi
PLENARY SESSIONS IN THE SAFARI ROOM	
08:05	Plenary Sessions: Chair: **Dr Washington Makoana**
Keynote address K4: (Online)	
08:05	**Prof Diego Correa,** Department of Physics and Meteorology, Faculty of Sciences of UNESP, Brazil: Innovative design of biomedical high entropy alloys.
Keynote address K5: (Online)	
08:35	**Prof Ulrich E. Klotz,** Munich University of Applied Sciences, Germany: From Phase Diagram to Digital Twin: An Integrated Approach to the Development of Precious Metal and Technical Alloys.
Keynote address K6:	
09:05	**Prof Peace Mkhonto**, Materials Modelling Centre, University of Limpopo, South Africa: Application of Computational Modelling in Reagents Design for Separation of Minerals and Adaptation of Machine Learning Approach

BREAKAWAY SESSIONS

BREAKAWAY SESSIONS

SAFARI	DAY LILY	ROSE ROOM
Session Chair: Dr Maria Mathabathe	**Session Chair: Prof Didier Nyembwe**	**Session Chair: Dr Donald Mkhonto**
Theme: Materials Engineering	**Theme: Product Design and Development**	**Theme: Process Development**
09:40		
Phase predictions and microstructural characterisation of Cu-modified low-nickel HerculesTM stainless steel. **Melanie Smit**	A pseudo-1D thermo-hydraulic design methodology for additively manufactured Archimedean spiral coil condensers. **Nicolaas Steenekamp**	Evaluation of thermal stability and phase transformation in β-type Ti-10Nb-1Ru alloy. **Duduzile Nkomo**
10:00		
A review on additive manufacturing of metal carbides. **Tumelo Moloi**	A low-cost UAV propulsion thrust and torque measurement rig. **Michael Thomson**	System dynamics-based modelling for remaining useful life estimation of bearings in rotating machinery. **Themba Mashiyane**
10:20		
Materials strength of spheroidal graphite iron plates welds in as-cast and heat-treated conditions. **Mokgohloa Caroline Mphela**	The potential for additively manufactured triply periodic minimal surface components to improve the efficiency of reciprocating compressors. **Annaléne Olwagen**	Evaluation of HHD62G medical-grade high-density polyethylene before use in material extrusion additive manufacturing for fabrication of craniomaxillofacial augmentation implants **Rebakakgosi Mohutsiwa**
10:40		
Hardness and microstructural property evaluation of chromium alloyed 22wt% Mn alloy compared to commercial 9wt% Ni alloy in as-cast and solution-treated conditions. **Lebedike Mampuru**	Investigating a lattice structure for a 316L stainless steel injection mould cavity. **Andile Ndlovu**	Performance evaluation of a polynomial regression based NUC for variable integration-time. **Mathews Chirindo**

11:00
TEA/COFFEE BREAK

BREAKAWAY SESSIONS

SAFARI	DAY LILY	ROSE ROOM
Session Chair: **Dr Francis Monaheng**	**Session Chair:** **Mrs Londiwe Motibane**	**Session Chair:** **Dr Bathusile Masina**
Theme: **Materials Engineering**	**Theme:** **AM Material and Part Characterisation**	**Theme:** **Process Development**
	11:30	
Analysis of high Mo content and its effect on compression strength of binary β-Ti-Mo alloys for vascular stent applications. **Nthabiseng Abigail Moshokoa**	Comparative evaluation of phase constitution and microstructure in directed energy deposition additively manufactured CP-Ti, Ti-11Nb and Ti-9Fe alloys. **Mavis Khathutshelo Nemavhola**	An initial dynamic time-driven activity-based costing approach for identification of cost drivers within the laser powder bed fusion process chain. **Tadiwanashe Zinzombe**
	11:50	
Metallurgical analysis of Ti–42 %Nb biomedical alloy subjected to different cooling conditions. **Linah Twala**	Hardness gradients and galvanic corrosion behaviour of hybrid laser powder bed fusion - Al10SiMg on wrought 6061 aluminium substrates. **Ngeleshi Michel Kibambe**	Experimental investigation of process characteristics in a 5-axis composite additive manufacturing system. **Daniel Kirkman**
	12:10	
Casting and characterisation of Ni-based filler materials used for welding of spheroidal graphite cast iron (SG42) . **Dieketseng Maya (online)**	The effect of ruthenium precursor chemistry on the morphology of electrodeposited coatings on 304L stainless steel. **Nomalungelo Maphanga**	Use of ultrasonic atomisation in recycling of used powder and scrap from stainless steel. **Donald Mkhonto**
	12:30	
Flexural performance of sustainable fibre-reinforced composites using basalt and flax. **Mpho Ntloane**	Antibacterial and biocompatibility properties of additively manufactured titanium–Cu alloy implants. **Nthabiseng Cholo**	

13:00
LUNCH BREAK

14:00 - 14:30
POSTER PRESENTATIONS IN MAKHULU
Chair: Dr. Bathusile Masina

BREAKAWAY SESSIONS

SAFARI	DAY LILY	ROSE ROOM
Session Chair: **Dr Daniel Kirkman**	**Session Chair:** **Dr Joseph Moema**	**Session Chair:** **Prof Kobus van der Walt**
Theme: **Materials Engineering**	**Theme:** **Rapid Casting**	**Theme:** **Industry presentations**
	14:30	
The effect of heat-treatment on 28% Mn and 9% Ni austenitic steels for use in cryogenic LNG applications. **Tokelo Taba**	Influence of sand grain fineness and print resolution (DX) on the mechanical properties of additive binder jetting manufactured sand moulds. **Jonathan Kabasele**	Additive manufacturing: from material characterization to quality performance. **Zwelihle Ndlovu & Bomkazi Sobuwa (Anton Paar)**
	14:50	
Effect of microstructure on corrosion behaviour of Ti-15Cu alloy subjected to different heat treatment cycles. **Zanele Phasha**	Integrating the UNSDGs into South Africa's 3D sand printing industry. **Neo Tshabalala**	CTI: a computational tool for industrial investment readiness in Africa. **Vince Mbanze (Nexusnode)**
	15:10	
Scanning strategy on the mechanical properties of heat treated additively manufactured 1.2709 tool steel. **Yoshlyn Naidoo**	Smart supplier selection in metal casting processes: integrating MCDM and industry 4.0 – a critical review. **Samson Oguntuyi**	From print to performance: unlocking additive manufacturing potential through heat treatment and smart hardness verification. **Wise Mukhola (Verder Scientific)**

15:30		
Material selection and traditional reconstruction techniques for cranial plate implants: a review. **Onesimo Mjiba**	Effect of FeSi-based inoculants on microstructure, indentation size effect and strain gradient plasticity in grey cast iron. **Pertunia Seema**	Microstructural characterisation of AM components using penetrative radiation techniques. **Andrew Venter (Necsa)**
15:50 TEA/COFFEE BREAK		

BREAKAWAY SESSIONS

SAFARI	DAY LILY	ROSE ROOM
Session Chair: Dr Washington Makoana		
Theme: Technology Innovation Agency support		
16:20		
The technology commercialization journey. **Dembe Nenzhelele**		
16:40		
Technology development funding. **Iodien Rensburg**		
17:00 CLOSURE		

18:30 for 19:00
GALA DINNER
Invited Speaker:
Dr Jeffrey Mabelebele, Vice-Chancellor of University of Limpopo

PROGRAMME

FRIDAY, 30 OCTOBER 2026

08:05	Welcoming: **Dr Marandela Mulaudzi**
PLENARY SESSIONS IN THE AUDITORIUM	
08:05	Plenary Sessions: Chair: **Prof André van der Merwe**
Keynote address K7	
08:05	**Prof Conrado Afonso**, Federal University of São Carlos (UFSCar), Brazil: 3D Printing by LPBF of Multiprincipal Equimassic β Ti-Nb-Zr(-Ta) alloys from Ultrasonic Atomized powder for Implant Applications.
Keynote address K8	
08:35	**Prof Mohamed Abdel-Hady Gepreel**, Egypt-Japan University of Science and Technology: Modeling the high temperature deformation of a novel TiNbTaMo alloy for biomedical applications.
Keynote address K9	
09:05	**Prof Alain Bernard**, Honorary President of France Additive, Honorary Professor Centrale Nantes, Fellow of the Academy of Technologies of France: Ontological approach for a systemic improvement of AM value chains
09:40 TEA/COFFEE BREAK	

BREAKAWAY SESSIONS

BREAKAWAY SESSIONS

SAFARI	DAY LILY	ROSE ROOM
Session Chair: Ms Keke Thejane		
Theme: Product Design and Development & AM Post Processing and Qualification		
	10:10	
Optimum processing of cpTi using laser powder bed fusion. **Nthabiseng Cholo**		
	10:30	
Cylindrical window mounting design for a mirror-steered optical system. **Andrew Baloyi**		
	10:50	
Effect of heat treatment on the microstructure and hardness of laser powder bed fusion manufactured Inconel 718. **Elelwani Tshisimba**		
	11:10	
Effect of heat treatment on microstructure and hardness of DED fabricated Ti-11Nb-9Fe alloy. **Dimakatso Moyan**		
11:40 CLOSURE		

12:00
FINAL LUNCH

RAPDASA

RAPID PRODUCT DEVELOPMENT ASSOCIATION OF SOUTH AFRICA

ABSTRACTS

ABSTRACTS TRACKS

1. Design & AM of Sailplane & Jewellery Parts Seminar.....94
2. Computational & Data-driven Modelling Seminar.....113
3. Materials Engineering.....140
4. Additive Manufacturing Material & Part Characterisation.....202
5. Computational & Data-driven Modelling.....241
6. Additive Manufacturing Post Processing & Qualification.....267
7. Product Design and Development.....282
8. Process Development.....305
9. Rapid Casting.....327
10. Industry Presentations.....339
11. Poster Abstracts.....344

01

ABSTRACTS

Seminar: Design and Additive Manufacturing of Sailplane and Jewellery Parts

Redesign of a sailplane tailwheel fork using topology optimisation for laser powder bed fusion manufacturing in Ti6Al4V(ELI)

Tristan Strydom[1*], *Lehlohonolo Francis* Monaheng[2], *Claudia* Polese[1&3], and *Johan* Bosman[4]

[1]School of Mechanical, Industrial and Aeronautical Engineering, University of the Witwatersrand, Johannesburg 2050, South Africa
[2]Department of Mechanical and Mechatronics Engineering, Faculty of Engineering, Built Environment and Information Technology, Central University of Technology Free State, Bloemfontein 9300, South Africa
[3]ARUA Centre of Excellence in Materials, Energy and Nanotechnology, University of the Witwatersrand, Johannesburg 2050, South Africa
[4]North-West University, School of Mechanical Engineering, Faculty of Engineering, Potchefstroom, South Africa

Abstract. Laser powder bed fusion (LPBF) enables the fabrication of lightweight aerospace components designed through topology optimisation (TO), yet fatigue concerns in LPBF parts is a limiting factor for its adoption in producing critical structural components. This study investigates the TO redesign of a legacy computer numeric control machined aluminium alloy sailplane tailwheel fork for production in Ti6Al4V(ELI) through L-PBF. Using Altair Inspire, the geometry was optimised to achieve a minimum 20% mass reduction while maintaining a 1.5 safety factor. Preliminary FEM analysis evaluates stress distributions against mandated standards.

1 Introduction

Laser powder bed fusion (LPBF), also termed selective laser melting (SLM), has gained widespread adoption in various industries, particularly aerospace, where there is substantial demand for components with high strength-to-weight ratios. This technology enables improved performance while reducing material wastage. Additionally, additive manufacturing (AM) facilitates the production of complex-shaped, consolidated components, thereby reducing manufacturing and assembly time and production cost, ultimately reducing the buy-to-fly ratio [1]. Such complex and lightweight parts are often achieved via topology optimisation (TO) and other design for additive manufacturing (DfAM) strategies aimed at minimising mass and material usage while maintaining structural stiffness. These optimised parts are often impossible to manufacture using conventional methods. Furthermore, AM enables the efficient use of high-performance materials that are conventionally difficult and costly to process, such as Ti6Al4V(ELI), thereby further enhancing the advantage of combining AM with TO.

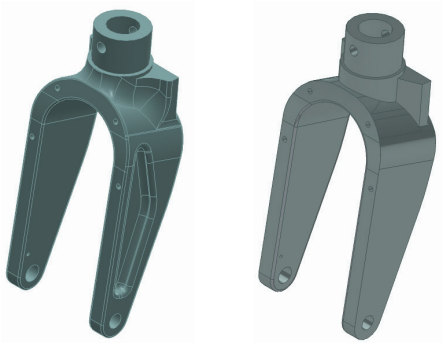
* Corresponding author: Tristan.Strydom@wits.ac.za

While a small number of certified parts have been produced via LPBF, such as the #4/5 bearing housing for the ATF3-6 turbofan engine used in the Dassault Falcon 20G [2], usage of LPBF to produce structural aircraft parts is still limited. A significant challenge associated with LPBF is the potential presence of defects, such as high surface roughness and pores, which adversely affect mechanical performance and significantly reduce fatigue life [1], [3]. These effects may be exacerbated when LPBF is used to manufacture topologically optimised components, where such designs do not account for manufacturing-induced defects and fatigue-related constraints.

The broader scope of the study aims to investigate using LPBF to produce a qualifiable critical aircraft component, similar to work by Monaheng et al. [4], however, with improvements to the work by addressing part failure under fatigue loading through suitable post-processing. This work presents the initial phase of the broader study, with an investigation into the redesign of an existing structural aircraft component using topology optimization and DfAM strategies.

2 Methodology

A suitable component for investigation was identified as the tailwheel fork of a sailplane, shown in Fig. 1 (a), which presented a non-flight-critical structural part that experiences substantial loadings to warrant the investigation of fatigue performance once TO was completed. The current production method for the legacy part employs traditional CNC machining out of an aluminium alloy. The first phase of work was the redesign of the tailwheel using TO. The goal was to replicate the results of [4] and reduce the mass of the tailwheel fork by a minimum of 20%, whilst retaining the mandated safety factor of 1.5, as required by aviation standards. The redesigned tailwheel fork will be printed in Ti6Al4V(ELI).



(a) (b)

Fig. 1. (a) Legacy design of the tailwheel fork, and (b) the simplified geometry of the tailwheel fork for topology optimisation.

As seen in Fig. 1. (b), the part was first simplified to allow for more material in the design space of the TO, as is common practice in part redesigns. The topology optimisation was then conducted using Altair Inspire, targeting a minimised mass whilst retaining a 1.5 factor of safety. This was achieved in Altair using the minimise mass function (where a safety factor must be identified) or the maximise stiffness function, which prioritises a reduction in mass

by selecting a percentage utilisation of the design space. The properties of the legacy part, simplified part, and various TO parts were examined and compared to assess the mass reduction. Once various TO designs were obtained, an analysis of the performance against the loading conditions was conducted as an FEM stress analysis. This was to investigate the effect of the TO on stresses generated within the part under the nominal and ultimate loads, and to assess the adherence to the required safety factor.

3 Results and discussion

Initial iterations using the "Minimise Mass" (MM) and "Maximise Stiffness" (MS) functions in Altair Inspire successfully achieved the target 20% mass reduction, though the resulting organic geometries necessitated a refinement of the design space to ensure printability via LPBF. It is likely that the use of Ti6Al4V, allowing for thinner wall thicknesses, accounts for a majority of the mass saving.

The FEM stress analysis of the optimised fork shapes indicates that while mass is reduced, peak stresses remain within the allowable limits for Ti6Al4V, and that a safety factor of 1.5 is achievable with significant mass reduction. A comparison between the "Maximise Stiffness" (MS) and "Minimise Mass" (MM) approaches revealed a more aggressive reduction in mass and more organic shapes in the MM approach versus more material left in the MS approach to ensure the target safety factor.

4 Conclusions

The redesign of the sailplane tailwheel fork met the dual criteria of a 20% mass reduction and a factor of safety of 1.5, demonstrating the efficacy of the DfAM workflow. It was found that TO and a transition to Ti6Al4V can successfully reduce the mass of a sailplane tailwheel fork, whilst maintaining part stiffness to achieve a 1.5 factor of safety. This indicates that the redesign of the tailwheel fork is possible, and that TO does not negatively impact theoretical part performance. While the static FEM results are promising, the next phase of work aims to address the impact of LPBF-induced surface defects on the part's fatigue life. This will involve developing an understanding of the optimised part's fatigue response through both simulation and physical testing.

References

1. B. Blakey-Milner, P. Gradl, P., G. Snedden, M. Brooks, J. Pitot, E. Lopez, M. Leary, F. Berto, A. du Plessis, Metal additive manufacturing in aerospace: A review. Mater. Des. **209**, 110008 (2021) https://doi.org/10.1016/j.matdes.2021.110008
2. A. Jensen, Honeywell Achieves FAA Certification For First Flight-Critical Engine Part Built From Additive Manufacturing. (Honeywell, 2020) https://aerospace.honeywell.com/us/en/about-us/press-release/2020/08/faa-certification-for-first-flight-critical-engine.
3. N. Sanaei, A. Fatemi, Defects in additive manufactured metals and their effect on fatigue performance: A state-of-the-art review. Prog. Mater. Sci. **117**, 100724 (2021) https://doi.org/10.1016/j.pmatsci.2020.100724
4. L. F. Monaheng, W. B. du Preez,, C. Polese, Failure analysis of a landing gear nose wheel fork produced in Ti6Al4V(ELI) through selective laser melting, Eng. Fail. Anal. **153**, 107548 (2023) https://doi.org/10.1016/j.engfailanal.2023.107548

Enhancing surface morphology of LPBF TI6AI4V(ELI) specimens through rotary and vibratory tumbling

Neo Moabi[1*], *Lehlohonolo Franscis* Monaheng[1], *Willie* du Preez[2], and *Attie* Jonker[3]

[1]Department of Mechanical and Mechatronics Engineering, Faculty of Engineering, Built Environment and Information Technology, Central University of Technology, Free State, Bloemfontein, 9300, South Africa
[2]Centre for Rapid Prototyping and Manufacturing, Faculty of Engineering, Built Environment and Information Technology, Central University of Technology, Free State, Bloemfontein, 9300, South Africa
[3]Jonker Sailplanes, Potchefstroom, 2520, North-West, South Africa

Abstract. Laser Powder Bed Fusion (LPBF) enables the fabrication of highly complex Ti6Al4V(ELI) aerospace components with high strength-to-weight ratio. However, the process often produces surfaces with high surface roughness and partially fused particles that negatively affect mechanical performance and fatigue life. Therefore, post-processing techniques are required to improve the surface condition of additively manufactured components. Surface finishing processes such as rotary tumbling and vibratory tumbling offer practical post-processing solutions for improving the surface integrity of L-PBF Ti6Al4V(ELI) specimens. These finishing techniques remove surface imperfections, resulting in smoother surfaces.

1 Introduction

Ti6AL4V is one of the most widely used titanium alloys in aerospace applications due to its high strength-to-weight ratio, corrosion resistance, and excellent mechanical performance [[1], [2]. The Extra-Low Interstitial (ELI) grade offers improved ductility and fracture toughness, making it suitable for safety-critical structural components [3]. Laser Powder Bed Fusion (LPBF) is widely used for the fabrication of complex titanium components, offering advantages such as reduced material waste and greater design flexibility compared to conventional manufacturing processes [4], [5].

Despite these advantages, L-PBF produced Ti6Al4V components often exhibit poor surface quality resulting from the layer-by-layer fabrication process. Partially fused powder particles, irregular surface morphology, and the stair-stepping effect contribute to the surface roughness Click or tap here to enter text.. These surface defects act as stress concentrators that promote crack initiation and propagation, thereby reducing fatigue performance and the overall mechanical reliability of components. In addition, the surface irregularities can negatively influence wear behaviour and corrosion resistance, ultimately limit the service life of critical aerospace components if left untreated [6], [7], [8].

To achieve the full potential of LPBF Ti6Al4V(ELI) for critical applications, enhancing surface integrity is essential. Surface finishing processes such as rotary and vibratory tumbling improve surface uniformity, remove loosely bonded powder, and reduce asperities through abrasive media interaction. By mitigating stress concentrations and smoothing external surfaces, tumbling plays a key role in improving mechanical performance and durability. This study investigates the effectiveness of these processes in enhancing the surface integrity of LPBF Ti6Al4V(ELI) specimens.

2 Methodology

In this study, Ti6Al4V(ELI) specimens were produced through LPBF in an EOSINT M290 Direct Metal Laser Sintering (DMLS) system. The process parameters are illustrated in Table 1 below.

Table 1. EOSINT M280 process parameters

Parameter	Laser Power (W)	Beam Diameter (µm)	Scanning Speed (mm/s)	Layer thickness (µm)	Hatch Spacing (µm)	Powder Bed Temperature (°C)
Value	170	75	1400	30	100	40

Six complex-shaped specimens were fabricated and subjected to a two-stage heat treatment to relieve residual stresses and optimise the microstructure. This involved an initial stress relief soak at 650°C for three hours, followed by an annealing treatment at 950°C for two hours. To enhance surface integrity, rotary and vibratory tumbling were compared, both utilising two kilograms of ceramic abrasive media. The media consisted of a triangular prismatic shape with 1 mm dimensions, selected for its hardness, wear resistance, and suitability for finishing titanium alloys without inducing chemical contamination. Rotary tumbling was conducted in a barrel tumbler for three hours at a constant rotational speed, while vibratory tumbling was performed in a plastic bucket for the same duration under dry conditions, also maintaining a constant speed.

3 Discussion

Both tumbling methods improved surface quality by removing loose powder and rough areas. Vibratory tumbling produced better surface results despite being conducted in a plastic container. This suggests that the high-frequency oscillation action may be more effective than rotary motion for finishing complex LPBF parts, even with less efficient energy transfer through plastic. The continuous vibration likely allowed the ceramic media to access hidden features and internal channels more thoroughly than the cascading action of rotary tumbling. Rotary tumbling in a metal enclosure still delivered acceptable results but did not outperform vibratory processing, indicating that process dynamics matter more than container material for these specimens.

4 Conclusions

Both rotary and vibratory tumbling enhanced the surface morphology of LPBF Ti6Al4V(ELI) specimens. Vibratory tumbling yielded a superior surface finish, suggesting vibration-based action is more effective for complex geometries, even within a plastic container. Rotary tumbling in a metal vessel also removed surface defects, though with less pronounced results. The 2 kg ceramic media charge provided sufficient abrasive action for both methods, with the plastic vibratory container potentially enabling better media flow. Both processes successfully eliminated partially fused particles.

References

[1] G. Welsch, R. Boyer, and E. W. Collings, *Materials Properties Handbook:* Titanium Alloys in Materials properties handbook, (ASM International, 1993)

[2] H. E. Evans, Oxidation failure of TBC systems: An assessment of mechanisms, Surf. Coat. Technol. **206**, no. 7, pp. 1512–1521(2011). https://doi.org/10.1016/j.surfcoat.2011.05.053

[3] M. J. Donachie Jr., Titanium: A Technical Guide, (ASM International, 2000).

[4] T. DebRoy, H.L. Wei, J,S, Zyback, T. Mukherjee, J.W. Elmer, J.O. Milewski, A.M. Beese, A. Wilson-Heid, A. De and W. Zhang, Additive manufacturing of metallic components – Process, structure and properties, Prog. Mater. Sci. **92**, pp. 112–224 (2018). https://doi.org/10.1016/j.pmatsci.2017.10.001

[5] I. Gibson, D. Rosen, B. Stucker, and A. Khorasani, *Additive* Manufacturing Technologies (Springer,2020)

[6] H. Miya, W. du Preez, and L. Monaheng, High cycle fatigue performance of TI6AL4V(Eli) specimens produced with inherent laser powder bed fusion surface roughness, South African Journal of Industrial Engineering, vol. **32**, no. 3, pp. 248–257 (2021). https://doi.org/10.7166/32-3-2659

[7] P.J. Withers and H.K.D.H. Bhadeshia, Residual stress. Part 1 – Measurement techniques, Materials Science and Technology, vol. **17**, no. 4, pp. 355–365 (2001). https://doi.org/10.1179/026708301101509980

[8] J. C. Williams and R. R. Boyer, Opportunities and issues in the application of titanium alloys for aerospace components, Metals (Basel)., vol. **10**, no. 62 (2020). https://doi.org/10.3390/met10060705

Conceptual and parametric design of a modified reciprocating compressor cylinder head with integral cooling channels and a finned piston

Junior Makhubela[1*], *Gys* Jacobs[1], and *Annalène* Olwagen[1]

[1]Department of Mechanical Engineering and Mechatronic Engineering, Central University of Technology, Free state, Bloemfontein, 9300, South Africa

Abstract. Reciprocating compressors operate under near-adiabatic conditions, leading to elevated gas temperatures, thermal stresses, and reduced efficiency. Conventional cooling is limited by manufacturing constraints, restricting complex internal geometries. This study presents the conceptual and parametric design of a modified reciprocating compressor incorporating three thermal management features: (i) a cylinder head with internal parallel cooling channels, (ii) a finned piston for enhanced convective heat transfer, and (iii) discrete liquid water into the compression chamber. Additive manufacturing enables fabrication of these complex geometries. The current focus is on establishing a parametric design framework to guide geometry, coolant flow, and thermal optimisation.

1 Introduction

Reciprocating compressors are widely used in industrial applications for gas compression and pneumatic systems [1, 2, 3]. During the compression process, the temperature of the gas increases significantly due to the thermodynamic nature of the compression cycle. In conventional compressors, this temperature rise leads to deviations from the ideal isothermal compression process, resulting in increased energy consumption and reduced thermodynamic efficiency [4].

Isothermal compression represents the most efficient compression process, as it minimizes the work required to compress a gas. However, achieving true isothermal conditions in practical compressor systems is difficult due to limitations in heat transfer between the compressed gas and the surrounding environment [5]. As a result, most practical compressors operate closer to polytropic compression processes.

Recent advances in manufacturing technologies, particularly additive manufacturing, have created new opportunities for the development of advanced cooling geometries that can significantly enhance heat transfer within compressor components [6]. By integrating cooling channels and extended heat transfer surfaces within the compressor structure, it becomes possible to remove heat more effectively during the compression process and move closer to isothermal compression conditions.

* Corresponding author: juniormakhubela77@gmail.com

2 Conceptual design of the modified cylinder head

The proposed design introduces a modified compressor cylinder head containing additively manufactured internal cooling channels and extended heat transfer surfaces. The design integrates multiple parallel coolant passages that allow a cooling fluid to circulate through the cylinder head structure during operation. These channels are arranged between internal fins that extend toward the compression chamber, thereby increasing the available heat transfer surface area.

The internal fins are attached to the piston assembly and move with the piston during operation. These fins extend into the compression chamber and interact thermally with the surrounding cylinder head structure. The cooling channels are located between these fins and allow coolant to flow through the cylinder head, removing heat generated during the compression process.

A coolant manifold is incorporated into the upper section of the cylinder head to distribute the cooling fluid into the individual cooling channels. The manifold allows uniform distribution of coolant into the parallel passages and ensures effective heat removal from the internal surfaces of the cylinder head.

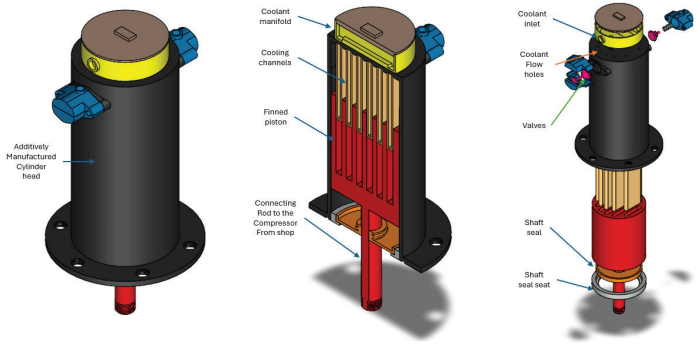


Fig. 1. Isometric, cross-section, and exploded views of the additively manufactured compressor cylinder head.

3 Design methodology

The conceptual design process involved the development of a parametric three-dimensional model using SolidWorks CAD software. The CAD model was used to define the geometry of the cooling channels, piston fins, coolant manifold, and sealing features. A cylinder bore diameter of approximately 100 mm was selected as the reference dimension for the design. Key design parameters considered in the conceptual design process included:

- Cooling channel diameter and spacing,
- Piston fin thickness and spacing,
- Coolant manifold geometry,
- Valve placement and cylinder head configuration,
- Bolt arrangement and flange dimensions,
- Sealing elements including O-rings and shaft seals

Preliminary calculations were performed to estimate the forces acting on the piston, the required bolt strength for the flange connection, and the spring stiffness required for the compressor valves. In addition, heat transfer correlations for forced convection in internal flow passages were considered to evaluate the potential heat removal capability of the cooling channels.

4 Heat transfer considerations

The primary objective of the proposed design is to enhance heat transfer from the compressed gas to the coolant circulating through the cylinder head. Heat transfer occurs through a combination of conduction and convection processes.

Heat generated during compression is first conducted through the piston fins and cylinder head structure. The heat is then transferred to the coolant flowing through the channels by forced convection. The convective heat transfer coefficient within the cooling channels is estimated using empirical correlations based on the Reynolds and Nusselt numbers for internal flow in parallel passages.

The use of multiple parallel cooling channels significantly increases the effective heat transfer area available for heat removal. This increased surface area improves the rate of heat transfer and contributes to reducing the temperature rise of the compressed gas. By removing heat more effectively during compression, the process will approach isothermal compression, thereby reducing the work required for compression.

5 Expected contribution

The conceptual and parametric design developed in this research provides a foundation for further experimental and numerical investigation of heat transfer within liquid-cooled compressor systems. The results of this work are expected to contribute to the development of more energy-efficient compressor technologies that operate closer to ideal isothermal compression conditions.

References

1. Y. A. Cengel and A. J. Ghajar, Heat and Mass Transfer: Fundamentals and Applications, (McGraw-Hill Education, New York 2015)
2. F. P. Incropera, D. P. DeWitt, T. L. Bergman, and A. S. Lavine, Fundamentals of Heat and Mass Transfer, (John Wily & Sons, 2021)
3. G. G. Jacobs and L. Liebenberg, The influence of timed coolant injection on compressor efficiency, Sustainable Energy Technologies and Assessments, vol. 18, pp. 175–189, (2016). https://doi.org/10.1016/j.seta.2016.10.010
4. Y. A. Cengel and M. A. Boles, Thermodynamics: An Engineering Approach, (McGraw-Hill Education, New York, 2019)
5. G. G. Jacobs and L. Liebenberg, The influence of controlled coolant injection on quasi-isothermal compression, Ph.D. thesis, North-West University, Faculty of Mechanical Engineering (2014)
6. I. Gibson, D. Rosen, B. Stucker, and M. Khorasani, Additive Manufacturing Technology, (Springer Cham, Switzerland, 2021)

Structural and elastic properties of two commercial binary Pt jewellery alloys – ab initio study

Maje Phasha[1*], *Melita* Lekganyane[2], *Joseph* Moema[1] and *Donald* Mkhonto[1]

[1]Advanced Materials Division, MINTEK, Private bag X 3015, Randburg, 2125, South Africa
[2]Department of Materials Science and Metallurgical Engineering, University of Pretoria, Pretoria, Hatfield 0028, South Africa

Abstract. First-principles calculations were carried out to study structural, thermodynamic and elastic properties of binary FCC Pt-Cu and Pt-Co commercial jewellery alloys. Based on their corresponding hardness values at 950 platinum (Pt) purity, the Pt-Cu and Pt-Co are categorized as soft and medium-hard alloys, respectively. Current results reveal that Pt-Cu solid solutions are more thermodynamically favourable than Pt-Co alloy compositions whereas predicted lattice parameters decreased with an increase in the composition of either alloying element. This trend which is attributed to both copper (Cu) and cobalt (Co) having smaller atomic radius compared to Pt.

1 Introduction

Platinum (Pt) has been used in jewellery since late 19th and early 20th centuries, most often as a base for precious gemstones such as diamond [1,2]. However, in its pure form, Pt is very soft to be considered in jewellery making [3]. Thus, to avoid scratching, denting and deforming in a short period of use, Pt is alloyed with several metals to increase the hardness and achieve other desired features [1,3]. The Pt jewellery alloys are hallmarked according to 950 (95 wt.%) and 900 (90 wt.%) platinum purity or fineness level [1-3]. Most common alloying elements considered for solid solution hardening are iridium (Ir), palladium (Pd), ruthenium (Ru), copper (Cu), cobalt (Co) and tungsten (W), whereas gallium (Ga) and indium (In) are recognized as heat-treatment hardened alloys, often resulting in precipitation of secondary phases [1-3].So far, Pt jewellery alloys can be classified into three categories based on their hardness, namely, soft alloys with < 120 HV(containing 5 to 10 wt.% Cu, Ir, Pd, Pd-Co, Cu-Co), medium-hard alloys with hardness range 120-150 HV (containing 5 wt.% Ru and Co), and hard alloys with hardness above 150 HV (bearing 5 wt.% Ga and In as well as their addition to Ru, Cu, Co or Au) [1,2]. In the current 21st century, there is a growing demand to design and develop solid solution strengthened Pt jewellery alloys with hardness above 150 HV [1], that easy to fabricate. Lately, computational materials modelling has proved to be a useful tool deployed in materials design. Using this research approach affords

* Corresponding author: majep@mintek.co.za

researchers a possibility to by-pass the cost barrier associated with platinum group metals (PGMs), thus providing an opportunity to respond adequately to the challenge in a cost viable manner. The current study investigates the structural, thermodynamic and elastic properties of commercial face centered cubic (FCC) binary Pt-Cu and Pt-Co jewellery alloy using the first-principles calculations. This work is aimed at predicting key mechanical properties such as hardness for soft and medium hard Pt jewellery alloys, to serve as a benchmark towards design and development of hard Pt jewellery alloys hardened via solid solution strengthening (sss).

2 Methodology

As shown in Fig. 1, a 2x2x2 FCC supercell structure comprised of 36 atoms was used to compute all properties of binary alloys considered in this study.

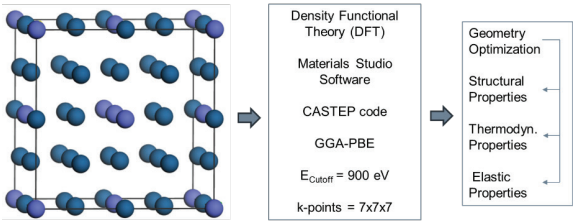


Fig.1. Schematic representation of the computational procedure employed.

3 Results and discussion

Figure 2(a) shows the lattice parameter a_0 decreases with an increase in the composition of the alloying element. This trend attributed to both Cu and Co having smaller atomic radius compared to Pt, is in accordance with available experimental data.

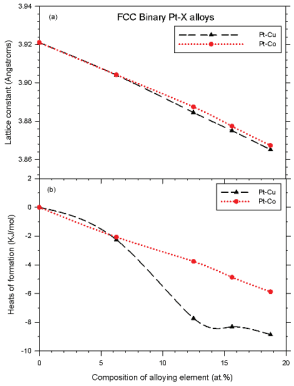


Fig. 2. Predicted (a) lattice constants and (b) calculated heats of formation of Pt-Cu and Pt-Co alloy compositions.

4 Conclusion

Despite Cu being slightly underestimated, the predicted lattice parameters decreased with an increase in the composition of either alloying element whereas Pt-Cu solid solutions were found to be more thermodynamically favourable. Due to high quality computational work carried in this study, predicted results are found to in excellent agreement with available experimental data, thus making it possible to reliably mimic key mechanical property trends observed in commercial alloys.

References

1. C.W. Corti, Johnson Matthey Technol. Rev. **66**, 418-434 (2022).
2. U.E. Klotz, T. Frye, Johnson Matthey Technol. Rev. **63**, 89-99 (2019).
3. T. Biggs, S.S. Taylor, E. van der Lingen, Platinum Metals Rev. **49**, 2-15 (2005).

A study into the laser powder bed fusion of customised pure platinum jewellery

Imdaadulah Adam[1*], *Willie* du Preez[1], *Charmaine* Johnston[2] and *Allan* Ross[3]

[1] Centre for Rapid Prototyping and Manufacturing, Central University of Technology, Free State, Bloemfontein, South Africa
[2]Council for Scientific and Industrial Research, Pretoria, South Africa
[3]Golden Soul Creations, Kaapschehoop, South Africa

Abstract. This study evaluates the feasibility of laser powder bed fusion (LPBF) to produce customised pure Pt jewellery. A four-phase methodology incorporating design for additive manufacturing (DfAM), multi-material validation, process optimisation, and market assessment was implemented. Results demonstrated that LPBF enables complex geometries and material efficiency advantages over traditional casting, particularly for high-complexity designs. However, surface finishing remains a critical post-processing requirement. Economic analysis indicated that LPBF is competitive for customised, high-value products, supporting its adoption within small medium and micro enterprises (SMMEs) in the jewellery sector.

1 Introduction

Additive manufacturing (AM) has evolved from a prototyping tool into a viable production method for low volume industries, offering enhanced design freedom and functional integration [1; 2]. Whilst traditional investment casting remains prevalent in the jewellery industry, material wastage, geometric limitations, and labour-intensive processes remain a concern. Studies by Gibson et al. [1] and Herzog et al. [2] established Laser Powder Bed Fusion (LPBF) as a mature metal AM process capable of producing complex, near-net-shape components with high material efficiency particularly for the processing of costly materials such as platinum (Pt) and platinum group metals (PGMs). Although AM of precious metals is less developed as compared to aerospace or biomedical sectors, Forno et al. [3] demonstrated the feasibility of processing gold alloys with acceptable density and mechanical properties. Process parameter optimisation remains critical, with Thomas [4] highlighting sensitivity to laser power, scan speed, and layer thickness, while Yadroitsev et al. [5] emphasized the role of support structures in ensuring thermal stability and geometric integrity. Despite the advantages offered by LPBF, several technical challenges remain, where surface finish is one of the most significant limitations of LPBF, particularly for industries where components need to be aesthetically pleasing. Strano et al. [6] showed that surface roughness in LPBF is strongly influenced by process parameters, layer thickness, and

* Corresponding author: iadam@cut.ac.za

part orientation. As a result, post-processing, such as polishing and finishing is required, especially in jewellery applications where aesthetic quality is critical. In this context, DfAM is widely recognised as a critical enabler for successful AM production of customised jewellery pieces. Kruth et al. [7] highlighted that conventional design approaches often fail to exploit AM's capabilities, leading to suboptimal builds, increased support structures, and higher post-processing burdens. In jewellery applications, where intricate geometries and aesthetic quality are paramount, DfAM becomes even more critical. Thomas [4] further demonstrated that geometric optimisation, particularly for overhangs and feature resolution, directly influences build success and surface quality in LPBF processes.

From an economic perspective, the viability of AM remains strongly dependent on part complexity and production volume. Thompson et al. [8] developed cost estimation models showing that AM becomes competitive when geometric complexity increases or when tooling costs for conventional processes are prohibitive. Ruffo et al. and Baumers et al. [9, 10] further quantified the cost drivers in AM, highlighting machine productivity, utilisation rates, and material costs as dominant factors. In the context of Pt jewellery, where raw material cost is exceptionally high, the material efficiency of LPBF presents a compelling advantage over traditional casting, which often requires excess material for sprues and gating systems. However, a notable gap exists between laboratory scale research and practical implementation within SMMEs. Most studies focus on material properties or process optimisation in controlled environments, with limited attention to real world adoption of AM technologies in industry. This study addresses this gap by presenting an industry driven study which integrates DfAM, multi-material validation, and conventional finishing workflows, thereby providing a practical route for LPBF adoption in the jewellery sector.

2 Methodology

A structured four-phase methodology was implemented to evaluate the feasibility of LPBF for customised Pt jewellery production. Initially, five existing CAD jewellery designs were subjected to DfAM optimisation, focusing on minimising overhangs, refining build orientation, and reducing support structure requirements. This was followed by a multi-material validation stage, where Al and Ti-6Al-4V builds were conducted to de-risk geometrical features and establish stable process parameters prior to processing pure Pt. Subsequently, optimised designs were fabricated in Pt using LPBF on an ORLas Creator LPBF system, with layer thickness maintained at 25 µm to balance surface resolution and build efficiency. Finally, all components underwent conventional jewellery post-processing, including polishing, finishing, and gemstone setting, after which a qualitative market assessment was performed to evaluate customer acceptance and commercial viability.

3 Results and discussion

The application of DfAM principles resulted in a noticeable reduction in support structure requirements, which in turn minimised material usage and post-processing effort while improving surface integrity in critical regions. The staged multi-material validation approach proved to be highly effective in identifying and resolving potential geometric and process-related issues prior to fabrication from pure Pt powder, significantly reducing the risk associated with high-value material builds. From a manufacturing perspective, LPBF demonstrated clear advantages in material efficiency, as components were produced closer to net shape without the need for excess material typically associated with sprues and gating systems in casting. However, as anticipated, surface finish directly from the LPBF process remained insufficient for final-use jewellery applications, necessitating conventional

polishing and finishing processes to achieve the required aesthetic quality. Economic observations indicated that LPBF becomes increasingly competitive as design complexity and mass increase, particularly where traditional methods would require substantial additional material and labour input. Overall, the results confirmed that while LPBF is not a universal replacement for traditional methods, it offers a compelling and viable alternative for high-complexity, customised platinum jewellery production.

5. Conclusion

This study demonstrated that LPBF is a technically feasible and economically viable solution for customised platinum jewellery under specific conditions. The structured four-phase methodology effectively mitigated risks.

References

1. I. Gibson, D.W. Rosen, B. Stucker, Additive manufacturing technologies, 3rd ed. (Springer, 2021)
2. D. Herzog, V. Seyda, E. Wycisk, C. Emmelmann, Additive manufacturing of metals. Acta Mater. 117, 371–392 (2016). https://doi.org/10.1016/j.actamat.2016.07.019
3. I. Forno, M. Actis Grande, A. Fais, On the application of electro-sinter-forging to the sintering of high-karatage gold powders. Gold Bull. 48, 127–133 (2015). https://doi.org/10.1007/s13404-015-0169-x
4. D. Thomas, The development of design rules for selective laser melting, Ph.D. thesis, University of Wales (2009)
5. I. Yadroitsev, I. Smurov, Selective laser melting technology: From single track stability to 3D parts. Phys. Procedia 5, 551–560 (2010). https://doi.org/10.1016/j.phpro.2010.08.083
6. G. Strano, L. Hao, R.M. Everson, K.E. Evans, Surface roughness analysis, modelling and prediction in selective laser melting. J. Mater. Process. Technol. 213, 589–597 (2013). https://doi.org/10.1016/j.jmatprotec.2012.11.011
7. J.P. Kruth, G. Levy, F. Klocke, T.H.C. Childs, Consolidation phenomena in laser and powder-bed based layered manufacturing. CIRP Ann. 56, 730–759 (2007). https://doi.org/10.1016/j.cirp.2007.10.004
8. M.K. Thompson, G. Moroni, T. Vaneker, G. Fadel, I. Campbell, I. Gibson, A. Bernard, J. Schulz, P. Graf, B. Ahuja, F. Martina, Design for additive manufacturing: Trends, opportunities, considerations, and constraints. CIRP Ann. 65, 737–760 (2016). https://doi.org/10.1016/j.cirp.2016.05.004
9. M. Ruffo, C. Tuck, R. Hague, Cost estimation for rapid manufacturing. Proc. Inst. Mech. Eng. B 220, 1415–1427 (2006). https://doi.org/10.1243/09544054JEM517
10. M. Baumers, P. Dickens, C. Tuck, R. Hague, The cost of additive manufacturing: Machine productivity and economies of scale. Int. J. Prod. Econ. 172, 193–201 (2016). https://doi.org/10.1016/j.ijpe.2015.02.015

First-principles study of thermodynamic and mechanical enhancement in V and Cr alloyed FCC platinum for jewellery applications

Mawisha Mafifi[1*], *Donald* Mkhonto[2], *Mwende* Mbilo[1], *Maje* Phasha[2] and *Edwin* Mapasha[1]

[1]Department of Physics, University of Pretoria, Private bag X20, Hatfield, 0028, South Africa
[2]Advanced Materials Division, MINTEK, Private bag X 3015, Randburg, 2125, South Africa

Abstract. In its purest state, platinum (Pt) is relatively soft, thus vulnerable to surface scratching, a distress in jewellery sector. As such, alloying Pt to enhance its mechanical integrity is crucial for improving its scratching resistance. For this reason, density functional theory (DFT) within Quantum Espresso package was deployed to investigate the contribution of alloying Pt with high corrosion resistance vanadium (V) and chromium (Cr) at various compositions (x). Thermodynamic stability investigation calculated using formation energies ranged from -0.5 to -3 eV for alloying composition of $3<x<19$. This suggests that $Pt_{1-x}V_x$ and $Pt_{1-x}Cr_x$ formation is exothermic, hence supporting the feasibility of the synthesis process at 0K. It is noticed that hardness of Pt alloy compositions increase significantly at higher alloying compositions.

1 Introduction

Platinum jewellery is a soft material that is sensitive to denting, scratching and loss of high lustre during customer experience and to improve the clientele experience, Pt is usually alloyed with different metals to enhance the hardness and strength while maintaining its original white colour and durability [1-2]. To enhance its mechanical durability and resistance to scratching, denting, and deformation, platinum is commonly alloyed with other metals to improve hardness and tailor additional properties. Platinum jewellery alloys are typically standardised according to their purity, with common fineness levels of 950 (95 wt. %) and 900 (90 wt. %) platinum [3-5]. The contribution of alloying Pt with high corrosion resistance vanadium (V) and chromium (Cr) at various concentrations (x) around the common fineness levels, was investigated using density functional theory (DFT) within the Quantum Espresso package.

2 Methodology

In this study, DFT approach was considered for carrying out calculations for thermodynamic stability and elastic properties using PWscf code of the Quantum ESPRESSO distribution.

* Corresponding author: mawisham@gmail.com

This approach was used to examine the thermodynamic stability, based on the formation energy analysis and mechanical strength using elastic constants of the FCC Pt-V and Pt-Cr alloy materials. Figure 1 clearly describe the structural aspects of alloys studied and the computational methodology followed:

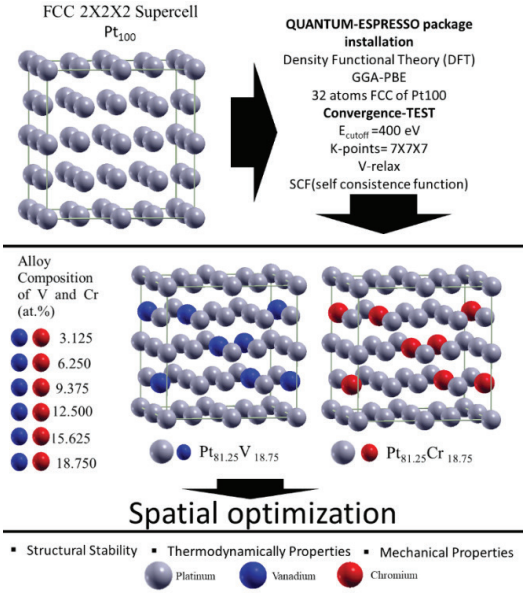


Fig.1. Schematic illustration of the computational process used in the study.

3 Results and discussion

Figure 2.a. depicts the calculated heats of formation for binary FCC $Pt_{1-x}V_x$ and $Pt_{1-x}Cr_x$ alloy compositions. It is noted the heats of formation decreases with increase in alloying composition, with negative values suggesting spontaneity formation of the material. An indication that the predicted alloys can be synthesizable under favourable conditions.

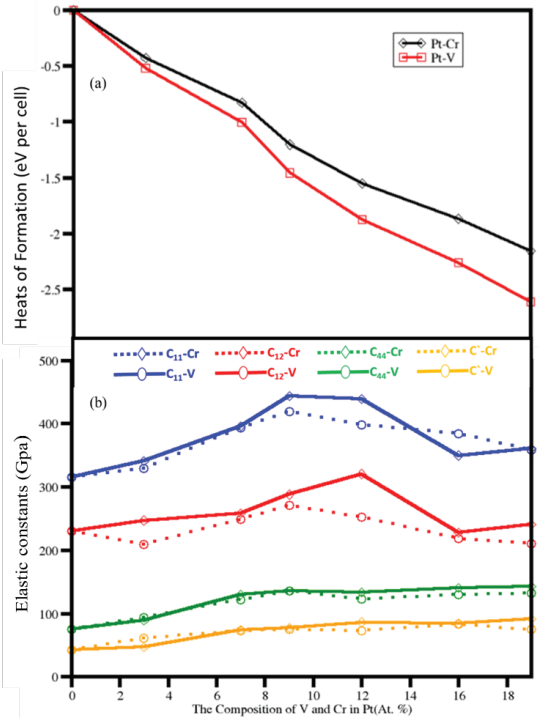


Fig.2. The calculated (a) heats of formation and elastic properties of binary FCC $Pt_{1-x}V_x$ and $Pt_{1-x}Cr_x$ alloy compositions.

4 Conclusion

The thermodynamically stability of both Pt-V_x and Pt-Cr_x compositions becomes more stable as the concentration increases. Such observation is supported by atomic bonding (d-band hybridization) due to orbital overlap across all compositions (0-18.750 at. %). However, when correlated with elastic properties, it becomes evident that maximum mechanical performance occurs at intermediate compositions, highlighting a trade-off between thermodynamic stability and mechanical optimization.

References

1. J. McGrath (2007) *Jewellery Materials Sourcebook*. London: A&C Black.
2. S.H. Avner (1974) *Introduction to Physical Metallurgy*. 2nd edn. New York: McGraw-Hill.
3. C.W. Corti, Johnson Matthey Technol. Rev. **66**, 418-434 (2022).
4. U.E. Klotz, T. Frye, Johnson Matthey Technol. Rev. **63**, 89-99 (2019).
5. T. Biggs, S.S. Taylor, E. van der Lingen, Platinum Metals Rev. **49**, 2-15 (2005).

02

ABSTRACTS

Seminar: Computational and Data-driven Modelling

Effect of $TiCl_4$ medium on Ti_{13} cluster: a molecular dynamics study

Andile Mazibuko[1]*, *and Hasani* Chauke[1]

[1]Materials Modelling Centre, University of Limpopo, Private bag X1106, Sovenga 0727, South Africa

Abstract. Industrial production is primarily achieved through the reduction of titanium tetrachloride ($TiCl_4$). However, the behaviour of titanium clusters during early stages of nucleation in the $TiCl_4$ medium remains insufficiently understood. In this study, classical molecular simulations using DL_POLY were employed to investigate the structural and thermal behaviour of a Ti_{13} cluster in $TiCl_4$. The rigid-ion model showed limited mobility due to electrostatic constraints. In contrast, the shell model exhibited enhanced structural fluctuations and mobility at high temperatures. These results provide atomistic insight into early-stage nucleation and establish a modelling approach that may support process optimisation of industrial titanium production.

1 Introduction

Titanium is widely valued for its high strength-to-weight ratio and excellent corrosion resistance, making it essential for aerospace and advanced engineering applications. Industrial production is commercially achieved through the reduction of titanium tetrachloride ($TiCl_4$) in the Kroll process [1,2]. However, the behaviour of titanium species during early stages of nucleation within the $TiCl_4$ medium remain insufficiently understood. This knowledge gap limits efforts to optimise titanium production processes [3,4]. In this study, classical molecular simulations using DL_POLY were employed to investigate the effect of the $TiCl_4$ medium on the structural and thermal behaviour of a Ti_{13} cluster. We report on how varying temperature affects the behaviour of the Ti_{13} cluster in the medium.

2 Methodology

The $TiCl_4$ medium were validated using the General Utility Lattice Program (GULP) [5]. Molecular dynamics simulations were performed using DL_POLY code [6] with an NVE ensemble. A radial cut-off of 9.95 Å was used, and the time step was set at 0.001 ps.

* Corresponding author: andileZibu@gmail.com

3 Results and discussion

Ti_{13} diffusivity was greater in the vacuum than in the $TiCl_4$ medium. Rigid-ion models showed limited mobility due to electrostatic constraints, whereas shell models exhibited high-temperature enhancements from medium polarisation. Ti-Ti bonds remained within 2.52 – 2.98 Å, preserving the icosahedral geometry [7]. Elongation-contraction patterns indicate dynamic bond flexibility, enabling mobility without structural collapse.

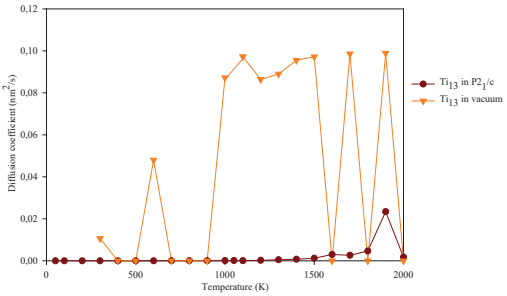


Fig. 1. Comparison of the diffusion coefficients for the Ti_{13} cluster in vacuum and within the $P2_1/c$ ($TiCl_4$) medium using the rigid-ion model.

4 Conclusion

The results demonstrate that the $TiCl_4$ medium significantly influences Ti_{13} cluster mobility and dynamics. Polarisation effects captured by the shell model enhance high-temperature transport behaviour, whereas rigid-ion interactions constrain cluster motion. Despite these effects, the persistence of Ti-Ti bond lengths confirms the stability of the icosahedral cluster geometry. These insights provide an atomistic basis for modelling early-stage titanium nucleation.

References

1. W.J. Kroll, The production of ductile titanium. Trans. Electrochem. Soc. **78**, 35 (1940)
2. N. Matsanga, M.K. Wakalenga, W. Nheta, An overview of thermochemical reduction processes for titanium production. Minerals. **15**, 17 (2024)
3. J.C. White, L.L. Oden, Continuous production of granular Ti, Zr and Hf or their alloy products. US Patent 5259862, 9 November 1993
4. M. El Khalloufi, O. Drevelle, G. Soucy, Titanium: An overview of resources and production methods. Minerals. **11**, 1425 (2021)
5. J.D. Gale, Gulp: A computer program for the symmetry-adapted simulation of solids. J. Chem. Soc. **93**, 629 (1997)
6. W. Smith, I.T. Todorov, A short description of DL_POLY. Mol. Simul. **32**, 935 (2006)
7. M. Castro, S.R. Liu, H.J. Zhai, L.S. Wang, Structural and electronic properties of small titanium clusters: A density functional theory and anion photoelectron spectroscopy study. J. Chem. Phys. **118**, 2116 (2003)

Computational mechanical behaviour in high entropy alloys

Abidemi. Adeyoye[1]*, *Patricia* Popoola[1], *Olawale* Popoola[2], *Samson* Adeosun[1], *Modupeola* Dada[1], and *Samuel* Skhosane[3]

[1]Department of Chemical, Metallurgical and Materials Engineering, Tshwane University of Technology, 0183 Pretoria, Gauteng, South Africa
[2]Center for Energy and Electric power, Electrical Engineering, Faculty of Engineering and Built Environment, Tshwane University of Technology, 0183 Pretoria, Gauteng, South Africa
[3]Laser Enable Manufacturing, Council for Industrial and Industrial research, Pretoria, South Africa

Abstract. The development of advanced materials requires a framework linking composition, microstructure, and performance. CALPHAD-based modelling enables rapid prediction of phase stability, accelerating alloy design. In this study, a closed-loop computational design system integrates composition selection, phase prediction, microstructure evolution, and property evaluation. The framework is applied to predict BCC phase stability in HEAs, with emphasis on ordering at elevated temperatures. This approach identifies optimal compositions, predicts phase constitution and mechanical response, and reduces experimental trial-and-error. The results highlight an efficient pathway for designing HEAs with improved thermal stability for high-temperature energy storage applications.

1 Introduction

High-temperature energy storage (HTES) technologies—including concentrated solar power (CSP), thermal batteries, and thermochemical reactors—require structural materials capable of operating under extreme thermal and chemical environments [1, 2]. These systems typically function at temperatures exceeding 1000 °C in oxidizing atmospheres, imposing stringent requirements on mechanical integrity, phase stability, and oxidation resistance. Conventional superalloys and ceramics, although widely utilized, are often limited by restricted compositional tunability, grain boundary degradation, and phase instability during prolonged exposure to elevated temperatures (≥1300 °C) [3].

The emergence of high-entropy alloys (HEAs) has introduced a paradigm shift in alloy design by exploiting compositional complexity to achieve enhanced performance [4, 5]. HEAs are composed of multiple principal elements—often including refractory metals such as Nb, Mo, Ta, W, and V—in near-equiatomic proportions. Their high configurational entropy promotes the stabilization of simple solid-solution phases, typically body-centered cubic (BCC) or face-centered cubic (FCC), while suppressing the formation of brittle intermetallic compounds [6]. These characteristics make refractory HEAs particularly

* Corresponding author: abidemiadeyoye@gmail.com

attractive for high-temperature applications, where retention of strength and structural stability is critical.

Among refractory systems, the Nb–Mo–V–Cr alloy system is widely recognized for forming stable BCC solid solutions with good high-temperature strength [7]. However, its practical application is hindered by poor oxidation resistance, primarily due to high oxygen solubility and the tendency for internal oxidation. This limitation has motivated the incorporation of non-refractory elements such as Al and Si, which can promote the formation of protective oxide scales (e.g., Al_2O_3 and SiO_2), thereby enhancing oxidation resistance and extending service life under harsh conditions [8]. Consequently, Al-containing BCC HEAs, such as $Al_xNbMoVCr$, offer a promising pathway for balancing mechanical performance with environmental stability.

Despite these advantages, the design of HEAs remains challenging due to the vast compositional space and complex thermodynamic interactions among constituent elements. Predicting phase stability, transformation behaviour, and microstructural evolution in such systems is non-trivial, particularly in the absence of comprehensive experimental phase diagrams [9]. To address this challenge, computational approaches have become indispensable. Techniques such as CALPHAD (CALculation of PHAse Diagrams), density functional theory (DFT), and machine learning (ML) enable efficient exploration of multicomponent systems by predicting thermodynamic stability, phase equilibria, and structure–property relationships [10].

In this study, a computationally driven design strategy is adopted to develop a high-temperature HEA with enhanced structural stability and oxidation resistance. Using CALPHAD-based modelling within the Thermo-Calc framework, the phase stability and compositional design of Al-containing refractory HEAs are systematically investigated. The approach focuses on identifying BCC-dominated compositions, evaluating their thermodynamic stability, and elucidating the underlying strengthening mechanisms. This work provides a predictive pathway for the development of advanced HEAs tailored for high-temperature energy storage and related extreme-environment applications.

2 Methodology and results

2.1 Materials selection

Alloy design and thermodynamic simulations were performed using Thermo-Calc software (version 2021a) with the TCHEA04 high-entropy alloy database. The phase stability and equilibrium phase constitution of the Nb–Mo–V–Cr–Al system were evaluated under isothermal conditions at 1000 °C and atmospheric pressure.

Table 1. Presents the elemental composition by weight percentage for the AlxNbMoVCr alloys.

Alloy	Actual Chemical compositions (wt. %)				
	Al	Nb	Mo	V	Cr
$Al_{0.1}$	0.92	31.55	32.58	17.30	17.66
$Al_{0.2}$	1.80	31.26	32.29	17.14	17.50
$Al_{0.3}$	2.70	30.98	31.99	16.99	17.34
$Al_{0.4}$	3.57	30.70	31.71	16.83	17.18
$Al_{0.5}$	4.42	30.44	31.43	16.69	17.03

3 Conclusion

This study outlines a computational framework for the design and thermodynamic assessment of Al-containing Nb–Mo–V–Cr high-entropy alloys for high-temperature energy storage applications. Using CALPHAD-based modelling, the approach aims to evaluate phase stability, identify BCC-dominated compositions, and assess the influence of Al addition on high-temperature performance and oxidation resistance.
The integration of thermodynamic simulations is expected to provide insight into phase equilibria and guide compositional optimization in complex alloy systems. The outcomes will support the development of design strategies for refractory high-entropy alloys and establish a foundation for future experimental validation.

Reference

1. M.M. Ramirez-Corredores, M. R. Goldwasser, E. Falabella de Sousa Aguiar, Perspectives and Future Views, in Decarbonization as a Route Towards Sustainable Circularity. Springer. 127-153 (2023)
2. T. Bauer, Fundamentals of high-temperature thermal energy storage, transfer, and conversion, in Ultra-high temperature thermal energy storage, transfer and conversion. Elsevier. 1-34 (2021)
3. P. Sengupta, I. Manna, Advanced high-temperature structural materials in petrochemical, metallurgical, power, and aerospace sectors—An overview. Springer. 79-131 (2022)
4. A. Adeyoye, P. Popoola, O. Popoola, S. Adeosun, M. Dada, Refractory high-entropy alloys for solid-state hydrogen storage: A computational design review. Int. J. Hydrog. Energy. **205**, 153291 (2026)
5. A.M. Oketola, T.A. Adegbola, T. Jamiru, O. Ogunbiyi, S. Salifu, Advances in high-entropy alloy research: Unraveling fabrication techniques, microstructural transformations, and mechanical properties, J. Bio-Tribo-Corros. **11**, 379 (2025)
6. H. Liu Y. Yao, High-Entropy Alloys and Compounds: Fundamentals, Functional High Entropy Alloys and Compounds (Wiley online library, 2025)
7. M. Yoshida T. Takasugi, Phase relation and microstructure of Nb-Cr-V and Nb-Cr-Mo alloy systems. Mater. Sci. Eng. **224**, 69-76 (1997)
8. S. Shu et al., On the high-temperature oxidation behavior of a niobium-bearing high nickel-chromium alloy: microstructural evolution and implications on oxidation mechanisms, Corros. Sci. **220**, 111261 (2023)
9. T. Burczynski, M. Pietrzyk, W. Kus, L. Madej, A. Mrozek, L. Rauch, Multiscale Modelling and Optimisation of Materials and Structures (John Wiley & Sons, 2022)
10. S. Zhu, D. Sarıtürk, R. Arróyave, Accelerating CALPHAD-based phase diagram predictions in complex alloys using universal machine learning potentials: Opportunities and challenges, Acta Mater. **286**, 120747 (2025)

Numerical simulation of Fano resonant electromagnetic split ring resonators

Realeboga Dikole[1*], and *Edwin* Magidimisha[1]

[1]Council for Scientific and Industrial Research, Defence and Security, Meiring Naudé Road, 0184 Pretoria, South Africa

Abstract. This paper studies Fano resonance response in asymmetric and nearly symmetric electromagnetic split-ring resonators, which are the fundamental building blocks of metamaterials. Our results confirm the close relationship between asymmetry and Fano resonance. Our results also show that slight changes in resonator symmetry can affect the Fano response, making the asymmetrical split-ring resonator suitable for high-accuracy sensing applications due to its sensitivity to perturbations. The nearly symmetric split-ring resonators, however, were found to be more suitable for frequency-selective surface and antenna-filter applications due to their wideband response across the frequency spectrum.

1 Introduction

Metamaterials are driving a significant transformation in contemporary optics by enabling the remarkable expansion of electromagnetic properties observed in naturally occurring materials. These include unusual phenomena such as optical magnetism, negative refraction and bianisotropy. Metasurfaces have emerged in recent years as a platform for tailoring subwavelength-thick optical components that can perform a wide range of optical functions. Such optical functions include beam deflection, focusing, waveplates and others. Over the past decade, numerous efforts have been made to develop various active materials and integrate them into practical applications. Some of these active materials include phase-change materials, liquid crystals, atomically thin materials, and transparent conducting oxides. Metasurfaces are metamaterials composed of artificial subwavelength structures that allow for exotic electromagnetic behaviour. Graphene and its unique electromagnetic properties are enabling novel applications in optical devices [1]. One of the many benefits of graphene is the ability to control its optical response [1]. One promising strategy to enhance graphene's optical response is to place it near metallic or dielectric photonic structures. This approach has been employed to design highly tunable infrared and THz metasurfaces enabling both amplitude and phase modulation.

2 Modelling Fano resonances

Several models have been employed to describe the Frano resonance phenomenon, but the simplest and most intuitive method is the use of oscillating electric charges. This is done by considering a structure that interacts with electromagnetic radiation. The electromagnetic wave causes electrons in the structure to oscillate through the excitation of a harmonic field it generates. This excitation can enter a resonant state when certain conditions are met. To describe the resonance, consider two oscillating charges A and B coupled by a constant g.

* Corresponding author: rdikole@csir.co.za

The resonance frequencies of the two charges are denoted by ω_a and ω_b, with the damping parameters denoted as γ_a and γ_b. A harmonic force is applied to oscillator A so that the equations of motion become:

$$\ddot{x}_a + \gamma_a \dot{x}_a + \omega_a^2 + g x_b = (qE_0/m)e^{i\omega t}, \quad (1)$$

$$\ddot{x}_b + \gamma_b \dot{x}_b + \omega_b^2 + g \boldsymbol{x_a} = 0. \quad (2)$$

Here, q denotes an oscillating charge such as an electron, m is its mass, and $x_{a,b}$ describes the oscillations of charges A and B. The overdots denote the first- and second-order time derivatives. Assuming a harmonic response of the oscillators, i.e $x_a = \varphi_a \exp(i\omega t)\, E_0/|E_0|$ and $x_b = \varphi_b \exp(i\omega t)\, E_0/|E_0|$, the amplitude of the response of the oscillators are given as [2]

$$\varphi_a = \frac{\omega_b^2 + i\gamma_b\omega - \omega^2}{(\omega_a^2 + i\gamma_a\omega - \omega^2)(\omega_b^2 + i\gamma_b\omega - \omega^2) - g^2}(q|\boldsymbol{E_0}|/m), \quad (3)$$

$$\varphi_a = \frac{\omega_b^2 + i\gamma_b\omega - \omega^2}{(\omega_a^2 + i\gamma_a\omega - \omega^2)(\omega_b^2 + i\gamma_b\omega - \omega^2) - g^2}(q|\boldsymbol{E_0}|/m), \quad (4)$$

respectively.

2.1 Fano resonant split-ring resonators

The primary contributor to the observation of Fano resonance in electromagnetic SRRs is the presence of asymmetry in the SRR [4]. The asymmetry in the SRRs produces a much steeper response than that obtained from their symmetric counterpart [3, 5, 6]. One of the main distinguishing features of Fano resonance is its asymmetric line profile [7]. Such an asymmetry arises from the coexistence of resonant transmission and resonant reflection [7]. The fundamental criterion for Fano resonance is the interference between a broad continuum and a narrow discrete resonance. In plasmonics, these conditions are satisfied by tunable coupled plasmonic structures made of plasmonic materials such as silver or gold [4]. The width and energies of the plasmon resonances are controlled by changing the geometry of the individual structures and the gap between them.

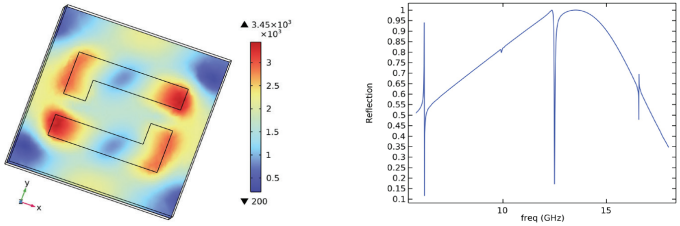
3 Method

We construct an asymmetric and a nearly symmetrical electromagnetic split-ring resonator. The geometries are constructed in COMSOL Multiphysics Simulation Software. The resonators are placed on a dielectric slab in a manner that allows for the transmission and reflection of incident radiation. That is, there is no ground plate present. In both cases, the dielectric material has a relative permeability of 2.1, a relative permeability of 1 and a zero conductivity. The SRRs are chosen as gold strips and are allowed to interact with the air. We employ periodic port boundary conditions, where an incident magnetic wave enters through the top port and interacts with the SRR configuration and exits through the bottom port. The induced electric field, and the $S11$ and $S21$ elements of the scattering matrices are computed through the finite element solver in COMSOL.

4 Results

Shown in figure 1 are the results associated with the L-shaped, nearly symmetric geometry. The induced electric field is plotted in figure 1 (a) at 13.8 GHz. The plot shows the electric field localisation in the gap region of the SRR, with charge confinement being apparent in

the capacitative regions of the SRRs. Figure 1 (b) shows the reflection plot associated with the incident field on the surface of the coupled SRRs. The reflection is plotted against frequency values ranging from 7 GHz to 17 GHz. Figure 1 (b) depicts multiple resonant features, beginning with a sharp dip at lower frequencies, showing a narrowband resonance with high field confinement. The resonances at higher frequencies point to the existence of a secondary mode with a more distributed field coupling. The plot possesses Fano-like resonance features.



(a) (b)

Fig. 1. The electric field distribution on the nearly symmetric coupled SRRs (a) and respective reflectance plotted over frequency values ranging from 7 GHz to 17 GHz.

References

1. D.A. Smirnova, A.E. Miroshnichenko, Y.S. Kivshar, A.B. Khanikaev, Tunable nonlinear graphene metasurfaces. Phys. Rev. B **92**, 161406 (2015).
2. B. Gallinet, Model of Coupled Oscillators for Fano Resonance*s* (Springer International Publishing, Cham, 2018), 109–136, ISBN 978-3-319-99731-5
3. P. Tassin, L. Zhang, R. Zhao, A. Jain, T. Koschny, C.M. Soukoulis, Electromagnetically induced transparency and absorption in metamaterials: The radiating two oscillator model and its experimental confirmation, Phys. Rev. Lett. **109**, 187401 (2012).
4. B. Luk'yanchuk, N.I. Zheludev, S.A. Maier, N.J. Halas, P. Nordlander, H. Giessen, C.T. Chong, The fano resonance in plasmonic nanostructures and metamaterials, Nature Materials **9**, 707 (2010).
5. B. Lahiri, S.G. McMeekin, R.M.D.L. Rue, N.P. Johnson, Enhanced Fano resonance of organic material films deposited on arrays of asymmetric split-ring resonators (a-srrs), Opt. Express **21**, 9343 (2013).
6. X. Wang, T. Liang, G. Li, J. Shen, B. Zhang, Fano resonance and sensing application based on terahertz asymmetric split-ring metasurfaces, J. Alloys Compd. **976**, 173130 (2024).
7. A.E. Miroshnichenko, S. Flach, Y.S. Kivshar, Fano resonances in nanoscale structures. Rev. Mod. Phys. **82**, 2257 (2010).

A comparison of classical machine learning and vision language models for TB diagnostics

Kelvin Mpofu[1*], *Nkgaphe* Tsebesebe[1] and *Sello* Manoto[1]

[1] Biophotonics, Council of Scientific and Industrial Research (CSIR), South Africa

Abstract. Tuberculosis (TB) remains a major global health challenge, and timely diagnosis is essential for effective treatment and disease control. Automated analysis of chest X-ray images using machine learning has shown strong potential for supporting clinical diagnostics. Previous studies using hyperparameter optimized machine learning algorithms, including convolutional neural networks (CNN), support vector machines (SVM), and decision trees, have achieved high classification performance on TB chest X-ray datasets, with accuracies exceeding 98%. In this work, we extend these investigations by evaluating the performance of a fine-tuned vision–language model (VLM) for tuberculosis classification and comparing its performance with traditional machine learning approaches. The study uses a publicly available TB chest X-ray dataset and evaluates models using standard clinical performance metrics including accuracy, sensitivity, precision, F1-score, and specificity. Traditional optimized models such as SVM, CNN, and decision trees provide strong baseline performance, achieving accuracies of 99.58%, 99.50%, and 98.33%, respectively. The proposed VLM-based approach is fine-tuned on the same dataset and assessed to determine whether transformer-based multimodal architectures can provide comparable or improved diagnostic performance. The results highlight the strengths and limitations of both traditional machine learning models and modern vision–language models in automated TB detection, providing insight into the role of emerging AI architectures in medical imaging diagnostics.

1 Introduction

Tuberculosis (TB) remains one of the most significant infectious diseases globally, caused by the bacterium Mycobacterium tuberculosis. The disease primarily affects the lungs and spreads through airborne transmission, posing a major public health challenge, particularly in developing countries. According to global health reports, millions of new TB cases are recorded annually, highlighting the need for rapid and reliable diagnostic methods [1–3]. Early detection is essential for reducing disease transmission and improving treatment outcomes.

* Corresponding author: kmpofu@csir.co.za

Chest X-ray imaging is widely used as a screening tool for pulmonary TB due to its accessibility and ability to reveal lung abnormalities associated with infection. However, manual interpretation of chest X-rays requires significant clinical expertise and may be prone to variability between clinicians. In recent years, artificial intelligence (AI) and machine learning (ML) techniques have been increasingly explored to assist radiologists in automated disease detection and medical image analysis [4–6]. Previous studies have demonstrated strong performance in TB detection using optimized machine learning algorithms such as support vector machines (SVM), convolutional neural networks (CNN), and decision trees, achieving classification accuracies exceeding 98% on publicly available datasets [7–9]. More recently, transformer-based architectures and vision–language models (VLMs) have emerged as powerful tools capable of learning complex visual representations and contextual relationships within data [10]. These models, inspired by large language model architectures, have shown promising performance in image understanding and multimodal reasoning tasks. In this work, we investigate the performance of a fine-tuned vision–language model for tuberculosis classification from chest X-ray images and compare its performance with traditional machine learning algorithms. The study evaluates model performance using clinical diagnostic metrics including accuracy, sensitivity, precision, F1-score, and specificity to assess the suitability of emerging transformer-based architectures for medical imaging diagnostics.

2 Methodology

2.1 Dataset

The experiments were conducted using a publicly available tuberculosis chest X-ray dataset obtained from Kaggle, developed by researchers from Qatar University and collaborating institutions. The dataset consists of chest radiographs categorized into two classes: tuberculosis-infected and normal cases. The dataset used in this work contains approximately 700 TB images and 3,500 normal images, providing a balanced benchmark for evaluating automated diagnostic models. All images were resized to a fixed resolution to ensure uniform input dimensions. Image preprocessing included normalization and scaling to reduce variability and improve model performance. The dataset was divided into training and testing subsets using an 80:20 ratio.

2.2 Traditional machine learning models

Three traditional machine learning algorithms were implemented as baseline classifiers: support vector machines (SVM), decision trees, and convolutional neural networks (CNN). The models were optimized using hyperparameter tuning and dimensionality reduction techniques to improve classification performance. Performance evaluation was conducted using standard confusion matrix metrics including accuracy, sensitivity, precision, specificity, and F1-score.

2.3 Vision–language model

To investigate the capability of modern transformer-based architectures, a vision–language model based on a Vision Transformer (ViT) backbone was fine-tuned on the same dataset. The pretrained model was adapted for binary classification by replacing the final

classification layer with a two-class output layer corresponding to TB and normal cases. Fine-tuning was performed using supervised learning with cross-entropy loss, allowing the model to learn TB-related imaging features directly from the dataset.

3 Results

The performance of the optimized machine learning models on the tuberculosis chest X-ray dataset is summarized in Table 1. The results demonstrate that the traditional machine learning models achieve very high diagnostic accuracy. The SVM classifier achieved the highest accuracy of 99.58%, followed by the CNN model with 99.50%, while the decision tree classifier achieved 98.33% accuracy. In addition to accuracy, the models demonstrated strong clinical diagnostic performance across sensitivity, precision, and specificity metrics. The SVM classifier achieved a sensitivity of 99.87%, indicating a strong ability to correctly detect TB-positive cases. The CNN model also showed strong classification performance with a high F1-score of 0.9962, reflecting balanced precision and recall. The proposed fine-tuned vision–language model was evaluated to determine whether transformer-based architectures could achieve comparable performance to optimized classical models. Preliminary results indicate that transformer-based models can learn meaningful radiographic features associated with tuberculosis infection. Although traditional models remain highly effective for structured medical imaging datasets, vision–language models offer potential advantages in representation learning and integration with multimodal diagnostic systems. These results highlight the continued relevance of classical machine learning models while also demonstrating the potential of transformer-based architectures for future AI-assisted medical diagnostics.

4 Conclusion

In conclusion, this study shows that both traditional machine learning models and vision language models can effectively detect tuberculosis from chest X-ray images. Optimized classical models, particularly SVM and CNN, achieve exceptionally high accuracy and remain reliable, efficient solutions for structured diagnostic tasks. While the vision language model does not surpass these models on this dataset, it demonstrates strong potential for learning complex representations and supporting future multimodal diagnostic systems. Overall, traditional methods remain highly effective, while transformer-based models offer promising opportunities for more advanced, integrated healthcare applications.

References

1. F. Cui, Y. Yue, Y. Zhang, Z. Zhang, H.S. Zhou, *ACS Sens.* **5**, 3346–3364 (2020).
2. World Health Organization, *Global Tuberculosis Report* (WHO, Geneva, 2023).
3. M.E.H. Chowdhury et al., *IEEE Access* **8**, 191586–191601 (2020).
4. G. Litjens et al., *Med. Image Anal.* **42**, 60–88 (2017).
5. A. Esteva et al., *Nature* **542**, 115–118 (2017).
6. S. Rajpurkar et al., *PNAS* **115**, 115–119 (2018).
7. T. Rahman et al., *IEEE Access* **8**, 191586–191601 (2020).
8. K. He, X. Zhang, S. Ren, J. Sun, *Proc. CVPR*, 770–778 (2016).
9. A. Krizhevsky, I. Sutskever, G. Hinton, *Adv. Neural Inf. Process. Syst.* **25** (2012).
10. A. Dosovitskiy et al., *ICLR* (2021).

A comparative analysis of classical planning algorithms for MAV navigation in dynamic subterranean environments

Trymore Aloni[1*], *Makhosazana* Moyo[2] and *Celik* Turgay[3]

[1] School of Mechanical, Industrial and Aeronautical Engineering, University of the Witwatersrand, Johannesburg, South Africa
* Corresponding author: 2217322@students.wits.ac.za

Abstract. Micro-aerial vehicles (MAVs) are increasingly deployed in subterranean environments for exploration, search and rescue, and infrastructure inspection. These underground settings present substantial challenges, including GPS-denied navigation, dynamic obstacles, limited visibility, and communication constraints. Classical planning algorithms such as A*, rapidly-exploring random trees (RRT), and RRT* have served as foundational approaches for MAV path planning, yet their comparative performance in dynamic subterranean conditions remains underexplored. This study evaluates A*, RRT, and RRT* for high-speed MAV navigation in dynamic underground environments, focusing on computational efficiency, path optimality, real-time replanning, and adaptability to moving obstacles. Results from customised simulation environments reveal the strengths and weaknesses of each planner and provide practical guidance for algorithm selection in real-world subterranean MAV applications.

1 Introduction

Subterranean environments, including underground mines, tunnel networks, cave systems, and collapsed structures, pose unique challenges for autonomous MAV navigation due to narrow passages, irregular terrain, and the absence of GPS signals [1], [2]. Traditional path-planning methods often struggle with the computational demands of real-time replanning in highly dynamic settings. Classical planning algorithms such as A*, RRT, and RRT* have been widely adopted for robot navigation tasks, each offering distinct advantages. A* is known for optimal pathfinding in known environments, RRT excels in rapidly exploring unknown spaces, while RRT* provides asymptotically optimal solutions [3], [4], [5]. Comparative studies have been done on classical planners[6], [7], [8], [9], [10], [11], while their work is very relevant but does not explore high speed navigation which this work does. Additionally, the suitability of these algorithms for high-speed MAV navigation in dynamic and confined subterranean environments has not been systematically compared. This study aims to critically evaluate these classical planning approaches to identify their effectiveness under the specific constraints imposed by underground operations, including limited onboard computation, battery constraints, and the need for rapid obstacle avoidance.

2 Methodology

A comparative evaluation framework was implemented in a high-fidelity simulation environment. A customised subterranean scenario was developed in Gazebo and ROS on Ubuntu, reproducing realistic underground conditions with varying corridor widths, dynamic obstacles, and poor lighting. The environment builds on the open CERLAB UAV-autonomy framework from Carnegie Mellon University[12]. Obstacle density follows prior studies at 15 obstacles per 45 m of tunnel, of which 5 are dynamic and 10 are static.

The MAV platform is modelled with realistic sensing (depth camera and IMU) under embedded compute constraints. The three planners (A*, RRT, and RRT*) are integrated with the MAV control system and assessed on computational time per planning cycle, path length and optimality, obstacle-avoidance success rate, replanning frequency in dynamic scenes, and scalability. Following the literature, speeds above 2 m/s in confined subterranean space are treated as high-speed [13]. The MAV is tested from 1.0 m/s to 5.0 m/s at a fixed obstacle density, with 100 trials per algorithm per condition to ensure statistical validity.

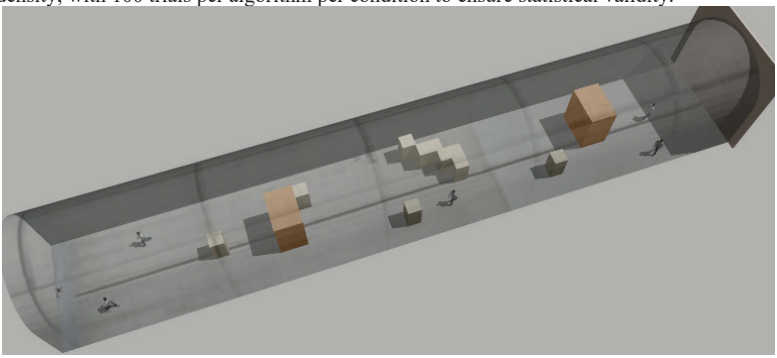


Fig. 1. Gazebo Simulation Environment set up [12]

The simulation architecture to be employed in this investigation is illustrated in Figure 2

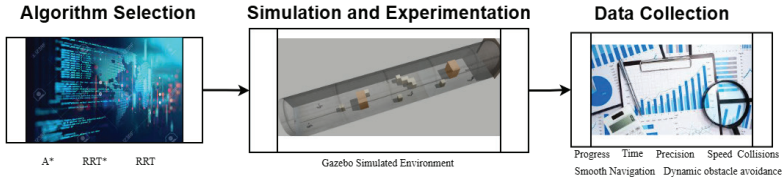


Fig. 2. Overview of the proposed comparative evaluation framework.

3 Results and discussion

A* delivers the most consistent path optimality in structured, known tunnel topology, but its deterministic global search carries a computational overhead that limits real-time use above about 2 m/s. RRT generates initial paths fastest through probabilistic sampling, which suits rapid exploration of unknown space, although its paths are less efficient and benefit from smoothing before deployment. RRT* recovers path quality through asymptotic convergence, at a computational cost that challenges real-time execution on resource-constrained platforms, particularly above 2 m/s [14].

Across the tested range a consistent pattern emerges: all three planners remain dependable at low speed but degrade sharply once the target speed exceeds the 2 m/s high-speed threshold, as the plan-then-execute cycle can no longer keep pace with a changing map. Dynamic-obstacle scenarios favour the sampling-based planners over A* because their replanning is more flexible, and where the overhead of RRT* proves prohibitive, RRT with path smoothing emerges as the most practical compromise between planning speed and path quality.

4 Conclusion

This study highlights the comparative strengths and limitations of classical planning algorithms for MAV navigation in dynamic subterranean environments. A* excels in structured scenarios with known topology, RRT-based approaches adapt better to dynamic obstacles and unknown space, and RRT* offers the best path quality at the expense of computational efficiency. The findings support informed planner selection for real-world subterranean MAV deployment, balancing path optimality, computational feasibility, and real-time performance. Future work will validate these results in physical underground environments and develop hybrid approaches that combine classical planning with adaptive learning for improved dynamic obstacle handling.

References

[1] R. Zhang, G. Hao, K. Zhang, and Z. Li, "Unmanned aerial vehicle navigation in underground structure inspection: A review," *Geological Journal*, vol. 58, no. 6, pp. 2454–2472, Jun. 2023, Accessed: Mar. 08, 2026. [Online]. Available: https://onlinelibrary.wiley.com/doi/epdf/10.1002/gj.4763

[2] J. Zhou, K. Mao, R. Wang, T. He, and L. Huang, "Autonomous Navigation Method for UAV Based on the Fusion of Laser SLAM and AprilTag," in *Journal of Physics: Conference Series*, Institute of Physics, 2025. doi: https://iopscience.iop.org/article/10.1088/1742-6596/3012/1/012002/pdf.

[3] A. Abdukodirov and J. Benndorf, "Recent Developments in Path Planning for Unmanned Ground Vehicles in Underground Mining Environment," Jun. 01, 2025, *Multidisciplinary Digital Publishing Institute (MDPI)*. doi: 10.3390/mining5020033.

[4] H. Cheriet, K. K. Badra, and C. Samira, "Comparative Analysis of UAV Path Planning Algorithms for Efficient Navigation in Urban 3D Environments," Aug. 2025, [Online]. Available: http://arxiv.org/abs/2508.16515

[5] C. Gómez Arnaldo, M. Zamarreño Suárez, F. Pérez Moreno, and R. Delgado-Aguilera Jurado, "Path Planning for Unmanned Aerial Vehicles in Complex Environments," *Drones*, vol. 8, no. 7, Jul. 2024, Accessed: Mar. 08, 2026. [Online]. Available: https://oa.upm.es/89575/1/10302867.pdf

[6] Y. Zheng, A. Li, Z. Chen, Y. Wang, X. Yang, and S. K. Im, "MPN-RRT*: A New Method in 3D Urban Path Planning for UAV Integrating Deep Learning and Sampling Optimization," *Sensors*, vol. 25, no. 13, Jul. 2025, doi: https://pmc.ncbi.nlm.nih.gov/articles/PMC12252450/pdf/sensors-25-04142.pdf.

[7] S. E. Tsai, S. M. Yang, and W. C. Sun, "The Study on Real-Time RRT-Based Path Planning for UAVs Using a STM32 Microcontroller," *Electronics (Switzerland)*, vol. 14, no. 24, Dec. 2025, doi: https://www.mdpi.com/2079-9292/14/24/4901.

[8] K. Tamanakijprasart, S. Mondal, and A. Tsourdos, "Dynamic Path Planning of UAV in Three-dimensional Complex Environment Based on Interfered Fluid Dynamical System," in *AIAA SciTech Forum and Exposition, 2024*, American Institute of Aeronautics

and Astronautics Inc, AIAA, 2024. doi: https://dspace.lib.cranfield.ac.uk/server/api/core/bitstreams/0f518fea-ed76-40d4-9785-6f703010f33c/content.

[9] F. Miao and H. Li, "Real-time path planning for unmanned aerial vehicles in complex three-dimensional dynamic environments using an enhanced fuzzy neural fluid dynamical system," *Eng. Appl. Artif. Intell.*, vol. 164, p. 113274, 2026, doi: https://doi.org/10.1016/j.engappai.2025.113274.

[10] W. Zhang, J. Li, W. Yu, P. Ding, J. Wang, and X. Zhang, "Algorithm for UAV path planning in high obstacle density environments: RFA-star," *Front. Plant Sci.*, vol. 15, 2024, doi: https://pmc.ncbi.nlm.nih.gov/articles/PMC11524861/pdf/fpls-15-1391628.pdf.

[11] J. Choi and Y. Choi, "Path Planning for Unmanned Aerial Vehicle: A-Star-Guided Potential Field Method †," *Drones*, vol. 9, no. 8, Aug. 2025, doi: https://www.mdpi.com/2504-446X/9/8/545.

[12] Zhefan Xu, "UAV Autonomy." Accessed: Mar. 14, 2026. [Online]. Available: https://github.com/Zhefan-Xu/CERLAB-UAV-Autonomy

[13] A. Wróblewski, A. Banasiewicz, P. Krot, P. Trybała, R. Zimroz, and A. Zinchenko, "A New Method of Airflow Velocity Measurement by UAV Flight Parameters Analysis for Underground Mine Ventilation," *Sensors*, vol. 25, no. 17, Sep. 2025, doi: https://cris.fbk.eu/retrieve/525f2860-496b-4b27-81e8-5813e06c5713/sensors-25-05300-v2.pdf.

[14] Z. Xu, Y. Xiu, X. Zhan, B. Chen, and K. Shimada, "Vision-aided UAV Navigation and Dynamic Obstacle Avoidance using Gradient-based B-spline Trajectory Optimization," in *Proceedings - IEEE International Conference on Robotics and Automation*, Institute of Electrical and Electronics Engineers Inc., 2023, pp. 1214–1220. doi: https://ieeexplore.ieee.org/stamp/stamp.jsp?tp=&arnumber=10160638.

Design and characterization of Si-Ge compounds for enhanced silicon-based anodes in advanced battery applications

Samson Singo[1]*, *Katlego* Phoshoko[2], *Tshidi* Mogashoa[1], *Phuti* Ngoepe[1] and *Raesibe* Ledwaba[1]

[1]Materials Modelling Centre, University of Limpopo, Private Bag x1106, Sovenga 0727, South Africa.
[2]Data Intensive Research Initiative of South Africa, Council for Scientific and Industrial Research, P.O. Box 395, Pretoria, 0001, South Africa.

Abstract. Silicon is a promising anode material for next-generation lithium-ion batteries due to its high theoretical capacity compared to graphite. However, its practical application is limited by severe volume expansion during cycling, leading to structural degradation, conductivity loss, and unstable SEI formation. This study explores germanium doping to improve the structural, electronic, and mechanical properties of silicon anodes. Cluster expansion and density functional theory calculations identified two stable phases, Ge_5Si and $GeSi_5$, which exhibit semiconducting behaviour with narrow band gaps and mechanical stability, though they remain brittle. Overall, germanium incorporation shows potential for enhancing silicon anode performance in advanced lithium-ion batteries.

1 Introduction

Silicon is a promising anode material for next-generation lithium-ion batteries due to its high theoretical capacity and abundance [1]. However, its practical use is limited by large volume expansion during cycling, which leads to structural damage, electrical contact loss, and unstable SEI formation [1, 2]. Doping silicon with alloying elements has been explored to improve its structural, electronic, and mechanical properties, with germanium emerging as a promising dopant due to its similar crystal structure, high lithium diffusivity, and good electrical conductivity [3]. Germanium incorporation can therefore modify local bonding environments and influence phase stability while preserving favourable electrochemical characteristics [4].

In this work, the effect of germanium doping on silicon is investigated using cluster expansion modelling combined with density functional theory calculations. The study aims to identify stable Ge doped Si phases and evaluate their structural, electronic, and mechanical properties, with the goal of understanding how controlled germanium incorporation can enhance silicon anode performance for advanced lithium-ion battery applications.

* Corresponding author: smsnsingo@gmail.com

2 Materials and methodology

The cluster expansion approach was applied to predict new germanium-doped silicon phases, with the cross-validation score serving as a metric to assess the predictive accuracy of the generated configuration sets [5]. Subsequently, density functional theory (DFT) calculations implemented in the Vienna Ab Initio Simulation Package (VASP) were performed to evaluate the structural and electronic properties of the identified phases [6-7]. The exchange-correlation effects were treated using the generalized gradient approximation within the Perdew-Burke-Ernzerhof (GGA-PBE) functional. Calculations were carried out with plane-wave cut-off energies of 730 and 400 eV, while Brillouin-zone sampling employed 7×7×7 and 9×9×9 k-point meshes generated using the Monkhorst–Pack scheme for Si and Ge_5Si and $GeSi_5$ respectively.

3 Results and discussion

Cluster expansion simulations predicted twenty-seven new phases, among which two ordered compounds, Ge_5Si and $GeSi_5$, were identified as thermodynamically stable and located on the DFT ground-state line with negative formation energies. Structural optimization was subsequently performed to relax their geometries, revealing that both phases crystallize in an orthorhombic symmetry. Electronic structure analysis, based on density of states and band structure calculations, indicates that both compounds exhibit semiconducting behaviour similar to pristine silicon, with narrow band gaps of 0.186 eV and 0.585 eV for Ge_5Si and $GeSi_5$, respectively. Mechanical properties were evaluated through the calculation of elastic constants, elastic moduli, and Pugh's and Poisson's ratios. The results confirm that both structures satisfy mechanical stability criteria; however, their Pugh's and Poisson's ratios fall below the recommended thresholds, indicating brittle behaviour.

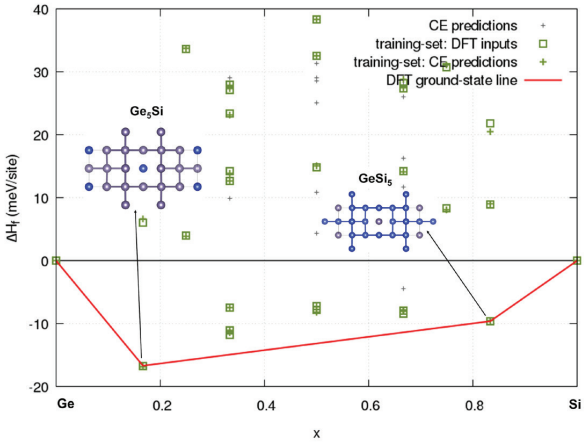


Fig.1. Cluster expansion of Si doped with Ge

4 Conclusion

This study demonstrates that germanium incorporation into silicon produces thermodynamically stable Ge doped Si phases with favourable structural and electronic characteristics. Cluster expansion identified Ge_5Si and $GeSi_5$ as stable ordered compounds that crystallize in orthorhombic symmetry and exhibit semiconducting behaviour with narrow band gaps. Mechanical analysis confirmed that both phases satisfy stability criteria, although their elastic descriptors indicate brittle behaviour. Overall, these findings suggest that controlled germanium doping offers a promising route to improve the structural integrity and electronic performance of silicon-based anodes, providing valuable insight for the design of advanced lithium-ion battery materials.

We sincerely acknowledge the National Research Foundation (NRF) for their financial support. This study utilized the computational resources of the Materials Modelling Centre (MMC) at the University of Limpopo and the Centre for High Performance Computing (CHPC) in Cape Town, South Africa.

References

1. C. Zhang, F. Wang, J. Han, S. Bai, J. Tan, J. Liu, Challenges and Recent Progress on Silicon-Based Anode Materials for Next-Generation Lithium-Ion Batteries. Small Struc., **2**, 2100009 (2021). https://doi.org/10.1002/sstr.202100009
2. R. Zhan, X. Wang, Z. Chen, Z.-W. Seh. Promises and Challenges of the Practical Implementation of Prelithiation in Lithium-Ion Batteries. Adv. Energy Mater., **11**, 2101565 (2021). https://doi.org/10.1002/aenm.202101565
3. C.-C. Hsieh, W.-R. Liu. Effects of nitrogen doping on Si/carbon composite anode derived from Si wastes as potential active materials for Li ion batteries. J. Alloys Compd., **790**, 829-836 (2019). https://doi.org/10.1016/j.jallcom.2019.03.242
4. L. Sun, L. Wang, Y. Liu, H. Wang, Z. Jin. Synergistic engineering of micron-sized porous silicon anodes via Ge doping and liquid metal alloy modification for high-energy-density lithium-ion batteries. J. Mater. Chem. A, **13**, 14346-14352 (2025). https://doi.org/10.1039/D5TA00298B
5. Q. Wu, B. He, T. Song, J. Gao, S. Shi. Cluster expansion method and its application in computational materials science Comput. Mater. Sci., **125**, 243–254 (2016). https://doi.org/10.1016/j.commatsci.2016.08.034
6. J. Hafner. Ab-initio simulations of materials using VASP: Density-functional theory and beyond. J. Comput. Chem., **29**, 2044–2078 (2008). https://doi.org/10.1002/jcc.21057
7. W. Kohn, L.-J. Sham. Self-Consistent Equations Including Exchange and Correlation Effects. Phys. Rev., **140**, A1133 (1965). https://doi.org/10.1103/PhysRev.140.A1133

Adsorption properties of Fe and Cr modified GaN monolayer for CH_2O gas detection

Malesela Makgoba[1*], *Abram* Mahladisa[1], *Malili* Matshaba[1], *Moshibudi* Ramoshaba[1], and *Thuto* Mosuang[1]

[1]University of Limpopo, Department of Physics, Private Bag X1106, Sovenga 0727, South Africa

Abstract. The adsorption of CH_2O on the surface of GaN monolayer doped with Fe and Cr has been investigated using density functional theory. Negative adsorption energies of -0.549 eV and -1.727 eV were attained for the adsorption of CH_2O on GaN monolayer doped with Fe and Cr respectively, implying energetically stable systems. The binding distance between the CH_2O gas and GaN monolayer doped with Fe and Cr were computed to be 2.262 Å (Fe-O) and 1.898 Å (Cr-O) respectively. The adsorption of CH_2O on GaN monolayer doped with Fe and Cr gas occurs though the oxygen atom.

1 Introduction

Sensing devices assist with noting and possible setting alarm on toxic and volatile gases which may escape unnoticed. To curb this problem, layered metal nitride semiconductors are being explored. Layered gallium nitride (GaN) has become research hotspot in this field [1, 2]. This is due to its enlarged surface areas, outstanding electrical and thermal conductivities. Nonetheless, the pristine layered nitride semiconductor materials gas sensors have their many challenges regarding some gas detection, which include weak adsorption capacity and less electron transfer. To address such issues, researchers have suggested metal doping as the alternative process for enhancing the performance of pristine GaN gas sensors [1]. As such, some noble metal doped GaN have been considered as potential materials for gas sensing applications [1]. This study explores the gas sensing properties of layered structure of GaN doped with Iron (Fe) and Chromium (Cr) towards gas sensing.

2 Computational details

The DMol^3 code enclosed within the material studio (MS) software, was utilised for all the DFT based geometry optimisations. The generalised gradient approximation (GGA) of Perdew-Burke-Ernzerhof (PBE) exchange correlation energy functional was applied for all geometry optimisations. The orbital cutoff radius of 6.5 Å and the K-points of 12x12x1 were attained after convergence test and further utilised for all the geometrical optimisation

* Corresponding author: malesela.makgoba@ul.ac.za

calculations. Double numerical plus polarization (DNP) was used as the basis atomic orbital set.

3 Results

Table 1. Adsorption parameters of CH_2O on the pure GaN surface and Fe and Cr doped GaN monolayer.

Systems	Adsorption energy (eV)	Adsorption Distance (Å)
GaN-CH_2O	-0.347	2.817 (N-C)
GaN-Fe-CH_2O	-0.549	2.262 (Fe-O)
GaN-Cr-CH_2O	-1.727	1.898 r-O)

4 Conclusion

The negative adsorption energies suggest energetically stable GaN-Fe/Cr-CH_2O systems. The more negative the adsorption energy, the more favourable and stronger the adsorption. As such, the adsorption energies suggest that the adsorption of CH_2O is more favourable on the surface of GaN monolayer doped with Cr. The adsorption of CH_2O occurs through the Oxygen atom on the surface of GaN monolayer doped with Fe and Cr. The shorter bond length was observed for Cr-O in the case of CH_2O being adsorbed on Cr decorated GaN monolayer which suggest stronger adsorption as also supported by the adsorption energy.

References

1. G.X. Chen, H.F. Li, D.D. Wang, S.Q. Li, X.B. Fan, J.M. Zhang, Adsorption of toxic gas molecules on pristine and transition metal doped hexagonal GaN monolayer: A first-principles study. Vacuum, **165**, 35-45 (2019).
2. C. Feng, H. Qin, D. Yang, G. Zhang, First-principles investigation of the adsorption behaviors of CH_2O on BN, AlN, GaN, InN, BP, and P monolayers. Materials, **12**, 676 (2019).

Effect of Ta on the magnetic and mechanical properties of $Fe_{50}Co_{43.75}Ni_{6.25}$ alloy

Dineo Maepa[1*], *Tshegofatso* Phaahla[1], *Ramogohlo* Diale-Boshielo[1,2], and *Hasani* Chauke[1]

[1]Materials Modelling Centre, University of Limpopo, Private Bag X 1106, Sovenga, 0727, South Africa
[2]Advanced Materials Division, MINTEK, Private bag X 3015, Randburg, 2125, South Africa

Abstract. FeCo alloys have received significant attention due to their superior magnetic properties, however it exhibits limited ductility. Alloying with elements such as Ni has been explored to improve the structural stability and ductility of FeCo alloys; however, achieving a balance between enhanced mechanical properties and high magnetic performance remains challenging. In this study, quaternary $Fe_{50}Co_{43.75-x}Ni_{6.25}Ta_x$ alloys were investigated using density functional theory with GGA-PBE functional. Ta substitution at Co sites was found to enhance thermodynamic, phonon stability, and ductility of $Fe_{50}Co_{43.75}Ni_{6.25}$ alloy. The results provide guidance for designing FeCoNi-based alloys with balanced mechanical and magnetic properties for advanced soft magnetic applications.

1 Introduction

FeCo-based soft magnetic alloys are highly attractive because of their strong ferromagnetic behaviour, elevated Curie temperature (~920–985 °C), and exceptionally high saturation magnetization (~2.4 T) [1]. However, despite its superior magnetic performance, B2-ordered FeCo exhibits poor ductility at room temperature, which limits its processability and industrial applicability [2]. Furthermore, enhancing their ductility and thermodynamic stability through alloying additions such as Ni can lead to a compromise in magnetic performance. In the present work, we therefore extend the system to a quaternary ($Fe_{50}Co_{43.75-x}Ni_{6.25}Ta_x$) alloy, aiming to evaluate how partial substitution with Ta can recover or enhance the magnetic characteristics while maintaining the mechanical properties.

2 Methodology

Spin-polarized density functional theory (DFT) calculations were carried out using the Vienna ab initio Simulation Package (VASP) within the projector augmented wave (PAW) framework. The exchange-correlation interactions were described using the generalized gradient approximation with Perdew-Burke-Ernzerhof (PBE) functional [3]. A plane-wave cutoff energy of 500 eV and a 12 × 12 × 12 Monkhorst–Pack k-point grid were selected after

* Corresponding author : 202028705@myturf.ul.ac.za

systematic convergence testing, and all structures were fully relaxed until the Hellmann–Feynman forces were below 0.01 eV/Å.

3 Results and discussion

Figure 1 illustrates how the elastic constants (C_{11}, C_{12}, C_{44} and C′) vary with Ta concentration in $Fe_{50}Co_{43.75-x}Ni_{6.25}Ta_x$ alloys. As the Ta content increases, the elastic constants satisfy $C_{11} > C_{12}$ and $C_{44} > 0$, indicating that the material remains mechanically stable according to the cubic crystal stability criteria.

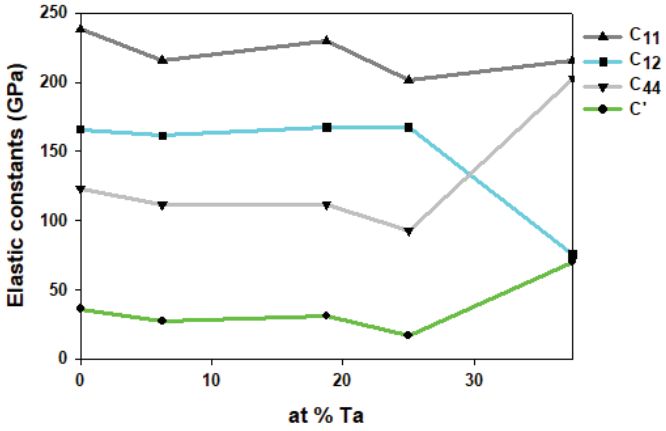


Fig. 1. Elastic constants (GPa) for $Fe_{50}Co_{43.75-x}Ni_{6.25}Ta_x$ against atomic % Ta, where $0 \leq x \leq 37.5$.

4 Conclusion

The addition of Ta in $Fe_{50}Co_{43.75-x}Ni_{6.25}Ta_x$ alloys was found to enhances ductility, thermodynamic and vibrational stability, particularly at a concentration of 37.5 at.%. However, it simultaneously lowers the Curie temperature and reduces magnetic strength.

The computational work presented in this study was conducted using the facilities of the Materials Modelling Centre at the University of Limpopo and the Centre for High-Performance Computing (CHPC) in Cape Town. The authors acknowledge the financial support provided by the South African Department of Science, Technology and Innovation (DSTI) through the Advanced Metals Initiative (AMI) at Mintek and the South African Research Chair Initiative (SARChI).

This research was funded by the Department of Science, Technology and Innovation (DSTI) - Advanced Materials Initiative (AMI), through the Ferrous Materials Development Network (FMDN).

The data supporting the findings of this study are available from the corresponding author upon reasonable request.

References

1. M. Muralles, J. T. Oh, and Z. Chen, Atomistic investigation of effect of alloying on mechanical properties and microstructural evolution of ternary FeCo-X (X = V, Nb, Mo, W). Comput. Mater. Sci. **241**, 113030 (2024).
2. L. Han et al., A mechanically strong and ductile soft magnet with extremely low coercivity. Nature **608**, 310–316 (2022).
3. A. E. Mattsson, P. A. Schultz, M. P. Desjarlais, T. R. Mattsson, and K. Leung, Designing meaningful density functional theory calculations in materials science – A primer. Modell. Simul. Mater. Sci. Eng. **13**, R1–R31 (2005).

Gaussian process regression versus response surface methodology for PBF-LB/M process qualification in dimensionless coordinates

Michael Thomson[1*], and *Thorsten* Becker[1]

[1]Centre for Materials Engineering, University of Cape Town, 7701 Cape Town, South Africa

Abstract. Response surface methodology (RSM) is widely used for PBF-LB/M process mapping, but its fixed quadratic form cannot capture the sigmoidal lack-of-fusion (LOF) to dense transition, and its uniform prediction intervals lack spatial reliability information. This study compares Gaussian process (GP) regression against 2nd order RSM in physics-based dimensionless coordinates (normalised enthalpy Π_H, overlap fraction ϕ, and layer penetration margin λ). Two literature datasets spanning the full LOF-to-dense transition were analysed. Leave-one-out cross-validation shows GP outperforms RSM (ΔR^2 = +0.09 to +0.20) with systematic RSM residual bowing in the transition zone. Plateau-only datasets confirm RSM suffices within a known dense regime.

1 Introduction

Laser powder bed fusion (PBF-LB/M) process mapping studies typically pursue either process optimisation, locating optimal parameters within a known operating window, or process qualification, defining process window boundaries with transferable, uncertainty-quantified results. Response surface methodology (RSM) is well-established for optimisation; a quadratic polynomial adequately represents the smooth response within the dense regime [1].

For qualification, however, RSM has structural limitations: the LOF-to-dense transition is sigmoidal, not quadratic, producing systematic prediction bias when the full process window is modelled. Moreover, filtering training data to high-density specimens, standard practice in many published studies, degrades model performance by removing the informative transition-zone gradient. This work addresses these gaps through a physics-based dimensionless framework reducing the process parameter space to three transferable inputs. GP regression is evaluated against 2nd order RSM on two independent literature datasets to test whether GP flexibility resolves this systematic bias and whether the dimensionless framework enables cross-material transfer.

2 Dimensionless process mapping framework

* Corresponding author: thmmic028@myuct.ac.za

Applying the Buckingham Pi theorem to the governing process and material property variables yields three primary dimensionless inputs [2–4]. The normalised enthalpy:

$$\Pi_H = \frac{\eta P}{\rho \Delta H_m \sqrt{\alpha v d^3}} \quad (1)$$

measures energy deposited relative to the energy required to melt a characteristic volume, where η is absorptivity, ρ density, ΔH_m latent heat of melting, α thermal diffusivity, and d spot diameter [2, 4]. The overlap fraction ϕ and the layer penetration margin λ:

$$\phi = \frac{d - h}{d} \quad (2)$$

$$\lambda = \frac{d - t}{d} \quad (3)$$

quantify track-to-track coalescence and re-melting depth respectively. Together, (Π_H, ϕ, λ) encode melt pool formation physics in a material-independent form, enabling process maps to transfer across systems via rescaling of material constants.

3 Datasets and methods

Six candidate datasets from the published literature were converted to dimensionless coordinates and screened against three criteria: n ≥ 10, RD range spanning at least 10 percentage points, and at least one specimen with RD < 95%. Two datasets met all criteria: an EOS M290/IN718 campaign [5, 6] (n = 45, d = 100 µm, RD 81.4–99.7%) and an EOS M270/Ti-6Al-4V campaign [7] (n = 16, d = 100 µm, RD 34.8–100.0%, fixed λ). Absorptivity was taken as η = 0.60 for IN718 and η = 0.27 for Ti-6Al-4V.

Three model classes were compared: 2nd order RSM (quadratic polynomial, 10 terms for 3-input and 6 terms for 2-input cases), 3rd order RSM, and GP regression with a Matérn-5/2 kernel and noise variance estimated by marginal likelihood. Performance was assessed by leave-one-out (LOO) cross-validation R^2.

4 Results

Table 1 summarises model performance. GP consistently outperforms 2nd order RSM in LOO R^2, with the largest improvement on Ti-6Al-4V where the RD range is widest. The 3rd order RSM partially recovers performance but at the cost of additional coefficients. Among the four screened-out datasets, two that remained within the dense plateau showed RSM performing comparably to GP, consistent with the qualification-versus-optimisation argument.

Table 1. LOO R^2 comparison for 2nd order RSM and GP regression across two independent datasets in dimensionless coordinates.

Property	EOS M290 / IN718	EOS M270 / Ti-6Al-4V
n	45	16
RD range (%)	81.4 – 99.7	34.8 – 100.0
Model inputs	3 (Π_H, ϕ, λ)	2 (Π_H, ϕ)
2nd order RSM LOO R^2	0.891	0.699
GP LOO R^2	0.981	0.899
ΔR^2 (GP − RSM)	+0.090	+0.200
2nd order mean LOO residual, LOF band	−1.59%	n.r. (3 LOF specimens)

Residual analysis reveals a consistent pattern: 2nd order RSM systematically overpredicts density in the LOF band (mean LOO residual of −1.59% for IN718; not reported for Ti-6Al-4V, with only three LOF-band specimens), with compensating underprediction in the dense plateau. This bowing arises because a quadratic surface cannot simultaneously represent the

steep sigmoidal rise and the flat plateau. A filtering sweep confirms that restricting data to high-*RD* specimens degrades LOO R^2 for both models, as filtering removes the informative transition gradient and leaves only noise-dominated plateau data.

5 Conclusions and ongoing work

Two conclusions are supported. First, 2nd order RSM exhibits systematic residual bowing across the LOF-to-dense transition, a structural limitation independent of dataset size or material. Second, GP regression resolves this bias while providing calibrated uncertainty that grows in data-sparse regions; directly relevant to qualification-oriented process mapping. Studies using 2nd order RSM across the full process window may carry systematic transition-zone bias not visible from aggregate R^2 statistics; this does not invalidate RSM for optimisation but indicates that qualification maps require non-parametric models. A purpose-designed experimental campaign is underway on a 400 W industrial PBF-LB/M machine for Ti-6Al-4V and Inconel 718 to provide the first machine-specific dimensionless process maps and test cross-material transferability.

References

1. R.H. Myers, D.C. Montgomery, C.M. Anderson-Cook, *Response Surface Methodology: Process and Product Optimization Using Designed Experiments*, (John Wiley & Sons, 2016)
2. D.B. Hann, J. Iammi, J. Folkes, A simple methodology for predicting laser-weld properties from material and laser parameters. J. Phys. D: Appl. Phys. **44**, 445401 (2011). https://doi.org/10.1088/0022-3727/44/44/445401
3. W.E. King, H.D. Barth, V.M. Castillo, G.F. Gallegos, J.W. Gibbs, D.E. Hahn, C. Kamath, A.M. Rubenchik, Observation of keyhole-mode laser melting in laser powder-bed fusion additive manufacturing. J. Mater. Process. Technol. **214**, 2915–2925 (2014). https://doi.org/10.1016/j.jmatprotec.2014.06.005
4. A.M. Rubenchik, W.E. King, S.S. Wu, Scaling laws for the additive manufacturing. J. Mater. Process. Technol. **257**, 234–243 (2018). https://doi.org/10.1016/j.jmatprotec.2018.02.034
5. C. Lu, J. Shi, Relative density and surface roughness prediction for Inconel 718 by selective laser melting: central composite design and multi-objective optimization. Int. J. Adv. Manuf. Technol. **119**, 3931–3949 (2022). https://doi.org/10.1007/s00170-021-08388-2
6. C. Lu, J. Shi, Simultaneous consideration of relative density, energy consumption, and build time for selective laser melting of Inconel 718: A multi-objective optimization study on process parameter selection. J. Clean. Prod. **369**, 133284 (2022). https://doi.org/10.1016/j.jclepro.2022.133284
7. J.J.S. Dilip, S. Zhang, C. Teng, K. Zeng, C. Robinson, D. Pal, B. Stucker, Influence of processing parameters on the evolution of melt pool, porosity, and microstructures in Ti-6Al-4V alloy parts fabricated by selective laser melting. Prog. Addit. Manuf. **2**, 157–167 (2017). https://doi.org/10.1007/s40964-017-0030-2

03

ABSTRACTS

Materials Engineering

First principles study of the structural, magnetic and electronic properties of $Fe_{50}Pt_{50-x}Cu_x$ alloys

Mashilo Matlala[1*], *Malili* Matshaba[2], *Ramogohlo* Diale-Boshielo[1, 3], *and Hasani* Chauke[1]

[1] Materials Modeling Centre, University of Limpopo, Private Bag X 1106, Sovenga 0727, South Africa
[2] Department of Physics, University of Limpopo, Private Bag X 1106, Sovenga 0727, South Africa
[3]Advanced Materials Division, MINTEK, Private bag X 3015, Randburg 2125, South Africa

Abstract. The $L1_0$ FePt alloy is the leading candidate for high density magnetic storage due to its high magnetic anisotropy energy and thermal stability. However, its application is limited by challenges such as high ordering temperature required to form $L1_0$ phase and chemical instability. Hence, ternary alloying of Cu was conducted to enhance the stability of the FePt. In this study, the magnetic, and electronic properties of $Fe_{50}Pt_{50-x}Cu_x$ were investigated using density functional theory. The results showed that Cu substitution reduces magnetic strength of the FePt. The findings provide insight into tailoring FePt-based alloys for potential applications in magnetic storage technologies.

1 Introduction

The $L1_0$ ordered FePt alloy is widely recognised for its large uniaxial magnetocrystalline anisotropy, high curie temperature and excellent thermal stability. These properties make FePt suitable for high density magnetic recording and spintronic devices [1]. Despite its superior magnetic performance, FePt alloy faces challenges including high ordering temperature required to form $L1_0$ phase and the high platinum content which increases the production cost. Ternary substitution at Pt site has emerged as important strategy to tailor the properties of FePt alloy while reducing the production cost. Among potential dopants, Cu is attractive due to its lower costs and good alloying combability with FePt.

This study focuses on Cu substitution on FePt to evaluate its influence on structural stability and magnetic behaviour using first-principles calculations.

2 Methodology and results

* Corresponding author: 202002565@myturf.ul.ac.za

First principles calculations were performed using density functional theory (DFT) within the general gradient approximation (GGA) [2] of Perdew-Burke-Ernzerhof (PBE) [3]. Calculations were carried out using the VASP code [4] using projector-augmented waves (PAW) method [5]. The plane wave cutoff energy of 400 eV and the k spacing of 0.07/Å were selected to ensure energy convergence.

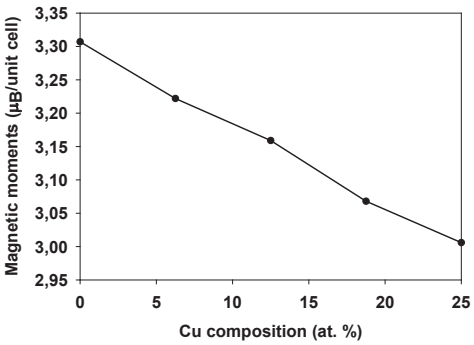


Fig. 1. Magnetic moments for $Fe_{50}Pt_{50-x}Cu_x$, where $0 \leq x \leq 25$.

3 Conclusion

The DFT was successfully used to study the effect of Cu on structural, magnetic and electronic properties of FePt alloy. The findings indicated that the Cu substitution reduces the magnetic moment and volume of the FePt alloy. Furthermore, electronic density of states revealed that magnetic properties are mainly dominated by Fe 3d state electrons.

References

1. N. Lethole, P. Ngoepe, and H. Chauke, Compositional Dependence of Magnetocrystalline Anisotropy, Magnetic Moments, and Energetic and Electronic Properties on Fe-Pt Alloys. Materials **15**, 5679 (2022).
2. J. P. Perdew, K. Burke, and M. Ernzerhof, Generalized Gradient Approximation Made Simple. Phys. Rev. Lett. **77**, 3865–3868 (1996).
3. J.P. Perdew, W. Yue, Correlation hole of the spin-polarized electron gas, with exact small-wave-vector and high-density scaling. Phys. Rev. B **24**, 13298 (1991)
4. J. Hafner and G. Kresse, The Vienna AB-Initio Simulation Program VASP: An Efficient and Versatile Tool for Studying the Structural, Dynamic, and Electronic Properties of Materials, in Properties of Complex Inorganic Solids, Boston, MA: Springer US, pp. 69–82 (1997).
5. P. E. Blöchl, Projector augmented-wave method, Phys. Rev. B. **50**, 17953–17979 (1994).

β-constrained crystallographic evolution of B19′ TiNi: a DFT study with comparison to experimental XRD data

Bongani Ngobe[1*, 2], *Mahlaga* Molepo[2], *Ramogohlo* Diale[1], *Donald* Mkhonto[1], and *Maje* Phasha[1]

[1]Advanced Materials Division, MINTEK, Private Bag X 3015, Randburg, 2125, South Africa
[2]School of Physics, University of the Witwatersrand, Private Bag 3, Wits, 2050, South Africa

Abstract. The martensitic transformation from B2 austenite to monoclinic B19′ martensite in TiNi alloy involves a crystallographic atomic distortion, quantified by the lattice parameters and monoclinic angle β. In this study, the lattice distortion associated with the B2 → B19′ transformation in TiNi is examined by comparing experimentally determined and density functional theory (DFT) predicted structural properties. TiNi alloy was produced and solution treated at 1050 °C, followed by rapid ice-water quenching to promote martensitic formation. Phase constitution and lattice parameters were determined using X-ray diffraction (XRD), while microstructural analysis were conducted using scanning electron microscopy coupled with energy dispersive spectroscopy (SEM-EDS) analysis. The results confirm the coexistence of cubic B2 austenite and monoclinic B19′ martensite, with the latter characterised by β ≈ 96.8°.

1 Introduction

Nitinol (TiNi) is one of the most extensively studied shape memory alloys due to its remarkable shape memory effect (SME) and superelasticity (SE), which originate from the reversible martensitic transformation between the high-symmetry B2 austenite and the low-symmetry monoclinic B19′ martensite [1,2]. The B2 phase crystallises in the cubic $Pm\bar{3}m$ structure with a lattice parameter of approximately a ≈ 3.00 Å [1, 3], whereas the B19′ martensite adopts a monoclinic structure ($P2_1/m$) with typical lattice parameters a ≈ 2.88–2.90 Å, b ≈ 4.62–4.64 Å, c ≈ 4.10–4.14 Å, and a monoclinic angle β ≈ 96–98° [1, 4]. This transformation involves a lattice shear that produces a crystallographic distortion of the parent B2 structure [1,2]. The monoclinic angle β, therefore, serves as a structural measure of the martensitic distortion, reflecting how the lattice accommodates the strain associated with the B2 → B19′ transformation.

Although the B2 → B19′ transformation in TiNi has been widely investigated, the influence of the heat treatment cycles on the resulting crystallographic distortion remains insufficiently quantified. In particular, variations in the monoclinic angle β may reflect differences in martensitic distortion, internal strain, or variant accommodation arising from

* Corresponding author: Bonganing@mintek.co.za and 2623288@students.wits.ac.za

processing conditions. At the same time, first-principles calculations provide predictions of the equilibrium B19′ structure, yet direct comparison with experimentally observed distortions is rarely addressed. The present work, therefore, investigates the B2 → B19′ transformation in TiNi by combining X-ray diffraction and microstructural observations with DFT modelling to evaluate how thermal history influences the experimentally observed martensitic distortion and how it compares with the predicted equilibrium structure.

2 Computational and experimental approach

First-principles calculations based on density functional theory (DFT) were employed to examine the crystallographic distortion associated with the B2 → B19′ transformation in TiNi [5]. The monoclinic B19′ structure was constructed from reported crystallographic data, and the monoclinic angle β was systematically varied to evaluate its influence on the lower temperature structural stability. For every fixed β value, the lattice parameters a, b, c and atomic positions were allowed to relax while maintaining the monoclinic symmetry, enabling determination of the energetically preferred martensitic distortion.

Guided by the predicted structural behaviour, experimental TiNi alloys were produced and subjected to controlled thermal treatments to examine the influence of thermal history on the B2 → B19′ transformation.

3 Results and discussions

Table 1 compares the crystallographic parameters of the B2 and B19′ phases obtained from XRD with those predicted by DFT. While the B2 lattice parameter shows good agreement between experiment and theory, the B19′ phase exhibits the characteristic monoclinic distortion, reflected by the lattice parameters and the monoclinic angle β.

Table 1. Comparison of experimentally determined (XRD) and DFT-predicted crystallographic parameters of B2 and B19′ TiNi.

Phase	Structure	Space Group	Lattice Parameters (Å)	β (°)	**Method**	Structural Role
B2	Cubic	Pm3m Pm-3m (221)	a = 2.998	90	XRD	Austenite
B2	Cubic	Pm-3m (221)	a = 3.011	90	DFT (GGA)	Austenite
B19’	Monoclinic	$P2_1/m$ (11)	a = 2.885, b = 4.622, c = 4.120	96.8	XRD	Martensite
B19’	Monoclinic	$P2_1/m$ (11)	a = 4.933, b = 4.061, c = 2.927	97.6	DFT (GGA)	Martensite

4 Conclusions

The results confirm the crystallographic distortion associated with the B2 → B19′ martensitic transformation in TiNi, as evidenced by the monoclinic lattice parameters and β angle obtained from XRD for the ice-water quenched condition. The comparison with DFT-predicted structural parameters shows consistent trends in the transformation from the cubic

B2 austenite to the monoclinic B19′ martensite. Further work will examine the influence of heat treatment and cooling conditions on the resulting martensitic distortion and its correlation with the predicted equilibrium structure.

References

1. K. Otsuka, X. Ren, Prog. Mater. Sci. **50**, 511–678 (2005). DOI: https://doi.org/10.1016/j.pmatsci.2004.10.001
2. J. Ma, I. Karaman, R.D. Noebe, Int. Mater. Rev. **55**, 257–315 (2010). DOI: https://doi.org/10.1179/095066010X12646898728363
3. K. Otsuka, C.M. Wayman, *Shape Memory Materials*, Cambridge University Press, Cambridge (1998).
4. Y. Kudoh, M. Tokonami, S. Miyazaki, K. Otsuka, Acta Metall. **33**, 2049–2056 (1985). DOI: https://doi.org/10.1016/0001-6160(85)90128-2
5. X. Huang, G.J. Ackland, K.M. Rabe, Nat. Mater. **2**, 307–311 (2003). DOI: https://doi.org/10.1038/nmat884

Coupled CFD–DQMOM modeling of titanium nanoparticle formation and size evolution during plasma-assisted vapor condensation

Alex Seya[1*], *Andrei* Kolesnikov[1], *Lucey* Mavhungu[1], and *Hertzog* Bissett[2]

[1]Department of Chemical, Metallurgical, and Material Engineering, Tshwane University of Technology, South Africa, Pretoria 0183, South Africa
[2]The South African Nuclear Energy Corporation SOC Ltd. (Necsa), Elias Motsoaledi Street Extension (Church Street West) R 104 Pelindaba, Madibeng Municipality, North West Province, 0240, South Africa

Abstract. The synthesis of nanoparticles via vapor condensation involves interactions among transport phenomena, kinetics, and particle population dynamics. These factors make it difficult to scale up for industrial production. This work presents a predictive Multiphysics framework that combines Computational Fluid Dynamics (CFD) and a Population Balance Model (PBM). This framework simulates nucleation, condensation, and growth processes during plasma-assisted titanium nanoparticle synthesis. The Direct Quadrature Method of Moments (DQMOM), in ANSYS Fluent, tracks the development of particle size distributions. Analyses show how reactor flow and thermal conditions impact particle formation mechanisms. The model helps transition from laboratory-scale studies to industrial powder manufacturing.

1 Introduction

The advanced application of spherical particles is of great importance in powder technology and additive manufacturing due to their flowability and high packing density. Examples of Titanium and its alloys are in high demand in the automotive, aerospace, biomedical, and pharmaceutical industries [1, 2] for their corrosion resistance and biocompatibility. Although these particles offer enumerated advantages, they also present some setbacks, such as the fact that producing spherical particles is not economically viable. To resolve this bottleneck, innovative development to minimize the cost through numerical models that create pathways to optimize the cost has rapidly increased in the last few decades, which is not only restricted to academic growth but also to the industrial revolution.

In this framework, the combination of Computational Fluid Dynamics (CFD) and the Population Balance Model (PBM) are used to describe the particle evolution in multiphase structure and to numerically understand the particle phase change, which is more complex than the experimental approach. For this instance, the widely commercial software ANSYS Fluent has been used to handle such combinations. It contains different types of particle

* Corresponding author: alexwatano@gmail.com

modeling in the population balance model [3], within which the Direct Quadrature Method of Moment (DQMOM) that solves efficiently the particle size distribution with the integration of (ref) the weights and abscissas in the quadrature equations. The DQMOM is well structured to evaluate the particle size distribution in many application such as fluidized bed reactor[4-6], a turbulent of non-premixed combustion[7], and stirred tank reactor etc. Numerically, the DQMOM is closely compared to the Lagrangian method where the discrete phase are tracked as parcel with same diameter and volume, the former has the advantage of controlling the statistics of individual particle in terms of the weight and abscissas.

2 Methodology

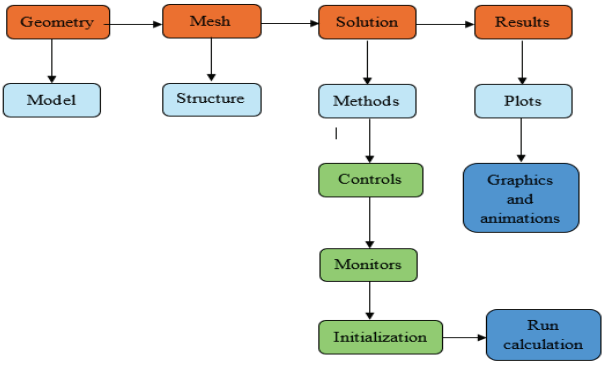


Fig. 1. Numerical methodology process flowchart.

The methodology approach is summarized in Figure 1, in which transport equations are solved.
The core of the framework lies in the Population Balance Equation [8], which tracks the particle size distribution (PSD) as a function of time, space, and local thermal conditions. And the general dynamic equation (GDE) for the synthesis of Titanium in the gas phase is defined by a number of density functions given as:

$$\frac{\partial n}{\partial t} + \nabla.(u_{\mathrm{n}}) = \nabla.(D\nabla_{\mathrm{n}}) + \left(\frac{\partial n}{\partial t}\right)_{\mathrm{nuc}} + \left(\frac{\partial n}{\partial t}\right)_{\mathrm{cond}} + \left(\frac{\partial n}{\partial t}\right)_{\mathrm{coag}} \quad (1)$$

where, u is the local velocity vector, D is the diffusion coefficient of particles.

3 Results

The expected results are a quantitative analysis of the nucleation and growth kinetics of the vapor phase, in which the temperature profile dictates the microscopic nucleation rate. The particle size distribution (PSD) evolution, which is a critical criterion for powder, and the quench gas flow rate that affects the final produced particles.

4 Conclusion

This study developed a predictive framework for producing titanium nanoparticles, linking vapor condensation to industrial powder metrics. It combines Classical Nucleation Theory (CNT) and the Quadrature Method of Moments (QMOM) in a 3D CFD environment. The work shows that properties like bulk density and flowability are set within microseconds of vapor condensation. Controlling the local thermal history of Ti vapor enables precise engineering of powders for aerospace and biomedical applications.

References

1. M. Asad and M. Sana, Potential of titanium based alloys in the biomedical sector and their surface modification techniques: A review. P I Mech Eng C-J Mec. **237,** 5503–5532 (2023). https://doi.org/10.1177/09544062231164506
2. M.J. Jackson, J. Kopac, M. Balazic, D. Bombac, M. Brojan, and F. Kosel, Titanium and titanium alloy applications in medicine, (Springer, 2016)
3. Ansys, ANSYS Fluent Population Balance Module Manual (Ansys, Inc, Canonsburg, PA 15317, 2013)
4. Y. Yao, J.-W. Su, and Z.-H. Luo, CFD-PBM modeling polydisperse polymerization FBRs with simultaneous particle growth and aggregation: The effect of the method of moments. Powder Technol. **272,** 142–152 (2015). https://doi.org/10.1016/j.powtec.2014.11.037
5. R. Fan, D.L. Marchisio, and R.O. Fox, Application of the direct quadrature method of moments to polydisperse gas–solid fluidized beds. Powder Technol. **139,** 7–20 (2004). https://doi.org/10.1016/j.powtec.2003.10.005
6. M. Kim, K. Lee, Y. Bak, and J.M. Lee, A two-way coupled CFD-DQMOM approach for long-term dynamic simulation of a fluidized bed reactor. Korean J. Chem. Eng. **38,** 342–353 (2021). https://doi.org/10.1007/s11814-020-0701-4
7. T. Kim and Y. Kim, DQMOM approach for poly-dispersed soot formation processes in a turbulent non-premixed ethylene/air flame. Chemical Engineering Science. **152,** 426–435 (2016). https://doi.org/10.1016/j.ces.2016.06.043
8. J.M. Blocher and I. Campbell, Vapor pressure of titanium. J. Am. Chem. Soc. **71,** 4040–4042 (1949). https://doi.org/10.1021/ja01180a048

Benchmarking artificial neural networks against traditional regression models for the scalable prediction of Ti-6Al-4V powder spheroidization

Justin Mbwebwe[1*], *Andrei* Kolesnikov[1], *Lucey* Mavhungu[1] and *Hertzog* Bissett[2]

[1]Department of Chemical, Metallurgical and Materials Engineering, Tshwane University of Technology, Pretoria 0185, South Africa
[2]The South African Nuclear Energy Corporation SOC Ltd. (Necsa), Elias Motsoaledi Street Extension (Church Street West) R 104 Pelindaba, Madibeng Municipality, North West Province, 0240, South Africa

Abstract. Spherical Ti-6Al-4V powder is critical for the additive manufacturing industry. One of the most preferred methods for its production is radio frequency inductively coupled plasma spheroidization. Optimizing this process is quite resource-intensive due to intricate interactions between process parameters. Artificial neural networks have demonstrated an impressive predictive accuracy. Nevertheless, their computational complexity relative to traditional regression models warrants justification before any industrial deployment. This study benchmarks a feedforward neural network against traditional linear and polynomial regression models. The comparison goes beyond standard error metrics. Predictive performances are translated into economic terms to quantify material waste and energy loss.

1 Introduction

In additive manufacturing (AM), the morphological properties of metal powders are of utmost importance [1]. They dictate consistency in powder layering and, subsequently, the quality of printed components [2]. One of the materials of choice in AM is Ti-6Al-4V (Ti64) due to its unique characteristics, such as corrosion resistance and biocompatibility [3]. To produce this special powder, radio-frequency inductively coupled plasma has emerged as a reliable method to convert irregular Ti64 particles into spherical powders [4].

However, this process requires carefully balancing and optimizing process parameters such as particle size, plasma power, gas flow rate, and powder feed rate [5]. In our Previous work, it was demonstrated that a feedforward neural network (FFNN), developed in PyTorch and trained on a hybrid experimental-computational dataset of 67 samples, could predict spheroidicity with impressive accuracy [6]. But a question lingered: could a simpler approach have worked just as well?

To transition the developed model from an academic prototype to an industrial production tool, in line with the goals of the 2026 conference, it is important to justify the deployment

* Corresponding author: justinmbwebwe@gmail.com

and use of a complex ANN model [7]. If conventional models perform nearly as well as the neural network in our specific context, the latter may become more of an academic burden. Conversely, if the neural network exhibits superior capabilities, the additional complexity and cost associated with its development would not only be justified but also essential.

This study, therefore, aims to benchmark the established FFNN against traditional mathematical regression models. The goal is to determine whether the neural network's higher computational costs yield worthwhile improvements in prediction accuracy in full-scale production.

2 Methodology

2.1 Dataset

The hybrid dataset described in our 2025 work [6], will be used to train multiple model types. The dataset consists of 23 experimental samples combined with 44 CFD-generated data points. The experimental data were generated using a Teksphero-15 RF plasma system at the South African Nuclear Energy Corporation (Necsa). Ti-6Al-4V Grade 23 powder was processed over particle sizes ranging from 25 to 125 µm and plasma powers of 10 to 15 kW, with spheroidicity determined by optical microscopy. On the other hand, computational data was determined using a validated ANSYS Fluent model that simulated the full four-parameter space: particle size (20-130 µm), plasma power (9-16 kW), gas flow (20-90 slpm), and powder feed rate (0.5-2.5 kg/h).

2.2 Models under comparison

The feedforward neural network will be benchmarked against two different approaches:

Firstly, a multiple linear regression model. This will constitute the simplest baseline. Spheroidicity will be modelled as a linear combination of the four parameters, assuming independent effects.

The second approach will be a polynomial regression model. In this scenario, second-order and third-order models incorporating interaction terms (e.g., particle size x plasma power) and quadratic terms (e.g., gas flow^2) will be developed.

2.3 Evaluation framework

Performance will be assessed across three dimensions:

Initially, a 5-fold cross-validation will be conducted to estimate predictive accuracy. Evaluation metrics, including mean absolute error (MAE), root mean square error (RMSE), and R^2, will be computed for all models. Because averages may hide details, error distributions across the parameter space will also be evaluated.

Secondly, training will deliberately be conducted on data subsets that exclude boundary regions (e.g., powers above 14 kW or feed rates above 2 kg/h). This will be done to test how each model predicts outcomes under the excluded conditions, keeping in mind that production environments often push beyond the tested parameters due to dynamic operating conditions [8].

Finally, for each model’s prediction errors, economic metrics including material waste, energy waste, and lost production time will be evaluated. These metrics have the potential to transform abstract error numbers into decisions a plant manager can act on.

3 Expected results and discussion

It is expected that the FFNN will outperform traditional regression models by a significant margin, due to its ability to capture non-linear plasma-particle interactions. For example, previous sensitivity analyses revealed that gas flow exhibits a parabolic effect on spheroidicity. The processing efficiency would normally increase initially before gradually decreasing at higher flow rates due to shorter particle residence times. Traditional linear models will most probably fail to capture these localized optimal ranges (e.g., 40-60 slpm gas flow combined with 0.6-1.0 kg/h feed rate). While polynomial models might approximate these curves, the multidimensionality of the parameter space suggests that the FFNN scales more efficiently. Thus, justifying its use in commercial optimization despite its higher initial development costs.

References

1. P. Muthuswamy, Influence of powder characteristics on properties of parts manufactured by metal additive manufacturing. Lasers Manuf. Mater. Process. **9,** 312–337 (2022). https://doi.org/10.1007/s40516-022-00177-3

2. F.A. Talebi*, et al.*, Spreadability of powders for additive manufacturing: A critical review of metrics and characterisation methods. Particuology. **93,** 211–234 (2024). https://doi.org/10.1016/j.partic.2024.06.013

3. Y. Xu*, et al.*, Experimental analysis of the multiaxial failure stress locus of commercially pure titanium at low and high rates of strain. Int. J. Impact Eng. **170,** 1–17 (2022). https://doi.org/10.1016/j.ijimpeng.2022.104341

4. J. Li, Z. Hao, Y. Shu, J. He, Fabrication of spherical Ti-6Al-4V powder for additive manufacturing by radio frequency plasma spheroidization and deoxidation using calcium. J. Mat. Res. Technol. **9,** 14792–14798 (2020). https://doi.org/10.1016/j.jmrt.2020.10.054

5. N. Nkhasi, W. d. Preez, H. Bissett, Plasma spheroidization and characterisation of commercial titanium grade 5 powder for use in metal additive manufacturing, in Proceedings of the RAPDASA-RobMech-PRASA-AMI Conference, CSIR International Convention Centre in Pretoria, South Africa, EDP Sciences, October – November 2023 (2023).

6. J. Mbwebwe, A. Kolesnikov, L. Mavhungu, H. Bissett, A hybrid experimental-computational approach for predicting Ti-6Al-4V powder degree of spheroidization, in Proceedings of the RAPDASA-RobMech-PRASA-AMI Conference, CSIR International Convention Centre, Pretoria, South Africa, MATEC Web of Conferences, October 2025 (2025).

7. P. Ritala, P. Aaltonen, M. Ruokonen, A. Nemeh, Developing industrial AI capabilities: An organisational learning perspective. Technovation. **138,** 1–19 (2024). https://doi.org/10.1016/j.technovation.2024.103120

8. H. Mahfoud, O. Moutaoukil, M. Toum Benchekroun, M. Latif, Real-Time Predictive Maintenance-Based Process Parameters: Towards an Industrial Sustainability Improvement. International Conference on Advanced Intelligent Systems for Sustainable Development (AI2SD'2023), Springer, Cham. **931,** 18–34 (2024). https://doi.org/10.1007/978-3-031-54288-6_3

A localised heat treatment process for hardenable steels

Maxwell Daymond Vos[1*], *Thorsten Hermann* Becker[1] and *James Anthony* Dicks[1]

[1]Centre for Materials Engineering, Department of Mechanical Engineering, University of Cape Town, South Africa

Abstract. Hardening of steels through martensitic transformation is useful to control the material's mechanical properties. However, when bulk martensitic transformation is performed, the material generally suffers brittleness. Therefore, this work set about to explore a surface heat treatment process for hardenable steel to produce localised hard martensitic regions surrounded by a matrix of softer non-martensitic regions using a non-uniform quenching plate. The spacing between these hardened regions was fabricated to be as small as feasibly possible, whilst maintaining adequate differential cooling to ensure non-uniform martensitic transformation. The final heat sink design produced samples with repeating hardened regions with a centre-to-centre distance being successfully reduced to 3 mm. Hardness differences between regions of over to 450 HV could be achieved, with absolute ranges from around 400 HV in non-hardened regions to over 900 HV in hardened regions.

1 Introduction

Hardenable steels can be reversibly altered between a ductile and hardened state through the use of appropriate heat treatment processes. More specifically, hardenable steels can form martensite when rapidly cooled, thus microstructurally presenting an opportunity to control mechanical properties [1]. Although hardness is often a desirable property, uniform hardening of the material through martensitic transformation usually suffers brittleness. To overcome this, forming martensite in spatially controlled locations on engineered parts can provide a balance between hardness and ductility locally, in effect producing a component with spatially graded properties. For example, case hardening is a common method used for improving the surface hardness of parts whilst preserving internal ductility and minimising geometric distortion [2]. However, many case hardening processes produce a uniformly hard surface and instead focus on the depth of hardening to control the mechanical properties of the part. On the other hand, further spatially controlling the surface location of hardening presents interesting opportunities to selectively control the mechanical properties. Although laser heat treatment is capable of this selective rapid heating and cooling to introduce martensitic regions, it is typically prohibitively expensive and cannot produce these heating and cooling rates at multiple locations on the surface simultaneously [3].

* Corresponding author: maxwellvosthefirst@gmail.com

This research turned towards the design of a heatsink quench-plate system capable of spatially controlled differential cooling for localised quenching to overcome these issues. Conceptually, a hardened region surrounded by unhardened material is reduced into a discrete 'dot' of hardened region made as small as possible, with many such dots then densely packed together. If these 'dots' are sufficiently small and densely packed, the part is less likely to suffer bulk brittleness, owing to the complementary properties of the adjacent non-hardened regions [4]. This approach allows for the whole part to be gradually heated to above its critical temperature, and the number of hardening locations can easily be controlled by adjusting the design of the heatsink. The primary focus of this research was to obtain a high-level understanding of the requirements to produce the desired spatially controlled localised heat treatment. We show that by altering the heatsink contact area and cooling configuration, samples with repeating hardened regions with minimised centre-to-centre distance and high hardness differences between regions could be achieved, setting this as a useful conceptual platform to achieve localised transformations in hardenable steels.

2 Methods, results and discussion

Initial estimates of cooling rates were established through simulations using SolidWorks, whereby the thermal transfer rates between the specimen and quench-plate interface were determined to establish suitable quenching times to achieve localised martensitic transformation (Figure 1).

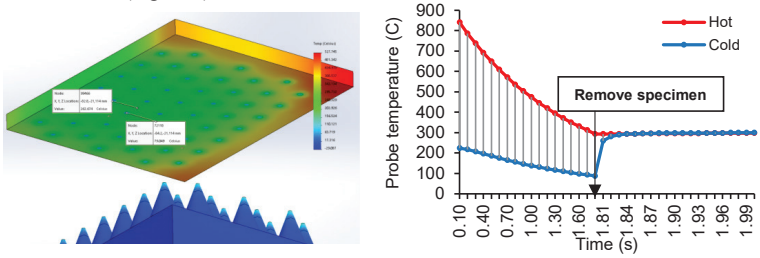


Fig. 1. a) SolidWorks simulation of thermal transfer between specimen and heat sink quench-plate and b) idealised contact and non-contact cooling curve comparison.

For physical experiments, sheet material of 1.6mm thick SAE-1085 high carbon steel was used during testing given its well established hardenability and industrial applicability. An initial heat sink was manufactured using commercially pure copper with varying spacing between contact points to establish the minimum distance achievable without losing distinct hard and soft regions (Figure 2a).

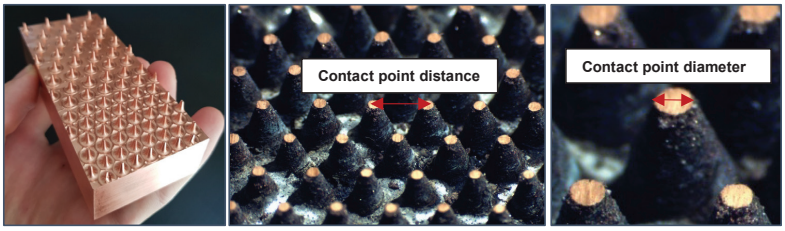


Fig. 2. a) Heat sink quench-plate with variable spacing between contact points, b) uniformly distributed contact point quench-plate.

A series of quench-plates with uniformly distributed contact points of constant contact point distance but different contact point diameters (0.35-0.90 mm) were also manufactured (Figure 2b and c). From these experiments, an optimal configuration of 3 mm between contact points and 0.65 mm diameter contact points were found to successfully produce distinct transformed regions within a matrix of untransformed material.

The hardness of the heat-treated specimens was measured using Vickers microhardness (Reichert HWDM-3, 100gF load) to ascertain the efficacy of localised martensitic transformation. Both line scans and surface maps were measured (Figure 3), which demonstrated that controlled local hardening could be achieved. Maxima in hardening were apparent at the centre of the heat-treated regions, with hardness values up to approximately 900 HV. On the other hand, adjacent regions that were not heat treated displayed appreciably lower hardness values of approximately 420 HV. Generally, there were differentially hardened zones within a 1mm diameter of the heat treatment, interspersed by 2mm distances of soft regions in between.

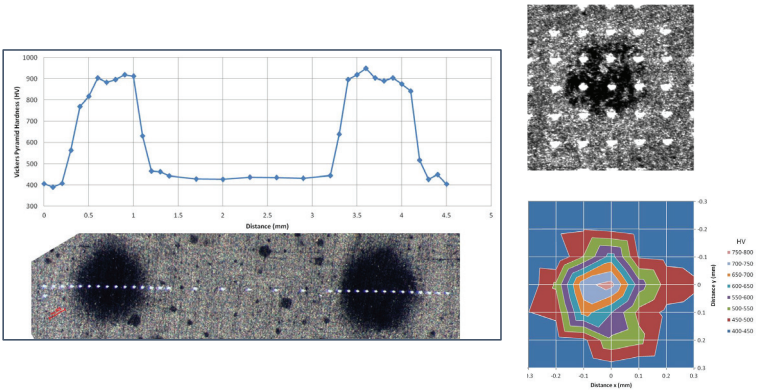


Fig. 3. Vickers hardness maps over hardened and non-hardened regions.

3 Conclusions

Small localised hardened regions within a matrix of unhardened material were successfully produced on the surface of 1.6mm thick SAE-1085 high carbon steel through quenching. The centre-to-centre distance of these hardened regions was reduced to 3mm through iterative design of the heat sink geometry, achieving differences of over 400 HV between the regions.

References

[1] G. Krauss, Steels: processing, structure, and performance (ASM International, Materials Park, 2015)

[2] J.R. Davis, Surface hardening of steels: understanding the basics (ASM International, Materials Park, 2002)

[3] A. Nath, S. Sarkar, Laser transformation hardening of steel, in Advances in laser materials processing (Elsevier, Amsterdam, 2018)

[4] Y. Zeng, W. Cheng, X. Li, Y. Sun, High strength-ductility synergy in an austenitic stainless steel by laser processing. Mater. Today Commun. **41**, 110329 (2024)

Effect of laser power on the microstructure and mechanical performance of CpTi/TiC composites deposited on Ti6Al4V by laser metal deposition

Xolile Michael Mdlalo[1*], and *Madindwa Peter* Mashinini[1]
[1]Department of Mechanical Engineering and Industrial Technology, Doornfontein Campus, University of Johannesburg, Johannesburg, South Africa

Abstract. Laser metal deposition (LMD) is an additive manufacturing technique used to produce titanium-based metal matrix composites with enhanced properties. In this study, CpTi/TiC composites containing 10 to 40 wt.% TiC were deposited on Ti6Al4V substrates using a Yb-fiber laser with powers ranging from 0.8 to 1.6 kW to investigate the effect of laser power on microstructure and mechanical performance. SEM observations revealed refined acicular alpha structures and improved TiC dispersion at higher laser powers. Microhardness increased from 383 HV for the substrate to 460 HV at 1.6 kW. Estimated tensile properties reached approximately 1545 MPa ultimate strength and 933 MPa yield strength.

1 Introduction

Titanium matrix composites reinforced with ceramic particles have attracted significant interest for aerospace and biomedical applications due to their high strength-to-weight ratio, corrosion resistance, and excellent mechanical performance. Laser metal deposition (LMD), a directed energy deposition additive manufacturing process, enables the fabrication and surface modification of advanced materials with controlled microstructures. Reinforcement of commercially pure titanium with titanium carbide (TiC) particles has been shown to improve hardness, wear resistance, and strength. However, the influence of laser processing parameters, particularly laser power, on the microstructure and mechanical behaviour of CpTi/TiC composites remains insufficiently understood. This study, therefore, investigates the effect of laser power on the microstructural evolution and mechanical performance of CpTi/TiC composites deposited on Ti6Al4V substrates via laser metal deposition.

2 Material and experimental procedure

Commercially pure titanium (CpTi) Powders were blended with titanium carbide (TiC) particles to produce composite powder mixtures containing 10–40 wt.% TiC reinforcement. The blended powders were deposited on Ti6Al4V substrates (baseplates) using a YLS-2000-TR Yb-fiber laser system via laser metal deposition (LMD). The laser power varied from 0.8 to 1.6 kW to evaluate its influence on deposition behaviour and resulting material properties. Microstructural characterization of the deposited composites was performed using scanning electron microscopy (SEM) to examine phase morphology, particle dispersion, and interfacial bonding between the deposited layer and the substrate. Mechanical performance was assessed through Vickers microhardness testing across the deposited layers. The

* Corresponding author: mike.mdlalo@gmail.com

corresponding tensile properties were estimated using empirical correlations between hardness and tensile strength.

3 Results and discussion

The microstructural evolution of the deposited CpTi/TiC composites was strongly influenced by the laser power during laser metal deposition. SEM observations revealed the formation of refined acicular α/α′ martensitic structures within the deposited layers, resulting from rapid solidification during laser processing. At lower laser powers, the deposited layers exhibited relatively coarse microstructures, occasional porosity, and a less uniform distribution of TiC reinforcement particles. As the laser power increased, improved melting and enhanced incorporation of TiC particles were observed, leading to more homogeneous particle dispersion and stronger metallurgical bonding between the deposited layer and the Ti6Al4V substrate. The higher energy input also contributed to reduced porosity and improved microstructural refinement. Microhardness measurements showed a significant increase in hardness within the deposited composite layers compared to the substrate. The Ti6Al4V substrate exhibited an average hardness of approximately 383 HV, while the deposited CpTi/TiC composites achieved hardness values up to 460 HV at a laser power of 1.6 kW. This increase in hardness can be attributed to the combined effects of TiC particle reinforcement, microstructural refinement, and rapid cooling associated with the laser metal deposition process.

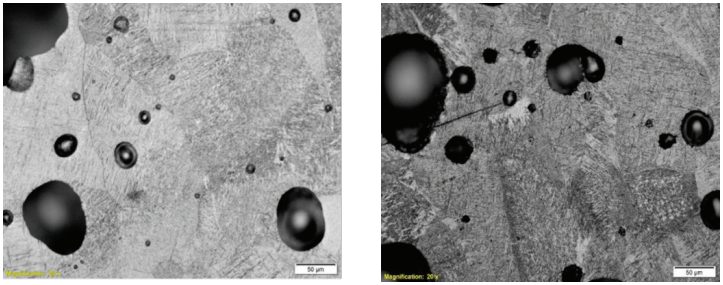


Fig. 1. SEM microstructure of CpTi/TiC composite deposited on Ti6Al4V showing acicular α/α′ martensitic structure and TiC particle dispersion.

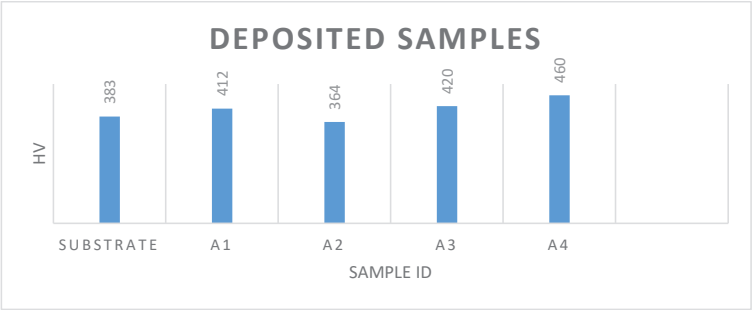


Fig. 2. Variation of microhardness of CpTi/TiC composites as a function of laser power.

4 Conclusion

This study investigated the effect of laser power on the microstructure and mechanical performance of CpTi/TiC composites deposited on Ti6Al4V substrates via laser metal deposition. The results demonstrated that laser power plays a critical role in controlling the microstructural evolution and resulting mechanical properties of the deposited composites. Higher laser power promoted improved melting behaviour, enhanced dispersion of TiC reinforcement particles, and stronger metallurgical bonding between the deposited layer and the substrate. Microstructural analysis revealed the formation of refined acicular α/α′ martensitic structures due to rapid solidification during laser processing. The incorporation of TiC particles and microstructural refinement resulted in a significant increase in hardness in the deposited layers compared with the substrate. The maximum microhardness value of approximately 460 HV was achieved at a laser power of 1.6 kW. Estimated tensile properties further indicated substantial improvements in strength, highlighting the potential of CpTi/TiC composites fabricated by laser metal deposition for high-performance engineering applications.

References

1. W.E. Frazier, “Metal Additive Manufacturing: A Review,” J. Mater. Eng. Perform, 23 (2014) 1917–1928.
2. J. Mazumder, D. Dutta, N. Kikuchi, N. Ghosh, “Closed-loop direct metal deposition: Art to part,” Opt. and Lasers in Eng, 34 (2000) 397–414.
3. A. Bandyopadhyay and S. Bose, Additive Manufacturing, CRC Press, 2015.

The effect of heat treatment on microstructure and hardness of 9% Ni and 25% Mn cast steels

Sibongile Mamonyane[1*], *Lebedike* Mampuru[1], and *Maje* Phasha[1]

[1]Advanced Materials Division, Mintek, 200 Malibongwe Drive, Randburg, South Africa

Abstract. Steels do not have many uses in their as-cast form and are subjected to heat treatment to improve their metallurgical and mechanical properties. This study investigated the effects that heat treatment (water quenching in particular) has on the microstructural and phase evolution as well as hardness of cast 9% nickel steel and 25% manganese steels. In both alloys under investigation, it was noted that the hardness decreased post heat treatment.

1 Introduction

Globally, there is an urgent need to transition to renewable energy with cleaner energy sources to mitigate the consequences of climate change. Liquefied natural gas (LNG) has garnered attention across various industries as a viable alternative energy source owing to its lower emissions and transport efficiency[1], [2] This has increased the global demand for the development of cost-effective structural materials that can maintain mechanical integrity at cryogenic temperatures. Historically, 9% nickel (9% Ni) steel has been used for the storage and transportation of LNG due to its excellent combination of strength and low-temperature toughness. The high and volatile cost of nickel has prompted research into high manganese austenitic steels as a viable replacement for cryogenic applications due to the cost of manganese being approximately a tenth that of nickel [3].

Austenitic steels are produced by casting and do not have many uses in their as-cast form. Often, heat treatment processes are employed to improve the microstructure and subsequently the mechanical properties of metals. Heat treatment of austenitic stainless steels is done to dissolve any carbide precipitates formed during casting, as well as to produce a homogenous austenitic microstructure [4]. This study will investigate the effects that solution heat treatment and water quenching have on the microstructure and hardness of cast 9% nickel steel and 25% manganese (25% Mn) steel.

2 Methods

The 9%Ni and 25% Mn steels were cast into sand moulds and air-cooled. Samples were removed from the moulds. Further sectioning was done to remove segments for heat

* Corresponding author: sibongilem@mintek.co.za

treatment. The heat treatment samples were heated up and soaked at 1000°C for an hour in a muffle furnace, followed by water quenching. All samples were ground and polished to a 1µm finish and etched to reveal the microstructure; the microstructure was observed using optical microscopy. The hardness of the samples was evaluated using a Vicker's hardness tester with a force of 10kgf, five indents were made and the results were averaged.

3 Results

3.1 Hardness

As presented in Fig. 1, hardness values for both alloys were observed to have decreased after heat treatment. The hardness of 9%Ni decreased from 426.6±2.8 HV_{10} to 349.6±4.6 HV_{10}, and the hardness of the 25%Mn steel reduced from 213.8±1.7 HV_{10} to 185.0±4.6 HV_{10}.

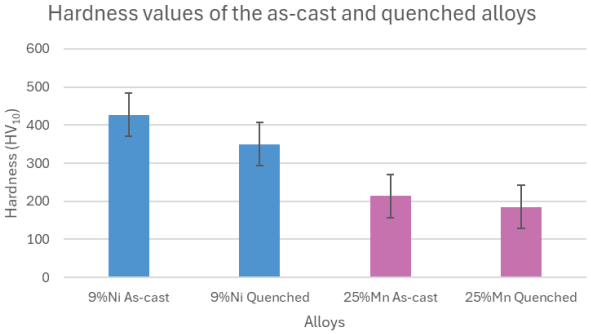


Fig. 1. Bar graph depicting the hardness values observed for both alloys in as-cast and heat-treated conditions.

3.2 Microstructure

Both alloys exhibited a coarser microstructure after they were heat-treated. This result is to be expected as the heat-treated grains were given enough time to enlarge, and the water quenching stopped any size reduction from occurring, locking the large grains in place. The 9%Ni displayed a martensitic microstructure for both samples. The 9%Ni steel microstructure showed prominent dendritic structures in the as-cast sample, whereas they were less prominent in the heat-treated sample. The 25%Mn steel samples displayed an austenitic microstructure.

4 Conclusion

Finer grains are associated with higher hardness values. The reduction in hardness of the alloys may be attributed to the coarsening of grains during heat treatment.

References

[1] S. Sun and M. Ertz, "Life cycle assessment and risk assessment of liquefied natural gas vehicles promotion," Renewable and Sustainable Energy Reviews **153**, 111769 (2022)

[2] N. Mohammad, W. W. Mohamad Ishak, S. I. Mustapa, and B. V. Ayodele, "Natural Gas as a Key Alternative Energy Source in Sustainable Renewable Energy Transition: A Mini Review," Front. Energy Res. **9**, 1–6 (2021)

[3] Y. Li, J. Li, D. Zhang, and Q. Pang, "Optimization of Mechanical Properties of High-Manganese Steel for LNG Storage Tanks: A Comprehensive Review of Alloying Element Effects," Metals **14**(2024).

[4] T.V. Rajan, C.P. Sharma and Ashok Sharma, Heat Treatment Principles and Techniques SECOND EDITION (PHI Learning Private Limited, New Dehli, 2011)

The effect of Nb and V on the metallurgical properties of FeCo alloy

Ramogohlo Diale-Boshielo[1,2*], *Bongani* Ngobe[1], *Joseph* Moema[1], *Hasani* Chauke[2], and *Maje* Phasha[1]

[1]Advanced Materials Division, MINTEK, Private bag X 3015, Randburg, 2125, South Africa
[2]Materials Modelling Centre, University of Limpopo, Private Bag X 1106, Sovenga, 0727, South Africa

Abstract. FeCo alloy is considered attractive soft material for a variety of technological applications, such as transformer cores and high-temperature magnets. This is due to its good ferromagnetic properties and excellent mechanical characteristics. However, binary FeCo is brittle at room temperature. Hence, metallurgical additions of V and Nb are considered to overcome these limitations. In this study, the effect of Nb and V on the microstructures and micro-Vickers hardness of FeCo alloy is investigated. The micro-Vickers hardness results of ternary alloys showed a decrease in hardness. Current results revealed that doping with 1 at. % V demonstrated lowest hardness, implying improved ductility.

1 Introduction

FeCo alloys, particularly with equiatomic $Fe_{50}Co_{50}$ composition, are well-known for having the highest saturation magnetization, good permeability and high Curie temperature, making them essential for high-performance applications like aerospace generators, transformer cores and automotive electric motors [1]. However, FeCo undergoes transformation to ordered B2 body-centered cubic (BCC) structure at low temperatures [2], maximizing its magnetic properties; though, it is extremely brittle under these conditions [3]. Due to this, industrial forming process of this material is difficult. Hence, the additions of ductile BCC transition elements such as vanadium (V) and niobium (Nb) are primarily considered to overcome the inherent brittleness of B2 FeCo while tailoring it for high-stress applications like high-speed aero-generators, despite the generally reduced magnetic moment. The current study examines the effect of V and Nb on the microstructure and mechanical properties of the FeCo alloy.

2 Methodology

A 100g of binary FeCo and ternary FeCo-M (M= Nb, V) alloys with 1 at. % Nb and V were produced by arc melting commercial pure elements (Fe, Co, Nb, and V). For homogeneity, the ingots were flipped and re-melted three times each under a controlled argon atmosphere

* Corresponding author: ram@mintek.co.za

to limit oxidation. In order to determine the metallurgical properties of the materials in the as-cast condition, the samples were mounted, ground, and polished to a 1µm finish. Scanning electron microscopy (SEM) was used to observe the microstructures of ternary FeCo-Nb and FeCo-V alloys samples in their as-cast form. Analyses were conducted across three different areas of study for each sample. The phases in the as-cast samples were detected using an X-ray diffractometer (XRD). XRD analysis was performed using a Bruker 8 Discovery XRD machine at a scanning rate of 0.5 °/s with a step size of 0.02º. Zwick Roell Vickers hardness testers were used to perform micro-Vickers hardness tests to assess material strength.

3 Results and discussion

Figure 1 shows the Micro-Vickers hardness of binary FeCo and ternary FeCo-1M (M= Nb, V) alloys. From the results, FeCo-1V alloy showed the lowest hardness of 211.83 Hv0.5 which may be attributed to coarse grains, resulting in a ductile behaviour.

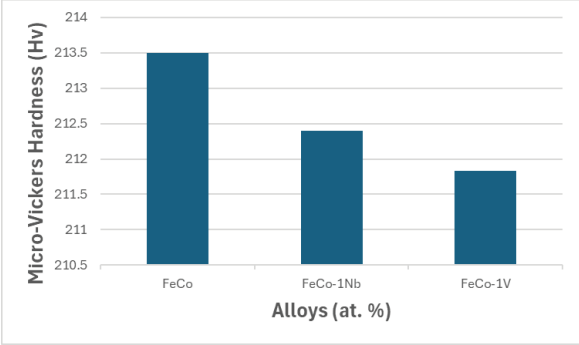


Fig. 1. Micro-Vickers hardness of As-cast FeCo, FeCo-1Nb and FeCo-1V alloys.

4 Conclusion

The effect of Nb and V on the microstructures and hardness of the FeCo alloy was investigated in as-cast condition. A micro-hardness of the FeCo-1V sample showed the lowest hardness as compared to FeCo and FeCo-1Nb samples. The findings suggest that FeCo-1V alloy can be used for the future development of magnetic components with reduced brittleness (improved ductility).

References

1. X. Liu. and A. Morisako, Journal of Applied Physics, **103**, 07E726 (2008).
2. I. Ohnuma, H. Enoki, O. Ikeda, R. Kainuma, H. Ohtani, B. Sundman and K. Ishida, Acta Materialia, **50**, 379-393 (2002).
3. T. Sourmail, Progress in Material Science, **50**, 816-880 (2005).

Finite element analysis of weight-strength trade-offs in Ti6Al4V sternal implant design

Eric Dlamini[1*], *Thywill* Dzogbewu[1,2], *Gerrie* Booysen[2], and *Deon* de Beer[2]

[1]Department of Mechanical and Mechatronics Engineering, Central University of Technology, Bloemfontein, South Africa
[2]Centre for Rapid Prototyping and Manufacturing, Bloemfontein, South Africa

Abstract. Titanium sternal implants fabricated via LPBF had been explored as a means of enabling patient-specific chest wall reconstruction, but conventional designs tend to be over-dimensioned in mass and stiffness. The present work investigates trade-offs between weight and strength in Ti6Al4V sternal implants using finite element analysis by comparing solid and lattice structures under normal breathing and coughing. The influence of structural and unit cell parameters on the relative density, stiffness, energy absorption capabilities, and achievable mass reduction is investigated. The study presents lattice architectures that could reduce implant mass while maintaining adequate strength and energy absorption capacity.

1 Introduction

Sternal reconstruction following trauma, infection, or congenital defects remains a demanding clinical challenge, requiring implants that balance mechanical strength with patient-specific anatomical and physiological demands [1]. Titanium alloy Ti6Al4V is widely adopted in biomedical applications due to its biocompatibility, corrosion resistance, and favourable strength to weight ratio, and 3D printability via additive manufacturing technologies including laser powder bed fusion (LPBF), which enables patient-specific reconstruction [2]. However, Ti6Al4V has a relatively high stiffness and density as compared to bone which can lead to stress shielding and patient discomfort [3]. Additive manufacturing (AM) has enabled the design of lightweight, lattice-structured implants with tuneable mechanical properties, offering opportunities to mitigate these limitations [4]. For instance, adjusting the unit cell type, strut diameter or surface thickness has an influence on the porosity and relative density which is ultimately expected to tune the effective elastic modulus of Ti6Al4V implants towards that of the cortical bone and costal cartilage while reducing implant mass [4, 5]. Despite promising advances, systematic evaluation of weight-strength trade-offs in Ti6Al4V sternal implants remains limited. Finite element analysis (FEA) provides a robust computational framework to simulate implant performance under physiological loading conditions, guiding design optimisation prior to experimental validation [6]. This study aims to investigate the mechanical implications of varying lattice

* Corresponding author: el-dlamini@outlook.com

configurations and densities in Ti6Al4V sternal implants, focusing on the balance between structural integrity, energy absorption capacity, and weight reduction.

2 Discussion

The proposed methodology integrates CAD-based lattice modelling with FEA simulations to assess stress distribution, deformation, and potential failure under representative thoracic loading scenarios. Strut-based body-centered-cubic (BCC), octet, and the auxetic re-entrant honeycomb lattice are parametrically varied in terms of density and geometry to allow quantification of how reductions in implant mass influence mechanical performance. Lattice architectures such as octet, diamond, and re-entrant honeycomb can achieve significant weight reductions while maintaining sufficient strength for orthopaedic applications [7, 8]. Most recent work highlights that lattice porosity and surface morphology strongly influence titanium ion dissolution, which has implications for long-term biocompatibility [9]. Therefore, manufacturing constraints of LPBF that can be evaluated without experimentation, such as the minimum printable strut diameters and surface roughness that is evaluated by the number of support structures needed [10], were considered. It is worth mentioning that further work integrating process-aware constraints and experimental validation would be necessary before translation to clinical use. Even within these constraints, linking mass, stiffness, stress metrics, and energy absorption capacity to unit-cell parameters can provide insight into how sternal implant performance depends on design choices and further lays the groundwork for both informed manual design and for more automated optimisation workflows such as topology optimisation in future studies [11].

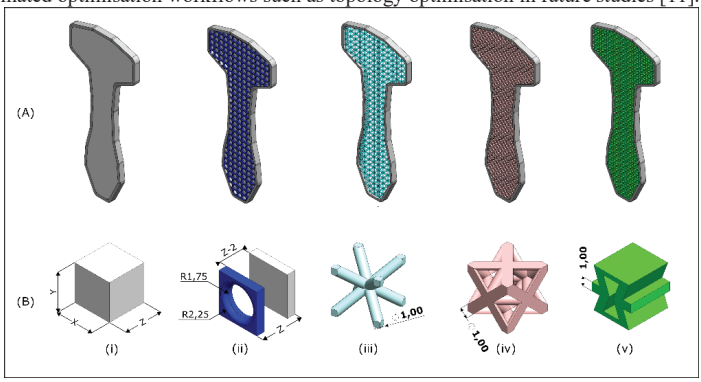


Fig. 1. Assignment of different lattice designs within the sternal implant.

3 Conclusions

This research seeks to establish a framework for evaluating weight-strength trade-offs in Ti6Al4V sternal implant design using finite element analysis. The study is expected to demonstrate that lattice-structured implants can be engineered to reduce mass without compromising biomechanical safety. The contribution lies in advancing computational methodologies for implant optimisation, offering insights that may accelerate the development of patient-specific and additively manufactured sternal implants. Ultimately, this work aims to support clinical adoption of lightweight, durable implants that improve patient outcomes and expand the role of additive manufacturing in reconstructive surgery.

References

1. W. Wenzhang, L. Zhaoru, Y Shiyan, F Qing, N Xuewei, S Guang, Y Wenjie, H Yi, Three-dimensional (3D)-printed titanium sternum replacement: a case report. Thorac. Cancer. **11**, 3375-3378 (2020).
   https://doi.org/10.1111/1759-7714.13655
2. E. Marin, A. Lanzutti, Biomedical applications of titanium alloys: a comprehensive review. Materials. **17**, 114 (2023).
   https://doi.org/10.3390/ma17010114
3. S.A. Naghavi, M. Tamaddon, P. Garcia-Souto, M. Moazen, S. Taylor, J. Hua, C. Liu, A novel hybrid design and modelling of a customised graded Ti-6Al-4V porous hip implant to reduce stress-shielding: an experimental and numerical analysis. Front. Bioeng. Biotechnol. **11**, 1092361 (2023).
   https://doi.org/10.3389/fbioe.2023.1092361
4. M. Rana, S. Karmakar, A. Bandyopadhyay, A. Roychowdhury, Design and manufacturing of patient-specific Ti6Al4V implants with inhomogeneous porosity. J. Mech. Behav. Biomed. Mater. **143**, 105925 (2023).
   https://doi-org.ezproxy.cut.ac.za/10.1016/j.jmbbm.2023.105925
5. A. Bandyopadhyay, F. Espana, V.K. Balla, S. Bose, Y. Ohgami, N.M. Davies, Influence of porosity on mechanical properties and in vivo response of Ti6Al4V implants. Acta Biomater. **6**, 1640-1648 (2010).
   https://doi-org.ezproxy.cut.ac.za/10.1016/j.actbio.2009.11.011
6. R. Alkentar, F. Mate, T. Mankovits, Investigation of the performance of Ti6Al4V lattice structures designed for biomedical implants using the finite element method. Materials. **15**, 6335 (2022).
   https://doi.org/10.3390/ma15186335
7. F. Distefano, S. Pasta, G. Epasto, Titanium lattice structures produced via additive manufacturing for a bone scaffold: a review. J. Funct. Biomater. **14**, 125 (2023).
   https://doi.org/10.3390/jfb14030125
8. A. Zhumabekova, A. Perveen, D. Talamona, Effect of the lattice structures on mechanical characterisation of additively manufactured Ti-6Al-4V for biomedical application. Adv. Mater. Process. Technol. **11**, 1285-1302 (2025).
   https://doi.org/10.1080/2374068X.2024.2379088
9. E. Seo, Y.N. Lee, W.Y. Shin, K. Kim, S.H. Jung, H.G. Kang, R. Kim, H. Sung, I.D. Jung, J.W. Park, Structural influence on titanium ion dissolution in 3D-printed Ti6Al4V orthopedic implants. Sci. Rep. **15**, 37122 (2025).
   https://doi.org/10.1038/s41598-025-21129-9
10. W. Ameen, A. Al-Ahmari, M.K. Mohammed, O. Abdulhameed, Evaluation of the support structure removal techniques for additively manufactured Ti6Al4V parts. Adv. Mater. Sci. Eng. **2022**, 2259974 (2022).
    https://doi.org/10.1155/2022/2259974
11. A. Al-Tamimi, C. Peach, P.R. Fernandes, A. Cseke, P.J.D.S. Bartolo, Topology optimization to reduce the stress shielding effect for orthopedic applications. Procedia CIRP. **65**, 202-206 (2017).
    https://doi.org/10.1016/j.procir.2017.04.032

Phase predictions and microstructural characterisation of Cu-modified low-nickel Hercules™ stainless steel

M Smit[1*], *LA* Cornish[2], and *K* Dyal Ukabhai[1]

[1]Advanced Material Division, Mintek, Randburg 2125, South Africa
[2]University of the Witwatersrand, Johannesburg 2000, South Africa

Abstract. The effect of 3 – 20 mass% Cu on Mintek's low nickel austenitic stainless steel, Hercules™ was assessed. Thermo-Calc™ (TCFe3 database) was used to predict the phase proportions. Copper-modified alloys were produced using the plasma melting capability of the Amazemet rePowder system. Compositions and microstructures (including phases) were studied after heat treatment (annealed at 1050°C for 1 h and water quenched, followed by ageing at 670°C for 4 h, and water quenched). The microstructures comprised of austenite with ferrite. Copper-rich precipitates were observed throughout the microstructures for alloys with ≥5 mass% Cu.

1 Introduction

Copper has attracted attention for touch surface applications in public spaces such as hospitals and clinics due to its antimicrobial properties [1-2]. The high cost, low strength and corrosion resistance of copper makes it impractical to replace stainless steel products for these applications, therefore Cu-containing stainless steels have been studied as novel antimicrobial stainless steels [3-5]. Lui *et al.* (2022) developed an antipathogen 316L stainless steel with 20 wt% copper, which killed COVID-19 within 3 - 6 h compared to unmodified 316L. Commercially available stainless steels (such as 316L) are expensive, mainly due to their high (9 wt%) Ni content. The aim of this study was to assess the effect of Cu additions on the microstructure and phase proportions of an alternative austenitic stainless steel alloy, Hercules™, with ≤2 wt% Ni, which would lead to a significant economical saving [6].

2 Experimental and results

2.1 Phase predictions of Cu additions to Hercules™

Thermo-Calc™ was used to predict the phase proportions of Hercules™ with several Cu variations: 3, 5, 10, 15, 20 wt%. Iron was reduced to allow for the copper additions and other

* Corresponding author: melanies@mintek.co.za

elemental constituents were kept similar to the base composition. Table 1 gives the phase amounts at different temperatures. At the proposed heat treatment (670°C), it was predicted that Hercules™ would comprise FCC_A1 (austenite), Table 1. The $M_{23}C_6$ carbide was low and sigma would require a long time to form [7] and could be disregarded. The Cu-containing experimental alloys had an additional FCC_A1# phase, which was likely a Cu-containing phase.

Table 1. Phase proportions from Thermo-Calc™ of Hercules™ and Cu-modified alloys at 670°C.

Alloy	Phases (g)			
	FCC_A1	FCC_A1#2	M23C6	Sigma
Hercules™	0.87	-	0.002	0.12
Hercules-3Cu	0.85	0.013	0.003	0.13
Hercules-5Cu	0.82	0.03	0.003	0.10
Hercules-10Cu	0.73	0.09	0.003	0.18
Hercules-15Cu	0.64	0.14	0.003	0.21
Hercules-20Cu	0.56	0.20	0.003	0.24

2.2 Characterisation of experimental alloys

2.2.1 Metallography Phase

Alloys were characterised in as-cast and heat treated (annealed at 1050°C for 1 h and water quenched, then aged at 670°C for 4 h, and water quenched) conditions. Cross-sections were taken from each alloy and prepared to a 1 µm surface finish, etched electrolytically with 10% oxalic acid. Figure 1 shows the microstructures of the experimental alloys which comprised austenite with some ferrite. Light contrast Cu-containing precipitates were observed in alloys containing ≥5 wt% Cu, Table 2. The size and distribution of the precipitates increased with increased Cu.

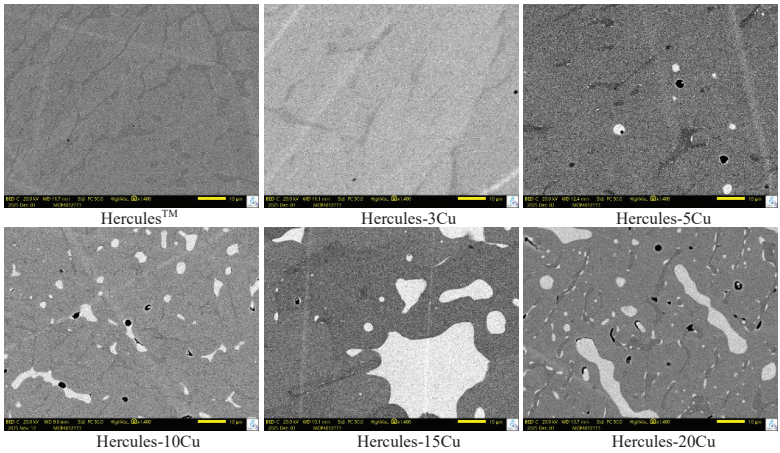


Fig. 1. SEM-BSE images of as-cast and heat treated Hercules™ alloys: a) as-cast and b) heat treated, showing: light austenite dendrites with dark contrast interdendritic phase (micron bars represent 10 µm).

Table 2. EDX analysis of the Cu-containing phase in the experimental alloys, wt%.

Alloy	Cr	Mn	Fe	Ni	Cu
Hercules™	No Cu-containing phase				
Hercules-3Cu	No Cu-containing phase				
Hercules-5Cu	2.5±1.0	20.3±1.1	8.6±3.0	2.9±0.5	65.6±3.5
Hercules-10Cu	1.9±1.3	16.9±1.6	6.7±4.4	1.5±0.2	73.7±5.1
Hercules-15Cu	1.2±0.2	17.2±1.2	4.7±0.9	2.0±0.1	75.4±2.3
Hercules-20Cu	1.6±0.8	15.9±1.1	5.3±2.3	1.7±0.2	76.0±2.0

2.2.2 Phase Analysis

Using X-ray diffraction (XRD), the phases in the alloys comprised mostly of austenite (*Fm*-3*m*) with ~1 - 14 wt% ferrite (*Im*-3*m*). Alloys with ≥5 wt% Cu contained a copper-rich phase $Cu_{0.359}Cr_{0.072}Mn_{0.242}Fe_{0.101}Ni_{0.226}$ (*Fm*-3*m*).

3 Conclusions

The experimental results compared well with the Thermo-Calc™ results, which predicted austenite and minor amounts of ferrite. The phase proportions of the Cu-rich phase were also predicted and increase withy increase in Cu content.

The microstructures were not properly homogenised with residual ferrite and large Cu-precipitates, which may result in poor corrosion and antimicrobial properties. Ideally ≥95 mass% austenite with nano-sized precipitates should be achieved.

The authors would like to acknowledge Mintek, University of the Witwatersrand and the Advanced Materials Initiative for assistance during the project and approval to publish the work.

References

1. G. Grass, C. Rensing, M. Solioz, Metallic copper as an antimicrobial surface. App Environmental Microbiology. 77(5) 1541–1547 (2011).
2. H.T. Michels, C.W. Keevil, C.D. Salgado, M.G. Schmidt, From laboratory research to clinical trial. Copper alloy surfaces kill bacteria and reduce hospital-acquired infections. Health Environments Research & Design Journal. 9(1) 64-79 (2015).
3. L.T. Lui, A.W.H. Chin, P. Yu, L.L.M. Poon, M.X. Huang, Anti-pathogen stainless steel combating COVID-19. Chem Eng J. 433, 133783 (2022).
4. Y. Dong, J. Li, D. Xu, G. Song, D. Liu, H. Wang, M.S. Khan, K. Yang, F. Wang, Investigation of microbial corrosion inhibition of Cu-bearing 316L stainless steel in the presence of acid producing bacterium Acidithiobacillus caldus SM-1. J Mater Sci Technol. 64, 176-186 (2021).
5. T. Xi, M.B. Shahzad, D. Xu, J. Zhao, C. Yang, M. Qi, K. Yang, Copper precipitation behaviour and mechanical properties of Cu-bearing 316L austenite stainless steel: A comprehensive cross-correlation study. Mater Sci Eng A. 675, 243-252 (2016).
6. R. Paton, J.S. Moema, J.C. Kerr, P.V.T. Scheers, K.P. Mokaleng, L Petrick, New Generation low nickel (≤2%) austenitic stainless steel for structural applications. Mintek Comm. C4076M (2005).
7. D.A. Aditya, H. Ardy, Y.S.F. Lantang, Y.S. Afrianti, N.F.F. Ilmi, U.S. Pasaribu, The study of sigma and carbide in cast austenite stainless-steel grade HH after 24 years of high-temperature service. Heliyon. 9(3), e14109 (2023).

A review on additive manufacturing of metal carbides

Tumelo Moloi[1]*, *Thywill Cephas* Dzogbewu[1], *Bathusile* Masina[2], and *Sisa* Pityana[2]

[1]Department of Mechanical and Mechatronics Engineering, Central University of Technology, Free State, Private Bag X20539, Bloemfontein 9300, South Africa
[2]Photonics Centre, Manufacturing Cluster, Council for Scientific and Industrial Research (CSIR), PO Box 395, Pretoria 0001, South Africa

Abstract. Metal carbides, particularly tungsten carbide (WC), titanium carbide (TiC), and niobium carbide (NbC), are widely used in modern tooling and wear-resistant industries due to their thermal stability, resistance to wear, and high hardness. Subtractive manufacturing and powder metallurgy processes are rendered less suitable for complicated geometries due to their high melting points and inherent brittleness. This review paper examines the current state of additive manufacturing (AM), as a transformative method for manufacturing materials that are usually hard to process. The efficacy of AM technologies, such as laser powder bed fusion (LPBF) and directed energy deposition (DED), to print metal carbides is evaluated, and the findings show that the most suitable technology greatly depends on the scope of the desired application.

1 Introduction

More than eighty elements in the periodic table are metals, most of which chemically react with carbon to produce carbide [1]. Metal carbides, often referred to as hard metals or cermets, occupy a unique function in materials science, bridging the gap between the fracture toughness of metals and the extreme hardness of ceramics [2]. Compounds such as WC, TiC, and NbC are the backbone of the global tooling, mining, and aerospace industries because they possess high hardness, great wear resistance, and high-temperature stability. Tungsten carbides combined with a cobalt binder form a cemented carbide, which offers a good balance of hardness and fracture toughness, while TiC and NbC provide a great boost to abrasive wear resistance. [3], [4]. Metal carbides are very brittle; because of this, they are usually combined with a binder metal (Co or Ni), which forms a continuous matrix that surrounds every single carbide grain. When a microcrack starts, it grows within the grains and eventually reaches the softer material, which is the binder. The binder will deform plastically, absorb the energy, and prevent the crack from propagating across the entire carbide part. Tungsten carbide is characterised by high room-temperature hardness, high density, and good fracture toughness when combined with a cobalt binder. It finds its application in lathes and milling machines, and the mining sector [3]. In contrast, Ti is nearly three times lighter and

* Corresponding author: moloitd7@gmail.com

offers better oxidation resistance, making it the preferred choice for high-speed finishing tools. Niobium carbide possesses the highest melting point amongst the three carbides and maintains its hardness at much higher temperatures (800 °C) than WC [3], [5].

Additive Manufacturing is a process of joining materials to make objects from 3D model data, usually layer upon layer [6], [7]. It typically uses metallic powders that are melted successively using a laser or electron beam source of energy [8]. While metals like titanium and steel have matured in the AM space, AM of carbides have shown a potential for manufacturing complex parts; however, carbides present unique challenges, such as (1) High melting points: carbides often exceed the effective operational range of standard laser systems; (2) Thermal shock: the rapid cooling rates (10^6 K/s) inherent in LPBF [9], [10], [11], often trigger catastrophic cracking in brittle carbide structures, which limits their use. This review paper critically synthesises recent advancements in the performance, microstructure, mechanical properties, processing challenges, and applications of WC, TiC, and NbC, using AM technologies, including LPBF and DED, to determine the most suitable technology for fabricating near-net-shape carbide components without the cracking or porosity typically associated with their high melting points and brittleness. While indirect AM methods, such as binder jetting, are capable of producing carbide cermets via post-print furnace sintering, this review is strictly limited to direct, high-energy density beam technologies, specifically LPBF and DED.

2 Conclusions

The study aimed to determine the most suitable technology for fabricating near-net-shape carbide components. From the obtained results, the following conclusions can be drawn.

- Tungsten carbide has the highest toughness and flexural strength and is more suited to be applied in heavy impact and high-pressure environments.
- Titanium carbide is more suited for lightweight aerospace bearings because of its low density.
- Niobium carbide has the highest melting and boiling points, suited for aerospace engine parts and specialised high-temperature cutting inserts.
- The most suitable technology greatly depends on the scope of the desired application.
- LPBF for complicated near-net-shape geometries, DED for large-scale wear components and cladding.

References

[1] W. A. Frad, “Metal Carbides,” *Advances in Inorganic Chemistry and Radiochemistry*, vol. 11, pp. 153–247, 1968.

[2] H. M. Ortner, P. Ettmayer, and H. Kolaska, “The history of the technological progress of hardmetals,” *Int. J. Refract. Metals Hard Mater.*, vol. 44, pp. 148–159, May 2014, doi: 10.1016/j.ijrmhm.2013.07.014.

[3] F. Miranda *et al.*, “Additive Manufacturing of Tungsten Carbide (WC)-Based Cemented Carbides and Niobium Carbide (NbC)-Based Cermets with High Binder Content via Laser Powder Bed Fusion,” *Metals (Basel).*, vol. 14, no. 12, Dec. 2024, doi: 10.3390/met14121333.

[4] D. Svetlizky *et al.*, "Directed energy deposition (DED) additive manufacturing: Physical characteristics, defects, challenges and applications," *Materials Today*, vol. 49, pp. 271–295, Oct. 2021, doi: 10.1016/j.mattod.2021.03.020.

[5] A. Malik, A. Basit, M. F. Ijaz, F. Anwar, M. A. Umer, and Y. Shao, "Microstructure and mechanical properties of TiC reinforced NbC-Ni4VC4Mo $_2$ C cermets," *Mater. Res. Express*, vol. 11, no. 9, p. 096518, Sep. 2024, doi: 10.1088/2053-1591/ad78b4.

[6] ASTM International, " Standard Terminology for Additive Manufacturing—Coordinate Systems and Test Methodologies," Ohio, 2013.

[7] D. L. Bourell, J. J. Beaman Jr., M. C. Leu, and D. W. Rosen, "A Brief History of Additive Manufacturing and the 2009 Roadmap for AM," Austin, Sep. 2009. Accessed: Nov. 13, 2024. [Online]. Available: https://www.turkcadcam.net/haber/2009/rapidtech-workshop/presentations/Presentation02.pdf

[8] T. Wohlers *et al.*, "History of Additive Manufacturing," *SSRN Electronic Journal*, 2023, doi: 10.2139/ssrn.4474824.

[9] A. M. Muiruri, "Investigation of the High Strain Rate Behaviour and Impact Toughness of Ti6Al4V (ELI) Parts Built by the EOS M280 DMLS System with Standard Process Parameters; As-Built and Stress Relieved," Central University of Technology, Free State, Bloemfontein, 2018.

[10] R. Condotta *et al.*, "Flowability of NbC-based cermets for additive manufacturing via L-PBF," *Academia Materials Science*, vol. 2, no. 3, Jul. 2025, doi: 10.20935/acadmatsci7795.

[11] Z. Anwer, C. Liu, B. L. Liu, R. M. Genga, J. Vleugels, and S. Huang, "A comparative study on the oxidation behaviour of NbC-Ni, WC-Co, and high entropy carbide-Ni based cermets," *Int. J. Refract. Metals Hard Mater.*, vol. 124, p. 106832, Nov. 2024, doi: 10.1016/j.ijrmhm.2024.106832.

Materials strength of spheroidal graphite iron plates welds in as-cast and heat-treated conditions

Caroline Mphela [1*], *Lebedike* Mampuru[1], *Duduzile* Nkomo[1], *Joseph* Moema[1] *and Maje* Phasha[1]

[1]Advanced Materials Division, MINTEK, Private bag X 3015, Randburg, 2125, South Africa

Abstract. In this study, spheroidal graphite (SG) iron plates sourced from a local foundry were machined to welding specification and subsequently welded using in-house developed nickel-based non-coated electrodes. Post-welding characteristics such as microstructure and mechanical properties were evaluated. Welding conditions were established to obtain a crack-free weld deposit on the spheroidal cast iron plates in as-cast as well as post-weld heat treatment (PWHT) conditions at constant heat. The effects of matrix structure on tensile and impact properties of both conventional and austempered spheroidal graphite (SG) irons were studied.

1 Introduction

Spheroidal graphite (SG) irons are unique engineering materials possessing good castability and attractive mechanical properties. The feature that all the members of SG-irons share is the roughly spherical shape of the graphite nodules. However, with a high percentage of graphite nodules present in the structure, the control of the SG-iron matrix structure is of potential importance. Several variables, including chemical composition, cooling rate, type, amount, and method of post-inoculation, amount of residual magnesium, and pouring temperature, can control the matrix structure of SG-iron [1]. Heat treating of SG-iron is also another route to produce a family of materials offering a wide range of properties obtained through matrix microstructure control [1].

It is generally accepted that its microstructure determines the mechanical properties of an engineering material. Regarding spheroidal graphite (SG) cast iron, the factors influencing its properties include the chemical composition [2] in addition to the size, distribution, volume fraction, and morphology of the individual microstructural constituents [2]. The mechanical properties of SG-cast iron as determined by the matrix structure have been the objective of many published studies. So far, there is compelling evidence to convince the design engineer to substitute steel with SG-cast iron in many applications. SG iron is difficult

* Corresponding author: carolinem@mintek.co.za

to weld because the heat breaks down the nodules and forms brittle microstructures (martensite) at the weld site, according to insights. Spheroidal cast iron metallography is altered by austempering heat treatment. Austempering spheroidal graphite iron aims to achieve certain microstructures that exhibit austenitic and bainitic matrix due to its exceptional combination of tensile strength and ductility. However, the welding of ADI parts remains a great problem during manufacturing. ADI provides the designer with a family of materials with attractive properties, usually at lower cost and weight than the competing materials. Therefore, the material has been recommended for high-duty applications. ADI with an austenitic-bainitic matrix, is a new type of engineering material and has gained increasing interest in research and industrial applications. One of the most common problems encountered by designers is the welding of ADI parts during manufacturing and the need to develop new welding consumables. Two problems are encountered during the welding of ADI; first, the formation of massive cementite in the as-welded ductile iron because of the fast-cooling rate; second, the properties of the ADI weld should match those of the ADI.
Thus, this study investigates and compares the strength of spheroidal cast iron and ADI welded with various nickel-based non-coated electrodes. The strength will be determined from the mechanical properties of the welds.[3].

2 Methodology

A The base material used for this investigation is a cast ductile iron with SG42/52 chemical composition, collected from a local foundry, then machined to 100mm x 10mm x 10 mm in size. A muffle furnace was used to heat-treat one of the samples after welding.

Phase analysis of the welded samples was conducted using the X-ray diffraction (XRD) technique, whereas the microstructural evolution was traced using an optical microscope (OM). A tensile machine was used to determine the strength of the welded material.

3 Results and discussion

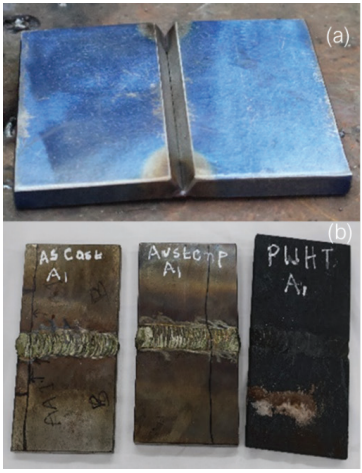


Fig. 1. Microstructure of furnace cooled Ti–42Nb alloy.

4 Conclusion

Hardness, microstructure, and tensile properties of both welded spheroidal cast iron plates in as received and austempered conditions are reported. The welds have shown no defects so far, and a comparison of the weld performance is compared.

References

1. M.F Hafiz, Mechanical properties of SG cast iron with different matrix, **36**, 1293-1300 (2001).
2. M. F. Hafiz, American Foundry Society, 1-8 (2009).
3. E. El Kashif, M.A Morsy, Welding of austempered cast iron, 10-12 (2009).

Hardness and microstructural evaluation of chromium alloyed 22 wt. % Mn alloy compared to commercial 9 wt. % Ni alloy in as-cast and solution-treated conditions

Lebedike Mampuru [1,2*], *Desmond* Klenam[2], *Michael* Bodunrin[2], *Joseph* Moema[1] and *Maje* Phasha[1]

[1] Advanced Materials Division, MINTEK, 200 Malibongwe Drive, RANDBURG, 2194, South Africa

[2] University of the Witwatersrand, Faculty of Engineering and the Built Environment, School of Chemical and Metallurgical Engineering,

Abstract. Research on storage tank materials has increased due to the expanding demand for storage of liquefied natural gas (LNG). Due to their low density, exceptional toughness, and strength, high manganese austenitic Fe-Mn alloys are favoured candidates for investigation in cryogenic applications. However, their yield strength is relatively low due to the face-centred cubic crystal structure. Alloying was identified as a way to improve the yield strength without compromising toughness at cryogenic temperatures. In this study, varying amounts of chromium (2.5, 3.5, & 4.5wt%) were added to 22wt% Mn alloys that were cast, and the effect thereof was studied.

1 Introduction

Due to the growing need for liquefied natural gas (LNG) storage, research on materials for the construction of storage tanks has intensified. Lightweight steels such as high manganese-bearing austenitic Iron-Manganese (Fe-Mn) alloys are being investigated globally for applications in industries such as automotive, marine, and energy sectors. These alloys are favoured candidates to take into consideration for such applications due to their ideal qualities, which include lower density, high toughness, and strength. They are cheaper when compared to the currently used 9wt% Nickel alloys and Invar alloys [1]. These alloys need to meet the minimum required mechanical properties of materials used in these applications, such as high yield strength and toughness at cryogenic temperatures. They should not be susceptible to hydrogen embrittlement [2], dislocation pileup and segregation of impurity elements on grain boundaries [3], or martensitic transformation during low-temperature deformation [4], as this may lead to loss of toughness in subzero applications.

High manganese Fe-Mn alloys are austenitic at room temperature, and they exhibit high ductility at subzero temperatures. However, because of their face-centred cubic (FCC) crystal structure, their yield strength is rather low. Alloying, grain refining, and regulating temperature,

* Corresponding author: lebidikem@mintek.co.za

strain, and strain rate during the forming process are common methods to improve the mechanical properties of high-iron manganese alloys [1]. Wang et al. have indicated that alloying with chromium can increase the yield strength of high iron manganese steel without compromising its exceptional low-temperature toughness [5]. Therefore, for this work, chromium, as an alloying element, is added to the Fe-Mn alloy to improve the yield strength and corrosion resistance.

In this paper, 22wt.% Mn alloys with Cr varying from 2.5wt.% (Alloy 1), 3.5.wt% (Alloy 2) and 4.5wt.% (Alloy 3) are explored and are compared to the 9 wt.% Ni alloy as a reference material. The focus is mainly on evaluating the effect of Cr on the mechanical and microstructural properties of 22wt% Mn alloys (as-cast and solution-treated at 1100°C) with a change in Cr content.

2 Methodology

A 50-kilogram medium-frequency induction furnace was used for melting and casting ingots. An alumina cast crucible backfilled with MR21 refractory material was installed in the induction furnace. Before the casting, the crucible was set up and baked for a few hours to eliminate any moisture that would interfere with the casting process. The 22wt.% Mn alloys with varying chromium content and the 9wt.% Ni alloy was cast in the form of 20kg ingots in the open air. The ingots were cast into an open silica gel-bonded sand mould. Their dimensions were (length by thickness) 260mm x 45mm.

Samples were sectioned from the ingots of Alloy 1, 2 and 3 for as-cast characterisation and solution treatment. The solution-treatment was carried out at 1100°C for an hour, then quenched in water. After being ground to 1200 grit, all specimens in the as-cast and austenitized states were polished to 6, 3, and 1 micron finishes. A Struers Abrapol20 polisher operating at 300 RPM and 150 N of force was used for all the grinding and polishing. Microstructural and phase studies were performed using optical microscopy (OM) and X-ray diffraction (XRD). 5% Nital was used as an etchant to expose the specimens' general microstructures. For analysis, an Olympus DSX 510 light microscope was utilised.

Vickers hardness was measured on the specimen using an EMCO hardness machine with a load of 10 kgf. An average of 5 indents was done per specimen, and the averages are reported.

3 Results and discussion

A change in the hardness of the 22wt.% Mn alloys were observed with the change in Cr content. Alloy 1 showed a hardness of 235 Hv10 and Alloy 2 was 10% lower than Alloy 1. Alloy 3 was 13% higher than Alloy 2 and 3.5% higher than Alloy 1. A change in hardness was also observed when comparing the as-cast and solution-treated samples. In literature, the drop in hardness in the solution-treated Mn alloys is attributed to the gradual dissolution of the secondary phases during austenitising [6].

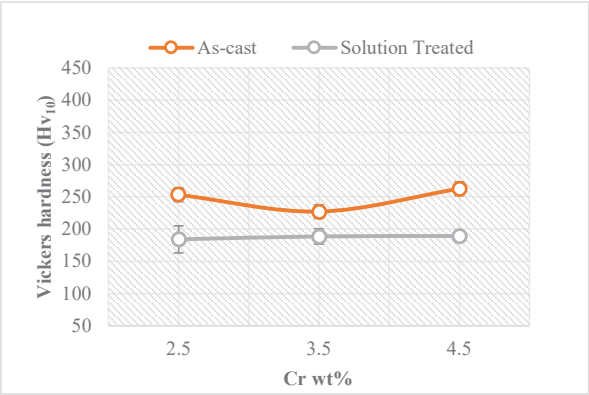


Fig. 1. The hardness graph of as-cast versus solution-treated specimens at different chromium amounts.

4 Conclusion

This work provides a platform to assess and compare the mechanical and microstructural properties of the as-cast and solution-treated 22wt.%Mn alloy containing varying Cr compositions, and compared with the 9wt.% Ni alloy. The preliminary properties assessment of the hardness showed a 10% increase in hardness between Alloy 2 and Alloy 3, and 3.5% between Alloy 1 and Alloy 3. Alloy 2 was slightly lower than Alloy 1 and Alloy 3. Solution-treated alloys showed a lower hardness than as-cast alloys.

References

1. L. Xia, L. Yan, H. Zhang, Y. Li, Z. Jiang, G. Li, Factors Affecting the Mechanical Performance of High Manganese Austenitic Steel. Met., **12**, 1405 (2022). https://doi.org/10.3390/met12091405
2. Y. Bai, Y. Momotani, M.C. Chen, A Shibata, N. Tsuji, Effect of grain refinement on hydrogen embrittlement behaviours of high-Mn TWIP steel. Mater. Sci. and Eng: A, **651**, 935–944 (2016). https://doi.org/10.1016/j.msea.2015.11.017
3. S. Curtze, V.T. Kuokkala, Dependence of tensile deformation behaviour of TWIP steels on stacking fault energy, temperature and strain rate, Acta. Mater., **58**, 5129–5141 (2010). https://doi.org/10.1016/j.actamat.2010.05.049
4. M. Koyama, T. Sawaguchi, T. Lee, C. S. Lee, K. Tsuzaki, Work hardening associated with e-martensitic transformation, deformation twinning and dynamic strain ageing in Fe-17Mn-0.6C and Fe-17Mn-0.8C TWIP steels. Mater. Sci. and Eng: A, **528**, 7310–7316 (2011). https://doi.org/10.1016/j.msea.2011.06.011
5. X. J. Wang, X. J. Sun, C. Song, H. Chen, W. Han, F. Pan, Enhancement of yield strength by chromium/nitrogen alloying in high-manganese cryogenic steel. Mater. Sci. Eng.: A, **698**, 110–116 (2017). https://doi.org/10.1016/j.msea.2017.05.023
6. X. Qiao, B. Li, X. Han, X. Zhang, X. Yang, Effect of solution treatment on mechanical properties and wear resistance of alloyed high-manganese steel, Met., **15**, 937 (2025). https://doi.org/10.3390/ met15090937

Analysis of high Mo content and its effect on compression strength of binary β-Ti-Mo alloys for vascular stent applications

Nthabiseng Abigail Moshokoa[1*], *Lerato* Raganya[2], *Nkutwane Washington* Makoana[3], *Mamookho Elizabeth* Makhatha[1] and *Maje* Phasha[4]

[1]Department of Metallurgy, School of Mining and Metallurgy and Chemical Engineering, University of Johannesburg, Doornfontein Campus, Johannesburg, South Africa.
[2]Advance Materials Engineering, Manufacturing Cluster, Council for Scientific and Industrial Research, Meiring Naude Road, Brummeria, Pretoria o184, South Africa.
[3]National Laser Center, Council for Scientific and Industrial Research, Meiring Naude Road, Brummeria Pretoria 0184, South Africa.
[4]Physical Metallurgy Group, Advanced Materials Division, Mintek, 200 Malibongwe Drive, Randburg 2125, South Africa.

Abstract. The design and development of metastable β-Ti alloys that possess high strength and high strain are gaining much research attention, especially in vascular stent applications. The aim on this study is to evaluate the influence of high content of Mo on the phase and compression properties of two binary alloys: Ti-10Mo and Ti-23Mo wt.% alloys designed using electronic parameters such as the B_0-M_d, the electron per atom (*e/a*) ratio and the Mo_{eq} methods. Phase evolution was experimentally evaluated after compression test using X-ray diffraction. The XRD pattern showed a combination of ω+α″+ β peaks in Ti-10Mo and α″+ β +R phase in Ti-23Mo. Compression strength and strain increased significantly from 1343 MPa to 2226 MPa and 29% to 37% respectively with an increase in Mo content and the hardness decreased from 407Hv to 362Hv.

1 Introduction

As the population of the elderly increases due to increase in life expectancy, vascular diseases have become a major global health concern, ranking as leading cause of death [1]. Types of vascular diseases such as cardiovascular and cerebrovascular diseases are the most leading cause of death amongst the vascular diseases worldwide [2]. Cardiovascular diseases such as coronary heart disease and coronary artery disease are not only lethal, but they also inflict a major health economic burden on most developed countries [3]. Different treatment and clinical trials have been implemented but they were found to be associated with catastrophic complications such as abruption of vessel closure and restenosis [4]. The above

* Corresponding authors : *Nthabisengmoshokoa@gmail.com,

challenges led to the emergence of vascular stents or coronary stents, which are defined as expandable mesh like tubular structures that are implanted in arteries with the purpose to expand and open the lumen without performing any open-heart surgeries [5]. A metallic material for an ideal stent is required to possess properties such as high strength, ductility, adequate radial loop strength and high elastic modulus to minimize elastic recoil in balloon expandable stents [6]. Current metallic materials used for the manufacturing of vascular stents include stainless steel, cobalt chromium alloys, Ni-Ti alloys, etc. Extensive work has been done and continues to be published on alloys designed for vascular stents with high strength and strain as opposed to the above-mentioned metallic materials. For example, the work by O'Brien *et al* on Ti-Ta and Ti-Ta-Ir alloys for balloon expandable (BE) stents [7]. Another work by Plaine *et al* on β Ti-29Nb-13Ta-4.6Zr alloy [8] and an investigation by Catanio Bortolan *et al* on Ti-Mo-Fe alloys [9]. The above-mentioned research studied demonstrate the wide investigations that have been conducted. However, there is still limited studies that explore the effect of increasing Mo content in binary alloys and their compression strength evaluated. Therefore, the current research work focuses on analysing the effect of high Mo content on the phases and compression strength of two binary alloys namely: Ti-10Mo and Ti-23Mo wt.%. electronic parameters such as Molybdenum equivalence (Moeq), the electron to atom ratio (e/a) and Bo-Md methods will be used as predictive tools to give guidance of the formation of phases and predicting the deformation mechanism.

2 Methodology

Two binary alloys: Ti-10Mo and Ti-23Mo alloys were produced using the arc melting system which is operated under inert environment. The cast ingots were solution treated in a tube furnace at 1100°C, held at that temperature for an 1hr and quenched in ice-water. The water quenched sample was subjected to compression test at room temperature where 3 specimens were tested, and compression properties were analysed. X-ray diffraction (XRD) was used to evaluate the phase evolution after compression test, the optical microscope (OM) was used to analyse the deformation mechanism.

3 Results and discussion

The XRD pattens before and after compression test for Ti-10Mo indicated peaks belonging to α″+ β+ ω phase and peaks belonging to α″+ β +R phase in Ti-23Mo. The OM micrographs showed β equiaxed grains and within the grains were parallel thin lines and needle-like structures of martensite. As the Mo content increased, compression strength increased from 1343 MPa to 2226 MPa, the strain from 29% to 37% and the hardness decreased notably from Hv MPa to 362 Hv.

4 Conclusion

According to the results, it can be summarised that increasing Mo content led to high compression strength and strain, however hardness decreased. The compression strength was higher compared to other stent metallic materials. While there are few studies on the compression properties of binary alloys, much improved mechanical properties were achieved in this study. The mechanical response of these alloys indicates strong potential for vascular stent applications.

References

[1] S.H. Im, D.H. Im, S.J. Park, Y. Jung, D.H. Kim, and S.H. Kim. *Progre in Mater Sci*, **126**, 100922 (2022).
[2] A.D Lopez, C.D. Mathers, M. Ezzati, D.T. Jamison, C.J.L Murray. *Lancet*, **367**, 1747-1757 (2006)
[3] M.Y. Ho, C.C. Chen, C.Y. Wang, S.H. Chang, M.J. Hsieh, C.H. Lee, V.C.C. Wu, and I.C. Hsieh. *Meta.*, **6**, 168(2016)
[4] M.A. Lincoff, J.J. Popma, S.G. Ellis, J.A. Hacker, and E.J. Topol, *J. of the American College of Cardio.*, **19**, 926-935 (1992).
[5] A. Jesús, and G. Sánchez. Thesis, University of Girona, Spain. (2019).
[6] N Korei, A. Solouk, M.H. Nazarpak, and A. Nouri. *Mater Today Comm*, **31**, 103467 (2022)
[7] B. O'Brien, J. Stinson, and W. Carroll. *Acta Biomater*, **4**, 1553–1559 (2008)
[8] A.H. Plaine, M.R.D. Silva, and C. Bolfarini. *J. of Mater Research and Tech*, **8**, 3852–3858 (2019).
[9] C. Catanio Bortolan, L.C. Campanelli, P. Mengucci, G. Barucca, N. Giguère, N. Brodusch, C. Paternoster, C. Bolfarini, R. Gauvin, and D. Mantovani. *J. of Alloys and Comp*, **925**, 166757 (2022)

Metallurgical analysis of Ti–42 %Nb biomedical alloy subjected to different cooling conditions

Linah Twala[1*], *Lucky* Sikhvivhilu[1], *Duduzile* Nkomo[1], *Joseph* Moema[1] *and Maje* Phasha[1]

[1]Advanced Materials Division, MINTEK, Private bag X 3015, Randburg, 2125, South Africa

Abstract. This study examines the effect of cooling rate on the microstructure, phase evolution and mechanical properties of Ti–42Nb alloy produced using arc-melting process under controlled environment. Subsequent heat treatment as carried in a vertical tube furnace evacuated and flushed with argon gas. Microstructural and phase analyses were conducted using optical microscopy (OM) and X-ray diffractometer (XRD) characterization techniques, respectively. A powerful combination of high-resolution imaging and elemental analysis through use of scanning electron microscopy (SEM) fitted with energy dispersive X-ray spectroscopy (EDS) was deployed to investigate any possible segregation occurrence. Furnace cooled sample exhibited a coarse and stable β phase microstructure with dendritic features near the edges.

1 Introduction

β type titanium (Ti) alloys are widely used for biomedical applications due their attractive properties such as attractive mechanical properties [1,2]. In comparison to most popular Ti–6Al–4V alloy with elastic modulus of 110 GPa, the Ti–42Nb alloy with low elastic modulus of about 50–60 GPa which is much closer to that of human bone has received much attention of late [3,4], more especially in additive manufacturing. In addition to low elastic modulus, Ti-42Nb alloy offers excellent biocompatibility and corrosion resistance rendering it a strong candidate for orthopedic and dental implant applications [1-4]. Recent advances in additive manufacturing (AM), especially laser powder bed fusion (LPBF), further enhance the potential of β Ti alloys by enabling microstructural refinement, texture control, improved phase stability and enhanced mechanical properties. These capabilities support lower elastic moduli than Ti–6Al–4V and contribute to improved biological performance through controlled elemental distribution and grain orientation applications [3,4]. Moreover, the field of metal AM of implants is constantly gaining popularity due to the unprecedented shape freedom it provides and the ability of combining solid and porous sections of implant within the same process

In this study, Ti–42Nb alloy produced using arc-melting process under controlled environment and subsequently heat treated to modify its microstructure. Thus, the effect of

* Corresponding author: linaht@mintek.co.za

cooling rate on the microstructure, phase evolution and mechanical properties of Ti-42Nb alloy were investigated.

2 Methodology

A 100g ingot of a biomedical Ti–42Nb alloy was produced from high purity titanium shavings and niobium granules. The starting material was arc-melting on a water-cooled copper hearth in argon filled atmosphere. The manufactured ingot was sectioned into 3 equal pieces and subjected to solution-treatment at 850 °C for 1 hour, followed by different cooling mediums. Microstructural and phase analyses of the heat-treated samples were conducted using optical microscopy (OM) and X-ray diffractometer (XRD) characterization techniques, respectively. A powerful combination of high-resolution imaging and elemental analysis through use of scanning electron microscopy (SEM) fitted with energy dispersive X-ray spectroscopy (EDS) was deployed to investigate any possible segregation occurrence.

3 Results and discussion

As shown in Fig. 1, the furnace cooled Ti–42Nb sample shows a coarse and stable structure at the center and edges of the sample. At the center, the grains are large and nearly round whereas at the edges of the sample the structure is still coarse but shows intense dendritic features. On the other hand, rapid cooling produced fine, dense needle-like structures, especially at the edges of the sample The middle region shows a less densely developed needle like structure, indicating slightly slower cooling and partial retention of the β phase. However, the end region exhibits a highly refined, densely interwoven needle like martensitic structure, reflecting the faster cooling rate at the sample surface. These differences demonstrate how local cooling variations influence the degree of martensitic transformation and microstructural refinement within the same specimen.

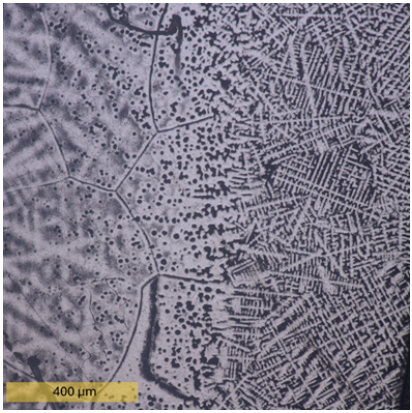


Fig. 1. Microstructure of furnace cooled Ti–42Nb alloy.

4 Conclusion

Overall, the cooling rate strongly affected the microstructure and phases present in the Ti–42Nb alloy. Rapid cooling produces fine, dense needle-like structures, especially at the edges of the sample whereas slow cooling resulted in a coarse, stable β phase with dendritic like features near the edges. Current results demonstrate that cooling rate significantly influences the microstructural features, phase transformation and resulting mechanical properties.

References

1. M. Niinomi, J. Artif. Organs. **11**, 105–110 (2008).
2. M. Geetha, A.K. Singh, R. Asokamani and A.K. Gogia, Prog. Mater. Sci. **54**, 397–425 (2009).
3. D. Pede et al, L.Y. Chen, Y.W. Cui and L.C. Zhang, Journal of Materials Research & Technology **19**, 4598-4612 (2022).
4. S.L. Sing, Int. J. Bioprint. **8**, 1–8 (2022).

Casting and characterisation of Ni-based filler materials used for welding of spheroidal graphite cast iron (SG42)

Dieketseng Maya[1*], *Takalani* Madzivhandila[1], *Lebedike* Mampuru[2], *Joseph* Moema[2], *Caroline* Mphela[2] *and Maje* Phasha[2]

[1]University of Johannesburg, Engineering Metallurgy, Johannesburg, South Africa
[2]Mintek, Advanced Materials Division, 200 Malibongwe Drive, South Africa

Abstract. This study establishes the weldability of spheroidal graphite cast iron (SG42) using Ni-Fe and Ni-Fe-Mn filler metals, aiming to identify which offers the best combination of toughness and strength for SG substrate. Filler metals were produced via controlled melting, casting, and thermomechanical processing into 2 mm sheets, then sliced into uncoated electrodes. Mechanical performance was assessed through Vickers hardness measurements in as-cast and hot-rolled conditions, compared against the SG42 plate. The binary and ternary fillers exhibited hardness values of 102HV and 95.0HV, respectively, while the SG42 plate measured 267HV indicating favourable hardness compatibility of the nickel-based fillers for welding applications.

1 Introduction

Welding cast iron is challenging but feasible, typically for repairing castings rather than joining them to other components. Repairs may occur in the foundry or after machining to address casting defects [1]. For spheroidal graphite (SG42) cast iron, nickel-iron (Ni-Fe) electrodes are preferred to achieve a strong, ductile, crack-resistant bond, offering higher strength and a lower coefficient of expansion than pure nickel rods; they also impart ferromagnetic properties to the weld deposit where magnetism must be preserved [2]. Weldability encompasses not only the ability to join metals but also material compatibility with the application and performance under service conditions. For cast irons, proper thermal management, particularly preheating and controlled cooling helps avoid rapid cooling induced hardness and mitigates common welding issues.

Electrode selection has a direct impact on the final microstructure. According to Sahoo et al [3], nickel-based and Ni-Fe electrodes are frequently used in welding DCI because of their strong graphitizing effect, which inhibits the production of Fe_3C and enhances ductility and toughness. Gupta et.al. [4] showed that several factors influence the weldability of cast irons, namely, (i) type of cast iron, (ii) chemical composition of cast iron, (iii) chemical composition of filler material, (iv) structure of the matrix, and (v) the welding process. Hence, the choice of suitable filler material remains critical for a particular type of cast iron. The aim of this

*Corresponding author: ed.maya.dm@gmail.com

study is to provide information on how welding conditions and filler material affect joint quality by analyzing microstructure, hardness, and tensile strength.

2 Methodology

2.1 Production of filler metals

The materials used for this investigation were a commercial spheroidal graphite cast iron (SG42 - ASTM A536) base plate, which was supplied by a local foundry, a binary (75wt.%Ni–25wt.%Fe) and ternary (44wt.%Ni–45wt.%Fe–11wt.%Mn) filler metals. The chemical composition of the materials in wt.% is given in Table 1.

Table 1. Chemical compositions of the SG42, and two filler metals (wt.%).

Material	Elements wt.%									
	C	Mn	Si	P	S	Cr	Cu	Ti	Ni	Fe
SG 42	4.23	0.56	3.15	0.015	0.008	0.1	0.38	0.04	-	Bal
Binary	-	-	-	-	-	-	-	-	75	25
Ternary	-	11	-	-	-	-	-	-	44	45

These alloys were melted from high-purity raw materials in accordance with targeted specifications. Melting was performed in an induction electric furnace under an argon purge to prevent oxidation and finally poured into the ingot mould. The subsequent hot forming processing of the ingots to wire-rod took place in two stages via ingot hot-rolling and then plate (12mm thick) hot-rolling. The controlled processing route ensured adequate chemical homogeneity and produced 4mm thick sheets suitable for machining into welding uncoated electrodes.

2.2 Mechanical testing

The mechanical characteristics of the joints were determined after cutting the welded samples into pieces of 90×20×5 mm. and their value correspond to the mean value of five measures. The Vickers hardness was determined using a Wilson Universal Hardness Tester machine with a load of 10kg, according to ASTM E92. The rest of strength parameters were determined in a tensile test machine from Instron, model 1342, at a constant crosshead speed of 1 mm/min.

3 Results and discussion

Fig. 1 shows the hardness values of the base metal, binary and ternary filler metals in different conditions. The hardness values of the nickel-based filler metals (high quality rod) are significantly lower than that of the base metal.

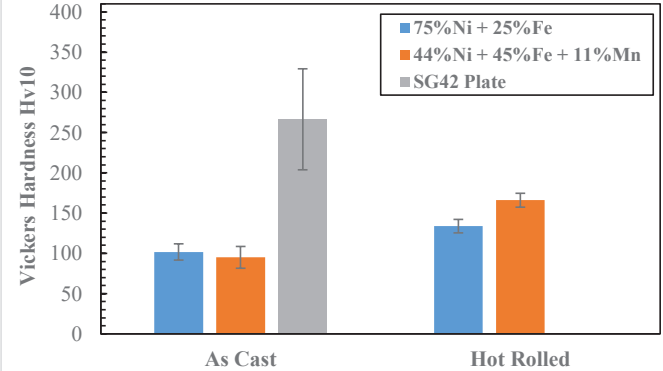


Fig. 1. Hardness tests results for the SG42 and produced filler metals.

4 Conclusion

The Ni-Fe filler metals are significantly softer than the SG42 base material (averaging ~267 HV). This lower hardness is advantageous for weldability. The softer filler accommodates thermal stresses and reduces the risk of brittle martensitic structures in the heat-affected zone. As a result, the Ni-based fillers offer favourable hardness compatibility with SG42, promoting sound welds with reduced cracking susceptibility.

References

1. A.U. Patwari, S.A. Bhuiyan, K. Noman, W.U. Navid., Defects and remedies in casting processes: a combinatorial approach between manual and digital optimization technique for enhanced quality casting. Disc. Mech. Eng. **3,** 39 (2024)
2. M. Pascual, C. Ferrer, E. Rayón, Weldability of spheroidal graphite ductile cast iron using Ni / Ni-Fe electrodes. J. of Metall. **45**(5), pp334 - 338, (2009)
3. P. Sahoo, T.K. Pal, Microstructure and mechanical properties of ductile iron welds using different electrodes, Weld. J. **84**(3), pp.101-109 (2005)
4. R.K. Bhatnagar, G. Gupta, A review on weldability of cast iron. Int. J. Sci. Eng. Res. **7**(5), pp.126–130 (2016)

Flexural performance of sustainable fibre-reinforced composites using basalt and flax

Mpho Ntloane[1,2*], *Sherlyn* Gabriel[1,2], *Steeve* Chung Kim Yuen[2], and *James Anthony* Dicks[1]

[1]Centre for Materials Engineering, Department of Mechanical Engineering, University of Cape Town, South Africa
[2]Blast Impact Survival Research Unit, Department of Mechanical Engineering, University of Cape Town, South Africa

Abstract. The growing demand for lightweight materials with excellent mechanical properties has increased interest in fibre reinforced polymer matrix composites for high-performance applications. However, most fibre and matrix materials currently used are non-renewable and energy intensive to produce. Sustainability in both the fibre and matrix components of the composite materials is important for reducing the overall environmental impact of composites. This paper presents the flexural performance of basalt, basalt/flax, glass, and Kevlar fibre reinforcements within a commercially available partially biobased epoxy matrix. Flexural properties of the composites were investigated in the 0/90° and ±45° orientations. Basalt fibre reinforcement exhibited the highest flexural properties across all materials, achieving a maximum in flexural modulus of 42.4±1.4 GPa and flexural strength of 353.9±13.9 MPa in the 0/90° orientation. These results demonstrate that basalt fibre offers a mechanically competitive, industrially relevant, and sustainable reinforcement within commercially available biobased epoxy matrix composites.

1 Introduction

Fibre reinforced polymer matrix (FRPM) composites can achieve excellent specific mechanical properties and have therefore been extensively incorporated into high-performance applications such as the automotive, marine, and aerospace fields [1, 2]. However, most common FRPM composites use petroleum-derived materials in both the reinforcing fibre (e.g., polyaramids, carbon) and polymer matrix (e.g., epoxy) that are energy intensive to produce and have a high CO_2 footprint (Table 1), making them unsustainable. Furthermore, most FRPM composites cannot be readily recycled, making their end-of-life fate undesirable. These factors motivate the need to develop more sustainable materials for use in FRPM composites. In terms of the fibre reinforcement, natural fibres from plant-based feedstocks (e.g., hemp, jute, flax) have been widely investigated as renewable materials [3-5]. Plant-based fibres typically consist of cellulose, hemicellulose, lignin and waxes [6]. Although these natural fibres are renewable and typically have orders of magnitude lower embodied energy and CO_2 footprint compared to traditional fibres (Table 1), they generally

* Corresponding author: ntlmph008@myuct.ac.za

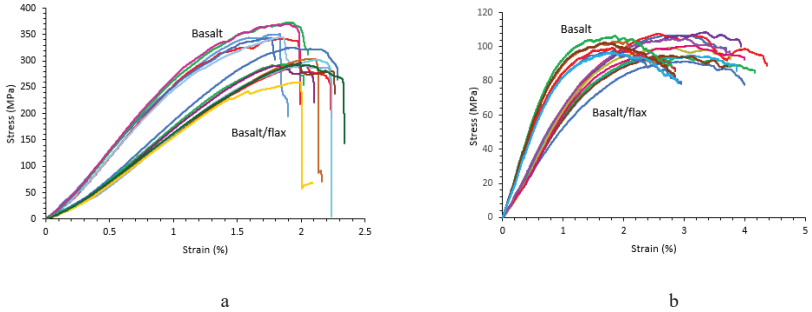
display relatively poor mechanical properties and are hygroscopic, limiting their applicability in high-performance applications [7, 8]. Basalt fibre presents as a promising sustainable alternative that may achieve competitive mechanical properties compared to traditional fibres. Basalt is a volcanic mineral abundant at the earth's surface. Basalt is composed of SiO_2 (48-54%), Al_2O_3 (12-18%), Fe_2O_3/FeO (9-14%), CaO (8-12%), MgO (3-8%), and other minor components. Although basalt is not renewable *per se*, it is abundant, accessible, and thus affordable to obtain [9, 10]. Furthermore, since crushed basalt can be directly melt spun into fibres at a relatively low temperature of 1450°C without any additives required, it has a low embodied energy, CO_2 footprint, and water consumption. These metrics are appreciably lower than synthetic fibres, and equivalent or even lower than glass and plant-based fibres, posing it as an environmentally promising material. To date, there remains a lack of direct comparison between using sustainable and traditional reinforcing fibres with commercially available biobased epoxy for FRPM composites. To address this, this research evaluates the four-point bending mechanical properties of sustainable composites composed of basalt and basalt/flax fibre reinforced biobased epoxy polymer matrix composites and compares these to traditional glass and Kevlar fibre reinforcements.

2 Materials, specimen manufacturing, and mechanical testing

Composites were prepared using the vacuum infusion with plain weave basalt fibre (127 g/m^2), plain weave basalt/flax fibre (95 g/m^2), plain weave glass (106 g/m^2), and plain weave Kevlar (110 g/m^2), with Gurit Bio-Prime 37 epoxy resin was as the matrix. The specimens were cut from the panels in the 0/90° and ±45° orientations using a waterjet in geometries in accordance with ASTM 7264. The cut specimens were post cured at 50°C for 16 hours. 4-point bending quasi-static flexural testing was performed on a Zwick Universal Testing Machine at 4 mm/min crosshead speed. 90° and 45° fibre orientations were tested with at least 5 repeat specimens per material, per orientation.

3 Results and discussion

The results in Figure 1 shows that the 0/90° fibre orientation exhibited higher flexural strength and modulus compared to the ±45° orientation. Basalt exhibited the highest flexural strength in both orientations. Basalt/flax composites exhibited brittle behaviour in the 0/90° orientation but demonstrated flexural strength higher than that of flax strength values reported in literature.



a b

Fig. 1: Stress vs strain curves of basalt and basalt/flax in the a) 0/90° and b) ±45° orientations.

The stress vs strain curves of basalt and basalt/flax fibres demonstrate good repeatability, indicating manufacturing consistency.

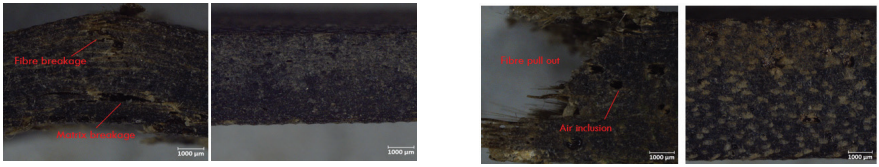


Fig. 2: Photographs showing the failure mechanisms of basalt in the a) 0/90°, b) ±45° and basalt flax in the c) 0/90° and d) ±45° fibre orientations.

The dominant failure mechanism in basalt 90° was fibre breakage and matrix cracking on the top and bottom surfaces respectively. For basalt flax, the dominant failure mechanism was fibre pull out and matrix cracking. Air inclusion can also be observed, which is a manufacturing flaw that could have contributed to the brittle failure of basalt/flax.

References

[1] Y. S. Amruth, K. N. Mohandas, and L. Sunith Babu, Mechanical characteristics study on basalt/epoxy laminates. Mater. Today: Proc., **46**. 4407-4411 (2021)

[2] D. K. Rajak, D. D. Pagar, P. L. Menezes, and E. Linul, Fiber-Reinforced Polymer Composites: Manufacturing, Properties, and Applications. Polymers, **11**. 1667 (2019)

[3] F. Bensadoun, I. Verpoest, and A. W. Van Vuure, In-service behaviour of flax fibre reinforced composites for high performance applications. PhD Thesis, KU Leuven, (2016)

[4] M. Ashadujjaman, A. Saifullah, D. U. Shah, M. Zhang, M. Akonda, N. Karim, and F. Sarker, Enhancing the mechanical properties of natural jute yarn suitable for structural applications. Mater. Res. Express, **8**. 055503 (2021)

[5] H. Zhang, Z. Zhong, and L. Feng, Advances in the Performance and Application of Hemp Fiber. Int. J. Simul.: Syst. Sci. Technol., **17**. 18.1 (2016)

[6] N. Bakar, S. Chin, J. Siregar, and S. Ngien, A review on physical, mechanical, thermal properties and chemical composition of plant fibers, in IOP Conf. Ser.: Mater. Sci. Eng., 736, 5. 052017 (2020)

[7] M. Syduzzaman, M. A. Al Faruque, K. Bilisik, and M. Naebe, Plant-based natural fibre reinforced composites: a review on fabrication, properties and applications. Coatings, **10**. 973 (2020)

[8] M. Bulut, M. Alsaadi, and A. Erkliğ, A comparative study on the tensile and impact properties of Kevlar, carbon, and S-glass/epoxy composites reinforced with SiC particles. Mater. Res. Express, **5**. 025301 (2018)

[9] C. Chen, Y. Ding, X. Wang, and L. Bao, Recent advances to engineer tough basalt fiber reinforced composites: A review. Polym. Compos., **45**. 12559-12574 (2024)

[10] P. Jagadeesh, S. M. Rangappa, and S. Siengchin, Basalt fibers: An environmentally acceptable and sustainable green material for polymer composites. Constr. Build. Mater., **436**. 136834 (2024)

The effect of heat-treatment on 28% Mn and 9% Ni austenitic steels for use in cryogenic LNG applications

Tokelo Taba[1], *Desmond* Kleman[1],*Michael* Bodunrin[1], *Lebedike* Mampuru[1,2], *Joseph* Moema[2] and *Maje* Phasha[2]

[1]University of Witwatersrand, Faculty of Engineering, School of Chemical and Metallurgy, Johannesburg, South Africa
[2]Advanced Materials Division, MINTEK, 200 Malibongwe Drive, Randburg, 2194, South Africa

Abstract. Heat treated high manganese Fe-Mn based alloys are explored worldwide as an alternative material to the conventional expensive alloys in the energy generation industries. Thermal processing of such alloys is considered important as it can result in favourable properties such as high toughness at low temperatures, good strength, and good weldability which are the key properties that render them attractive candidates for cryogenic applications. One major considered application is in the energy sector for construction of large tanks to store liquified natural gas (LNG). LNG is one of the alternative energy sources that can ease over reliance on already strained coal and renewable energies. In this study, the effect of heat treatment process on microstructure and mechanical properties of 28 wt.% Mn and 9 wt.% Ni steels is investigated. The preliminary assessment of the hardness properties showed that the 28 wt.% Mn has a much lower hardness than 9 wt.% Ni steel in both as-cast and heat-treated conditions.

1 Introduction

Heat treatment is one of the key processes in metallurgy that is capable of altering microstructure of metallic materials, leading to subsequent enhanced mechanical properties. For 9% nickel steel, good strength and low temperature toughness are possible with a microstructure containing nickel-rich ferrite and stable high carbon austenite [1]. These properties can be achieved by double-normalizing and tempering or quenching and tempering. The double-normalizing is carried out at around 900 and 800 ℃ to produce a homogeneous structure. The water quenching is performed from about 800 ℃ and this results in material with a martensite and bainite microstructure. The tempering for both heat treatments is performed at about 565-610 ℃, the core difference between the two is yield strength, the double-normalized has a lower yield strength of 515 MPa and the quenched has a 585 MPa yield strength. These steels are vulnerable to temper embrittlement if exposed to temperatures between 370 and 540 ℃ for a prolonged period [3]. Long extended holding times during tempering results in the retained austenite being unstable and decomposing to fresh martensite upon cooling and thus lowering the overall impact toughness.

On the other hand, the process of heat-treating high manganese alloys typically involves heating the alloy to high temperatures in the ranges of 1050-1100°C, this is done to dissolve secondary phases followed by rapid water quenching to achieve tough, single phase austenitic steel. The heat treatment process is crucial for optimizing their mechanical properties. This process often involves austenitizing, quenching, and tempering. During the austenitizing process, the steel is heated to a temperature where austenite forms, followed by rapid cooling (quenching) to form phases that enhance strength. Subsequent tempering can relieve internal stresses and improve ductility. In the current study, the heat treatment of Mn content 28 wt.% is explored comparing it to that of 9 wt.% Ni alloy as a reference material. The focus is mainly on producing similar or better cryogenic properties to those of 9 wt.% Ni upon heat treatment and thermo-mechanical processes.

2 Methodology

The as-cast 28% Mn and 9% Ni steel samples cast in the foundry environment. Smaller samples were sectioned from cast ingots to prepare for metallurgical evaluation. These samples were mounted, grinded, polished, and etched using 5% nital for microstructural observation under an optical microscope (OM). Other sectioned samples were tested for hardness using a Vickers hardness tester at a load of 10kg. A second set of sectioned samples were solution treated at a temperature of 1100 °C for 1 hour in a muffle furnace, followed by water quenching. Similar steps as above were followed in the same order to get the microstructures and hardness values.

3 Results

As shown in Fig. 1, the 28% Mn and 9% Ni steels showed substantially difference in hardness in both as-cast and heat-treated conditions. These results show that the hardness of 28% Mn steel in as-cast and solution treated conditions does not differ much. his could be attributed to little microstructural alteration during heat treatment, hence similar hardness values. The hardness results of the solution treated 9% Ni steel is significantly lower than that for the as-cast as a result of the solution treatment dissolving the secondary phases in the alloy.

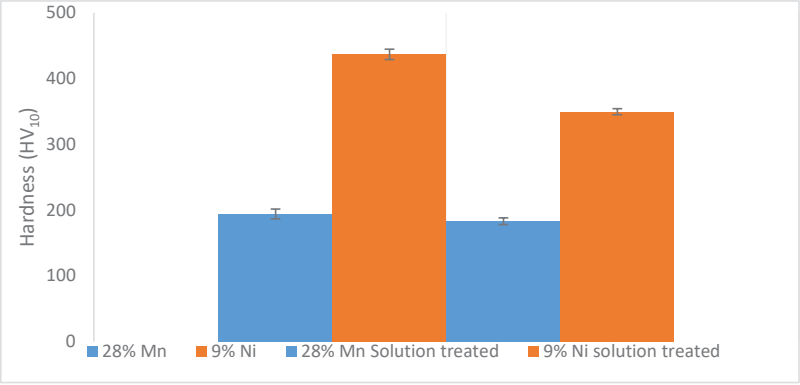


Fig. 1. Bar graph comparing the hardness of 28% Mn steel to 9% Ni steel for as-cast and solution treated conditions.

4 Conclusion

This work assesses and compares the hardness of as-cast and solution treated 28 wt.% Mn alloy to that of 9 wt.% Ni steel. The hardness results showed that the 28 wt.% Mn has a much lower hardness than 9 wt.% Ni steel in r both as-cast and heat-treated conditions. Current results show that hardness of 28% Mn steel in as-cast and solution treated conditions does not differ much due to little microstructural alteration during heat treatment process

References

1. Hilkes, J. & Neessen F.,2007.' Welding 9% nickel steel for liquefied natural gas (LNG) applications' *welding and cuttings* No.2
2. Huang, X., Zhang, L., & Wang, Y. Materials Science and Engineering: A, **765**, 138274 (2019).
3. Park, M. Kim, J. Pyo, C. Son, J. & Kim, J. *Materials* **14**,1659 (2021).

Effect of microstructure on corrosion behaviour of Ti-15Cu alloy subjected to different heat treatment cycles

Zanele Helen Phasha[1**], *Donald* Mkhonto[2] & *Mamookho Elizabeth* Makhatha[1]

[1] Department of Metallurgy, School of Mining and Metallurgy and Chemical Engineering, University of Johannesburg, Doornfontein Campus, Johannesburg, South Africa
[2]Advanced Materials Division, MINTEK, Private bag X 3015, Randburg, 2125, South Africa

Abstract. Current study explores the correlation between microstructure and corrosion performance of binary Ti-15Cu alloy subjected to different heat treatment cycles which resulted in variance of microstructures. The ingot was produced by arc melting process conducted under inert atmosphere. Two sectioned pieces of the ingot were subjected to heat treated at 900 ℃ and 1050 ℃ for 2h, followed by furnace cooling to room temperature. Heat treated samples were further machined to plates of about 3mm thickness and used for phase, microstructural and electrochemical analysis. The volume fraction and size of Ti_2Cu phase was observed to increase with an increase in heat treatment temperature.

1 Introduction

In biomedical applications, titanium (Ti) and its alloys are widely used due to their attractive properties [1]. Although Ti alloys have superior mechanical properties needed for implants in biomedical field, they are difficult to process by cheaper casting process. High melting temperature, strong affinity to interstitial elements and reactivity with mould material make processing of titanium alloys complex [2]. To mitigate these challenges, Ti alloys can be produced using advanced enclosed systems such as arc-melting furnaces that operate under inert atmosphere. Thus, alloying Ti with copper (Cu) does not only benefit from the use of advanced melting techniques [1, 2], but Ti-Cu alloys also have excellent anti-bacterial, corrosion and osseointegration properties [1].

At low Cu compositions, the equilibrium microstructure of Ti-Cu alloys consists of α-Ti matrix and the intermetallic Ti_2Cu phase [3]. It was discovered that with an increase in Cu content, the volume fraction of the intermetallic Ti_2Cu also increases [2, 4]. An increase in Cu amount in Ti-Cu alloys was found to significantly decrease the electrochemical performance of Ti-Cu alloys [2], which is undesirable. However, upon heat treatment the corrosion performance of the Ti-Cu alloys was improved [2]. Moreover, heat treatment processes such as annealing and ageing of the mechanical milled Ti-Cu metal powders have

* Corresponding author: phashazh@gmail.com

been reported to enhance the mechanical properties, corrosion resistance and antibacterial rate by the redistribution of Cu and size distribution of Ti_2Cu precipitates [5, 6]. This is an indication that microstructural and macrostructural morphologies influence the corrosion behaviour and other mechanical properties of metallic materials [2, 7, 8]. The amount of the secondary phase and its distribution in the binary alloys are important parameters that can impact both the mechanical properties and electrochemical performance [7]. Thus, the current study explores this correlation further by subjecting Ti-15Cu alloy to different heat treatment cycles resulting in variant microstructures and evaluating how these microstructures influence the corrosion behaviour.

2 Materials and method

High purity metal shavings of Ti (99.5%) and Cu (99.99) were used to prepare an alloy ingot of Ti-15 wt.% Cu composition (here referred to as 85Ti-15Cu). The ingot was produced by melting metal shavings on a a water-cooled copper hearth using the arc melting furnace operating under controlled environment consisting of vacuum level below 3 x 10^{-4} bar, flushed with argon. To ensure homogeneity, the ingot was inverted six times during the melting process. The ingot was sectioned into two pieces which were heat treated at 900 °C and 1050 °C for 2h, followed by furnace cooling to room temperature. Heat treated samples were further machined into pieces of about 3mm thickness and used for phase, microstructural and electrochemical analysis.

3 Results and discussion

Figure 1 shows the SEM microstructures of of the 85Ti-15Cu alloy heat treated at 900 and 1050 °C.

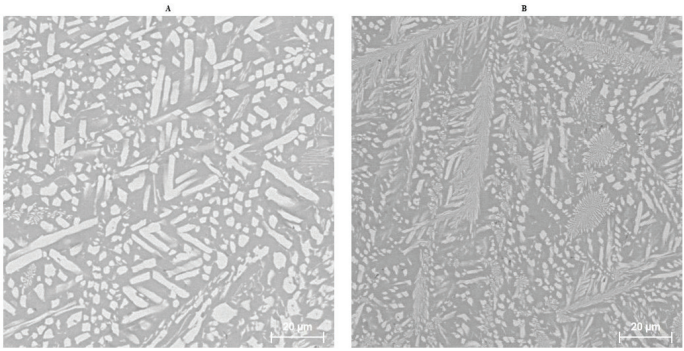


Fig. 1. SEM of the 85Ti-15Cu heat treated at (A) 900 and (B) 1050 °C.

4 Conclusion

The 85Ti-15Cu alloy sample heat treated at 1050 °C shows superior corrosion performance compared to the one heat treated at 900 °C. The Ti_2Cu phase in the sample heat treated at 900 °C has a lath-type (platelet) shape, while that heat treated at 1050 °C formed coarser dendritic microstructures.

References

[1] Z. Wang *et al.*, "Effect of Cu content on the precipitation behaviors, mechanical and corrosion properties of as-cast Ti-Cu alloys," *Materials,* vol. 15, no. 5, p. 1696, 2022.

[2] W. R. Osório, C. M. Freire, R. Caram, and A. Garcia, "The role of Cu-based intermetallics on the pitting corrosion behavior of Sn–Cu, Ti–Cu and Al–Cu alloys," *Electrochimica Acta,* vol. 77, pp. 189–197, 2012.

[3] L. Shao *et al.*, "The effect of Cu content and Ti2Cu precipitation on the combustion behaviour and mechanism of Ti-xCu alloys," *Corrosion science,* vol. 190, p. 109641, 2021.

[4] Z. H. Phasha, M. E. Makhatha, M. Phasha, and D. Mkhonto, "Average oxidation state of Ti-Cu alloys comprised of lower temperature α-Ti (Cu) and Ti2Cu phases," in *MATEC Web of Conferences*, 2025, vol. 417: EDP Sciences, p. 06019.

[5] F. Ionescu, L. Reclaru, L. C. Ardelean, and A. Blatter, "Comparative analysis of the corrosion resistance of titanium alloys intended to come into direct or prolonged contact with live tissues," *Materials,* vol. 12, no. 17, p. 2841, 2019.

[6] E. Zhang, X. Wang, M. Chen, and B. Hou, "Effect of the existing form of Cu element on the mechanical properties, bio-corrosion and antibacterial properties of Ti-Cu alloys for biomedical application," *Materials Science and Engineering: C,* vol. 69, pp. 1210–1221, 2016.

[7] W. R. Osório, C. M. Freire, and A. Garcia, "The effect of the dendritic microstructure on the corrosion resistance of Zn–Al alloys," *Journal of Alloys and Compounds,* vol. 397, no. 1-2, pp. 179–191, 2005.

[8] W. R. Osório, C. M. A. Freire, and A. Garcia, "Dendritic solidification microstructure affecting mechanical and corrosion properties of a Zn4Al alloy," *Journal of Materials Science,* vol. 40, no. 17, pp. 4493–4499, 2005.

Scanning strategy on the mechanical properties of heat treated additively manufactured 1.2709 tool steel

Lerato Tshabalala[1], *Yoshlyn* Naidoo[1*], and *Charmaine* Johnston[1]
[1]Council for Scientific and Industrial Research (CSIR), Pretoria, South Africa

Abstract. This paper investigates the influence of laser scanning strategy and post-process heat treatment on the tensile properties of 1.2079 tool steel fabricated by Selective Laser Melting (SLM). Specimens were produced using two scanning strategies, an island (chessboard) strategy and a unidirectional (no-islands) strategy, and subjected to three heat treatment conditions, i.e. as-built, solution annealing (SA) in a Hot Isostatic Pressing (HIP) cycle at 900 °C, and SA combined with aging at 500 °C (SA+A). The results establish scanning strategy and HIP-based heat treatment as the primary process levers for optimising the mechanical performance of SLM-produced 18Ni-300 maraging steel.

1 Introduction

The DIN 1.2709 tool steel achieves ultra-high strength through precipitation of $Ni_3(Ti,Mo)$ intermetallics in a low-carbon martensitic matrix [1], making it attractive for aerospace tooling and wind tunnel model components. Selective Laser Melting (SLM) enables near-net-shape fabrication of complex geometries but introduces cellular martensitic substructures, elemental microsegregation, and residual stresses that differ from conventionally processed materials [2, 3]. Two process variables, laser scanning strategy and post-process heat treatment, critically determine the final mechanical properties and are systematically investigated.

2 Experimental procedure

Gas-atomised AP&C 18Ni-300 powder (10–45 µm) was processed on a Concept Laser MLab 200R (190 W, 1050 mm/s, 30 µm layer, >99.999% Ar) to produce rods. Five specimen conditions were tested: Sets A, B, D used an island (chessboard) scanning strategy; Sets C, E, F used a unidirectional (no-islands) strategy. Three heat treatments were used, i.e.

1. as-built (AB),
2. solution annealing in HIP (SA) at 900 °C / 100 MPa / 4 h,
3. SA and aging in HIP (SA+A) at 900 °C / 4 h followed by 500 °C / 6 h with furnace cooling.

Round tensile specimens were machined and tested as per ASTM E8/E8M [4, 5], on an Instron 1342 servo-hydraulic machine ($n \geq 5$ per condition). Microstructural examination was then performed using a JEOL JSM-6010PLUS Scanning Electron Microscope (SEM).

3 Results, discussion and conclusion

Tensile results for all heat treatment conditions are summarised in Figure 1 for the optimum strategy; this is the scan strategy without islands. In the as-built condition, the no-islands strategy (Set C) produced substantially higher elongation ($12.7 \pm 2\%$) than the island strategy (Sets A/B: ~3.7–3.9%), attributed to reduced melt-pool boundary density and lower lack-of-fusion porosity under continuous unidirectional scanning. The Ultimate Tensile Stress (UTS) and Yield Stress (YS) were comparable across as-built strategies (~1080–1134 MPa and ~1020–1076 MPa respectively), confirming that precipitate state is the primary strength determinant in the as-built condition.

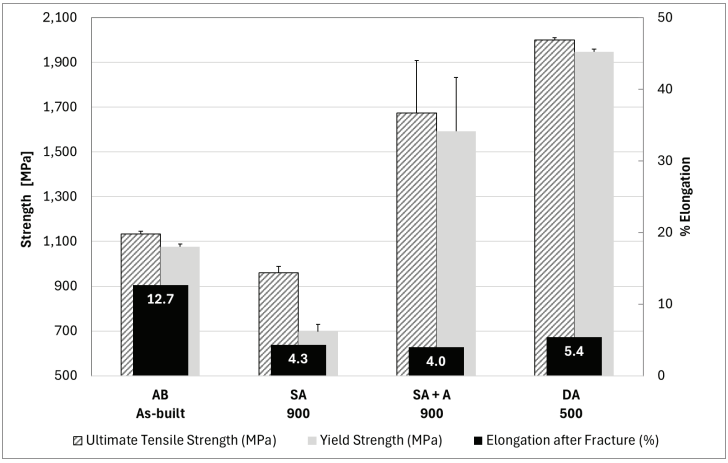


Fig. 1. Tensile properties for optimum specimen conditions

After SA in HIP at 900 °C, the strength decreased relative to the as-built condition (Set D: UTS 960 ± 30 MPa; Set E: UTS 1021 ± 8 MPa), as expected for an unaged, solution-annealed microstructure. Importantly, elongation converged to ~4.3–4.4% regardless of scanning strategy, confirming that HIP pressure effectively eliminates the as-built porosity differences between strategies. The elastic modulus increased to 168–182 GPa, reflecting relief of SLM-induced residual tensile stresses. The no-islands strategy retained a ~6% UTS advantage over island scanning even after full solution annealing.

The SA+A in HIP condition (Set F) produced the highest measured properties: UTS 1675 MPa, YS 1592 MPa, E 186 GPa, and elongation 3.96%, all within the conventional SA+A datasheet range (UTS 1900–2250 MPa, YS 1800–2160 MPa, E 176–184 GPa, elongation 3.5–6%). The step-change in strength relative to SA-only confirms successful $Ni_3(Ti,Mo)$ precipitation during the 500 °C aging step. The measured UTS, while within the datasheet range, sits toward the lower bound; further optimisation of aging duration and cooling rate may yield higher peak strengths. The Direct Aging (DA) procedure

at 500 °C / 6 h aging, applied to no-islands specimens, achieved tensile properties consistent with conventionally processed material, validating this post-processing route for component fabrication.

The authors acknowledge support from the CSIR Aerospace Systems Impact Area, the Advanced Materials and Manufacturing Unit as well as the Photonics Centre.

This work was funded through the Aeronautical Defence Evaluation and Research Institute (ADERI) program of the South Africa Air Force (SAAF).

References

[1] M. Jägle, P. Choi, J. van Humbeeck and D. Raabe, "Precipitation and austenite reversion behaviour of a maraging steel produced by selective laser melting," *J. Mater. Res,* vol. 29, no. 17, 2014.

[2] P. Krakhmalev, G. Fredriksson, M. Thuvander, M. Åsberg, A. M. Vilardell, C. Oikonomou, G. Maistro, A. Medvedeva and N. Kazantseva, "Influence of heat treatment under hot isostatic pressing (HIP) on microstructure of intermetallic-reinforced tool steel manufactured by laser powder bed fusion," *Materials Science and Engineering: A,* no. 772, 2020.

[3] Y. Bai, D. Wang, Y. Yang and H. Wang, "Effect of heat treatment on the microstructure and mechanical properties of maraging steel by selective laser melting," *Materials Science and Engineering: A,* no. 760, 2019.

[4] L. Jiang, C. Chen and M. Zhang, "ffect of Heat treatment on the Properties of a High Alloying Maraging Steel fabricated by Laser Metal Deposition," *Met. Mater. Int.,* no. 29, 2023.

[5] ASTM, *E8/E8M-22: Standard Test Methods for Tension Testing of Metallic Materials,* American Society for Testing Materials (ASTM) International, 2022.

Material selection and traditional reconstruction techniques for cranial plate implants: a review

Onesimo Mjiba[1*], *Jacobus* van der Walt[1], *Gerrie* Booysen[2] and *Joseph* Nsengimana[1]

[1]Department of Mechanical and Mechatronics Engineering, Central University of Technology, Free State, South Africa
[2]Centre for Rapid Prototyping and Manufacturing, Central University of Technology, Free State, South Africa

Abstract. Cranial reconstruction restores skull integrity and protects the brain after craniotomy or trauma. Traditional reconstruction methods such as bone grafts involve additional surgery and complications, while titanium implants produced through Laser Powder Bed Fusion (LPBF) are often unaffordable within resource-constrained South African public healthcare systems. Polymethyl methacrylate (PMMA) is a biocompatible and radiolucent polymeric material which can offer a cost-effective alternative. Highlighting advances in Additive Manufacturing (AM), this review traces the evolution of cranial reconstruction materials and methods Addressing challenges associated with cost affordability, the selection of applicable materials and methods focuses on improvement of health conditions of the patient.

1 Introduction

Patients may undergo surgery due to conditions such as brain tumours, trauma, or aneurysms, which can exert pressure on the brain and lead to increased intracranial pressure. This pressure can cause headaches, seizures, and cognitive or motor function problems [1]. To relieve these symptoms and prevent further damage, patients need to undergo a procedure called a craniotomy, where a section of the skull is temporarily opened for surgeons to access the brain, to remove the brain tumour or to clip the aneurysm. Surgeons typically employ a C-shaped incision for the craniotomy procedure [2]. This incision pattern is designed to preserve key branches of the superficial temporal artery and other vessels supplying the scalp and underlying bone, thereby maintaining blood flow to the resected area. Preserving this vascular supply is crucial in preventing osteonecrosis [2]. In more complex or emergency surgeries such as those involving open trauma with bone fracture or contaminated wounds which may lead to infection, the bone flap may be removed entirely [4]. This is also applicable to severe cerebral swelling to allow the brain to swell without restriction, a practice known as decompressive craniectomy [5]. In these instances, the dura mater and the scalp become the only protective barriers over the brain, significantly increasing the risk of secondary trauma, intracranial infection and cosmetic deformities due to skull asymmetry

* Corresponding author: omjiba@gmail.com

[2]. To mitigate these risks, especially during long-term recovery or permanent placement, the fabrication and implantation of a substitute cranial plate become imperative.

2 Discussion

Material selection for cranial implants relies on factors such as patient age, defect size and location, cause, soft tissue condition, socio-economic issues and preference of surgeons [6]. Biocompatibility, mechanical strength equivalent to the bone, radiolucency, sterilizability and cost affordability are the main requirements of the used material [7]. Small defects categorized as Class 1 are best treated using the patient's own bone (autographs) due to their biological compatibility. Medium (Class 2) defects can use autographs, and synthetic materials can be used as alternatives when natural grafts are not suitable. Large or complex (Class 3) defects typically require synthetic material since autographs become impractical [7,9]. Traditional techniques have relied on autologous bone graft, which is ideal, but requires additional surgery to harvest the bone [6, 8]. Artificial material such as perforated titanium sheets, present challenges including difficulty in shaping due to material spring-back and a visible outline of the implant in fair-skinned patients [9]. Polymethyl Methacrylate (PMMA) bone cement implants cast from an impression taken of the defect in theatre provides an alternative. However, the curing time for the cement can prolong surgery, and uneven cooling or improper mixing may cause imperfections [1, 7]. While Additive Manufacturing (AM) techniques, particularly Laser Powder Bed Fusion (LPBF) for titanium alloys [9] offer customised solutions but are often too expensive and inaccessible in a resource-constrained South African public healthcare system.

3 Conclusion

The evolution of cranial implant materials and manufacturing techniques reflects a continuous effort to improve patient clinical outcomes. From the inherent limitations of autografts and early titanium sheets to the advanced capabilities of LPBF for custom titanium implants, progress has been substantial. The adoption of AM in cranioplasty has provided high customisation and accuracy. However, challenges related to cost and accessibility persist, particularly in public healthcare settings. This review explores the evolution of material selection for cranial implants, from traditional bone grafts and perforated titanium alloy sheets to PMMA and discusses the shift towards AM for more efficient and customisable production.

References

1. N. Nevalainen, T. M. Luoto, G. L. Iverson, V. M. Mattila and T. T. Huttunen, "Craniotomies following acute traumatic brain injury in Finland—a national study between 1997 and 2018," Acta Neurochir., **164**, pp. 625–633 (2022).
2. T. Okuyama, K. Kurisu, M. Hokari, K. Miyata, K. Uchida, K. Asaoka, K. Itamoto and M. Fujimura, "Successful treatment with urgent revascularization and parent artery occlusion for a ruptured intratumoral aneurysm following prior meningioma surgery: Illustrative case," J. Neurosurg. Case Lessons, 5, Article 21 (2023).

3. G. P. Rao, M. Imran, R. N. Raju, P. Sandeep and K. A. Reddy, “Mini-craniotomy for chronic subdural hematoma: A reliable surgical option,” Asian J. Neurosurg., **19**, pp. 256–262 (2024).
4. F. Chaddad-Neto, J. M. Campos Filho, H. L. Dória-Netto, M. H. Faria, G. C. Ribas and E. Oliveira, “The pterional craniotomy: Tips and tricks,” Arq. Neuropsiquiatr., **70**, pp. 727–732 (2012).
5. H. S. Yang, D. Hyun, C. H. Oh, Y. S. Shim, H. Park and E. Kim, “A faster and wider skin incision technique for decompressive craniectomy: n-shaped incision for decompressive craniectomy,” Korean J. Neurotrauma, **12**, p. 72 (2016).
6. L. Bilton, S. B. Harvey, B. I’Ons and H. Green, “Novel technique of post mortem cranial bone reconstruction using 3D printed skull clips: Technical note,” Ann. 3D Print. Med., **10**, Article 100104 (2023).
7. C. N. T. Kim, C. X. Binh, V. T. Dung and T. V. Toan, “Design and mechanical evaluation of a large cranial implant and fixation parts,” Interdiscip. Neurosurg., **31**, Article 101676 (2023).
8. J. Abdel Hay, T. Smayra and R. Moussa, “Customized polymethylmethacrylate cranioplasty implants using 3-dimensional printed polylactic acid molds: Technical note with two illustrative cases,” World Neurosurg., **105**, pp. 971–979.e1 (2017).
9. N. K. Sahoo, M. N. Rangan, K. Tomar and S. Bhat, “Classification of the residual cranial defects and selection of reconstruction materials,” J. Craniofac. Surg., **28**, pp. 1694–1701 (2017).

04

ABSTRACTS

Additive Manufacturing Material and Part Characterisation

Characterisation of titanium metal powder produced by ultrasonic atomisation from scrap parts

K Dyal Ukabhai[1*], *D R Boyes*[2], D Blaine[2] and *D Mkhonto*[1]

[1]Advanced Materials Division, Mintek, Randburg, South Africa
[2]Department of Mechanical and Mechatronic engineering, Stellenbosch University, Stellenbosch South Africa

Abstract. While additive manufacturing is prized as a low waste technology, the process does produce scrap powder that is not currently reused. There is interest in improving the sustainability of additive manufacturing to support a circular economy. Mintek currently houses ultrasonic atomisation equipment for producing powder and recycling of scrap. The aim of this work was to use this process to produce powder from recycled titanium and study its suitability for laser powder bed fusion. Test results of the ultrasonically atomised powder showed that the particles were spherical and had good flowability and apparent density. The 20 kHz powder produced a larger particle size powder than the 40 kHz powder. Only the 40 kHz has powder characteristics that make it suitable for laser powder bed fusion.

1 Introduction

Additive manufacturing (AM) is an industry that has experienced significant growth over the past decades, and as techniques and methods continue to evolve, global forecasts indicate that it will continue to expand rapidly [1]. Laser powder bed fusion (L-PBF) is a prominent AM technology that has been successfully implemented in South Africa [2]. L-PBF employs a high power (>100 W) laser to selectively fuse layers of metal powder, enabling the creation of intricate, net-shape components. Metal powders have a high level of recyclability and are good candidates for developing a circular economy for additive manufacturing [3, 4]. For L-PBF, after printing the desired parts, the loose, unmelted powder that surrounds the built part is collected and, very often, reused. Typically, a 80 µm mesh sieve is used to separate the powder into powder for reuse (< 80 µm) with the remaining powder (> 80 µm) discarded as scrap [4]. The reuse powder is then mixed with the virgin powder in the powder bin, with several reuse cycles successfully being reported for different powder alloys [4]. However, with extra focus on making AM more sustainable and building a circular economy around this industry, researchers are focusing on both on the reuse of powder for L-PBF, as well as recycling of scrap parts and powder into powder suitable for L-PBF [4]. A potential pathway

* Corresponding author: kiyaashadu@mintek.co.za

for recovering material is to recycle scrap parts and powder by reprocessing them into powder suitable for L-PBF [4].

In 2023, Mintek commissioned the Amazemet rePowder Ultrasonic atomisation (UA) and alloy development equipment. The equipment uses ultrasonic acoustic waves to convert molten metal feedstock for different alloys, with low to high melting points, into metal powder [3]. Powder characteristics, such as particle size distribution (PSD) and powder morphology, affect the flowability and packing density of the powder bed, as well as the absorption of laser energy, melting and solidification behaviour [4]. The quality of the metal powder feedstock for L-PBF significantly influences the quality of the as-built material. Currently, most L-PBF powder is imported into South Africa and scrap powder and parts are discarded. The purpose of the study was to produce UA titanium powder from scrap parts, using the Amazemet rePowder system at Mintek, and evaluate its suitability for L-PBF.

2 Experimental procedures

2.1 Powder production

Titanium bars (~32 x 12.7 x 6.8 mm), produced from titanium powder by press and sinter processing, were provided as scrap parts. The bars were melted into 10-mm diameter rods using vacuum arc melting to provide suitable feedstock for the rePowder system. The rods were fed into a plasma torch that melts the metal, and the stream of molten titanium was atomised at two sonotrode frequencies, controlled by the 20 kHz and 40 kHz transducers, respectively. Before melting and atomising, the atomisation chamber was purged three times, by flushing with argon and pulling a vacuum thereafter. This is done to remove any oxygen or other contaminant gases and to ensure an inert process atmosphere during the plasma melting and UA process.

2.2 Powder analysis

To analyse the particle shape (sphericity) and porosity, the powder was mounted in epoxy resin, ground and polished, and the microstructure was evaluated using optical microscopy. The particle size distribution analysis was measured by laser diffraction (Micrometrics Saturn DigiSizer 5200) to determine the D10, D50 and D90 particle sizes by volume fraction. The flowrate and apparent density of the powders were measured according to ASTM B855, B964, B417 and B212, respectively. The angle of repose was measured according to ASTM D6393. Spreadabilty was tested using a custom built rig that uses a recoater blade to spread a layer of powder over a test surface. The quality of the spread is evaluated by powder bed density and % coverage metrics.

3 Results and discussion

Tables 1-3 summarise all the results collected from the different analyses. The powders were very spherical with little internal porosity, and the UA powder was more spherical than the CP-Ti. As expected, the PSD for the 20 kHz powder was broader with a higher D50 than the 40 kHz powder, as seen in Table 2. The narrower PSD of the CP-Ti and 40 kHz Ti powders indicate their suitability for L-PBF. The flowrates for the UA powders are slightly slower than the virgin CP-Ti. The apparent density of the powders is similar. The angle of repose (AOR) was the best for the 40 kHz powder and the lowest for the 20 kHz powder, providing

an indication of the cohesivity of the powders with the 40 Hz being the least cohesive. The spreadability of the 40 kHz Ti was the best, showing 96% coverage vs 41% for the 20 kHz powder.

Table 1. Powder morphology results

	Description	Notes
CP-Ti	Spherical	81% Sphericity, 4% Porosity, 6% Agglomerates
40 kHz Ti	Highly spherical	95% Sphericity, 2% Porosity, 3% Agglomerates
20 kHz Ti	Highly spherical	86% Sphericity, 3% Porosity, 11% Agglomerates

Table 2. Particle size distribution results

Powder	D10 (µm)	D50 (µm)	D90 (µm)
CP-Ti	20.7	32.5	43.6
40 kHz Ti	47.6	61.3	76.6
20 kHz Ti	84.9	111.6	146

Table 1. Flowability and density results.

Powder	Flow rate (s/50g)	SD	AoR (°)	SD	Apparent density (g/cm^3)	SD
CP-Ti	35.38	0.43	24.37	0.28	2.59	0.13
40 kHz Ti	27.71	0.12	25.32	0.13	2.63	0.15
20 kHz Ti	29.8	0.08	23.23	0.20	2.61	0.11

4 Conclusions

Overall, it can be concluded that the reprocessed UA powders are more spherical than the virgin Cp-Ti powder. The 40 kHz powder is suitable for L-PBF. Although the 20 kHz is not suitable for L-PBF it could be used for powder coating and other AM processes, such as DED and EBM that require larger size particles. All powders had good flowability and apparent density.

5 References

1. T. C. Dzogbewu, S. K. Fianko, N. Amoah, S. Afrifa Jnr and D. de Beer, Additive manufacturing in South Africa: critical success factors, Heliyon, **8**(11), (2022).
2. W. Ji, R. Zhou, P. Viveganantha, M. See Wu, H. Gao and K. Zhou, Recent progress in gradient structured metals and alloys, Progress in materials science, **140**, 1011, (2023).
3. T. Bulbulia, Mintek's AMAZEMET acquisition to support SA's additive manufacturing ambitions, 2023, available at:

https://www.miningweekly.com/article/minteks-amazemet-acquisition-to-support-sas-additive-manufacturing-2023-11-24, accessed on 5 March 2026.

4. Moghimian, P., Poirié, T., Habibnejad-Korayem, M., Zavala, J.A., Kroeger, J., Marion, F. and Larouche, F. Metal powders in additive manufacturing: A review on reusability and recyclability of common titanium, nickel and aluminum alloys, Additive Manufacturing, 43, 102017 (2021).

Correlation between microstructure and mechanical properties in A356 aluminium alloy

P.K Sekgata, *M.N* Mathabathe*

School of Chemical and Metallurgical Engineering, Faculty of Engineering and Built Environment, University of the Witwatersrand, South Africa

Abstract. A356 alloy exhibits attractive and desirable properties to the automotive industry, however due to its "soft" nature and low hardness it needs further development to improve its hardness, ductility and wear rate. The present study reviews the additions of strontium (Sr) and titanium (Ti) to A356 aluminum alloy and evaluates how the resulting morphological changes influence its mechanical properties. Strontium additions resulted in the formation of fibers in the Al matrix within the microstructure of the alloy which improves the strength and ductility of the alloy. On the other hand, the additions of Ti lead to the formation of finer grains through grain refinement, reducing porosity and improving ultimate tensile strength (UTS) and elongation.

1 Introduction

Weight saving and fuel efficiency are of high paramount in automotive and aerospace industries. One of weight saving methods that are currently being explored by automotive and airplanes manufacturers uses light materials and A356 Al alloy proves to be one of the alloys that is being researched extensively [1-2]. Although this alloy shows impressive traits, it still needs improvement for it to have a longer service life. One of the methods that can be used is studying the microstructure of the alloy as it is directly linked to the mechanical properties of the alloy. Additions of Strontium and Ti to A356 alloy alter the microstructure, and their effects are visible on the microstructure eventually affecting the mechanical properties of this alloy. Strontium forms fibers in the Al matrix, enhancing ductility and fatigue life, while Ti refined grains enhancing UTS and tensile elongation of the alloy. Literature show that the cooling times of the alloy lead to formation of different morphologies in the microstructure which also affect the mechanical properties of the alloy [3-4]. Different morphologies presented in these studies are finger bundle with <111> direction and highly branched morphology with <100> direction. These morphologies are represented in Figure 1.

* Corresponding author: maria.mathabathe@wits.ac.za

2 Methodology

As cast A356 Al alloy was fabricated using investment casting process. The alloys were solution treated and cooled in water and air cooling. The casted slab was sectioned into smaller samples for easy handling. The samples were then metallographically prepared and ready for SEM-EBSD analysis as demonstrated by the process flow in Figure 1.

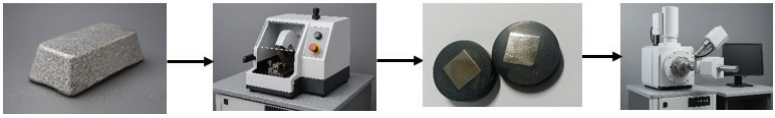


Fig. 1. Metallographic sample preparation for SEM-EBSD

3 Results and discussion

SEM-EBSD was used to examine phase transformations and morphological evolution. The results indicated micrographs displaying highly branched to finger-bundles structures as shown in Figure 2.

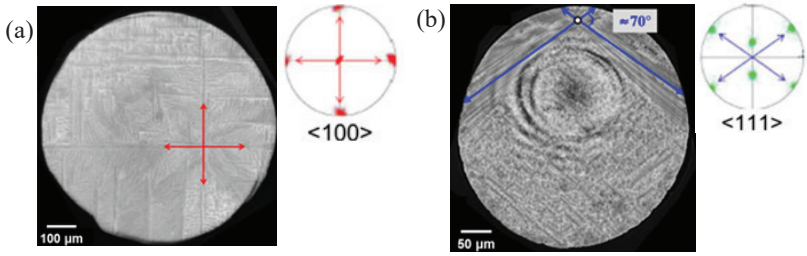


Fig.. 2. (a) SEM-EBSD data showing pole figure maps of highly branched morphology and (b) finger bundle morphology of aluminum alloy as reported in [4] that was produced via investment casting.

Finger bundle morphology forms an elongated parallel primary arms along the <111> crystallographic direction as a result of water quenching, where side branching is limited resulting in less spread-out microstructure with finer secondary arm spacing. On the other hand, highly branched morphology forms when cooling rates are much lower (air cooling) when compared to high cooling rates in finger bundle. These cooling rates lead to more branching from the trunk of the dendrite creating intricate tree-like network in the microstructure. Finger bundle exhibit reduced inter-dendritic porosity and solute entrapment which improves ductility, while branched microstructure promote stress concentrations.

4 Conclusion

Both alloying elements (Sr and Ti) and the resulting morphologies have effects on the microstructure of the alloy, particularly under different cooling conditions (water and air cooling) following solution treatment. The addition of alloying elements improves the strength, ductility and elongation while refined morphologies (finger bundle and highly branched structures) also enhance strength and ductility of A356 alloy. Furthermore, refined

morphologies also reduce stress concentrations and promote homogeneity within the dendritic structure.

References

[1] R. Ian. Mackay, *Development of a new durable AL-Si alloy for the next generation of engine block casting*. Library and Archives Canada = Bibliothèque et Archives Canada, 2008.

[2] Z. Jin *et al.*, "A Study of the Creep-Fatigue Damage Mechanism of a P92 Welded Joint Using Nanoindentation Characterization," *Metals (Basel).*, vol. 15, no. 1, Jan. 2025, doi: 10.3390/met15010053.

[3] S. K. Shaha, F. Czerwinski, W. Kasprzak, J. Friedman, and D. L. Chen, "Microstructure and mechanical properties of Al-Si cast alloy with additions of Zr-V-Ti," *Mater. Des.*, vol. 83, pp. 801–812, Oct. 2015, doi: 10.1016/j.matdes.2015.05.057.

[4] W. Jiang, X. Chen, B. Wang, Z. Fan, and H. Wu, "Effects of vibration frequency on microstructure, mechanical properties, and fracture behavior of A356 aluminum alloy obtained by expendable pattern shell casting," *International Journal of Advanced Manufacturing Technology*, vol. 83, no. 1–4, pp. 167–175, Mar. 2016, doi: 10.1007/s00170-015-7586-0.

Comparison of additively manufactured lattice structure types for sustainable basalt fibre reinforced sandwich panel composites

James Anthony Dicks[1*], *Amelia* Crill[1,2], and *Sherlyn* Gabriel[1,3]

[1]Centre for Materials Engineering, Department of Mechanical Engineering, University of Cape Town, South Africa
[2]Swarthmore College, Pennsylvania, United States of America
[3]Blast Impact Survival Research Unit, Department of Mechanical Engineering, University of Cape Town, South Africa

Abstract. The use of non-stochastic three-dimensional lattice structures as core materials in sandwich composites allows for complex lattice geometries and high specific properties to be achieved. In particular, vat photopolymerisation additive manufacturing allows these types of lattices to be fabricated using mechanically relevant polymeric materials with high resolution fidelity. This work explored the influence of different lattice structure types and their interrelationship with fabrication constraints on the mechanical behaviour of the materials. Furthermore, preliminary investigation into their application within basalt fibre reinforced sandwich composites was demonstrated to achieve sustainable materials with desirable mechanical properties.

1 Introduction

Composite sandwich panels commonly employ porous cores such as a foamed cellular materials or 2D lattices like honeycomb structures. Although there has been a wide variety of different materials used in these porous cores, the available defined non-stochastic porous morphologies have remained somewhat limited by fabrication technologies. More recently, the use of additive manufacturing (AM) has opened opportunities to explore more complex three-dimensional lattice geometries. In broad classification, these include triply periodic minimal surfaces (TMPS), strut-based lattice geometries, and plate-based lattice geometries. These 3D lattice types confer different mechanical behaviour, and controlling their parameters (e.g., unit cell size, wall/strut thickness) allows precise tailoring of their performance within the sandwich panel. From a mechanical point-of-view, TPMS lattices have often displayed the most promising behaviour to suit the role of sandwich panel cores owing to uniform stress distribution from the continuous walls [1]. Several different AM technologies have been explored for fabrication, with vat photopolymerisation AM presenting benefits in material choice, resolution fidelity, and structural isotropy [2]. However, when these lattices are fabricated using vat photopolymerisation, certain pragmatic

* Corresponding author: james.dicks@uct.ac.za

limitations present themselves. Most importantly, during the layer-by-layer fabrication, incomplete polymerisation is almost always apparent to maximise interlayer adhesion and improve layer cure times [3]. Post-curing is therefore generally performed on the complete fabricated part to achieve near-complete polymerisation throughout the material. However, owing to the attenuation of UV irradiance through the material, it can become difficult to achieve sufficient UV exposure at the interior regions of large components. It is thus the case that TPMS structures may not always be an appropriate choice of lattice geometry when fabricated using vat photopolymerisation AM owing to the continuous curvature of walls making it implausible for light to penetrate throughout the lattice component. This is further exacerbated by the need to fabricate thin solid walls on the outside of the lattices to allow adequate adhesion between the core and exterior panels for sandwich composites. On the other hand, strut-based lattices have a more open geometric structure, typically facilitating a greater degree of light penetration and hence better UV irradiance to successfully allow post-curing throughout the interior of the component. Aside from these factors, it is somewhat surprising to note that very little research has been demonstrated using vat photopolymerisation AM fabricated strut-based lattices within sandwich composites, thus furthering the basis to explore these types of lattices [4, 5].

This study compares different lattice types (TMPS gyroid, Fischer-Koch, octet truss, rhombic dodecahedron, and diamond) to ascertain which lattice type is best suited towards fabrication using vat photopolymerisation AM for application in sandwich panel composites. We apply these different lattice types as core materials within sustainable basalt fibre reinforced polymer matrix sandwich composites using a partially biobased epoxy matrix [6]. The mechanical performance of the different lattices was ascertained using uniaxial compression testing and 4-point flexural testing of the sandwich panels to understand the interrelationship between lattice geometry and fabrication scope to achieve a synergistic understanding to enhance the potential of using vat photopolymerisation AM fabricated lattice cores within sandwich panel composites.

2 Lattice design and AM

The lattice structures STL files were designed using custom software based on Python scripts. STL files were sliced in Chitubox and additive manufacturing was performed using a masked stereolithography 3D printer (GK3 Ultra, Uniformation, China) installed with a removable spring steel build platform using PLA-Pro resin (eSun, Taiwan). A layer height of 25 µm, lift speed of 45 mm.min^{-1}, and retract speed of 60 mm.min^{-1} was used. The 3D printed models were washed with isopropanol to remove excess resin and then post-cured in a UV chamber (UW-02, Creality, Taiwan) for 15 min.

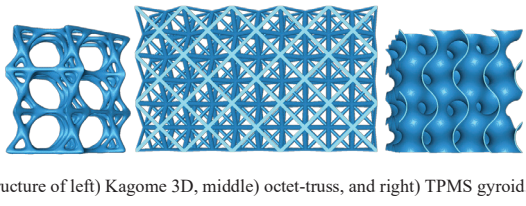


Fig. 1. Lattice structure of left) Kagome 3D, middle) octet-truss, and right) TPMS gyroid.

3 Sandwich panel construction

Sandwich panels were produced by preparing fibre reinforced polymer matrix panels with wet layup and directly adhering to the core with mechanical pressing. Briefly, epoxy resin

and hardener (BioPrime 37 and Ampreg 3X, Gurit, Switzerland) were mixed in a ratio of 100:29 and homogenised for 5 minutes. Six layers of basalt fabric (200 gsm plain weave, Conan, Australia) were laid up for each side of the sandwich panels, and the entire composite sandwich layup was placed between layers of peel-ply and breather fabric. A uniform mechanical compressive pressure was applied, and the epoxy was allowed to cure under ambient conditions for 24 h, followed by post-curing in an oven at 60°C for 16 h.

4 Mechanical properties and characterisation

Mechanical testing was performed on a Universal Testing Machine (Zwick-Roel, Germany) equipped with a 10 kN load cell and integrated video extensometer (LIMESS, Germany). Uniaxial compression testing was performed in accordance with ASTM D1621 and WK76163 using 30×30×30 mm^3 specimens and a crosshead speed of 3 $mm.min^{-1}$. Flexural 4-point bend testing was performed on sandwich panels according to ASTM C393 using 30×65×200 mm^3 specimens, a crosshead speed of 6 $mm.min^{-1}$, span support of 150 mm, mid spans of 50 mm, and load span of 50 mm. Each test was performed using 5 repeat specimens with results reported as the average with standard deviation. Fracture surfaces were examined using a stereo optical microscope with NIS-Elements Imaging software (Nikon SMZ25, Nikon, Tokoyo, Japan).

5 Conclusion

The printability and post-curing efficacy of different lattice structure types were investigated within the context of constructing sustainable basalt fibre reinforced sandwich composites. The lattice structure type and its scope to be printed using vat photopolymerisation AM led to differing mechanical properties within the sandwich panels, providing insights into their applicability within this context.

References

[1] M. S. Hossain, M. M. Hossain, and S. Nilufar, *An Overview of Additive Manufacturing of Triply Periodic Minimal Surface (TPMS) Structures.* Polymers, **17**. (2025)

[2] R. Guerra Silva, M. J. Torres, and J. Zahr Viñuela, *A Comparison of Miniature Lattice Structures Produced by Material Extrusion and Vat Photopolymerization Additive Manufacturing.* Polymers, **13**. 2163 (2021)

[3] J. A. Dicks, M. I. Hoosain, and O. Mbele, *Multi-Objective parametric optimisation of masked stereolithography additive manufacturing using the response surface method.* South African Journal of Industrial Engineering, **35**. 52-65 (2024)

[4] S. A. M. Ghannadpour, M. Mahmoudi, and K. Hossein Nedjad, *Structural behavior of 3D-printed sandwich beams with strut-based lattice core: Experimental and numerical study.* Composite Structures, **281**. 115113 (2022)

[5] M. Mahmoudi, S. A. M. Ghannadpour, and K. H. Nedjad, *Functionally graded multi-morphology lattice structures as an optimized sandwich core via digital light processing additive manufacturing.* Materials & Design, **238**. 112710 (2024)

[6] P. Jagadeesh, S. M. Rangappa, and S. Siengchin, *Basalt fibers: An environmentally acceptable and sustainable green material for polymer composites.* Construction and Building Materials, **436**. 136834 (2024)

Simulation framework and thermal descriptor extraction for directed energy deposition of Ti-Nb-Zr alloys

Tinashe A. Matyatya[1*], *Wallace R.* Matizamhuka[2], *Thomas B.* Tengen[3], *Sisa L.* Pityana[4], and *Nana K. K.* Arthur[5]

[1,3] Department of Industrial Engineering & Operations Management and Mechanical Engineering, Vaal University of Technology, Andries Potgieter Blvd, Vanderbijlpark 1911, South Africa
[2] Department of Chemical and Metallurgical Engineering, Vaal University of Technology, Andries Potgieter Blvd, Vanderbijlpark 1911, South Africa
[4,5] CSIR Photonics Centre, Laser Enabled Manufacturing, Pretoria Campus, South Africa

Abstract. Beta-type Ti-Nb-Zr alloys are candidates for lower-modulus orthopaedic implants, but DED thermal cycling governs phase and microstructural evolution. This study establishes a numerically verified transient thermal framework for five-layer Ti-28Nb-7Zr deposition on Ti-6Al-4V. ANSYS Mechanical/MAPDL combined an exactly normalised Gaussian source, swept-segment activation, temperature-dependent proxy properties, enthalpy phase change, convection and radiation. The model delivered 45.043 kJ with a 3.32% maximum energy-balance residual; the global peak was 1848.96 °C. Time-step and mesh checks supported robust sustained descriptors. Experimental calibration remains necessary before absolute thermal prediction.

1 Introduction

Titanium alloys are widely used for load-bearing biomedical implants, but the elastic modulus of Ti-6Al-4V remains substantially higher than that of cortical bone and can promote stress shielding [1]. Beta-stabilised Ti-Nb-Zr alloys provide a route to lower stiffness without vanadium; solution-treated Ti-28Nb-7Zr has exhibited a Young's modulus near 29 GPa [2].

Laser-based directed energy deposition (DED) enables localised deposition and in situ alloying of elemental Ti, Nb and Zr powders [3,4]. Process parameters regulate heat input and thermal history, which in turn influence phase retention, grain morphology, residual stress and defects [4]. Because the interaction zone is localised and rapidly evolving, a verified numerical framework is valuable for extracting model-wide and local descriptors before experimental calibration.

The aim was therefore to establish a computationally tractable, numerically verified five-layer Ti-28Nb-7Zr DED framework and to extract thermal descriptors suitable for later design-of-experiments, sensitivity analysis and surrogate modelling. The framework is

* Corresponding author: tinashem@vut.ac.za

intended to support comparative process screening, not to directly predict melt-pool fluid flow, final microstructure or Young's modulus.

2 Methodology

The model comprised a 25 × 25 × 5 mm Ti-28Nb-7Zr reserve build on a 35 × 35 × 7 mm Ti-6Al-4V substrate. Five 0.20 mm layers were activated to capture cyclic reheating and thermal accumulation. Layers 1, 3 and 5 were scanned parallel to X and Layers 2 and 4 parallel to Z. Temperature-dependent proxy conductivity and heat-capacity data were used, with a 300 kJ·kg^{-1} phase-change enthalpy increment between 1800 and 1900 °C, initial and ambient temperatures of 25 °C, h = 10 W·m^{-2}·K^{-1}, emissivity ε = 0.35 and a bonded interface.

A 300 W Gaussian source with absorptivity η = 0.40 was normalised at every position to apply exactly 120 W absorbed power. The raster used 42 lines per layer, 36 source positions per line, 0.553659 mm realised hatch spacing and 12.7 mm·s^{-1} scan speed. Swept-segment activation followed the physical source trajectory. The selected production mesh used 0.42 mm build and 1.50 mm substrate sizing, with 87,931 nodes and 108,403 assembled elements.

Verification comprised source-power integration, energy-balance closure, a one-layer time-step study at 0.099300087, 0.049650044 and 0.024825022 s, and fixed-volume mesh sensitivity at 0.50, 0.45 and 0.42 mm build sizes. Responses included global temperature history, layer-centre reheating, interface/substrate temperatures and vertical gradients.

3 Results and discussion

Exact normalisation imposed 120.000 W at every deposition position. The five-layer sequence delivered 45.04252 kJ with a maximum absolute energy-balance residual of 3.320%. The medium-to-fine time-step difference was 2.717% in instantaneous peak temperature and no more than 1.243% in sustained temperatures; fixed-volume B050-to-B042 mesh differences remained below 0.75%.

The global peak reached 1848.96 °C at 302.2695 s. End-of-layer maxima increased from 1236.9 °C after Layer 1 to 1732.3 °C after Layer 5, then decreased to 845.15 °C after five seconds of cooling, demonstrating progressive thermal accumulation with a diminishing later-layer increment.

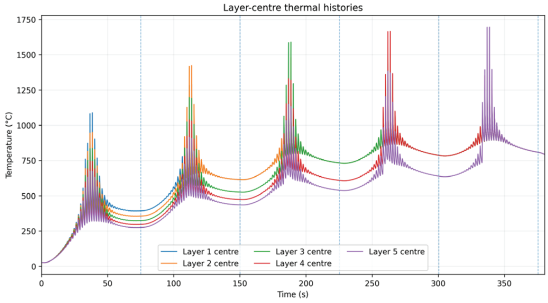


Fig. 1. Layer-centre temperature histories showing repeated local heating, interlayer accumulation and reheating during the five-layer simulation.

Layer-centre deposition peaks increased from 1089.34 to 1696.43 °C. Layer 1 was reheated by 200.59 °C and Layer 2 by 57.52 °C, while Layers 3-5 reached their maxima during their

own deposition. The build-substrate interface peaked at 1208.59 °C; lower and delayed substrate responses demonstrated conductive attenuation.

The net top-to-bottom gradient decreased from 0.716 to 0.309 $K \cdot mm^{-1}$ during cooling. Repeated peaks, the rising thermal baseline and delayed substrate response are qualitatively consistent with published DED studies [5]. Because TNZ high-temperature properties and the phase-change interval are proxies and no process-matched thermal measurement was available, the results support trends and mechanisms rather than calibrated absolute melt-pool temperatures.

For later decision support, sustained and fixed-volume temperatures are the most robust primary responses; instantaneous peaks, reheating, substrate temperatures and path-averaged gradients are secondary/trend indicators, while single-node extrema are diagnostic.

4 Conclusions

A five-layer Ti-28Nb-7Zr transient thermal framework using normalised Gaussian power, swept activation, temperature-dependent proxy properties, enthalpy phase change, convection and radiation was numerically verified. Energy, time-step and mesh checks support comparative descriptor extraction. The model captured thermal accumulation, early-layer reheating, substrate attenuation and gradient relaxation. These descriptors can support subsequent design-of-experiments, sensitivity analysis and surrogate modelling, but experimental calibration remains required before absolute thermal prediction or predictive optimisation.

This research received no external funding.

References

1. M. Niinomi, Mechanical biocompatibilities of titanium alloys for biomedical applications. J. Mech. Behav. Biomed. Mater. **1**, 30–42 (2008). https://doi.org/10.1016/j.jmbbm.2007.07.001
2. M.H.C. Tan, A. Dareh Baghi, R. Ghomashchi, W. Xiao, R.H. Oskouei, Effect of niobium content on the microstructure and Young's modulus of Ti-xNb-7Zr alloys for medical implants. J. Mech. Behav. Biomed. Mater. **99**, 78–85 (2019). https://doi.org/10.1016/j.jmbbm.2019.07.014
3. F. Arias-González et al., In-situ laser directed energy deposition of biomedical Ti-Nb and Ti-Zr-Nb alloys from elemental powders. Metals **11**, 1205 (2021). https://doi.org/10.3390/met11081205
4. D. Svetlizky et al., Directed energy deposition additive manufacturing: Physical characteristics, defects, challenges and applications. Mater. Today **49**, 271–295 (2021). https://doi.org/10.1016/j.mattod.2021.03.020
5. J.C. Heigel, P. Michaleris, E.W. Reutzel, Thermo-mechanical model development and validation of directed energy deposition additive manufacturing of Ti-6Al-4V. Addit. Manuf. **5**, 9–19 (2015). https://doi.org/10.1016/j.addma.2014.10.003

Effect of alloying on microstructure and mechanical properties of high chromium white cast iron (HCWCI) for mill liner application

Joseph Moema[1*], *Lebedike* Mampuru[1], and *Maje* Phasha[1]
[1]Mintek, Advanced Materials Division, 200 Malibongwe Drive, South Africa

Abstract. High chromium white cast irons (HCWCIs) offer good wear resistance but struggle under high impact wear. This study investigated how adding vanadium (V) and niobium (Nb) affects the microstructure and strength of hypereutectic HCWCI castings. Optical microscopy confirmed that additions of V and Nb refined the primary proeutectic M_7C_3 carbides and promoted the formation of fine MC carbides. Three-point bending tests showed that the refined alloys had improved fracture toughness and hardness compared to commercial equivalents. The best performance came from the 1 wt% V addition, which achieved grain refinement, MC carbide formation, and solid-solution strengthening from vanadium.

1 Introduction

High chromium white cast irons (HCWCIs) offer good hardness and can be compositionally tailored to improve impact, abrasion, and corrosion resistance. However, their performance often remains inadequate. Studies over the last decade [1] attribute their high wear resistance to a combination of hard M_7C_3 carbides (M = Fe, Cr, and other carbide formers) embedded in a ductile ferrous matrix. When a hardened martensitic matrix is required for better abrasion resistance and mechanical support of the M_7C_3 carbides, toughness becomes critical to prevent quench cracks [2]. An alternative approach to improving abrasive wear resistance is to add elements with high affinity for carbon. For instance, niobium [3] and mixed carbide formers have been shown to enhance the abrasive wear resistance of high chromium white cast irons.

High chromium white cast irons (HCWCIs) perform well in abrasive conditions such as wet ore grinding. They contain >1.8 wt% C and >11 wt% Cr, plus optional alloying elements like Mo, Mn, Cu, and Ni. Their hardness, ductility, and toughness are enhanced by strong, blocky M_7C_3 carbides. Depending on carbon content, HCWCIs are classified as hypoeutectic (2–3.6 wt% C), eutectic (~3.6 wt% C), or hypereutectic (>3.6 wt% C).

In conventional HCWCIs, higher carbon increases carbide volume fraction but lowers impact toughness, making it difficult to balance wear resistance and toughness. Research over the past decades has therefore focused on adding one or more alloying elements to modify microstructures, aiming to improve hardness, wear resistance, impact toughness, and corrosion resistance [4]. Alloying elements influence solidification and refine austenite

*Corresponding author: josephm@mintek.co.za

dendrites, as well as the size and morphology of primary carbides. Accordingly, the initial goal of this research project was to modify primary and secondary eutectic M_7C_3 carbides into globular shapes for enhanced impact toughness. This work investigates the microstructure and mechanical properties of industrially manufactured alloys modified with vanadium (V) and niobium (Nb).

2 Methodology

2.1 Production of ball mill liners

This study used a hypereutectic high chromium white cast iron (HCWCI) conforming to ASTM A 532 Class III (see Table 1). Two alloy compositions were selected along with the reference. As part of a pilot-scale manufacturing process, prototype liners of each alloy were melted and cast at a local foundry using a 500 kg induction furnace under controlled conditions. Ferro vanadium (Fe-V) and ferro-niobium (Fe-Nb) were added as carbide formers and grain refiners. After casting, the ingots from each alloy were heat treated.

Table 1. Composition (wt. %) of abrasion resistant irons according to ASTM A532-87 (wt.%).

Material	Elements wt.%									
	C	Mn	Si	P	S	Cr	Ni	Ti	Nb	V
Reference	2.96	0.66	1.18	0.02	0.043	26.7	0.15	0.04	-	0.11
Alloy 1_V	2.62	0.65	0.74	0.015	0.021	27.8	0.06	0.03	-	1.21
Alloy 2_Nb	2.67	0.66	0.76	0.014	0.019	25.8	0.05	0.04	0.30	0.10

2.2 Mechanical testing

To evaluate the influence of alloying elements on the fracture toughness of the HCWCIs, bending strength was determined using three-point bend test samples with size of 50 mm x 75 mm x 500 mm. The samples were cut from the as cast and heat-treated ingots. The three-point bend test was done in an Instron 1175 machine along with Bluehill 2 software, according to the ASTM standard B528-16. The load was applied at a constant rate of 5 mm/min until fracture.

3 Results and discussion

Table 2 presents the three-point bending tests results on the refined alloys showed improved fracture toughness versus commercial equivalents. The results revealed marked improvements in mechanical properties and wear performance by adding carbide forming elements.

Table 2. The experimental results of the fracture strength.

Alloy	Fracture Load (N)	Stress (MPa)
Reference	184	442
Alloy 1_V	212	501
Alloy 2_Nb	243	583

4 Conclusion

Fracture toughness increased with the increased alloying content in the of the HCWCI due to the formation MC carbide and grain refinement of M_7C_3 carbides, with the addition of Nb. Over all, the additions of alloying element did improve toughness of the tested wear properties.

References

1. O. Gutnichenko, V. Bushlya, J. Zhou, J.E. Ståhl, Tool wear and machining dynamics when turning high chromium white cast iron with pcBN tools, Wear, **390–391**, Pages 253-269 (2017).
2. I. Goto, K. Fukuchi, K. Kurosawa, Effects of solidification conditions on the microstructural morphologies and strengths of hypereutectic high-chromium white cast iron castings, Mater. Sci. Eng. A, **886**, (2023).
3. R.J. Chung, X. Tang, D.Y. Li, B. Hinckley, K. Dolman, Microstructure refinement of hypereutectic high Cr cast irons using hard carbide-forming elements for improved wear resistance, Wear **301** (1–2), 695–706 (2013).
4. S. Fashu, V. Trabadelo, Development and Performance of High Chromium White Cast Irons (HCWCIs) for Wear Corrosive Environments: A Critical Review. Metals 2023, **13**, 1831 (2023).

Effect of surface preparation techniques on hybrid investment cast-additive manufactured Ti-6Al-4V components

Kim du Preez, [1], *Kalenda* Mutombo [2], *Deon* De Beer [3]

[1]Technology For Special Operations, Defence and Security, Council for Scientific and Industrial Research, 11 Jan Celliers Street, Stellenbosch, Western Cape, 7600, South Africa
[2]Titanium Centre of Competence, Manufacturing, Council for Scientific and Industrial Research, Meiring Naudé Road, Brummeria, Pretoria 0185, South Africa
[3]School for Mechanical Engineering, North-West University, Potchefstroom Campus, 11 Hoffman Street, Potchefstroom 2531, South Africa

Abstract. Hybrid manufacturing combining investment casting (IC) and additive manufacturing (AM) provides a promising route for producing large and geometrically complex Ti-6Al-4V components. However, the integrity of hybrid components is strongly influenced by the surface condition of the cast substrate prior to additive manufacturing. This study investigates the influence of different surface preparation techniques on hybrid manufactured Ti-6Al-4V specimens produced using IC and Laser Engineered Net Shaping (LENS). Wettability, microstructure and hardness across the IC–AM interface were evaluated using contact angle measurements, microscopy and microhardness profiling. The results indicate that chemically milled and polished surfaces provide improved wettability and more uniform diffusion zones compared to as-cast and sandblasted surfaces.

1 Introduction

Hybrid manufacturing that combines investment casting (IC) and additive manufacturing (AM) offers a promising route for producing large and geometrically complex titanium components. Ti-6Al-4V is widely used in aerospace and biomedical applications due to its high strength-to-weight ratio and corrosion resistance. In hybrid manufacturing, a cast substrate is combined with additively manufactured features, allowing complex structures to be produced more efficiently.

A critical factor affecting the integrity of hybrid components is the surface condition of the cast substrate prior to additive deposition. Surface preparation influences melt pool behaviour, wettability and interfacial bonding between the IC substrate and the AM material. This study evaluates the influence of different surface preparation techniques on the interfacial behaviour of hybrid manufactured Ti-6Al-4V components.

Previous work by the authors investigated the tensile properties and microstructural characteristics of additive manufactured and investment cast Ti-6Al-4V alloys, providing a foundation for the current study on hybrid manufacturing interfaces [1].

2 Experimental

Ti-6Al-4V grade 23 rods were produced by investment casting and subsequently subjected to five surface preparation techniques: as-cast, just-cut, chemically milled, polished and sandblasted. Additive deposition was performed using an Optomec LENS™ 850-R system to produce single-track and multilayer hybrid specimens.

The wettability between the molten metal and the substrate was evaluated through contact angle measurements based on Young's equation. Microstructural characterisation of the IC–AM interface was conducted using optical microscopy and scanning electron microscopy. Vickers microhardness measurements were performed across the interface to evaluate hardness variation and diffusion zone characteristics.

3 Results and discussion

Single-track deposition experiments revealed differences in melt pool behaviour depending on the surface preparation method. Chemically milled and polished surfaces produced more uniform deposition tracks with reduced spatter compared to as-cast and sandblasted surfaces.

Table 1. Single layer contact angles for different surface preparations

Surface preparation	Contact angle (°)
Chemically milled	26.97
Polished	27.38
As-cast	28.25
Cut	30.22
Sandblasted	32.05

Contact angle measurements (Table 1) indicated improved wettability for chemically milled and polished substrates. The chemically milled surface exhibited the lowest average contact angle (26.97°), followed by the polished surface (27.38°), while sandblasted surfaces showed the highest values (~32°).

Microstructural analysis revealed a distinct interface between the investment-cast substrate and the additively manufactured region. The IC region exhibited a coarse α+β Widmanstätten microstructure, while the AM region showed a finer microstructure resulting from rapid solidification during deposition.

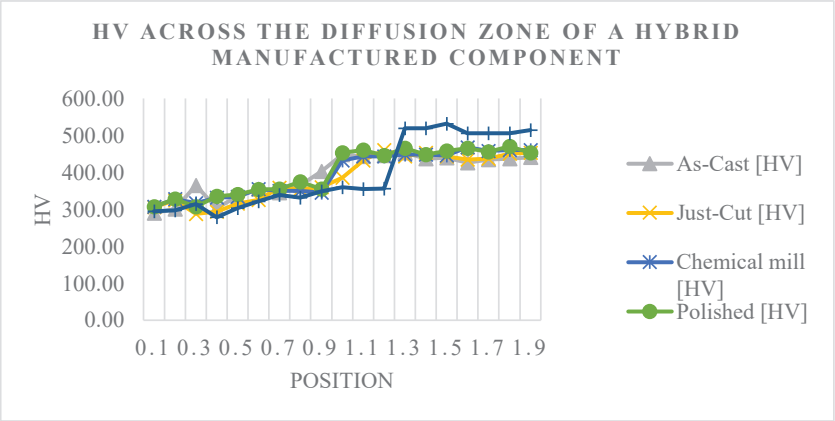


Fig. 1. Vickers Hardness (HV) profile across Hybrid Manufactured (HM) specimens with different surface preparations.

Hardness measurements given in Figure 1, demonstrated a transition from approximately 280–320 HV in the IC region to values exceeding 440 HV in the AM region. Chemically milled and polished samples exhibited smoother hardness transitions across the diffusion zone, indicating improved metallurgical bonding.

4 Conclusion

Surface preparation significantly influences the interfacial behaviour of hybrid manufactured Ti-6Al-4V components. Chemically milled and polished surfaces provided improved wettability, more uniform diffusion zones and smoother hardness transitions across the IC–AM interface. In contrast, as-cast and sandblasted surfaces exhibited less favourable bonding characteristics. These findings highlight the importance of appropriate surface preparation for improving the integrity of hybrid manufactured titanium components.

References

1. K. Beyl, K. Mutombo, and C. P. Kloppers, “Tensile properties and microstructural characterization of additive manufactured, investment cast and wrought Ti6Al4V alloy,” *IOP Conf Ser Mater Sci Eng*, vol. 655, p. 12023, 2019, https://iopscience.iop.org/article/10.1088/1757-899X/655/1/012023

Mechanical and corrosion behaviour of TiC thin films deposited on brass substrate by RF magnetron sputtering

Musibau Ogunlana[1,2*], *Wallace* Matizamhuka[2], and *Francois* Du Rand[1]

[1]Technology Transfer and Innovation unit, Vaal University of Technology, Vanderbijlpark, Private Bag X021, Vanderbijlpark, 1911, South Africa
[2]Chemical and Metallurgical Engineering Department, Andries Potgieter Avenue, Vanderbijlpark, Private Bag X021, Vanderbijlpark, 1911, South Africa

Abstract. Titanium carbide (TiC) thin film was successfully coated on brass substrates by radio frequency magnetron sputtering (RFMS) method and characterized for surface effects using mechanical and corrosion tests. The hardness tests were conducted on thin film's surface using MH-6 series digital microhardness tester for precision purposes. There were 10 indentations performed on each sample with the load application of 245 mN at 5 sec dwell time. Finite element analysis of the indentation was performed to verify the experimental tests using Ansys Mechanical solver software. The indentation impression revealed to be crack-free and no traces of delamination of thin films were observed from the surface of the substrate, which however in agreement with the finite element simulation analysis. The corrosion tests on the other hand were conducted on 1 cm^2 thin film coated samples using potentiodynamic polarization apparatus by AUTOLAB potentiostat galvanostat equipment, whereby used as the working electrode, silver chloride (AgCl) acted as the reference electrode, and graphite rod acted as the counter electrode. Thus, 0.5 M (3 wt.%) sodium chloride (NaCl) solution was used as the corrosion medium at open circuit potential (OCP) for 2 hr and at scan rate of 0.002 V/s. Corrosion behaviours were observed with high resolution scanning electron microscopy for passive layer, which prevent the surface from oxidation. This paper reports the Vickers hardness indentation and corrosion behaviours of TiC thin film coated on brass substrates using RFMS technique for surface engineering applications, which includes cutting tools and heat exchangers.

1 Introduction

Titanium carbide (TiC) transition-metal-carbide ceramic has mostly attracted the attention of researchers due to its substantial properties which includes wear, corrosion and mechanical properties for cutting and machining tools applications. TiC displays a higher melting point of 3067 ^{O}C, a chemical inertness against most acids, apart from hydrofluoric acid (HF) and

* Corresponding author: musibauo@vut.ac.za and emmbbyola@gmail.com

nitric acid (HNO_3). TiC has shown a great development recently due to the increase in manufacturing applications of this functionally graded material [1-3, 5].

Table 1. Processing parameters for TiC thin film deposition on brass substrates.

Sample	Sputtering power (W)	Sputtering time (min)	Temperature (^{O}C)	Ar gas flow rate (sccm)
SC1	200	120	80	10
SC2	250	120	100	10.5

2 Experimental setup

Figures This consists of materials used for the deposition of TiC thin films on brass substrates using RFMS techniques. The high purity (99.5%) solid TiC target manufactured by HHV Ltd Company, United Kingdom with the diameter of 75 mm and 3 mm thickness, which was coated on brass substrates with the dimensions 55 x 18 x 3 mm placed in a sputtering plasma chamber for the sputtering process. Thin films coating process were performed using RFMS equipment (HHV-TF500) with varied sputtering power between 200 W and 250 W, respectively. The deposition time was fixed at 120 minutes and as well as the sputtering temperature between 80 ^{O}C and 100 ^{O}C were observed. Thin films were deposited at a working pressure of 4.68 x 10^{-2} Torr in the non-reactive condition using Ar at varied gas flow rate between 10 and 10.5 sccm. Thus, Figure 1 presented the schematic diagram of the radio frequency magnetron sputtering (RFMS) process for TiC thin films deposited on brass substrates. Hence, microhardness tests were performed using 6/MH-3 automated/manual turret rotation digital Vickers microhardness tester according to ASTM-E384 standard [10] for mechanical properties. The indentation process is however based on the parameters such as test load of 245 mN at dwell time of 5 s with 10 indents on each sample.

3 Results and discussion

3.1 Mechanical analysis

Mechanical behaviour of the coated TiC thin film on brass materials using Vickers pyramid microhardness indenter to measure the hardness values was evaluated. There are 10 indentations performed on each sample with an applied of 245 mN at 5 seconds dwell time. Table 1 shows the process parameters used during the deposition process of thin film coating on the substrate.

3.2 Corrosion analysis

Potentiodynamic polarization analysis for corrosion behaviour was performed on the coated film surfaces of brass (base) materials in 3 wt.% NaCl solution (0.5 M) at room temperature (RT) for 2 hrs open circuit potential (OCP) process. Corrosion tests were performed with the help of the following three electrodes, which includes prepared sample of 1 cm^2 area as the working electrode, a reference electrode of silver chloride (AgCl) and graphite rod placed parallel to the working electrode serves as the counter electrode.

4 Conclusion

TiC thin films were successfully coated on brass materials using RF magnetron sputtering process at controlled processing parameters. It was revealed that sample SC2 at 250 W sputtering power was produced with higher microhardness when compared to sample SC1 at 200 W. In addition, potentiodynamic polarization measurements for corrosion behaviour of the coated thin film samples showed that, the sample SC2 has a lower corrosion rate when compared to sample SC1 with a higher corrosion rate.

References

1. H. Larhlimi, O. Abegunde, Y. Samih, A. Ghailane, M. Makha, and J. Alami, Effect of carbon content on the structural, mechanical and corrosion properties of TiC films deposited using a HiPIMS discharge. Surface & Coatings Technology. **451,** (2022)
2. O.O. Abegunde, E. Akinlabi, O.P. Oladijo, J.D. Majumdar, Surface Integrity of TiC Thin Film Produced by RF Magnetron Sputtering, in Proceedings of the 2nd International Conference on Sustainable Materials Processing and Manufacturing (SMPM 2019), Procedia Manufacturing, **35** (2019) 950–955
3. H. Larhlimi, A. Ghailane, M. Makha, J. Alami, Magnetron sputtered titanium carbide-based coatings: A review of science and technology. Vacuum. **197,** (2022)
4. S.C. Mojaki, S.B. Mishra, A.K. Mishra, Synthesis, characterization and material properties of titanium carbide nanocomposite derived from biochar. Materials Letters. **264,** (2020)
5. A. Saurabh, C.M. Meghana, P.K. Singh, P.C. Verma, Titanium-based materials: synthesis, properties, and applications. Materials Today: Proceedings, **56** (2022) 412–419

Comparative evaluation of phase constitution and microstructure in directed energy deposition additively manufactured CP-Ti, Ti-11Nb and Ti-9Fe alloys

Mavis Khathutshelo Nemavhola[1*], *Wallace R* Matizamhuka[1], *Nana K.K* Arthur[2] and *Ronald* Machaka[3]

[1]Department of Chemical and Metallurgical Engineering, Vaal University of Technology, Andries Potgieter Blvd, South Africa
[2]CSIR, Photonics Centre, Laser Enable Manufacturing, Pretoria Campus, South Africa.
[3]IdyaFactory Co, Newcastle 2300, New South Wales, Australia.

Abstract. β-type titanium alloys are widely used in advanced structural applications because of their high strength-to-weight ratio and corrosion resistance. Alloying elements such as niobium (Nb) and iron (Fe) are commonly used as β-stabilisers; however, Nb is expensive and may pose processing challenges during additive manufacturing due to its high melting temperature. In this study, CP-Ti, Ti-11Nb and Ti-9Fe alloys were fabricated using Directed Energy Deposition Additive Manufacturing (DED-AM) and analysed using XRD, OM, SEM and EBSD. The results of Ti-9Fe displayed a nearly equal dual-phase β + α/α' distribution, whereas Ti-11Nb displayed a primarily α/α' microstructure with a significant ω-phase content (22.33 vol.%). The Vickers microhardness results showed that Ti-9Fe had 428±61 HV0.5 while Ti-11Nb had 258±9 HV0.5, indicating the impact of phase composition on mechanical response. These findings indicate that Fe, with a Mo-equivalent approximately seven times higher than Nb per weight percent, more effectively suppresses the β → α/α′ transformation under the rapid solidification conditions of DED, retaining a near-equal β + α/α′ dual-phase constitution compared to the predominantly martensitic Ti-11Nb microstructure.

1 Introduction

Titanium and its alloys are widely used in aerospace, biomedical, and advanced structural applications because of their high specific strength, corrosion resistance, and attractive mechanical properties [1]. Pure titanium undergoes an allotropic transformation from the hexagonal close-packed (HCP) α phase to the body-centred cubic (BCC) β phase at approximately 882 °C [12]. The stability of these phases and the temperature at which the α → β transformation occurs provide the fundamental basis for controlling the microstructure and properties of titanium alloys [5,2]. Upon cooling from the β phase field, the equilibrium

* Corresponding author: K.Nemavhola@gmail.com

transformation in pure titanium results in the reformation of the HCP α phase. However, the transformation path and resulting microstructure can change considerably when alloying elements are introduced or when cooling occurs under non-equilibrium conditions.

The addition of alloying elements can alter the relative stability of the α and β phases and consequently modify the phase constitution of titanium alloys. Niobium (Nb) and iron (Fe) are both β-stabilising elements, although they influence the Ti phase equilibria through different metallurgical mechanisms [3,4]. Nb is an isomorphous β stabiliser that increases the stability range of the BCC β phase and lowers the β-transus temperature. Because Nb forms an extensive solid solution with titanium, increasing Nb content progressively shifts the alloy towards β-phase stability [4,5]. Consequently, Ti-Nb alloys can exhibit α + β or predominantly β microstructures depending on Nb concentration and thermal history.

In contrast, Fe is a eutectoid β stabiliser and has a substantially stronger β-stabilising effect on a weight-percent basis than Nb [4,5]. At sufficiently high Fe concentrations and under appropriate thermal conditions, the Ti-Fe system can undergo eutectoid decomposition of the β phase, with the formation of α and TiFe-containing constituents [5]. Thus, unlike Nb, Fe can influence the phase constitution not only through β-phase stabilisation but also through the possibility of intermetallic phase formation. The differences between the Ti-Nb and Ti-Fe systems are therefore important when considering their behaviour during the rapid thermal cycles associated with additive manufacturing [5,9].

The relative β-stabilising ability of alloying elements can be quantitatively compared using the molybdenum-equivalent (Mo-equivalent) concept. The Mo-equivalent provides an empirical measure of the combined β-stabilising contribution of alloying elements relative to Mo and is commonly used to estimate the degree of β-phase stability in titanium alloys [8,9]. For the alloying elements considered in the present study, Fe and Nb have Mo-equivalent coefficients of approximately 2.5 and 0.35, respectively. Thus, on a weight-percent basis, Fe contributes approximately seven times more to the Mo-equivalent than Nb. The approximate Mo-equivalent contribution of an alloy can therefore be expressed as:

$$Mo_eq = 2.5(Fe) + 0.35(Nb) + \cdots \quad \text{(Equation 1)}$$

where the elemental concentrations are expressed in wt.%.

Based on this relationship, the 11 wt.% Nb addition in Ti-11Nb corresponds to an approximate Mo-equivalent of 3.85 wt.%, whereas 9 wt.% Fe in Ti-9Fe corresponds to approximately 22.5 wt.%. These values place the two alloys in markedly different regions of β-phase stability. In general, Mo-equivalent values above approximately 10–12 wt.% are associated with increased potential for β-phase retention at room temperature, although the actual phase constitution depends strongly on composition, cooling rate, thermal history, and transformation kinetics [8,9]. Therefore, Mo-equivalent should be regarded as an indicator of β-stabilising potency rather than as a direct prediction of the final phase fractions obtained under non-equilibrium processing conditions.

The equilibrium phase relationships described above do not necessarily predict the microstructures obtained during additive manufacturing. Directed Energy Deposition (DED) involves repeated localised melting and solidification, resulting in steep thermal gradients, rapid cooling rates, repeated reheating, and complex thermal histories [1,2]. Under such non-equilibrium conditions, diffusion-controlled transformations may be suppressed, and metastable phases may be retained at room temperature.

During rapid cooling from the β phase field, the β → α transformation can be partially or completely suppressed, depending on alloy composition and cooling rate. Consequently, metastable phases such as hexagonal α′ martensite, orthorhombic α″ martensite, and the hexagonal ω phase may form in addition to the equilibrium α and β phases [5-7]. The relative formation of these phases is strongly dependent on β-phase stability. In alloys with

insufficient β stabilisation, rapid cooling can promote martensitic transformation of β to α′ or α″, whereas stronger β stabilisation can result in increased retention of metastable β at room temperature [6,7].

The ω phase is of particular interest because it can form through a diffusionless transformation within the β phase at relatively low β-stabiliser concentrations [6,7]. Its formation can significantly modify the mechanical response of β-containing titanium alloys. Therefore, understanding the competition between β retention, martensitic transformation, and ω-phase formation is essential for interpreting the microstructures produced by DED.

The resulting phase constitution has a direct influence on the mechanical properties of titanium alloys. The α′ and α″ martensitic phases, retained β phase, and ω phase exhibit different crystallographic structures and deformation characteristics, resulting in substantial differences in hardness, strength, elastic response, and ductility [6,7,10]. In particular, the formation of ω can increase hardness and strength but may reduce ductility when present at sufficiently high-volume fractions. Williams et al. [10] reported that increasing ω-phase fractions can increase yield strength while progressively affecting ductility, with pronounced embrittlement occurring at higher ω contents.

Accordingly, differences in β-phase retention and metastable phase formation between Ti-Nb and Ti-Fe alloys are expected to produce corresponding differences in mechanical response. Characterising both the phase constitution and microstructure is therefore necessary to establish the relationship between β-stabiliser chemistry, transformation behaviour, and hardness in DED-manufactured titanium alloys.

Although Ti-Nb alloys have been extensively investigated for biomedical and additive manufacturing applications, comparatively little attention has been given to Fe as an alternative, low-cost β-stabiliser for DED processing. Furthermore, direct comparisons between Nb- and Fe-containing titanium alloys fabricated under identical DED conditions remain limited. Such a comparison is particularly relevant because Nb and Fe exhibit substantially different β-stabilising potency when expressed in terms of the Mo-equivalent approach and have distinct phase-equilibrium characteristics.

In the present study, CP-Ti, Ti-11Nb, and Ti-9Fe alloys were fabricated using Directed Energy Deposition Additive Manufacturing under identical processing conditions. The resulting phase constitution and microstructural characteristics were investigated using X-ray diffraction (XRD), optical microscopy (OM), scanning electron microscopy (SEM), and electron backscatter diffraction (EBSD), while Vickers microhardness was used to assess the corresponding mechanical response. The study aims to establish how the distinct β-stabilising characteristics of Nb and Fe influence phase retention and transformation under the rapid-solidification conditions of DED.

The novelty of this work lies in the direct comparative assessment of CP-Ti, Ti-11Nb, and Ti-9Fe under identical DED processing conditions, with particular emphasis on the relationship between Mo-equivalent β-stabilising potency, phase constitution, microstructural development, and hardness. The selected compositions provide a useful comparison between an Nb-containing alloy with a relatively low Mo-equivalent (~3.85 wt.%) and an Fe-containing alloy with a substantially higher Mo-equivalent (~22.5 wt.%).

2 Methodology and results

2.1 Powder preparation and characterisation

Commercially pure titanium (CP-Ti), niobium (Nb), and iron (Fe) powders of spherical shape and more than 99 weight percent purity (wt.%) were procured from Weartech PTY TLD (South Africa) and used as the starting materials. Alloy compositions of Ti-11Nb and Ti-9Fe (wt.%) were prepared by blending elemental powders in the required proportions using a

Turbula® Schatz T2C three-dimensional mixer for 30 minutes at 40 rpm to obtain a homogeneous powder mixture. During mixing, neither binders nor process control agents were used.

2.2 Directed energy deposition fabrication

An Optomec LENS 850-R (Laser Engineered Net Shaping) DED system was used to create bulk samples of Ti-11Nb and Ti-9Fe. To reduce oxidation and contamination, all depositions were performed in a continuously purged argon environment, with oxygen concentrations kept below 100 ppm during processing. For all alloy compositions, a constant volumetric energy density of 263 J/mm³ was used, calculated using Equation 1. To ensure a consistent thermal history and enable direct microstructural comparison, all other deposition parameters were held constant across the two alloy systems (Table 1). Rectangular sample coupons measuring 12 × 12 × 15 mm were the final sample geometries.

$E = P / (v \times h \times t)$ …… (Equation 2)

Where: E = volumetric energy density, P = laser power, v = scan speed, h = hatch spacing, t = layer thickness.

Table 1. Laser parameters employed for additive manufacturing using premixed powder blends.

Laser power (W)	Scan speed (mm/s)	Powder feed rate (g/min)	Hatch spacing (mm)	Layer thickness (mm)	Energy density (J/mm³)
300	10.58	2.6	0.54	0.2	263

2.3 Microstructural characterisation

The Ti standard preparation methods were followed in the metallographic preparation of the samples. Kroll's reagent (2 vol.% HF, 6 vol.% HNO_3, balanced with distilled water) was used to etch samples for 3-8 seconds to reveal microstructural features for optical and Scanning Electron Microscopy (SEM) imaging. An Olympus BX51M optical microscope was used for optical microscopy (OM). To characterise microstructural characteristics, such as previous β-grain morphology, columnar-to-equiaxed transitions, and melt-pool boundaries, images were taken on etched surfaces. A JEOL JSM-6010Plus/LA field-emission scanning electron microscope operating in backscattered electron (BSE) and secondary electron (SE) imaging modes was used to perform high-resolution microstructural characterisation. An accelerating voltage of 20 kV was used for the analyses. While SE imaging was utilised to characterise surface topography and fine microstructural properties such as α-lath shape and widths, BSE imaging was used to evaluate phase contrast and element distribution.

Phase identification was carried out by X-ray diffraction (XRD) using a PANalytical X'Pert Pro X-ray diffractometer with Cu Kα radiation (λ = 1.54060 Å) running at 45 kV and 40 mA. With a step size of 0.03° and a dwell period of 0.88 s/step, diffraction patterns were gathered throughout a 2θ range of 20°-90°. Rietveld refinement using MAUD (Materials Analysis using Diffraction, version 2.99) software was used for quantitative phase analysis and lattice parameter determination. Fit quality was evaluated using the weighted-profile R-factor (R^{WP}) and the goodness-of-fit (χ^2) parameter, and refinements were continued until convergence was reached. The improved scale factors were used to obtain the relative volume fractions of the α, α′, ω, and β phases. Using a Zeiss Crossbeam 540 FIB-SEM for high-resolution imaging, crystallographic texture, grain morphology, and phase distribution were examined using the electron backscatter diffraction (EBSD) technique.

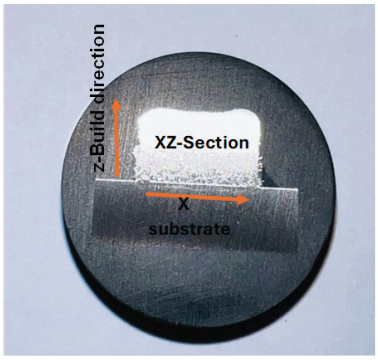


Fig. 1. Photograph showing the sectioning location and orientation of the DED-AM specimen relative to the substrate and build direction. The analysed **XZ-section** contains the build direction (Z-axis), which is normal to the substrate surface.

2.4 Mechanical testing

In compliance with ASTM E384, polished and unetched cross-sections were subjected to Vickers microhardness measurements using a Zwick Roell Vickers Microhardness tester with an applied force of 500 gf and a dwell period of 10 seconds. To capture any hardness gradients caused by compositional or microstructural banding, 20 indentations were made per sample, along the build and transverse directions at regular intervals. The mean ± standard deviation was used to report the results.

3 Results and discussion

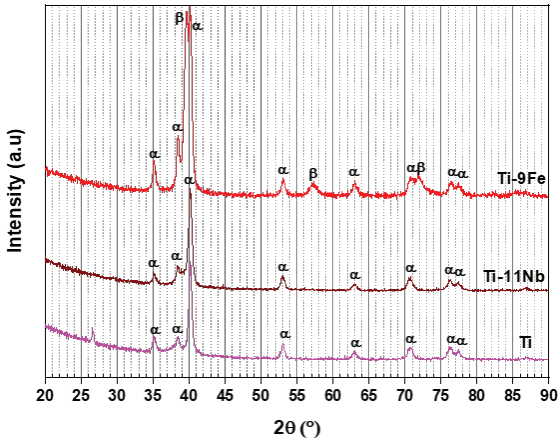


Fig. 2. XRD patterns of as-deposited Ti, Ti-11Nb and Ti-9Fe alloys fabricated via DED at an energy density of 263 J/mm³.

4 Conclusion

Ti-9Fe and Ti-11Nb alloys were successfully fabricated via DED-AM using elemental powder blending at a volumetric energy density of 263 J/mm³. XRD and Rietveld refinement confirmed that Ti-9Fe retains a near-equal β + α/α′ dual-phase constitution (Mo-eq ~22.5%), while Ti-11Nb is predominantly α/α′ martensitic with a significant athermal ω-phase content of 22.33 vol.%, consistent with its low Mo-equivalent (~3.85%).

References

1. T. DebRoy, H. Wei, J. Zuback, T. Mukherjee, J. Elmer, J. Milewski, A. Beese, A. Wilson-Heid, A. De, and W. Zhang, Additive manufacturing of metallic components – Process, structure and properties. Prog. Mater. Sci., 92, pp. 112–224 (2018).
2. S. Tshephe, S. Akinwamide, E. Olevsky, and P. Olubambi, Additive manufacturing of titanium-based alloys: A review of methods, properties, challenges, and prospects. Heliyon, 8, e09041 (2022).
3. A. Del Bosque, P. Fernández-Arias, and D. Vergara, Titanium additive manufacturing with powder bed fusion: A bibliometric perspective. Appl. Sci., 14, p. 10543 (2024)
4. X. Luo, L. Miu, and Y. Luo, Titanium alloys for biomedical applications: A review on additive manufacturing process and surface modification technology. J. Mater. Sci. Rev. (2024).
5. D. Banerjee and J.C. Williams, Perspectives on titanium science and technology. Acta Materialia, 61(3), pp. 844–879 (2013). https://doi.org/10.1016/j.actamat.2012.10.043
6. J. Ballor, T. Li, F. Prima, C.J. Boehlert and A. Devaraj, A Review of the Metastable Omega Phase in Beta Titanium Alloys: The Phase Transformation Mechanisms and Its Effect on Mechanical Properties. International Materials Reviews, 68(1), pp. 26–45 (2023). https://doi.org/10.1080/09506608.2022.2036401
7. S.L. Sing, J. An, W.Y. Yeong and F.E. Wiria, Laser and Electron-Beam Powder-Bed Additive Manufacturing of Metallic Implants: A Review on Processes, Materials and Designs. Journal of Orthopaedic Research, 34(3), pp. 369–385 (2016). https://doi.org/10.1002/jor.23075
8. S. Wei, S.J. Kim, N. Kang, Y. Zhang, Y. Zhang, R. Bhatt, I.J. Beyerlein and E.J. Lavernia, Strong and Ductile Titanium–Oxygen–Iron Alloys by Additive Manufacturing. Nature, 616, pp. 73–79 (2023). https://doi.org/10.1038/s41586-023-05952-6
9. G. Lütjering and J.C. Williams, Titanium, 2nd ed. Berlin: Springer (2007). ISBN 978-3-540-71397-5.
10. J.C. Williams, B.S. Hickman and H.L. Marcus, The effect of omega phase on the mechanical properties of titanium alloys. Metallurgical Transactions, 2, pp. 1913–1919 (1971). https://doi.org/10.1007/BF02913423
11. B. Dutta and F.H. Froes, Additive Manufacturing of Titanium Alloys: State of the Art, Challenges and Opportunities. Elsevier, Amsterdam (2016). ISBN: 978-0-12-804782-8
12. M. Geetha, A.K. Singh, R. Asokamani and A.K. Gogia, Ti based biomaterials, the ultimate choice for orthopaedic implants – A review. Progress in Materials Science, 54, pp. 397-425 (2009). https://doi.org/10.1016/j.pmatsci.2008.06.004

Hardness gradients and galvanic corrosion behaviour of hybrid laser powder bed fusion-Al10SiMg on wrought 6061 aluminium substrates

Ngeleshi Michel Kibambe[1*], *Lerato* Semetse [1], *Mpinda Bob* Mampuya[1], *Mosima Edith* Maja [1], Samson Dare Oguntuyi[1], Velile Vilane [2], and *Peter Apata* Olubambi [1]

[1]Centre for Nanoengineering and Advanced material, University of Johannesburg, South Africa
[2] Center for High Resolution Transmission Electron Microscopy, Nelson Mandela University, South Africa

Abstract. This study investigates the microstructural integrity and electrochemical stability of hybrid components fabricated by depositing AlSi10Mg via Laser Powder Bed Fusion (LPBF) onto a wrought 6061 aluminium alloy substrate. Microhardness profiling reveals a significant mechanical gradient across the assembly: the refined cellular-dendritic structure of the LPBF-AlSi10Mg achieves a high hardness of 130 Hv, while the 6061 substrate maintains a base hardness of 90Hv, and the interface exhibits an intermediate value of 80Hv. Electrochemical evaluation in a 3.5 wt.% NaCl environment demonstrates a distinct galvanic relationship where the LPBF-processed section acts as the active (anodic) component and the substrate remains relatively noble (cathodic), resulting in a fair, intermediate corrosion potential for the hybrid system. Notably, the corrosion initiates at the interface due to the potential disparity and propagates into the LPBF part, preferentially following the fish-scale melt pool boundaries. The localized dissolution of these boundaries acts as a precursor to stress-corrosion cracking (SCC) under environmental loading, highlighting that while the hybrid assembly offers robust metallurgical bonding, the active nature and morphological susceptibility of the LPBF layer remain critical constraints for the long-term structural integrity of these aluminum hybrids.

* Corresponding author : ngeleshik@gmail.com

1 Introduction

The strategic integration of Additive Manufacturing (AM) with conventional wrought alloys, known as Hybrid Additive Manufacturing (HAM), has emerged as a transformative approach for the aerospace and automotive sectors[1]. By depositing high-performance alloys like AlSi10Mg via Laser Powder Bed Fusion (LPBF) onto established structural bases such as 6061 aluminium, engineers can achieve localized reinforcement and complex geometry functionalization while maintaining cost-efficiency[2].However, the metallurgical compatibility between the rapidly solidified LPBF layer and the age-hardened substrate creates a complex gradient of mechanical and electrochemical properties that significantly influences structural durability[3].

2 Materials and methods

2.1 As received samples

The SLMed Al10SiMg alloys, the wrought 6061 substrate and the hybrid LPBF onto 6061 substates were characterise using hardness machine for mechanical properties and electron microscopy for microstructure analysis. All specimens were used in the as-received condition. Prior to characterisation, surfaces were prepared following standard metallographic procedures. The samples were sequentially ground using SiC abrasive papers (P200 to P1200) to remove surface irregularities. This was followed by polishing with diamond suspension to obtain a mirror-like finish.

2.2 Electrochemical tests

The Electrochemical measurements were conducted to evaluate the corrosion behaviour SLMed Al10SiMg alloys, the wrought 6061 substrate, the hybrid LPBF onto 6061 substates. Tests included Open Circuit Potential (OCP), Electrochemical Impedance Spectroscopy (EIS), Potentiodynamic Polarization (PDP), and Cyclic Potentiodynamic Pola rization (CPP), performed in a 3.5 wt. % NaCl electrolyte. Prior to testing, prepared samples were cold mounted to expose a defined working surface**.** A conventional three-electrode cell configuration was employed, comprising the sample as the working electrode, a platinum mesh as the counter electrode, and an Ag/AgCl electrode as the reference.

3 Results and discussion

SEM micrographs in Figure 1a reveal that crack initiation occurs within the fish-scale morphology of the LPBF AlSi10Mg, which behaves as the active anodic component. In Figure 1b, the SEM line scan confirms the 6061 substrate remains noble at the expense of the active LPBF layer, establishing a clear galvanic relationship. Figure 1c illustrates that corrosion eventually initiates at the interface due to this potential disparity. Once established, the corrosion front propagates into the LPBF section, preferentially following the melt pool boundaries. This sequence drives the stress-corrosion cracking (SCC) mechanism that dictates the hybrid's structural failure.

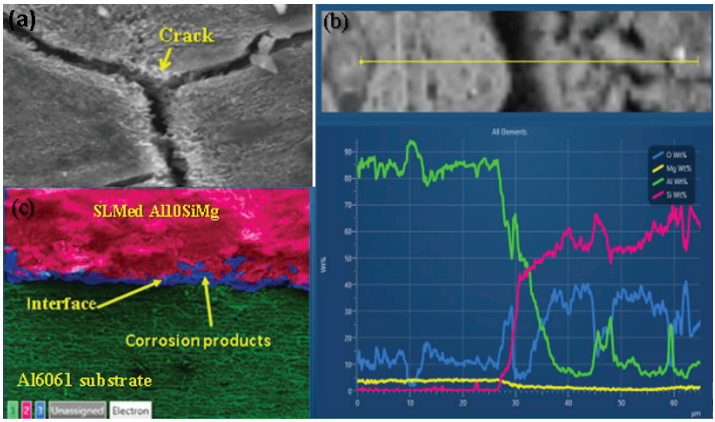


Fig. 1.: SEM micrograph of failure mechanism

References

1. [1] V.V.P. Jr, A. Fleisher, Hybrid additive manufacturing of steels and alloys. **6**, (2020)
2. [2] S.H. Emon, D.S. Shim, A Review of the Quality Control and Mechanical Properties in Hybrid Additive Manufacturing. Int. J. Precis. Eng. Manuf. **26**, 2515–2550 (2025)
3. [3] A. Jiménez, P. Bidare, H. Hassanin, F. Tarlochan, S. Dimov, K. Essa, Powder-based laser hybrid additive manufacturing of metals: a review. Int. J. Adv. Manuf. Technol. **114**, 63–96 (2021)

The effect of ruthenium precursor chemistry on the morphology of electrodeposited coatings on 304L stainless steel

Nomalungelo Maphanga[1,2*], *Ramogohlo* Diale-Boshielo[3], *Joseph* Moema[3], *Desmond* Klenam[1,2], and *Michael* Bodunrin[1,2]

[1]Department of Chemical and Metallurgical Engineering, University of the Witwatersrand, Private Bag 3, Wits, 2050, Johannesburg, 2000, South Africa
[2]Next Frontiers in Advanced Materials Lab, Faculty of Engineering and the Built Environment, University of the Witwatersrand, Private Bag 3, Wits, 2050, Johannesburg, 2000, South Africa
[3]Advanced Material Division, Mintek, Private Bag X 3015, Randburg, 2125, South Africa

Abstract: Cathodic modification of stainless steel with ruthenium is a proven strategy to enhance corrosion resistance in reducing acidic environments. This preliminary study investigates the morphological characteristics of a highly porous ruthenium micro-coating synthesised using a $RuCl_3$ and HCl bath. Compared to conventional dense nano-films deposited from nitrosyl precursors, the porous architecture provides a massively larger electrochemically active surface area. Initial electrochemical testing in 1 M sulphuric acid indicated that the porous coating exhibits significantly enhanced corrosion resistance compared to dense nano-films reported in literature. This work highlights the critical role of precursor chemistry in optimising coating architecture.

1 Introduction

Cathodic modification with noble metals, particularly ruthenium, has demonstrated to significantly improve the corrosion resistance of stainless steels in reducing acidic media [1]. The traditional approach involves bulk alloying or the application of dense surface coatings to facilitate the hydrogen evolution reaction (HER), which anodically polarises the substrate into its passive region. Recent studies have focused on pulse electrodeposition of dense ruthenium nano-films using nitrosyl precursors to minimise noble metal usage while maintaining protection.

However, the electrocrystallisation process is highly sensitive to bath chemistry. The effect of alternative precursor chemistry, specifically chloride-based baths, on coating morphology has not been fully explored in this context. This study investigates the morphological characteristics of ruthenium coatings deposited from a ruthenium(III) chloride ($RuCl_3$) and hydrochloric acid (HCl) bath and compares them with those reported in literature.

*Corresponding author: Nomalu0803@gmail.com

2 Experimental methods

Ruthenium coatings were electrodeposited onto 304L stainless steel substrates. Prior to deposition, the 30 × 25 × 6 mm substrates were mechanically polished using 600-grit paper to obtain a uniform surface finish. The samples were then rinsed with deionised water, and degreased in warm methanol to remove organic contaminants. To control the effective deposition area and minimise edge effects, the edges and back of the samples were masked, leaving an exposed central area of approximately 1 cm^2. This ensured a consistent cathode-to-anode area ratio and promoted uniform coating thickness. Surface activation was carried out by immersing the masked samples in a 10% sulphuric acid solution containing trace amounts of ferric chloride at 80 °C for approximately 60 s. This was done to remove native oxide layers. The samples were then rinsed with deionised water and immediately transferred into the plating bath to prevent surface re-passivation.

The plating bath was prepared by dissolving 11.2 g oxalic acid dihydrate, and 1.5 g ammonium chloride in 130mL distilled water while slowly stirring. This was followed by the addition of 14 mL of 32% hydrochloric acid and 3 g ruthenium (III) chloride. The solution was diluted to a final volume of 200 mL with distilled water and stirred and heated to 100°C for 24 hours, then aged for 72 hours prior electrodeposition to allow for stabilisation of ruthenium complexes.

Pulse electrodeposition was conducted using a three-electrode configuration consisting of the stainless steel substrate as the working electrode, a graphite counter electrode, and an Ag/AgCl reference electrode. Deposition was carried out under galvanostatic control using a pulse-on time of 3 s and pulse-off time of 45 s. The applied current density was 0.4 A/cm^2, and the total deposition time was approximately 1800 s.

Surface morphology was characterised using Scanning Electron Microscopy (SEM), and elemental composition was analysed via Energy Dispersive X-ray Spectroscopy (EDS). Preliminary electrochemical corrosion performance was evaluated in 1 M H_2SO4.

3 Results and discussion

SEM analysis revealed a stark contrast in coating architecture compared to literature. While traditional nitrosyl baths produce dense, flat nano-films prone to mud-cracking and spallation under stress [2], the $RuCl_3$/HCl bath produced a highly porous, interconnected micro-matrix that is shown in figure 1. This structure is consistent with dynamic hydrogen bubble templating (DHBT), where the high acidity promotes simultaneous hydrogen gas evolution during electrodeposition, acting as a dynamic template [3].

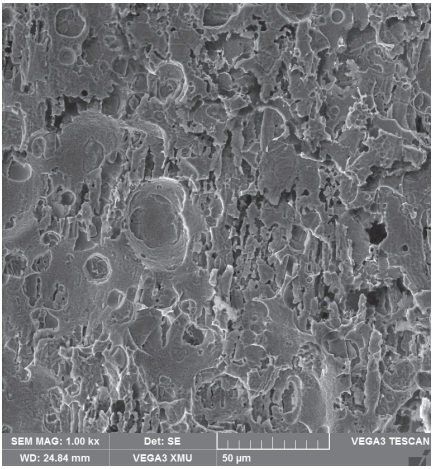


Fig. 1. SEM micrograph at 1000x magnification showing the highly porous, interconnected micro-matrix of the ruthenium coating deposited from the $RuCl_3$/HCl bath.

EDS composition analysis confirmed the presence of ruthenium on the surface, alongside iron and chromium signals from the substrate. The porous architecture provides a massively larger electrochemically active surface area compared to dense films.

Preliminary electrochemical testing in 1 M H_2SO4 indicated that the porous coating exhibited significantly enhanced corrosion resistance compared to dense films reported in literature. Orders of magnitude improvement in polarization resistance was observed.

4 Conclusion

The $RuCl_3$/HCl plating bath altered the electrocrystallisation process, synthesising a highly porous ruthenium micro-coating via DHBT. This deviation resulted in a coating morphology that is fundamentally different from conventional dense nano-films. The porous structure shows promising preliminary corrosion resistance, offering a highly effective strategy for protecting stainless steel in aggressive acidic environments.

References

[1] J. H. Potgieter, A. M. Heyns, and W. Skinner, The corrosion of PGM-containing duplex stainless steels in reducing acids. J. South. Afr. Inst. Min. Metall. **92**, 125 (1992)

[2] F. Moyo, J. W. van der Merwe, and D. Wamwangi, Corrosion performance of pulse plated ruthenium: Dependence on pulse-off time. Surf. Coat. Technol. **307**, 971 (2016)

[3] H. Jiang, N. Cong, H. Jiang, M. Tian, Z. Xie, H. Fang, Dynamic hydrogen bubble template electrodeposition of Ru on amorphous Co support for electrochemical hydrogen evolution, Int. J. Hydrogen Energy. **48**, 21599 (2023)

Antibacterial and biocompatibility properties of additively manufactured titanium–Cu alloy implants

Nthabiseng Cholo[1*], *Thywill Cephas* Dzogbewu[1], *Olga* de Smidt[2], *Rose* Kadye[3], and *Earl* Prinsloo[3]

[1]Department of Mechanical and Mechatronics Engineering, Central University of Technology, Free State, South Africa
[2]Centre for Applied Food Sustainability and Biotechnology (CAFSaB), Central University of Technology, Free State, South Africa
[3]Biotechnology Innovation Centre (RUBIC), Rhodes University, Makhanda 6140, South Africa

Abstract. Direct metal laser sintering (DMLS) is an Additive manufacturing technique able to produce commercially pure titanium (cpTi) and Ti6Al4V biomedical implants. To compensate for the lack of antibacterial properties of Ti and its alloys, Cu is often added to the biomaterial. The concentration of Cu should be monitored to prevent cell toxicity and to maintain the biocompatibility of the Ti-based implant. In the present study, the antibacterial efficacy of DMLS in situ alloys of Ti64-*x*Cu and Ti-*x*Cu (x = 0, 3, 6 wt.%) was evaluated against *Staphylococcus aureus* and *Escherichia coli*. The antibacterial effect of Cu was not established. HeLa cells were used to observe the biocompatibility of the alloys in vitro. Fluorescence images from live/dead staining showed that Cu did not compromise the biocompatibility of cpTi and Ti64; thus, with modifications, Ti64-Cu may be an alternative biomaterial.

1 Introduction

Additive manufacturing techniques such as direct metal laser sintering (DMLS) are preferred for the manufacturing of complex implant parts and offer patient-specific customisation [1]. DMLS applies digital models to manufacture parts layer-by-layer in a time- and cost-efficient manner [2]. The material selected to manufacture the implant plays a crucial role in its performance and life expectancy [1]. Titanium (Ti) and its alloys, particularly Ti6Al4V, are widely used in the manufacturing of orthopaedic and dental implants to repair and regenerate diseased or damaged bone tissue because of their excellent properties of biocompatibility, mechanical strength, wear and corrosion resistance [3]. However, Ti and Ti64 do not possess antibacterial properties, and infection remains one of the most serious complications in medical implants [4]. Copper is an essential trace element in the human body and is alloyed into Ti implants for the gradual release of ions for antibacterial purposes [5]. DMLS is able to fabricate biomedical implant parts from a novel composition of Ti-based/Cu powders.

* Corresponding author: nhlapo86@gmail.com

Nonetheless, Cu at high concentration may be cytotoxic and hinder the implant/tissue integration required for biocompatibility [6]. The present study aimed to observe the antibacterial properties and the cell integration of DMLS-manufactured Ti64-*x*Cu and Ti-*x*Cu (x = 3, 6 wt.%) in vitro.

2 Methodology

The powders used were commercially pure Ti (cpTi), pre-alloyed Ti6Al4V ELI (Ti64) and Cu. The DMLS technique was used to manufacture Ti64-*x*Cu (x = 3, 6 wt.%, denoted as Ti64-3Cu and Ti64-6Cu) and cpTi-*x*Cu (x = 3, 6 wt.%, denoted as Ti-3Cu and Ti-6Cu). Sample discs (ø10 × 2 mm) were manufactured with the parameters listed in Table 1. The Ti64 and cpTi discs were used as the control. The samples were used in their as-built condition.

Table 1. DMLS processing parameters for titanium/Cu compositions.

Metal powder	Laser power (W)	Scanning speed (m/s)	Hatch distance (µm)	Powder layer thickness (µm)
Ti64	170	1.25	80	30
Ti64-3Cu	170	0.2	80	50
Ti64-6Cu	150	0.1	80	50
cpTi	170	0.6	80	50
Ti-3Cu	170	0.6	80	50
Ti-6Cu	150	0.4	80	50

The ion release rate of Cu ions was determined by immersing the test specimens in 2.5 mL of NaCl at 37 °C for 24 hrs. The concentration of the released ions was examined using inductively coupled plasma mass spectrometry (ICP-MS).

For analysis of the antibacterial properties, *Staphylococcus aureus* (*S. aureus*) ATCC 25923 and *Escherichia coli* (*E. coli*) ATCC 25922 were used and were enumerated using the disc diffusion assay and broth dilution method after 24 hrs of incubation at 37 °C. The media used were sterile tryptone soy agar (TSA) and tryptone soy broth (TBS).

An immortalised HeLa cell line was used to study the biocompatibility of test samples. The cells were cultured in DMEM High Glucose supplemented with 10 % (v/v) heat-inactivated fetal calf serum and 1% 50/50 penicillin/streptomycin (100 U/ml) antibiotic solution. The harvested cells were then seeded at a seeding density of 1×10^5 cells/well in 24-well plates containing Ti64-*x*Cu and Ti-*x*Cu (x = 0, 3, 6 wt.%) specimens. The well plates were incubated in a 5% CO_2 incubator at 37 °C for 24 hrs. For imaging and viability, ReadyProbes™ Cell Viability Imaging Kit (Blue/Green) by Invitrogen™ was used. Images of the fluorescence-stained cells were captured on the Invitrogen™ EVOS™ FL Auto 2 Imaging System.

3 Results and discussion

The ion release results showed a minor difference in the Cu ion concentrations released from the Ti64 samples. For the cpTi specimens, Ti-6Cu showed a considerably greater release of Cu ions than the Ti-3Cu and the control cpTi sample.

The disc diffusion assay illustrated that the Cu-bearing samples were similar to the Cu-free reference sample and did not exhibit zones of inhibition. Likewise, the broth dilution method did not display inhibition of *S. aureus* and *E. coli* by the samples of Cu-alloyed Ti64 and cpTi. The lack of antibacterial properties displayed may be expected since the Cu ion release rate was very low.

The fluorescence of the Cu-alloyed samples and the Ti64 and cpTi control samples was similar, which may imply that the addition of Cu did not adversely affect the interaction of these materials with HeLa cells. On the other hand, the observed lack of cell toxicity may be attributed to the minimal release of Cu ions. The study of Vilardell et al. [7] illustrated that the alloying of Ti6Al4V with 3 at.% Cu during DMLS did not show cell cytotoxicity, but inhibited cell proliferation, and cell mineralisation appeared to be higher for samples with 3 at.% Cu content.

4 Conclusion

This study involved the observation of antibacterial capacity against *S. aureus* and *E. coli* of DMLS-fabricated Ti-*x*Cu and Ti64-*x*Cu (x = 3, 6 wt.%) samples and their biocompatibility with HeLa cells. The Cu content neither promoted the antibacterial property nor did it adversely affect the natural biocompatibility of Ti64 and cpTi. This was associated with the low Cu ion release concentration. Further modifications to Ti64-Cu and Ti-Cu alloys to improve the antimicrobial property while monitoring their cellular interactions are required for clinical functionalisation of these alloys.

Reference

1. V. Goyal, G. Verma, U.S. Dixit, In-vitro study of Ti6Al4V alloy fabricated by laser-based additive manufacturing for orthopedic implant applications, Proc. Inst. Mech. Eng. Part E J. Process Mech. Eng. **240**, 4096-4110 (2026). https://doi.org/10.1177/09544089241289723
2. P. Jamshidi, M. Aristizabal, W. Kong, V. Villapun, S.C. Cox, L.M. Grover, M.M. Attallah, Selective laser melting of Ti-6Al-4V: The impact of post-processing on the tensile, fatigue and biological properties for medical implant applications. Materials (Basel). **13**, 2813 (2020). https://doi.org/10.3390/ma13122813
3. C. Zhang, H. Zhang, W. Peng, A. Feng, J. Hu, W. Wang, H. Yuan, Q. Li, Q. Fu, 3D-printed Ti6Al4V thoracic fusion cage: Biomechanical behavior and strengthening mechanism. J. Mater. Res. Technol. **31**, 2685–2695 (2024). https://doi.org/10.1016/j.jmrt.2024.07.021
4. I. Milošev, D. Sacer, B. Kapun, C. Xie, A. Krash, and P. Rodič, Effect of copper addition to titanium alloy prepared by additive manufacturing for biomedical applications. ECS Meet. Abstr. **MA2025-02**, 1156–1156 (2025). https://doi.org/10.1149/MA2025-02151156mtgabs
5. L. Luo, Q. Zhong, Z.Q. Chen, X.H. Wu, S.M. Li, Z.Z. Xue, Y.J. Lu, K. Luo, W. Zhao, 3D-printed copper-containing tailored titanium alloys with corrosion resistance, biocompatibility, and anti-inflammatory properties for enhanced guided bone regeneration. Front. Bioeng. Biotechnol. **13**, 1647678 (2025). https://doi.org/10.3389/fbioe.2025.1647678

6. E. Zheleva, M.P. Nikolova, Perspective on copper-enhanced titanium implants: Functions, fabrication, and safety. Mater. Des. **265**, 115861 (2026). https://doi.org/10.1016/j.matdes.2026.115861
7. A. M. Vilardell, P. Krakhmalev, I. Yadroitsava, I. Yadroitsev, N. Garcia-giralt, In vitro characterization of in situ alloyed Ti6Al4V (ELI)-3 at .%Cu obtained by laser powder bed fusion. Materials (Basel). **14**, 7260 (2021). https://doi.org/10.3390/ma14237260.

05

ABSTRACTS

Computational & Data-driven Modelling

Prediction of stable structures in Ti-V-Mn AB_2-type alloys using a cluster expansion approach

Vukosi Chauke[1*], *David* Tshwane[2,3], and *Hasani* Chauke[1]

[1]Materials Modelling Centre, University of Limpopo, South Africa
[2]National Institute for Theoretical and Computational Sciences (NITheCS), South Africa.
[3]Department of Mechanical and Mechatronics Engineering, Central University of Technology, South Africa.

Abstract. The structural stability of Ti–V–Mn AB_2-type alloys was investigated using a cluster expansion approach to explore the configurational space of the alloy system. A set of ordered configurations was generated and used to construct an effective cluster expansion model capable of predicting formation energies for numerous atomic arrangements. The resulting ground-state diagram reveals several thermodynamically stable ordered structures across the composition range between TiV_2 and $TiMn_2$. Twelve stable configurations were identified along the convex hull, providing insight into the ordering behaviour and phase stability of Ti–V–Mn AB_2 alloys.

1 Introduction

Ti–V–Mn AB_2-type alloys are widely studied for their potential applications in hydrogen storage due to their favourable thermodynamic and structural properties [1, 2]. The stability and ordering behaviour of these alloys are strongly influenced by the distribution of transition metal atoms within the crystal lattice. Understanding the configurational stability of such systems is essential for predicting new ordered phases and guiding experimental alloy design. Cluster expansion (CE) methods provide an efficient framework for exploring the configurational space of multicomponent alloys by expressing the total energy as a function of atomic configurations on a fixed lattice [3, 4]. This approach enables the prediction of ground-state structures and phase stability across a wide range of compositions without the need to evaluate every possible configuration directly. In this study, the cluster expansion method is employed to investigate the configurational stability of Ti–V–Mn AB_2-type alloys and to predict stable ordered structures across the composition range.

2 Methodology and results

* Corresponding author: vukosichauke@gmail.com

2.1 Methodology

The structural stability of Ti–V–Mn AB_2-type alloys was investigated using the cluster expansion method implemented within the MedeA computational environment. Starting from the hexagonal C14 Laves phase structure, a set of symmetrically distinct configurations was generated by varying the distribution of V and Mn atoms on the B sublattice while keeping Ti atoms fixed on the A sites [2].

A cluster expansion Hamiltonian was constructed by fitting effective cluster interactions to a selected set of reference structures [3, 4]. The resulting model was used to predict the formation energies of numerous configurations within the configurational space of the alloy system. The quality of the cluster expansion was assessed using cross-validation analysis to ensure reliable energy predictions [3].

The predicted formation energies were used to construct the ground-state diagram and identify thermodynamically stable ordered structures across the composition range.

2.2 Results

The cluster expansion model was applied to explore the configurational space of the Ti–V–Mn AB_2 system. The predicted formation energies were used to construct the binary ground-state diagram, which reveals several stable ordered structures along the composition range between TiV_2 and $TiMn_2$ [2].

The convex hull highlights twelve thermodynamically stable configurations, indicating strong ordering tendencies within the alloy system. These stable arrangements minimize the formation energy and provide insight into the configurational stability and phase behaviour of Ti–V–Mn AB_2 alloys.

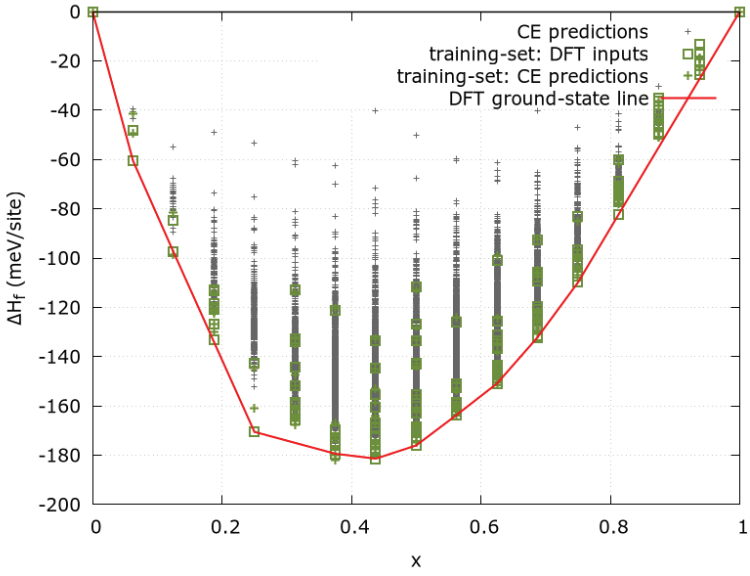


Fig. 1. The binary ground-state diagram, showing the formation energies and the convex hull of the predicted stable structures.

3 Conclusion

The cluster expansion study of Ti–V–Mn AB_2-type alloys successfully predicted thermodynamically stable ordered structures across the compositional range. The ground-state diagram highlights twelve stable configurations, demonstrating significant ordering tendencies in the system. These results provide critical insight into the configurational stability and phase behaviour of Ti–V–Mn alloys, offering guidance for experimental alloy design and potential hydrogen storage applications. The study also demonstrates the effectiveness of cluster expansion in predicting stable phases efficiently, without the need for exhaustive first-principles calculations.

This research was carried out at the University of Limpopo's Materials Modelling Centre (MMC). We acknowledge Centre for High-Performance Computing (CHPC) based in Cape Town for their computing resources.
This research received NRF funding. All work was supported by the authors' institution.
All data reported in this work is available upon request to the corresponding author.

References

1. J.M. Sanchez, Cluster expansion and the configurational theory of alloys, Phys. Rev. B **81**, 224202 (2010).
2. J.M. Sanchez, Cluster expansions and the configurational energy of alloys, Phys. Rev. B **48**, 14013 (1993).
3. A. van de Walle and G. Ceder, Automating first-principles phase diagram calculations, J. Phase Equilibria **23**, 348–359 (2002).
4. X. Zhang and M.H.F. Sluiter, Cluster expansions for thermodynamics and kinetics of multicomponent alloys, J. Phase Equilib. Diffus. **37**, 44–52 (2016).

Comparative performance analysis of OpenCV and ArrayFire for computer vision systems

Patrick Malatjie[*], and *Teboho* Sekopa[2]

[1]Council for Scientific and Industrial Research, Optronic and Sensor Systems, Pretoria, South Africa
[2]Council for Scientific and Industrial Research, Optronic and Sensor Systems, Pretoria, South Africa

Abstract. In this paper, we evaluate two Python computer vision libraries for the construction of computer vision pipelines. The execution speeds of the computer vision function, and neural network containers are compared across different image sizes, bit depths, CPUs (Central Processing Unit), and GPUs (Graphical Processing Unit). These estimates are further used to predict execution speeds of image processing pipelines. Finally, a recommendation for the usage of each library with regards to available hardware, image sizes and image pipelines are given.

1 Introduction

In a recent 2022 survey of parallel computing for computer vision systems, the lack of comparative evaluations for computer vision libraries was evident [2]. This paper addresses this shortcoming by evaluating three popular Python computer vision libraries.

1.1 Performance evaluation

The two Python libraries, OpenCV and ArrayFire , are evaluated with respect to image-processing functions provided by the libraries. The functions are evaluated on CPU and GPU levels across three different computer architectures. It is important to note that the evaluation excludes image loading.

1.2 Machine vision pipeline evaluation

Using the three libraries, three different machine vision algorithms are implemented. The expected performances are estimated, measured, and compared. The algorithms evaluated are a BayerFilter Demosaicing, the Harris corner detector, depth estim ation through block matching and a machine learned feature detector.

2 Results

* Corresponding author: author@email.org

The results of all the experiments are normalised to represent the number of operations required by the implementation. The comparison of the results from the various libraries demonstrates the performance needs in proportion to image size.

3 Conclusion

The evaluation of the different Python computer vision libraries provides the machine vision designer a reference on what execution speeds can be expected for specific algorithms. It further assists the designer to select the appropriate library to implement a specific machine vision system and can support in the specification of computer hardware for such systems. The evaluation further provide insight on the appropriate use of CPUs and GPUs.

References

1. R.M. Haralick, Performance characterization in computer vision, in Proceedings of the British Machine Vision Conference (BMVC), pp. 1–8 (1992)Jaiswal, D., & Kumar, P. (2022). A survey on parallel computing for traditional computer vision. Concurrency and Computation: Practice and Experience, 34(4), e6638.
2. D. Jaiswal, P. Kumar, A survey on parallel computing for traditional computer vision. Concurrency Comput. Pract. Exp. 34, e6638 (2022), V., Patel, K., & Melonakos, J. (2012). ArrayFire: a GPU acceleration platform. In Modeling and simulation for defense systems and applications VII (Vol. 8403, pp. 49-56). SPIE.
3. D. Jaiswal, P. Kumar, A survey on parallel computing for traditional computer vision. Concurrency Comput. Pract. Exp. 34, e6638 (2022)Bradski, G., & Kaehler, A. (2000). OpenCV. Dr. Dobb's journal of software tools, 3(2).
4. J. Malcolm, P. Yalamanchili, C. McClanahan, V. Venugopalakrishnan, K. Patel, J. Melonakos, ArrayFire: A GPU acceleration platform, in Modeling and Simulation for Defense Systems and Applications VII, Proc. SPIE 8403, 49–56 (2012)
5. M. Goli, VisionCpp: A SYCL-based computer vision framework, in Proceedings of the 4th International Workshop on OpenCL, pp. 1–4 (2016)
6. G. Bradski, A. Kaehler, OpenCV. Dr. Dobb's J. Softw. Tools 3(2) (2000)

The structural, magnetic, and elastic properties of the $Mn_{50}Al_{50-x}Mg_x$ alloys: a DFT study

Thabang Mokwena[1*], *Ramogohlo* Diale-Boshielo[1,2*], *Phuti* Ngoepe[1*] and *Hasani* Chauke[1]

[1]Materials Modeling Centre, University of Limpopo, South Africa
[2]Advanced Materials Division, Mintek, South Africa.

Abstract. The $L1_0$ $Mn_{50}Al_{50}$ is a promising hard magnetic material due to its good magnetic characteristics, high magnetic moment, and high Curie temperature. However, this alloy has drawbacks such as metastable and brittleness. The structural and magnetic characteristics of $L1_0$ $Mn_{50}Al_{50-x}Mg_x$ structures were investigated using density functional theory. Their thermodynamic stability was evaluated from the heats of formation. The introduction of Mg in MnAl compromises the thermodynamic stability. Additionally, the addition of Mg to MnAl improves the Curie temperature.

1 Introduction

MnAl exhibits strong magnetocrystalline anisotropy, good corrosion resistance, low density, and is composed of abundant elements, making it attractive for permanent magnet applications [1]. The τ-phase forms at 50-60 at. % Mn, and was found to be brittle [2]. However, this phase tends to decompose into nonmagnetic phases above 973 K [3]. Ternary alloying was identified as a potential solution to these setbacks. This work utilizes the supercell method within density functional theory in order to gain more clarity of its ferromagnetic behaviour through the addition of Mg as a ternary alloying element.

2 Methodology and result

Figures and tables, as originals of good quality and well contrasted, are to be in their final form, ready for reproduction, pasted in the appropriate place in the text. Try to ensure that the size of the text in your figures is approximately the same size as the main text (10 point). Try to ensure that lines are no thinner than 0.25 point.

* Corresponding author: 201819981@myturf.ul.ac.za

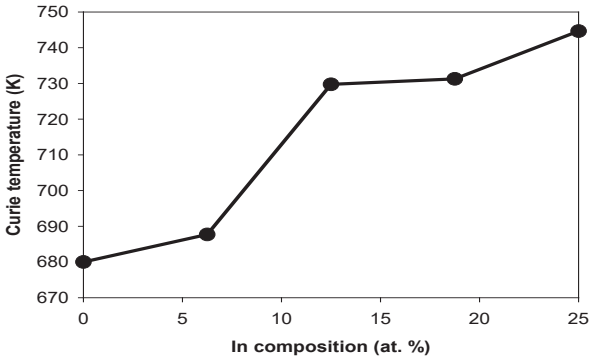


Fig. 1: The Curie temperature against atomic percent Mg for $Mn_{50}Al_{50-x}Mg_x$ alloys ($0 \leq x \leq 25$).

3 Conclusion

DFT was used to examine the structural and magnetic properties of $Mn_{50}Al_{50-x}Mg_x$ alloys. The findings showed that the introduction of Mg compromises thermodynamic stability. As the concentration of Mg increases, so does the magnetic moment, indicating that Mg improves the magnetic strength. The addition of Mg to MnAl was found to increase the Curie temperature with increasing Mg content. The findings show that Mg enhances the operating temperature of MnAl.

References

1. H. Kono, On the ferromagnetic phase in manganese–aluminium system. J. Phys. Soc. Jpn. 13, 1444–1451 (1958).
2. T. Mokwena, R. G. Diale, P. E. Ngoepe, and H. R. Chauke, The phase stability of the binary Mn–Al alloys using cluster expansion and first-principles calculations. SAIP Conf. Proc., 135–140 (2024).
3. T. Mix, F. Bittner, K. H. Müller, L. Schultz, and T. G. Woodcock, Alloying with a few atomic percent of Ga makes MnAl thermodynamically stable. Acta Mater. 128, 160–165 (2017).
4. M. Ben G. Kresse and J. Furthmüller, Efficient iterative schemes for ab initio total-energy calculations using a plane-wave basis set. Phys. Rev. B 54, 11169–11186 (1996).

Unsupervised learning for biomedical data classification

Kelvin Mpofu[1*], *Sipho* Chauke[1], and *Patience* Mthunzi-Kufa[2]

[1]Biophotonics, Council of Scientific and Industrial Research (CSIR), Pretoria 0081, South Africa.
[2]School of Science, College of Science, Engineering and Technology, University of South Africa 0083, South Africa.

Abstract. This work presents an exploration of classical unsupervised learning algorithms for clustering high-dimensional biomedical data derived from single-cell RNA sequencing (scRNA-seq) experiments. We evaluated multiple techniques, including K-Means, DBSCAN, Gaussian Mixture Models (GMM), Spectral Clustering, Agglomerative Clustering, and Affinity Propagation, to classify immune cell populations within peripheral blood mononuclear cells (PBMCs). Performance was assessed using Silhouette Scores and Adjusted Rand Index (ARI), revealing that Spectral Clustering achieved the highest ARI (0.65) and Silhouette Score (0.25), followed closely by GMM and Agglomerative Clustering (ARI ≈ 0.60; Silhouette ≈ 0.21). K-Means also performed well in label alignment (ARI = 0.62), despite lower cohesion (Silhouette = 0.085). In contrast, DBSCAN failed to detect valid clusters under the tested parameters (ARI = 0.0), and Affinity Propagation produced over-fragmented results (Silhouette = 0.02).

1 Introduction

In translational medicine, cell-based therapy is the new focal point for developing rapid therapeutic platforms for early disease detection and diagnosis. Cell-based therapy can provide pathophysiological information that can create opportunities for personalized medicine. In recent years, PBMCs have been researched for their cell-based therapy and as potential disease biomarkers. In clinical and precision medicine, PBMCs play a pivotal role in identifying immune responses and their biomarkers. In mammals, PBMCs consist of T lymphocytes, B lymphocytes, natural killer cells, monocytes, dendritic cells, and several induced cytokines (i.e., Interlukin-1α, interlukin-1β, and TNF). These contain a larger proportion of resting, naïve immune cells; however, the other portion is made up of other cell types and memory/pre-activated cells. These proportions vary in individuals, mainly due to their physiological state. PBMCs are typically isolated from whole blood samples, using gradient centrifugation (Figure 1). This makes them easily accessible sources of immune cells. Contrary to that, since PMBCs are peripheral mononuclear cells, these cells represent immune cells found in blood only, which are phenotypically different from other immune cells found in non-vascularized tissues such as the lymph nodes and the intestines.

* Corresponding author: kmpofu@csir.co.za

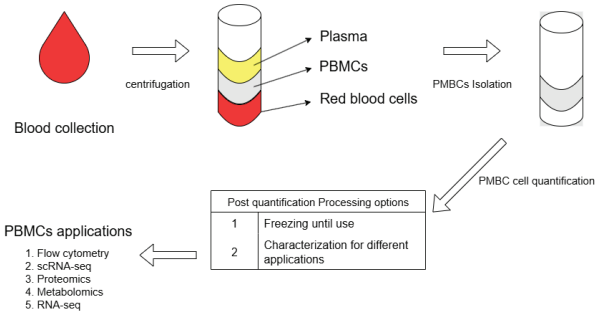


Fig. 1. A summary of the isolation of PBMCs from blood, specifically highlighting the applications of their use as isolated cells.

Unsupervised learning methods are indispensable in biomedical data analysis, especially for single-cell RNA sequencing (scRNA-seq), where data typically lack explicit labeling. Classical clustering techniques such as K-Means and DBSCAN have been extensively used due to their simplicity and interpretability. Nevertheless, these algorithms face substantial limitations, including difficulty in effectively handling high-dimensional, sparse, and noisy data. Addressing these challenges is crucial to improving computational efficiency and the reliability of classification outcomes in biomedical contexts. Recent advancements have increasingly incorporated machine learning into biosensing and biomedical diagnostics, illustrating substantial improvements in accuracy and efficiency. Cui et al. [1] highlighted machine learning's role in enhancing biosensor performance, particularly in managing complex biological data. Previous studies predominantly applied supervised learning, necessitating labeled datasets, which are often scarce or expensive to obtain. Unsupervised learning thus presents an attractive alternative, but classical methods like K-Means and DBSCAN may inadequately capture complex cellular heterogeneity, prompting exploration and evaluation of a broader range of unsupervised clustering algorithms.

2 Methodology

Our methodology involved rigorous evaluation of classical unsupervised clustering techniques, including K-Means, DBSCAN, Gaussian Mixture Models (GMM), Spectral Clustering, Agglomerative Clustering, and Affinity Propagation, utilizing publicly accessible scRNA-seq datasets from PBMC samples. Data preprocessing comprised standard normalization steps, dimensionality reduction using principal component analysis (PCA), and filtering of low-quality or sparse data points. Algorithm performance was evaluated against multiple criteria, including Silhouette Score, Davies-Bouldin Index, and computational efficiency measured by runtime. This comprehensive evaluation facilitated direct comparison, highlighting the strengths and limitations of each algorithm concerning real-world biomedical classification tasks.

3 Results

Preliminary results demonstrated significant differences in clustering performance across the tested algorithms. Specifically, the K-Means algorithm was sensitive to the choice of cluster numbers (k-values), significantly affecting its performance metrics. The Silhouette Score

indicated optimal clustering at intermediate values of k, revealing an essential balance between computational efficiency and accurate classification of cell populations. These findings are visually summarized in Figure 2.

4 Conclusion

The comprehensive evaluation presented in this study underscores the substantial potential and challenges associated with applying classical unsupervised learning techniques to scRNA-seq data analysis. By benchmarking multiple clustering algorithms systematically, we established foundational insights necessary for selecting and optimizing algorithms tailored to biomedical diagnostics. Future research will focus on hybrid and advanced clustering methods, combining classical and modern machine learning techniques to enhance robustness and accuracy in practical biosensing applications.

References

1. F. Cui, Y. Yue, Y. Zhang, Z. Zhang, H.S. Zhou, Advancing Biosensors with Machine Learning. ACS Sens. **5**, 3346-3364 (2020).

Automated micrograph feature extraction and machine learning surrogate benchmarking for bead geometry prediction in LMD repair of Al-Si alloys

Laone Ronaldo Pilane[1], *Annelize* Botes[1], *Kumeshan* Reddy[2], and *Dreyer* Bernard[1]
[1]Department of Mechanical Engineering, Nelson Mandela University, Gqeberha, South Africa
[2]Department of Electrical Engineering, Nelson Mandela University, Gqeberha, South Africa
Corresponding author: s232273200@mandela.ac.za

Abstract. This study presents an automated micrograph feature extraction and machine learning benchmarking framework for bead geometry prediction in LMD repair of Al-Si alloys. A three-stage YOLOv8–SAM pipeline enables rapid calibrated extraction of clad bead geometry, eliminating manual measurement. Six regression models were benchmarked using 5-fold cross-validation, overfitting diagnostics, and statistical significance testing. Gaussian Process Regression achieved the highest predictive accuracy (Height $R^2 = 0.96$; Aspect Ratio $R^2 = 0.87$; Dilution $R^2 = 0.90$) and demonstrated robust generalisation on a small dataset. The framework delivers a transferable, data-efficient pipeline for LMD process development in the EV repair and remanufacturing sector.

Keywords: Laser Metal Deposition; Machine Learning; Automated Feature Extraction; Gaussian Process Regression; YOLOv8

1 Introduction

Laser Metal Deposition (LMD) is gaining significant traction for the repair and remanufacturing of metallic components in high-value sectors. For the automotive and electric vehicle (EV) industries, LMD presents a technically viable alternative to full component replacement, particularly for aluminium-silicon (Al-Si) structural components susceptible to surface wear, corrosion-induced damage, and impact loading [1]. Repair quality is governed by three bead geometry descriptors measurable from polished cross-sections: clad height (H), controlling dimensional restoration accuracy; aspect ratio (AR = H/W), determining track overlap and surface finish; and dilution (D), quantifying base-metal mixing and bond quality [2]. Machine learning surrogate models have been proposed to construct data-driven mappings between process parameters and bead geometry responses [3, 4]. However, two persistent bottlenecks constrain their reliability: the scarcity of experimental data in LMD research, and the operator-dependent, inconsistent nature of manual micrograph measurements that scale poorly with increasing sample size. Furthermore, model selection in the LMD literature is frequently performed without systematic benchmarking, resulting in inconsistent performance reporting and limited

guidance for practitioners [3]. This study addresses both bottlenecks by presenting a transferable automated data collection pipeline and a statistically grounded model selection framework for small-dataset LMD bead geometry prediction.

2 Methodology

An 89-sample experimental dataset was generated by depositing Al12Si powder onto Al-Si alloy substrates using a Trumpf TruLaser Robot 5020 LMD cell (TruDisk 4001, $\lambda = 1030$ nm). Three process parameters were varied using Discrete Latin Hypercube Sampling: laser power P (1400–2800 W), scan speed v (0.4–1.8 m/min), and powder feed rate $\dot{m}$ (1.5–10.0 g/min). Bead geometry was extracted from optical cross-sectional micrographs via a three-stage automated pipeline: (1) image preprocessing and per-image scale calibration; (2) YOLOv8 [5] transfer learning-based coarse bead detection; and (3) Segment Anything Model (SAM) [6] instance segmentation for calibrated extraction of bead height, width, aspect ratio, and dilution — replacing manual measurement entirely.

Input features comprised the three process parameters augmented with a physics-informed Linear Energy Density term (LED = P/v, J/mm). Six regression models were benchmarked against bead height, aspect ratio, and dilution targets: Gaussian Process Regression (GPR), Support Vector Regression (SVR), Random Forest (RF), Artificial Neural Network (ANN), and two stacking ensembles (RF+ANN and GPR+ANN). Models were evaluated using 5-fold out-of-fold predictions with R^2, MAE, and MAPE metrics, a CV–OOF gap overfitting diagnostic, Wilcoxon signed-rank significance testing ($\alpha = 0.05$), and SHAP feature importance analysis [7].

3 Results and discussion

The YOLOv8–SAM pipeline achieved reliable bead localisation across all 89 samples (mAP@0.5:0.95 > 0.90), with binary masks consistent with manual segmentation on a held-out verification subset, substantially reducing data collection time compared to manual measurement. Table 1 presents the performance of the two leading models. GPR achieved the highest predictive accuracy for bead height ($R^2 = 0.955$, MAE = 64.6 µm) and aspect ratio ($R^2 = 0.874$, MAE = 0.038), and remained statistically equivalent to ANN for dilution ($R^2 = 0.902$, $p = 0.83$, Wilcoxon). Critically, GPR maintained a low CV–OOF gap across all targets (max: 0.034), confirming robust generalisation. In contrast, SVR and RF exceeded the 0.05 overfitting threshold (gaps of 0.209 and 0.198 respectively), indicating significant generalisation risk at N = 89. SHAP analysis identified heat input (P/v) as the dominant predictor for bead height and dilution, while powder feed rate $\dot{m}$ primarily governed aspect ratio — findings consistent with underlying thermophysical deposition mechanisms.

Table 1. Performance of top-performing models — 5-fold OOF (N = 89)

Model	H R^2	H MAE (µm)	AR R^2	AR MAE	D R^2	D MAE (%)	Max CV–OOF Gap
GPR	0.955	64.6	0.874	0.038	0.902	3.44	0.034
ANN	0.940	78.3	0.804	0.042	0.895	3.39	0.075

4 Conclusions

This study presented a transferable automated micrograph feature extraction pipeline and a statistically rigorous ML benchmarking framework for LMD bead geometry prediction of the Al-Si alloy. The YOLOv8 + SAM pipeline eliminated manual measurement, substantially reducing data collection time. GPR was identified as the statistically superior surrogate for small-dataset LMD regression, outperforming SVR, RF, ANN, and both stacking ensembles for bead height and aspect ratio, while remaining equivalent to ANN for dilution. CV–OOF diagnostics revealed significant overfitting risk in RF and SVR, highlighting the inadequacy of cross-validation R^2 alone as a model selection criterion in small experimental datasets.

References

[1] A. Dass, A. Moridi, State of the art in directed energy deposition: From additive manufacturing to materials design. *Coatings* **9**, 418 (2019). https://doi.org/10.3390/COATINGS9070418

[2] D. Chernyavsky, D.Y. Kononenko, J.H. Han, H.J. Kim, J. van den Brink, K. Kosiba, Machine learning for additive manufacturing: Predicting materials characteristics and their uncertainty. *Mater. Des.* **227**, 111699 (2023). https://doi.org/10.1016/j.matdes.2023.111699

[3] L.R. Pilane, A. Botes, K. Reddy, D. Bernard, Machine learning based process optimisation in laser metal deposition: A systematic review. *Sci. Afr.* **31**, e03169 (2026). https://doi.org/10.1016/j.sciaf.2025.e03169

[4] R. Dai, H. Guo, J. Liu, M. Alfano, J. Yuan, Z. Zhao, Predictive modeling and optimization of layer-cladded Ti-Al-Nb-Zr high-entropy alloys using machine learning. *Coatings* **14**, 1319 (2024). https://doi.org/10.3390/coatings14101319

[5] G. Jocher, A. Chaurasia, J. Qiu, Ultralytics YOLOv8 (2023). https://doi.org/10.5281/zenodo.8347926

[6] A. Kirillov et al., Segment anything, in Proc. IEEE/CVF Int. Conf. Comput. Vis. (ICCV), (2023), pp. 3992–4003. https://doi.org/10.1109/ICCV51070.2023.00371

[7] S.M. Lundberg, S.-I. Lee, A unified approach to interpreting model predictions, in Adv. Neural Inf. Process. Syst. (NeurIPS) **30**, 4765–4774 (2017)

Electronic charge-transfer dynamics of Zn-O co-adsorption on MO_2 (M= Mn, Ti, V) (110) surfaces in Zn-air batteries

Percy Ngobeni[1*], *Phuti* Ngoepe[2] and *Khomotso* Maenetja[1]

[1,2]Materials Modelling Centre, University of Limpopo, South Africa

Abstract. The study examines how zinc interacts with MnO_2, TiO_2, and VO_2 (110) surfaces to assess their suitability for Zn-air batteries. Calculations show that Zn-O binds strongly to MnO_2 because of favorable Zn-O coordination, while it binds weakly or detaches from TiO_2 and VO_2. Charge-transfer analysis confirms that MnO_2 accepts significantly more electron density from Zn, whereas TiO_2 and VO_2 show minimal interaction. Overall, MnO_2 provides the most stable and electronically compatible surface for Zn, suggesting that Mn-rich surfaces could enhance Zn-air battery performance.

1 Introduction

Zinc-air batteries are emerging as one of the most promising energy storage technologies due to their high energy density, safety, and cost-effectiveness [1]. However, their performance is critically dependent on how zinc atoms adsorb and interact with catalyst surfaces. Transition metal dioxides (MO_2), particularly on the (110) surface, provide a structurally stable and catalytically active platform for oxygen reduction and evolution reactions [2], yet the mechanisms of Zn adsorption and charge transfer remain poorly understood. Investigating these processes at the atomic scale is essential for identifying stable adsorption sites, understanding redox behavior, and optimizing electronic properties that govern battery efficiency.

By applying density functional theory (DFT), this work aims to unravel the adsorption energetics and charge-transfer pathways of Zn-O on MnO_2, TiO_2, VO_2, and related oxides, thereby guiding the rational design of cathode materials. The insights gained will not only advance fundamental surface science but also accelerate the development of rechargeable Zn-air batteries with improved cycle life, efficiency, and commercial viability.

* Corresponding author: khehlapercy0@gmail.com

2 Materials and methodology

Density Functional Theory (DFT) calculations will be employed to investigate Zn adsorption and charge-transfer mechanisms on MO_2 (110) surfaces (MnO_2, TiO_2, VO_2). The simulations will be performed using plane-wave pseudopotential codes such as VASP [3] and CASTEP [4], which allow accurate treatment of periodic systems. The Generalized Gradient Approximation (GGA) with the Perdew-Burke-Ernzerhof (PBE) functional will be applied to describe exchange-correlation effects, ensuring reliable predictions of adsorption energies and electronic properties [5]. Calculations were carried out with the VASP code. We used a cut-off energy of 500 eV and a Monkhorst-Pack Brillouin zone sampling scheme with a 6x6x1 k-point mesh for the (110) surfaces. Surface models will be constructed by cleaving bulk structures along the (110) plane, followed by slab geometry optimization to minimize residual stresses. A vacuum slab of 17Å is introduced to avoid spurious interactions between periodic images. Zn atoms will be adsorbed on various surface sites.

3 Results and discussion

We begin by examining the various sites on the MO_2 surface that are favorable for Zn adsorption. We tested different adsorption sites, and the results are shown in Table 1 below. On the MO_2 (110) surface, Zn can adsorb at three characteristic oxygen-defined positions, namely the O_M_Zn_hollow, O_b_Zn_adjacent, Zn_hol_O+above, and Zn_O_opposite sites, which differ in their coordination environments and degrees of surface bonding.

Table 1: Zn-O co-adsorption energies for the MO_2 (110) surface at different orientations.

Adsorption sites	MnO_2	TiO_2	VO_2
O_M_Zn_hollow	-7.880	-1.580	-1.320
O_b_Zn_adjacent	-8.120	-1.750	3.870
Zn_hol_O+above	-6.860	-1.570	-1.590
Zn_O_opposite	-8.210	12.10	-1.460

MnO_2 exhibits the strongest and most consistent Zn-O adsorption (-8.210 eV), indicating highly favorable binding and effective stabilization of reaction intermediates. TiO_2 shows moderate adsorption strength (-1.570 eV) but strong site dependence, with some configurations being highly unfavorable (+12.10 eV). VO_2 displays the greatest variability, with adsorption energies ranging from favorable (-1.320 eV) to unfavorable (+3.870 eV), reflecting strong geometry dependence. Overall, MnO_2 is the most promising material for stable Zn-O intermediate adsorption, outperforming both TiO_2 and VO_2.

4 Conclusion

The study shows that Zn-O interacts very differently with MnO_2, TiO_2, and VO_2 surfaces. MnO_2 provides the strongest and most stable Zn adsorption, supported by

high binding energies, shorter Zn-O bonds, and significant electron transfer from Zn to surface oxygen. In contrast, Zn-O binds weakly to TiO_2 and VO_2, with large Zn surface separations and minimal charge exchange, leading to Zn detachment. These results highlight MnO_2's superior surface chemistry for Zn-O co-adsorption and suggest that Mn-rich or engineered oxide surfaces could enhance interfacial stability and performance in Zn-air batteries.

We gratefully acknowledge the financial support provided by the National Research Foundation (NRF). The computational work presented in this study was carried out using the resources of the Materials Modelling Centre (MMC) at the University of Limpopo and the Centre for High-Performance Computing (CHPC) in Cape Town, South Africa.

References

1. T. Zhou, N. Zhang, C. Wu, and Y. Xie. Energy Environ. Sci. **13**, 1132-1153 (2020).
2. K.P. Maenetja and P.E. Ngoepe. ACS omega. **7**, 25991-25998 (2022).
3. G. Kresse, J. Furthmuller. Phys. Rev. B. **54**, 11169 (1996).
4. M.C. Payne, M.P. Teter, D.C. Allan, T.A. Arias and A.J. Joannopoulos. Rev. Mod. Phys. **64**, 1045 (1992).
5. J.P. Perdew, K. Burke and M. Ernzerhof, Phys. Rev. B. **77**,3865-3866 (1996).

First-principles study of the effect of Ni and Pt addition on the ductility of brittle FCC iridium: structural, mechanical, and electronic properties

Thabo Nhlenyama[1*, 2], *Prince* Mkwae[1], *Bongani* Ngobe[2] and *Maje* Phasha[2]

[1]Department of Physics, University of Zululand, KwaDlangezwa, South Africa
[2]Advanced Materials Division, MINTEK, Randburg, South Africa

Abstract. Iridium-based alloys have potential for high-temperature applications due to their high melting point and oxidation resistance. However, their brittle character limits formability, particularly during the fabrication of structural components. Density functional theory calculations using CASTEP were employed to investigate the structural, mechanical and electronic properties of Ir-Pt and Ir-Ni binary alloys, $Ir_{32-x}M_x$ (x = 0 - 6, M = Pt or Ni. The results show that alloying with Pt and Ni maintains mechanical stability while slightly reducing lattice stiffness. An increase in the B/G ratio above 1.75 indicates improved ductility, suggesting potential for manufacturing structural components at low temperature.

1 Introduction

Iridium-based alloys have emerged as important candidates for high-temperature structural applications, particularly in aerospace propulsion systems where materials must endure extreme environments exceeding 1300 °C [1-2]. The platinum group metals, specifically iridium, offer superior melting points and oxidation resistance [3]. Despite these advantages, the fundamental mechanical and electronic properties of Ir–Pt and Ir–Ni binary systems remain incompletely characterised, necessitating a systematic investigation into their structural stability [1].

The controlled addition of platinum (Pt) or nickel (Ni) into the iridium (Ir) lattice provides a flexible strategy for driving ductility. The approach helps to overcome the inherent brittleness of pure iridium, which commonly restricts its broader industrial structural use. Alloying presents a viable route for improving the mechanical performance and applicability of iridium-based materials. This study systematically evaluates the elastic constants, Cauchy pressure, and electronic characteristics of Ir–Pt and Ir–Ni intermetallics to establish a rigorous framework for alloy design.

2 Methodology and results

* Corresponding authors: 201973498@stu.unizulu.ac.za and bonganing@mintek.co.za

The results reported in this work were obtained using density functional theory (DFT) as implemented in the Cambridge Serial Total Energy Package (CASTEP) [4]. The interaction between valence electrons and ionic cores was described using the projector augmented plane-wave method. For accurate comparison, the exchange–correlation effects were treated using the Perdew–Burke–Ernzerhof (PBE) functional within the generalised gradient approximation (GGA).

A plane-wave energy cut-off of 600 eV and a 7 × 7 × 7 Monkhorst–Pack k-point grid were employed, which were found to be sufficient to achieve convergence of the total energy. The calculations were performed on iridium-based binary alloy supercells with the composition $Ir_{32-x}M_x$, where x=0 - 6 and M=Pt or Ni, representing substitutional alloying of iridium with platinum and nickel atoms.

3 Results and discussion

Table 1 presents the elastic constants and the derived mechanical properties of the binary Ir-based alloy compositions investigated in this study using the FCC 2x2x2 supercell. The elastic constants C_{11}, C_{12}, and C_{44} indicate that all the investigated alloys satisfy the Born-Huang mechanical stability criteria.

The addition of Pt and Ni slightly reduces the elastic constants compared to Ir_{32}, suggesting a small decrease in lattice stiffness. The bulk modulus (B) and shear modulus (G) indicate a small decrease in stiffness compared to pure Ir_{32}. The C_p values for Ir-Pt (-6.85 to 13.16) and for Ir-Ni (-4.82 to 18.77), suggesting improved mechanical stability of the alloys. The B/G ratio increases (especially $Ir_{29}Pt_3$ and $Ir_{29}Ni_3$), implying a potential improvement in ductility compared to Ir_{32}.

Table 1. Elastic and mechanical properties of Ir supercell crystal in GPa.

	C_{11}	C_{12}	C_{44}	C_P	B	G	B/G
Ir_{32}	604.11	248.20	261.44	-13.24	366.84	224.09	1.64
$Ir_{31}Pt_1$	593.69	246.91	253.76	-6.85	362.50	217.84	1.66
$Ir_{30}Pt_2$	582.82	245.68	250.50	-4.82	358.06	213.73	1.67
$Ir_{29}Pt_3$	571.36	246.63	233.72	13.16	354.88	201.98	1.76
$Ir_{31}Ni_1$	582.82	245.68	250.50	-4.82	358.06	213.73	1.67
$Ir_{30}Ni_2$	572.97	248.23	251.75	-3.52	356.48	211.16	1.69
$Ir_{29}Ni_3$	557.77	249.20	230.43	18.77	352.05	196.21	1.79

4 Conclusion

All investigated alloys satisfy the mechanical stability criteria for cubic crystals. The addition of Pt and Ni slightly reduces lattice stiffness, hence, it improves the Cauchy pressure and Pugh's ratio. The alloys with B/G values above the 1.75 threshold possess the potential to form structural products at low temperatures for use at extreme high-temperature environments.

References

1. Yu, W., et al., **Rare Metals**, 43, 1243–1256 (2024). https://doi.org/10.1007/s12598-025-03543-0
2. Jiang, X.P., et al., **Rare Metals**, 44, 9036–9052 (2025). https://doi.org/10.1007/s12598-025-03543-0

3. C.P. Liang et al., Materials Chemistry and Physics, **133**, 140-143 (2012). https://doi.org/10.1016/j.matchemphys.2011.12.080.
4. Segall, M.D., et al., Journal of Physics, **14**, 2717-2744 (2002). https://doi.org/10.1088/0953-8984/14/11/301

Atomistic simulation synthesis of Li_xTiO_2 nanoporous as an anode electrode material for energy storage in lithium-ion batteries

Blessing Rikhotso[1*], *Malili* Matshaba[2], *Dean* Sayle[3] and *Phuti* Ngoepe[1]

[1]Materials Modelling Centre, University of Limpopo, Private Bag x1106, Sovenga 0727, South Africa
[2] Department of Physics, University of Limpopo, Private Bag X1106, Sovenga 0727, South Africa.
[3]University of Kent, School of Physical Sciences, Canterbury, Kent, CT2 7NZ, United Kingdom

Abstract. Nanoporous-architectured Li_xTiO_2 is a promising anode material for lithium-ion rechargeable batteries due to its high lithium storage capacity and thermal stability during electrochemical cycling. Molecular dynamics simulations were used to investigate thermal behaviour of nanoporous $Li_{0.03}TiO_2$, $Li_{0.04}TiO_2$, and $Li_{0.07}TiO_2$ using amorphization–recrystallisation approach. The nanoporous structures were generated from amorphous precursors, cooled to 0 K, and heated to 1500 K. Structural stability was analysed using configuration energies, Ti–O RDF, and simulated XRD patterns. The results reveal polymorphic domains of rutile-brookite phases, increased lithium diffusivity with temperature, demonstrating favourable structural stability and ion transport properties for high-performance lithium-ion battery applications.

1 Introduction

Nano-architecture Titanium dioxides (TiO_2) materials are commonly utilised as electrodes in primary alkaline batteries, secondary lithium batteries and recently lithium air batteries, which are attractive candidates as anode electrode materials for mobile electronic devices and automotive applications [1]. Amongst the large variety of TiO_2 nanostructures, nanoporous TiO_2 may appear amorphous or crystalline depending on the temperature conditions may experience during charging and discharging, characterized by intergrowths of various proportions of rutile and brookite polymorphs [2], microtwinning defects [3], point defects [4], such as Ti^{4+} vacancies and Ti^{3+} substitutional. Moreover, these combined defects are very crucial and influence properties of this compound as electrical conductivity [5] the discharge of dry cell [6] ion-exchange [7] ion-absorption [8], and gas reactivity [9], all of which are central to its utilization within battery systems. The structural characterization of nanoporous TiO_2 by diffraction techniques along with its analysis is quite a challenge to be obtained experimentally hence an attempt at the atomistic level was required to test the influence of temperature dependence to prevent thermal runaway.

* Corresponding author: nkateko.rikhotso@ul.ac.za

2 Materials and methodology

A 'cube' of TiO_2 particles comprising 15 972 atoms (5324 titanium and 10648 oxygen atoms), was cut from the parent (bulk) material. The coordinates of all the ions comprising this cube were then changed to increase the lattice parameter by 36.3% (tension-induced amorphization) and MD simulation was applied at 2000 K to amorphise the TiO_2; MD conditions have been reported previously [1,2] Lithium ions were then inserted at random positions in the amorphous TiO_2; coordinates were chosen to ensure that Li ions were not positioned on top of other atoms in the simulation cell. To facilitate charge neutrality, an equivalent number of Ti^{i4+} species were reduced to Ti^{3+}. Again, the Ti^{3+} ions were peaked randomly. Constant pressure MD simulation performed at 2000 K with 50 kbar pressure was imposed upon the system. The MD was continued until the system was no longer changing energetically then a nanoporous system was intercalated with Li^+ atoms to produce structures shown in Fig. 1. The final step including relieving the pressure and cooling the system to 0 K, which acts as a (pseudo) energy minimization. Systems with 150,200 and 350 lithiums ions (Li_xTiO_2) were considered.

3 Results and discussion

Fig. 1 shows an amorphized porous nanostructure with 0.03, 0.04 and 0.07 lithium concentrations respectively. Observing from the structure lower concentration give less clustering of lithium atoms and higher concentrations more clustering of lithium atoms. Lithium distribution tends to move away from the pores then moves right within the structures. The Ti and O atoms are disorderly arranged making the lithium atoms to move freely.

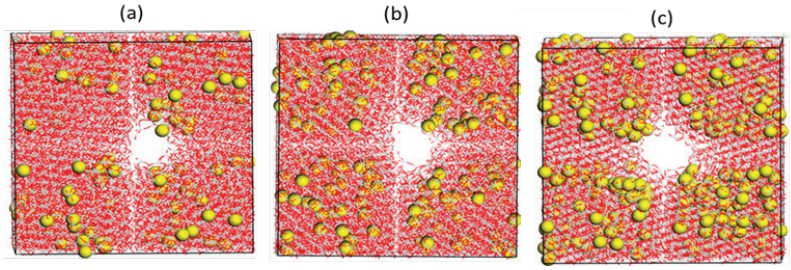


Fig. 1. Amorphous Nanoporous Structures of TiO_2 with (a) 0.03, (b) 0.04 and (c) 0.07 lithium-ion concentrations at 2000 K.

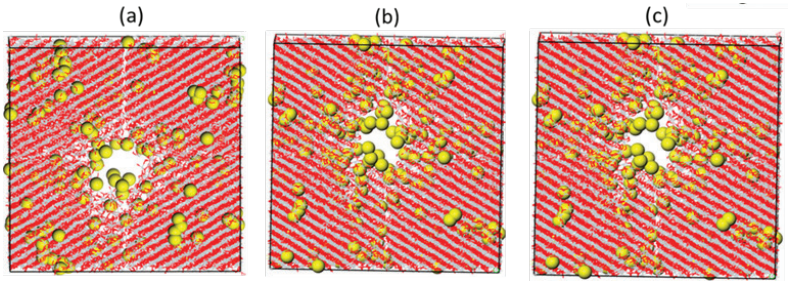


Fig. 2. Recrystallised nanoporous structures of TiO2 with (a) 0.03, (b) 0.04 and (c) 0.07 lithium-ion concentrations at 2000 K.

4 Conclusion

TiO_2 nanoporous was successfully lithiated, recrystallised and cooled to 0 K by molecular dynamics simulation. The Li_xTiO_2 nanoporous was characterised by the RDFs, XRDs and microstructures which all revealed the presence of rutile, anatase and brookite crystal structures which act as a good material for LIB. Li_xTiO_2 nanoporous structure is an excellent anode electrode material candidate confirmed by its ability to accommodate more Li^+ contents and withstand high temperature.

All calculations were performed at the Materials Modelling Centre (MMC), University of Limpopo and the Centre for High Performance Computing (CHPC) in Cape Town. This work is supported by the CSIR-MerSETA and the South African Department of Science Technology and Innovation, Energy Storage Research, Development and Innovation Consortium.

References

1. B. Rikhotso, P. Ngoepe, *MATEC Web Conf.* **392**, 04012 (2025). https://doi.org/10.1051/matecconf/202539204012
2. B. N. Rikhotso, M. G. Matshaba, D. C. Sayle, P. E. Ngoepe, *Opt. Mater.* **102**, 109831 (2020). https://doi.org/10.1016/j.optmat.2020.109831sciencedirect
3. M. G. Matshaba, D. C. Sayle, T. X. T. Sayle, P. E. Ngoepe, *J. Phys. Chem. C* **120**, 14001–14008 (2016). https://doi.org/10.1021/acs.jpcc.6b04770kar.kent.ac
4. Z. Y. Weng, H. Guo, X. M. Liu, S. L. Wu, K. W. K. Yeung, P. K. Chu, *RSC Adv.* **3**, 24758–24775 (2013). https://doi.org/10.1039/C3RA44031A.
5. M. Baumann, J. F. Peters, M. Weil, A. Grunwald, *Energy Technol.* **5**, 1071–1083 (2017).
6. B. Battke, T. S. Schmidt, D. Grosspietsch, V. H. Hoffmann, , *Renew. Sustain. Energy Rev.* **25**, 240–250 (2013). https://doi.org/10.1016/j.rser.2013.04.023
7. W. Wang, Q. Sa, J. Chen, Y. Wang, H. Jung, Y. Yin, *ACS Appl. Mater. Interfaces* **5**, 6478–6483 (2013). https://doi.org/10.1021/am402350nlink.springer
8. J. A. Yuwono, P. Burr, C. Galvin, *ACS Appl. Mater. Interfaces* **13**, 1791–1806 (2021). https://doi.org/10.1021/acsami.0c17097pubmed.ncbi.nlm.nih
9. J. F. Peters, M. Weil, *Resources* **5**, 46 (2016). https://doi.org/10.3390/resources5040046

First principles study of electronic and thermoelectric properties of hexagonal tungsten disulphide (WS_2)

Moshibudi Ramoshaba[1*], *Malesela* Makgoba[1], and *Thuto* Mosuang[1]

[1]University of Limpopo, Department of Physics, Private Bag X1106, Sovenga 0727, South Africa

Abstract. Using density functional theory (DFT), this study investigates the electronic and thermoelectric properties of hexagonal tungsten disulphide (WS_2), with lattice constants of $a = b = 6.27$ bohr (*3.32* Å) and $c = 22.81$ bohr (*12.07* Å). Electronic properties suggest hexagonal WS_2 as an intrinsic semiconductor with an indirect band gap of 1.4 eV, which is consistent with the reported band gap of bulk 2H-WS_2. Thermoelectric calculations suggest that hexagonal WS_2 exhibits promising thermoelectric performance under both p- and n-type conditions. In particular, the high Seebeck coefficient, a figure of merit (ZT) greater than 1, and a conversion efficiency exceeding 5% for both carrier types demonstrate its potential for ambipolar thermoelectric applications. These properties further suggest hexagonal WS_2 as a promising material for solar-energy conversion, thermoelectric power generation, and waste-heat recovery, particularly in applications where both electron and hole transport can be exploited.

1 Introduction

Tungsten disulfide (WS_2) is a prominent member of the transition metal dichalcogenides (TMD) family. WS_2 can exist in various forms, including thin films, nanorods, and inorganic nanotubes. This material has attracted considerable interest due to its remarkable properties, including high carrier mobility, tunable band gap, and strong light-matter interactions. WS_2 appears promising as a thermoelectric material due to its high Seebeck coefficient (S) and low thermal conductivity (κ). The sharp density of states near the Fermi level of tungsten atoms contributes to its high Seebeck coefficient. Its thermal stability makes it suitable for both low and high-temperature thermoelectric applications [1].

2 Computational details

A full-potential all-electron density funtional theory (DFT) package based on the first principles calculations linearized augmented plane waves was used in this study. An open-source code which is called Exciting code [2] was used. Generalized gradient approximation (GGA) proposed by Perdew, Burke, and Ernzerhof (PBE_sol) revised for solids was used for

* Corresponding author: moshibudi.ramoshaba@ul.ac.za

the exchange and correlation functional energy. Through the calculating, the k-points 4 x 4 x 4 was used for electronic and elastic properties. 40 x 30 x 30 k-points were used for thermoelectric properties.

3 Results

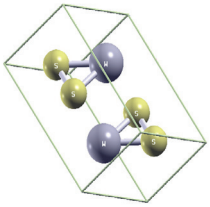


Fig. 1. Typical hexagonal crystal lattices of WS_2

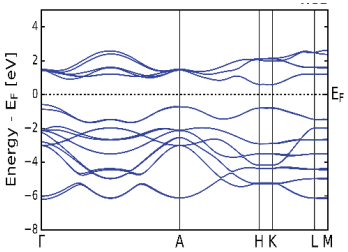


Fig. 2. Calculated electronic band structures of hexagonal WS_2

Table 1. Maximum and average values of figure of merit (ZT_{max} and ZT_{avg}) and efficiency (η) hexagonal WS_2 corresponding to the temperature.

	-0.136 eV (p-type)	**0.136 eV (n-type)**
ZTmax	3.28 (300 K)	3.28 (300 K)
ZT_{avg}	1.87 (300-1000 K)	2.09 (300-1000 K)
η (%)	24.27	25.83

4 Conclusion

In summary, density functional theory (DFT) was utilized successfully to comprehensively investigate electronic and thermoelectric properties of hexagonal WS_2. The structural optimization produced lattice parameters of $a = b = 6.27$ Bohr (3.32 Å) and c = *22.81* Bohr (*12.07* Å). The electronic structure results identify hexagonal WS_2 as an intrinsic semiconductor with an indirect band gap of approximately 1.4 eV, consistent with the reported indirect band-gap character of bulk 2H-WS_2. Furthermore, the thermoelectric results demonstrate that hexagonal WS_2 exhibits promising thermoelectric performance for both p- and n-type conductivities at 300 K. The material showed a Seebeck coefficient exceeding 1000 μV/K, a thermoelectric figure of merit (*ZT*) greater than 1, and a conversion efficiency above 5% for both carrier types. These findings suggest that hexagonal WS_2 is a promising thermoelectric material with potential applications in thermoelectric energy conversion technologies.

References

1. T. Murugadass, V. Vijay, J. Archana, M. Navaneethan, S. Harish, and K.D. Nisha, Lattice strain induced enhancement in the thermoelectric performance of WS2− yTey nanostructures. Applied Surface Science **714**, 164361 (2025).

2. A. Gulans, S. Kontur, C. Meisenbichler, D. Nabok, P. Pavone, S. Rigamonti, Sagmeister, U. Werner and C. Draxl, Exciting: a full-potential all-electron package implementing density-functional theory and many-body perturbation theory. Journal of Physics: Condensed Matter, **26**(36), 363202 (2012).

06

ABSTRACTS

Additive Manufacturing Post Processing and Qualification

Microstructure-hardness response to localised laser tempering of LMD 17-4 PH stainless steel

Michael Femi Olabisi[1*], *Annelize* Botes[1], and *Bernard* Dreyer[1]

[1]Mechanical Engineering Department, Nelson Mandela University, Port Elizabeth, South Africa

Abstract. Laser metal deposition (LMD) of 17-4 PH stainless steel produces a thermally softened heat-affected zone (HAZ) that compromises repaired components. Hardness recovery across the clad-HAZ-substrate region was characterised following sub-critical localised laser-based heat treatment (LBHT) at peak surface temperatures of 480-498 °C. Vickers microhardness increased in every zone, most in the HAZ: from 328.3 ± 20.6 HV to 411.0 ± 12.5 HV (+82.7 HV, +25.2%), within the reported H900 range, and hardness scatter decreased throughout. SEM/EDS resolved no change in the bulk Cu content of the HAZ (2.75-3.46 wt% before, 2.73-3.33 wt% after), so the hardness increase must reflect solute redistribution below the resolution of EDS. Nb-rich particles (up to 4.25 wt% Nb), present in both conditions, are interpreted as markers of solidification micro-segregation rather than as the primary strengthening agent. The behaviour is consistent with ε-Cu precipitation, the established mechanism in this ageing window, but this is inferred rather than observed: no TEM, EBSD, XRD or atom probe analysis was performed. LBHT recovers HAZ hardness without full-component solution treatment, supporting its use as a targeted route for LMD repair.

1 Introduction

Laser metal deposition (LMD) is a directed energy deposition additive manufacturing process that builds and restores metallic components by melting powder feedstock onto a substrate with a focused laser beam. Among the alloys used in aerospace, defence and petrochemical applications, 17-4 PH (UNS S17400) precipitation-hardened martensitic stainless steel is prominent for its combination of high strength, moderate corrosion resistance and good processability [1]. A persistent challenge is spatially non-uniform hardness across the deposited clad, the heat-affected zone (HAZ) and the substrate: the steep thermal gradients of the moving melt pool subject the HAZ to a thermal history capable of partially dissolving or over-ageing the strengthening precipitates. In 17-4 PH the principal strengthening phase is nanoscale ε-Cu, which forms coherent clusters during ageing in the 480-498 °C window [2,4].

Conventional remediation involves full solution annealing and ageing of the entire component. This is energy-intensive, introduces distortion in geometrically complex parts, and may adversely affect substrate regions already in a satisfactory condition [2]. Localised laser-based heat treatment (LBHT) applies a defocused beam to a targeted zone, inducing the ageing cycle only where it is needed. Localised laser exposure is not itself new: intrinsic tempering during multi-layer deposition is known to control the hardness and fatigue response of repaired high-strength steels [5]. What has not been systematically reported is how hardness recovery is distributed across the clad-HAZ-substrate sequence of a precipitation-hardened alloy, and which micron-scale compositional features accompany it.

* Corresponding author: s232271240@mandela.ac.za

These observations must be interpreted against nanoscale work that the present technique set cannot access: atom probe and transmission electron microscopy studies of 17-4 PH aged near 480 °C report Cu-rich precipitates of the order of a few nanometres [4], while Nb-rich particles form during solidification and are already present in the as-built condition [3]. Two questions follow. First, if the bulk EDS compositions of the HAZ before and after LBHT are similar, which redistribution mechanism produces the observed hardness increase? Second, what is the role of the Nb-rich particles that appear as bright features in backscattered electron (BSE) imaging: are they discrete nucleation sites, or indicators of micro-segregation that indirectly modulate precipitation kinetics?

2 Methodology

Single-track clads were deposited on wrought 17-4 PH (AISI 630 / UNS S17400) discs supplied in the solution-annealed Condition A and furnace-aged to H900 (480 °C, 1 h, air cool) to provide a peak-aged deposition substrate. Deposition and heat treatment were both performed in an enclosed six-axis robotic laser cell (TRUMPF TruLaser Robot 5020) fitted with a TruDisk 4001 disk laser at 1030 nm, using gas-atomised 17-4 PH powder delivered through a three-way coaxial cladding nozzle under argon. Deposition used 1800 W at 0.0133 m s^{-1} (135.34 J mm^{-1}) with a 3 mm spot at 12 mm stand-off. Single-track deposits were used deliberately so that HAZ changes could be attributed to the thermal cycle of a single pass.

For LBHT the cladding nozzle was removed and the stand-off increased to 17 mm, enlarging the beam footprint and reducing the incident power density below the melting threshold. Parameters were selected from a 3 by 3 matrix on the criterion that the peak surface temperature fall within the 480-498 °C H900-equivalent ageing window and remain well below the Ac1 transformation temperature of approximately 680 °C. No constant-power condition sustained that narrow band, so a two-stage sequence was adopted: a starting pass at 600 W to enter the range quickly, followed immediately by a holding pass at 400 W to sustain it, both at 0.2 m s^{-1} (3.0 and 2.0 J mm^{-1}). Four K-type thermocouples spot-welded 2 mm from the clad track edge recorded peaks of 502-527 °C at the sensor positions, with approximately 90-200 s above 480 °C. Control specimens omitted the LBHT step.

Cross-sections transverse to the track were mounted, polished to 0.5 µm (ASTM E3) and etched with Marble's reagent. Vickers microhardness was measured to ASTM E384 at HV0.3 along a traverse perpendicular to the clad-substrate interface, three indentations per region per condition (n = 3), with a system measurement uncertainty of approximately ± 10 HV. SEM/EDS used a JEOL JSM-IT100 in secondary and backscattered electron modes with an Oxford Instruments Xplore 15 detector at 15-20 kV and standardless XPP quantification. Two limits govern the interpretation of the EDS data: at these voltages the electron interaction volume in an Fe-based matrix is of the order of 1 µm, so no nanoscale phase can be chemically resolved; and the 1σ quantification uncertainty is typically ± 0.29 wt% for both Cu and Nb, so differences of that magnitude are reported as trends rather than quantified values. The procedure is summarised in Fig. 1.

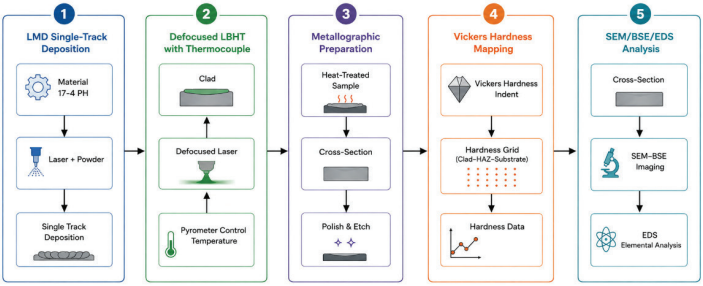


Fig. 1. Overview of the experimental methodology, running from substrate preparation and prior heat treatment, through single-track LMD deposition and localised laser-based heat treatment with thermocouple monitoring, to sectioning and metallographic preparation, Vickers microhardness mapping across the clad-HAZ-substrate sequence and SEM/EDS characterisation of the same cross-sections. Control (non-HT) specimens follow the same route with the LBHT step omitted.

3 Results and discussion

In the as-deposited condition the clad (327.0 ± 13.0 HV) and the HAZ (328.3 ± 20.6 HV) were of comparable hardness, both below the substrate (394.0 ± 35.9 HV) and close to the Condition A baseline of 324.2 HV; the lowest HAZ value recorded was 305 HV. Following LBHT, hardness increased in all three zones: the clad by 51.3 HV to 378.3 ± 16.8 HV (+15.6%), the substrate by 45.3 HV to 439.3 ± 10.0 HV (+11.5%), and the HAZ by 82.7 HV to 411.0 ± 12.5 HV (+25.2%), the largest absolute and relative gain and within the range reported for the conventional H900 condition. The standard deviation decreased in every zone, most markedly in the substrate (± 35.9 to ± 10.0 HV) and the HAZ (± 20.6 to ± 12.5 HV), indicating a more uniform mechanical response. With three indentations per zone, however, the data do not show that the magnitude of the LBHT response differs statistically between the three regions.

BSE imaging resolved no precipitate contrast within the matrix in either condition. This is expected rather than anomalous: the Cu-rich precipitates reported for this alloy and ageing window are of the order of a few nanometres [4], one to two orders of magnitude below the resolution achievable here. What BSE did resolve were occasional bright particles at grain boundaries and in interdendritic regions, more numerous and more regularly distributed in the post-LBHT HAZ. EDS point analysis identified these as Nb-rich, returning up to 4.25 wt% Nb, with adjacent matrix Cu at approximately 2.72 wt%; the particles themselves returned no anomalous Cu. Critically, EDS resolved no change in the bulk Cu content of the HAZ as a result of treatment: 2.75-3.46 wt% before and 2.73-3.33 wt% after, ranges that overlap and whose difference is smaller than the quantification uncertainty.

The hardness increase therefore cannot be attributed to any compositional change at the scale accessible to EDS and must arise at a finer scale. The applied thermal cycle lies within the window in which Cu-rich precipitation is the dominant hardening reaction in 17-4 PH [2,4], and ε-Cu precipitation from a Cu-supersaturated matrix is the interpretation most consistent with the observations: precipitation redistributes Cu over nanometre distances, invisible both to the approximately 1 µm EDS interaction volume and to BSE imaging, and would raise

hardness without altering any composition measured at the micron scale. This mechanism is inferred rather than observed. No TEM, atom probe, EBSD or XRD analysis was performed, so contributions from martensite recovery, retained austenite transformation and residual stress relaxation cannot be excluded, and the reduction in hardness scatter is compatible with several of these.

The Nb-rich particles are accordingly not interpreted as the primary strengthening agent. They are neither Cu-enriched themselves nor confined to the treated condition; Nb-rich particles form during primary solidification and are present in the as-built state [3], so their distribution records solidification conditions rather than the subsequent treatment. They are better understood as the visible marker of the micro-segregation pattern with which the enhanced HAZ response is associated. Consistent with this, post-LBHT HAZ regions containing these particles returned matrix Cu at the upper end of the measured range (up to 3.33 wt%) and coincided with the highest recorded hardness of approximately 425 HV, whereas the clad, which solidifies rapidly and uniformly, showed uniform Cu (3.02-3.37 wt%) and no comparable association. As these differences are of the same order as the quantification uncertainty, the association is reported as a consistent trend rather than a quantified correlation.

The hardness achieved after LBHT (HAZ 411 HV, substrate 439 HV) falls within the range reported for furnace-aged 17-4 PH in the H900 condition, typically 380-440 HV [1,2]. No matched furnace-aged deposit was produced, so this is a comparison against published values rather than against a control. On that basis, localised treatment recovered HAZ hardness to within the reported range without full-component re-solution treatment, depositing thermal energy only in the affected zone. Notably, the zone most affected by deposition-induced softening is also the zone that responds most strongly to localised treatment; this should be tested on multi-track and multi-layer deposits before it is relied upon in practice.

4 Conclusions

Localised laser-based heat treatment at peak surface temperatures of 480-498 °C increased Vickers hardness in all three zones of the clad-HAZ-substrate sequence of LMD 17-4 PH, with the largest absolute and relative gain in the HAZ (328.3 ± 20.6 to 411.0 ± 12.5 HV; +82.7 HV, +25.2%), and reduced hardness scatter in every zone. EDS resolved no change in the bulk Cu content of the HAZ as a result of treatment, so the increase must reflect a redistribution of solute below the resolution of the technique. Nb-rich particles (up to 4.25 wt% Nb) were more densely distributed in the HAZ than in the clad and were spatially associated with regions of elevated hardness, but they are interpreted as markers of solidification-driven micro-segregation rather than as the primary strengthening phase. The recovery is most consistent with ε-Cu precipitation during LBHT, although this is inferred from the hardness response and the unchanged bulk composition rather than directly observed. LBHT recovered HAZ hardness to within the range reported for furnace-aged H900 material without full-component re-solution treatment, supporting its use as a targeted, low-distortion post-processing route for LMD repair. Direct confirmation of the mechanism by TEM or atom probe tomography, and extension to multi-track and multi-layer deposits, are the objectives of ongoing work.

References

1. H.R. Lashgari, Y. Xue, C. Onggowarsito et al., Microstructure, tribological properties and corrosion behaviour of additively manufactured 17-4PH stainless steel: effects of scanning pattern, build orientation, and single vs. double scan. Mater. Today Commun. **25**, 101535 (2020). https://doi.org/10.1016/j.mtcomm.2020.101535

2. T. Muslim, T. Karagoz, S. Kurama et al., Laser metal deposition of 17-4 PH stainless steel: geometrical, microstructural, and mechanical properties investigation for structural applications. CIRP J. Manuf. Sci. Technol. **41**, 69-79 (2023). https://doi.org/10.1016/j.cirpj.2022.12.010

3. S. Cheruvathur, E.A. Lass, C.E. Campbell, Additive manufacturing of 17-4 PH stainless steel: post-processing heat treatment to achieve uniform reproducible microstructure. JOM 68, 930-942 (2016). https://doi.org/10.1007/s11837-015-1754-4

4. Z. Wang, X. Fang, H. Li, W. Liu, Atom probe tomographic characterization of nanoscale Cu-rich precipitates in 17-4 precipitate hardened stainless steel tempered at different temperatures. Microsc. Microanal. 23, 340-349 (2017).

5. C. Barr, R. Abdul Rahman Rashid, S. Palanisamy, J. Watts, M. Brandt, Examination of steel compatibility with additive manufacturing and repair via laser directed energy deposition. J. Laser Appl. 35, 022015 (2023). https://doi.org/10.2351/7.0000952

Digital twin-based monitoring and data management in the laser powder bed fusion process chain using a learning integrated manufacturing system

Kekeletso Thejane[1 *], *Willie* du Preez[2], and *Gerrie* Booysen[2]

[1] Department of Mechanical and Mechatronics Engineering, Faculty of Engineering, Built Environment and Information Technology, Central University of Technology, Free State, South Africa
[2] Centre for Rapid Prototyping and Manufacturing, Faculty of Engineering, Built Environment and Information Technology, Central University of Technology, Free State, Bloemfontein, South Africa

Abstract. Full monitoring of the LPBF process chain is crucial, especially in medical and industrial environments where strict control is required across the entire process chain. This includes continuous monitoring of the build process and heat-treatment procedures. In this work, the Learning Integrated Manufacturing System (LIMS) was used as the central computing platform. Data from the EOS M290 and the T-M Super Series vacuum furnace were acquired for each process, displayed, visualised and analysed in real-time. The monitoring capability was further strengthened through MATLAB analysis, where triggers and alerts were generated whenever abnormalities occurred during the build process.

1 Introduction

Monitoring during the build and post-processing stages of the LPBF process chain is crucial, particularly for medical applications where strict process control is required. The build process must be monitored layer by layer, while post-processing heat treatment must be monitored to ensure that the correct cycle is applied. For this reason, automated data flow from production to post-processing is essential.

In this study, the Learning Integrated Manufacturing System (LIMS) supported process monitoring by acquiring process data and tracking each stage in real time. Data were also transferred to MATLAB through RESTful APIs for analysis, trigger implementation, and alert generation as part of the digital twin development. Similar studies by Liu et al. [1] and Lu et al. [2] have shown the value of digital twin technology for advanced manufacturing data management.

* Corresponding author: kthejane@cut.ac.za

2 Process monitoring and data management using LIMS

In this work, two systems, namely the EOS M290 LPBF machine and the T-M Super Series vacuum furnace, were monitored. Both systems were connected to the LIMS to enable the acquisition and capture of process data, including process parameters and operating cycles. To further extend the monitoring capability, the EOS M290 build process was integrated with MATLAB for detailed analysis and the generation of triggers when abnormalities were detected.

2.1 Data acquisition from systems to LIMS

The EOS M290 and the vacuum furnace were successfully connected to the LIMS through the Central University of Technology (CUT) local area network using static IPv4 addressing. This placed both within the same subnet for reliable communication. This setup allowed both systems to communicate with the LIMS and formed the basis for data acquisition.

2.2 MATLAB analysis and trigger development

The LIMS platform hosted an MTConnect agent that published real-time machine-state and sensor data through a RESTful HTTP interface. Using the MTConnect REST API, process data from the EOS M290 were continuously retrieved in structured XML format, including both real-time and historical measurements linked to SI0201-4385. Here, SI refers to the system-generated identifier assigned by the EOS M290 to the machine data stream. These data were then used in MATLAB for analysis, trigger development, and alert generation during process monitoring.

3 Results

The results included the recoater axis torque which was successfully monitored during live EOS M290 operation. Although different parameters were monitored in this study, the recoater axis torque was used to demonstrate the trigger system. During the recoater movement, the torque signal fluctuated above and below zero, as expected, because the recoater changed direction during operation. As shown in Fig. 1, most values remained within the normal operating range, indicating stable recoater behaviour.



Fig. 1. Recoater axis torque signal acquired during live EOS M290 monitoring, and alert detection based on the defined torque trigger parameters

Further analysis showed that the torque peaks were generally 0.15 Nm, which was regarded as the normal peak value during recoater operation. Peaks above 0.20 Nm were classified as warning level, while peaks exceeding 0.45 Nm were classified as spike level. Although higher peaks, such as 0.375 Nm, were detected in real time during operation, they were not harmful to the process, and normal recoater operation was maintained throughout.

4 Conclusion

This study demonstrated the successful integration of the EOS M290 and the vacuum furnace with the LIMS for centralised monitoring and data acquisition. By employing standardised interfaces and RESTful APIs, data accessibility was improved and external analysis was supported. The results further confirmed that LIMS, together with MATLAB-based analysis, can support digital twin development through real-time monitoring, trigger generation, and improved data management across the LPBF process chain.

References

1. C. Liu, L. le Roux, C. Körner, O. Tabaste, F. Lacan, and S. Bigot, Digital Twin-Enabled Collaborative Data Management for Metal Additive Manufacturing Systems. J. Manuf. Syst. **62**, Jan. (2022). doi: 10.1016/j.jmsy.2020.05.010
2. Y. Lu, P. Witherell, and A. Donmez, A Collaborative Data Management System for Additive Manufacturing, in Proceedings of the ASME 2017 International Design Engineering Technical Conferences and Computers and Information in Engineering Conference (IDETC/CIE 2017), Cleveland, Ohio, USA, August 6-9 (2017)

Effect of heat treatment on the microstructure and hardness of laser powder bed fusion manufactured Inconel 718

Elelwani Tshisimba[1*], *Nkutwane* Makoana[2], *Walace* Matizamhuka[1], *Khathutshelo* Nemavhola[1], and *Nana* Arthur[2]

[1]Chemical & Metallurgical Engineering Department, Vaal University of Technology, South Africa.
[2]National Laser Centre, Council for Scientific and Industrial Research, South Africa.

Abstract. Laser Powder Bed Fusion (LPBF) is a well-known additive manufacturing technique capable of producing complex components. However, its high solidification rate often results in undesirable material properties. Studies have shown that post-processing methods such as homogenization, solution annealing, and double aging can significantly improve the properties of Inconel 718 alloy. This study investigates the effects of different heat treatments on Inconel 718 by varying cooling rates and temperatures.

1 Introduction

LPBF is an additive manufacturing process characterized by extremely high cooling and solidification rates, which often lead to the formation of non-equilibrium microstructures and elemental segregation [1]. In Inconel 718, this rapid solidification promotes a fine cellular–dendritic structure and the formation of undesirable phases such as Laves and δ phases in interdendritic regions.

Post-processing heat treatment is commonly used to modify the microstructure by reducing segregation, dissolving detrimental phases, and promoting the precipitation of strengthening phases such as γ′ and γ″ [2]. However, most heat treatment schedules were originally developed for wrought or cast Inconel 718 and may not be fully suitable for LPBF materials due to their unique microstructural features.

Therefore, a better understanding of the microstructural evolution of LPBF-produced Inconel 718 during heat treatment is needed. This study investigates the effect of heat treatment, focusing on cooling method and temperature, on the microstructure of LPBF-fabricated Inconel 718.

2 Methodology and results

As-built Inconel 718 samples produced by LPBF were provided by CSIR and sectioned into 1 cm × 1 cm specimens. Heat treatment was performed at Vaal University of Technology using a Nabertherm HT 40/17 high-temperature box furnace, and the samples were

* Corresponding author: elelwanitshisimba@gmail.com

characterized using optical microscopy (OM), scanning electron microscopy (SEM), and micro-Vickers hardness testing.

The OM and SEM of the as-built material revealed melt pool gain boundaries morphology and fine dendritic structure with a γ phase matrix attributed by rapid solidification. The hardness of the as-built was 310HV.

After heat treatment OM and SEM revealed δ phase precipitation along grain boundaries with different morphologies. Water-quenched samples after homogenization showed reduced δ phase formation, while air-cooled samples after homogenization exhibited increased δ phase content, as shown in Figure 1. The highest δ phase fraction was observed in the sample subjected to air-cooled homogenization followed by solution annealing at 935°C, attributed to the lower solution annealing temperature.

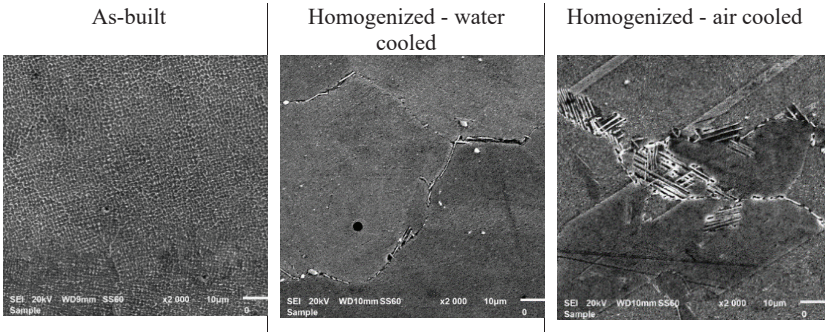


Fig. 1. SEM images showing different microstructures before and after heat treatment

Hardness measurements correlated with microstructural changes: the lowest hardness was observed in the air-cooled homogenized and solution-annealed sample, while the highest hardness was measured in the sample that received only solution annealing and double aging. The lower hardness in water- and air-cooled homogenized samples is attributed to full recrystallization during homogenization.

3 Conclusion

Based on the results it can be concluded that heat treatment improved the microstructure and mechanical properties of Inconel 718 as printed by LPBF. The results revealed water cooling increased hardness than air cooling, by limiting the precipitation of δ phases and lower solution annealing temperature reduced hardness of the material. Solution annealing and double aging increased the hardness of the alloy better than the homogenized sample. Further tests are needed to help in determining the presence of strengthening phases and strength of the alloy, which is relevant to application of Inconel 718. Nevertheless, this study reveals the effect of heat treatment and the effect of delta phases within the microstructure of the alloy.

References

1. S.K. Sahu, S. Mohapatra, B.S. Meher, A. Behere, R.P. Dalai, Effect of Heat Treatment on the Microstructure and Mechanical Properties of Laser Powder Bed Fusion-Processed

Inconel 718 Superalloy, J. Mater. Eng. Perform. (2026), DOI: 10.1007/s11665-026-13616-5.

2. M. Zhao, J. Song, Q. Tang, Z. Zhang, Q. Feng, Q. Han, H. Wu, Laser powder bed fusion of Inconel 718-based composites: Effect of TiB_2 content on microstructure and mechanical performance, Opt. Laser Technol. 167 (2023), DOI: 10.1016/j.optlastec.2023.109596.

Effect of heat treatment on microstructure and hardness of DED fabricated Ti-11Nb-9Fe alloy

Dimakatso Moyan, *Wallace R.* Matizamhuka[1], *Khathutshelo* Nemavhola[1], and *Kabelo M.* Raselabe[1].
1. Department of Chemical and Metallurgical Engineering, Vaal University of Technology, Andries Potgieter Blvd, 1900, Gauteng, South Africa.
Corresponding Author: Dimakatsomoyan@gmail.com

Abstract. Directed Energy Deposition enables the production of near-net-shape titanium parts with complex geometries. However, rapid solidification, residual stresses and chemical segregation may lead to microstructural heterogeneity. Thus, heat treatment after deposition is required to homogenise the microstructure and to control the phase evolution in metastable β-Ti alloys. The present work was aimed at producing DED Ti-11Nb-9Fe alloy and subsequently solution-treating it at 1100°C for 24 hrs, water-quenching and aging at 500°C and 600°C for 4, 8 and 12 hrs in an argon atmosphere. Effects of aging temperature and holding time on phase evolution, microstructural evolution and hardness were studied by X-ray diffraction (XRD), optical microscopy, scanning electron microscopy and Vickers microhardness measurements. Solution treatment gave a more homogeneous β-microstructure and reduced segregation. XRD analysis showed β-related reflections in the as-built condition, while additional α-related reflections became evident after aging, indicating α-phase formation within the retained β matrix. The aging heat treatment at 500°C was most effective in forming fine secondary features in the β matrix and showed the highest hardness of 493±22 $HV_{0.5}$ after 12 hrs. On the other hand, at 600°C, microstructural coarsening and lower hardness values were observed, indicating the onset of over-aging. These results suggest that the DED-fabricated Ti-11Nb-9Fe alloy is optimally strengthened by aging at 500°C.

1 Introduction

Titanium alloys are common in aerospace, biomedical, and structural applications because they are strong, corrosion-resistant, and biocompatible [2]. The widely used Ti-6Al-4V alloy performs well in these areas, but its higher elastic modulus relative to natural bone can lead to stress shielding in implants [3]. To address this, researchers have developed metastable β-titanium alloys containing elements such as niobium (Nb), molybdenum (Mo), and iron (Fe) to lower the elastic modulus while maintaining high strength [4]. Ti-Nb-based alloys are especially promising, as Nb is non-toxic and enhances both corrosion resistance and mechanical compatibility. Titanium alloys produced by additive manufacturing exhibit a different microstructure than those produced by traditional methods. In DED, the process involves local melting, rapid solidification, and repeated heating and cooling, resulting in steep temperature gradients and complex solidification patterns. This often leads to columnar β grains, leftover stresses, and chemical segregation in the material [1]. These features can cause unstable phases and inconsistent mechanical performance if the material is used as

built. Heat treatment after manufacturing is important for adjusting the microstructure and improving the reliability of additively manufactured titanium alloys. A common method is solution treatment followed by aging, which helps control how secondary phases form in metastable β-titanium alloys. The way these phases form depends a lot on the aging temperature and time[5]. In this study, a Ti-11Nb-9Fe alloy fabricated by Directed Energy Deposition was solution-treated and then aged at different temperatures to compare microstructural evolution and hardness changes. Optical microscopy and X-ray diffraction were used to study phase changes, and Vickers microhardness testing measured mechanical response. The goal is to determine the optimal aging condition to improve the hardness of DED-fabricated Ti-Nb-Fe alloys.

2 Methodology and results

The DED -fabricated Ti-11Nb-9Fe samples were solution-treated at 1100°C for 24 hours and water-quenched to retain the β-phase structure. Aging heat treatment was performed at 500°C and 600°C for 4,8 and 12 hours, respectively, in an argon atmosphere to promote controlled precipitation within the β matrix. Samples were etched with Kroll etchant, and microstructural characterisation was performed by optical microscopy after metallographic preparation. Hardness measurements were performed using a Vickers microhardness tester with a load of 500g and dwell time of 10s, with 10 indentations taken for each condition to obtain an average value.

The results indicate that solution treatment homogenised the β microstructure by reducing chemical segregation from the deposition process. Aging heat treatment promoted precipitation strengthening, holding time also influenced hardness evolution. At 500 °C, hardness increased progressively with increasing holding time, reaching the highest value after 12 hours, indicating continued precipitation strengthening within the β matrix due to the formation of fine α/α precipitates. In contrast, at 600 °C, hardness initially increased but decreased after prolonged aging, suggesting the onset of over-aging caused by precipitate coarsening.

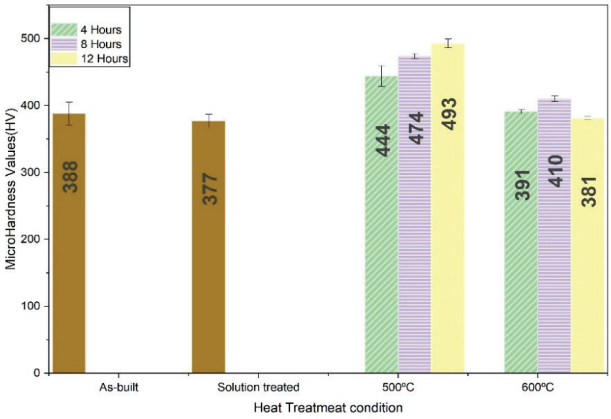


Fig. 1. Hardness evolution of the DED-fabricated Ti-11Nb-9Fe alloy as a function of aging time at different holding times and temperature.

3 Conclusion

Hardness increased with holding time at 500 °C, reaching a maximum after 12 hours, indicating optimal precipitation strengthening within the β matrix. At 600 °C, hardness increased initially but decreased after prolonged aging, suggesting the onset of over-aging due to precipitate coarsening. These results highlight the importance of controlling aging temperature and time to optimise the mechanical performance of additively manufactured β-titanium alloys.

References

1. A. Saboori, D. Gallo, S. Biamino, P. Fino and M. Lombardi,An overview of additive manufacturing of titanium components by directed energy deposition: Microstructure and mechanical properties, Appl. Sci., 7, 883, (2017), https://doi.org/10.3390/app7090883
2. M. Geetha, A.K Singh, R. Asokamani, R. and A.K Gogia, Ti based biomaterials, the ultimate choice for orthopaedic implants – A review, Prog. Mater. Sci., 54, 397–425, (2009), https://doi.org/10.1016/j.pmatsci.2008.06.004
3. L. Zhang and L. Chen, A review on biomedical titanium alloys: Recent progress and prospect, Adv. Eng. Mater., 21, 1801215, (2019), https://doi.org/10.1002/adem.201801215
4. S. Guo, Q Meng, X. Zhao,Q. Wei and H. Xu, Design and fabrication of a metastable β-type titanium alloy with ultralow elastic modulus and high strength, Sci. Rep., 5, 14688, (2015), https://doi.org/10.1038/srep14688

Y. Chen, Z. Du, S. Xiao,L. Xu and J. Tian (2014) 'Effect of aging heat treatment on microstructure and tensile properties of a β high-strength titanium alloy', Journal of Alloys and Compounds, 586, pp.588–592.

07

ABSTRACTS

Product Design and Development

A pseudo-1D thermo-hydraulic design methodology for additively manufactured Archimedean spiral coil condensers

Nicolaas Steenekamp[1]*and *Gys* Jacobs[1]

[1] Department of Mechanical and Mechatronic Engineering, Central University of Technology, South Africa

Abstract. Research on heat transfer and pressure drop in Archimedean spiral coil heat exchangers remains limited, particularly for condensation applications. Additive manufacturing enables the fabrication of compact spiral coil condensers that are difficult to produce using conventional methods. This paper presents a pseudo-one-dimensional thermo-hydraulic design framework for cross-flow air-cooled Archimedean spiral coil condensers intended for small-scale Organic Rankine Cycle systems. The condenser is represented by three regime-based segments corresponding to vapour desuperheating, two-phase condensation, and liquid subcooling. Established heat-transfer and pressure-drop correlations are combined with hydraulic-diameter substitutions to represent rhombic internal channels required by additive manufacturing constraints. The framework provides a practical preliminary design methodology prior to refinement through experimental testing.

1 Introduction

Organic Rankine Cycle (ORC) systems provide a promising method for recovering low-grade waste heat. For small-scale systems, compact heat exchangers are required to achieve high surface density while maintaining small installation footprints [1]. Curved tubes such as spiral coils can enhance heat transfer due to centrifugal forces [2], although this improvement is accompanied by increased pressure losses [3]. Archimedean spiral coils have received limited research attention, partly due to manufacturing challenges [3]. Additive manufacturing enables the fabrication of complex spiral geometries that are difficult to produce using conventional methods. However, reliable thermo-hydraulic correlations for condensation in spiral coils remain scarce [4]. Consequently, preliminary design methods based on one-dimensional modelling remain an essential starting point for development of this condenser.

* Corresponding author: steenekampnk@gmail.com

2 Geometry representation

The proposed condenser consists of a finned Archimedean spiral coil arranged in cross-flow with ambient air. The working fluid flows through a continuous spiral tube while air passes across the external finned surface. To satisfy additive manufacturing constraints, the internal channel is represented by a rhombic cross-section rather than a circular tube. This geometry ensures that internal wall angles remain above approximately 45° relative to the build plane, allowing the channel to remain self-supporting during powder-bed fusion processes [5][6]. Hydraulic diameter substitutions are therefore used to apply conventional smooth-tube correlations to the non-circular geometry [4][7].

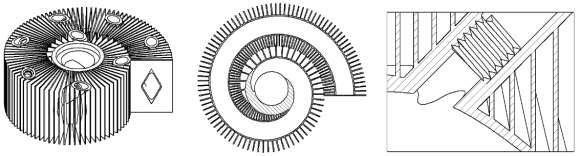


Fig. 1. Conceptual CAD model of the additively manufactured rhombic Archimedean spiral coil condenser.

Additive manufacturing also requires consideration of powder removal and manufacturability [8]. Internal channels must allow evacuation of residual powder, and materials such as AlSi10Mg are commonly selected due to their favourable thermal conductivity and compatibility with powder-bed fusion systems [5][9], see Fig. 1.

3 Thermo-hydraulic modelling framework

The condenser is modelled using a pseudo-one-dimensional control-volume framework consisting of three sequential regimes: vapour desuperheating, two-phase condensation, and liquid subcooling. For each segment, local heat-transfer coefficients and pressure losses are calculated using established correlations [4].

Single-phase heat transfer is estimated using the Dittus–Boelter, Sieder–Tate, or Gnielinski correlations depending on the Reynolds number range [7]. Pressure losses are calculated using the Darcy–Weisbach equation with friction factors determined from classical correlations [10]. Although spiral curvature introduces additional form drag, these relations provide a practical baseline for preliminary design.

Condensation heat transfer is estimated using the Cavallini correlation for horizontal tubes, which accounts for transitions between stratified and annular flow regimes [11][12]. Two-phase pressure losses are estimated using Lockhart–Martinelli type relations. Air-side heat transfer is evaluated using Colburn j-factor correlations for finned heat exchangers together with standard fin-efficiency relations.

4 Numerical solution procedure

For a prescribed condenser heat duty and inlet conditions obtained from an ORC cycle model, the developed solver determines heat transfer coefficients, pressure losses, and the required tube length for each regime. The total tube length is subsequently mapped to an Archimedean spiral defined by the inner diameter, outer diameter, and spiral pitch.

5 Conclusion

A pseudo-one-dimensional thermo-hydraulic design framework for additively manufactured Archimedean spiral coil condensers has been presented. The approach combines established heat-transfer and pressure-drop correlations with hydraulic-diameter substitutions to represent rhombic internal channels imposed by additive manufacturing constraints. The framework provides a baseline design tool for estimating heat transfer performance, pressure losses, and required spiral tube length for micro-scale ORC condensers. Future work will focus on experimental validation and refinement of correlations for spiral coil geometries.

References

[1] B. Zohuri, 'Compact Heat Exchangers Design for the Process Industry', in *Compact Heat Exchangers*, Springer International Publishing, 2018, pp. 57–185. doi: 10.1007/978-3-319-29835-1_3.

[2] S. Kakac, H. Liu, and A. Pramuanjaroenkij, *Heat Exchangers Selection, Rating, and Thermal Design Third Edition*, 3rd ed. Boca Raton: Taylor & Francis Group, 2012.

[3] R. H. Patil, 'Fluid flow and heat transfer analogy for laminar and turbulent flow inside spiral tubes', *International Journal of Thermal Sciences*, vol. 139, pp. 362–375, May 2019, doi: 10.1016/j.ijthermalsci.2019.01.036.

[4] N. Steenekamp and G. Jacobs, 'The potential for additive manufacturing of compact horizontal spiral tube condensers', *MATEC Web of Conferences*, vol. 417, p. 08008, 2025, doi: 10.1051/matecconf/202541708008.

[5] S. C. Venter, G. G. Jacobs, and J. Du Preez, 'DESIGN CONSIDERATIONS FOR DEVELOPING AN ADDITIVE MANUFACTURED TI-6AL-4V COMPACT COUNTER-FLOW HEAT EXCHANGER FOR APPLICATION IN ORGANIC RANKINE CYCLES', in *RAPDASA Conference proceedings*, 2018, pp. 192–200.

[6] D. C. Bester and M. Shange, 'DESIGN FOR ADDITIVE MANUFACTURING: AN INTRODUCTION TO DESIGN RULES AND CONSTRAINTS FOR HIGH SPEED SLM', in *RAPDASA Conference proceedings*, 2019, pp. 413–420.

[7] F. P. Incropera, D. P. Dewitt, T. L. Bergman, and A. S. Lavine, *Fundamentals of heat and mass transfer*, 6th Edition. John Wiley and Sons, 2007.

[8] F. Careri, R. H. U. Khan, C. Todd, and M. M. Attallah, 'Additive manufacturing of heat exchangers in aerospace applications: a review', Nov. 25, 2023, *Elsevier Ltd*. doi: 10.1016/j.applthermaleng.2023.121387.

[9] I. Kaur and P. Singh, 'State of the art in heat exchanger additive manufacturing', *Int. J. Heat Mass Transf.*, vol. 178, Oct. 2021, doi: 10.1016/j.ijheatmasstransfer.2021.121600.

[10] R. K. Shah and D. P. Sekulic, 'FUNDAMENTALS OF HEAT EXCHANGER DESIGN', 2003.

[11] H. Zhang, X. Fang, H. Shang, and W. Chen, 'Flow condensation heat transfer correlations in horizontal channels', *International Journal of Refrigeration*, vol. 59, pp. 102–114, Nov. 2015, doi: 10.1016/j.ijrefrig.2015.07.013.

[12] S. C. Blose, D. R. E. Ewim, A. C. Eloka-Eboka, and A. O. Adelaja, 'Improved correlation for predicting heat transfer coefficients during condensation inside smooth horizontal tubes', *International Journal of Low-Carbon Technologies*, vol. 18, pp. 750–763, Feb. 2023, doi: 10.1093/ijlct/ctad052.

A low-cost UAV propulsion thrust and torque measurement rig

Michael Thomson[1*], and *Arnold* Pretorius[1]

[1]MechatronicSystems.Group, Department of Mechanical Engineering, University of Cape Town, South Africa

Abstract. This paper describes the design, construction, and characterisation of a low-cost UAV propulsion thrust and torque measurement rig developed at the University of Cape Town. Using fused filament fabrication (FFF) and commodity hardware, the rig can measure thrust and torque simultaneously from brushless DC motor and propeller combinations. Development followed an iterative rapid prototyping approach, culminating in a custom printed circuit board targeting 1 kHz data acquisition. Static load testing confirmed high linearity; however, dynamic testing revealed significant throttle-correlated noise whose source is currently under investigation. Future work targets noise characterisation and mechanical redesign.

1 Introduction

Accurate characterisation of UAV propulsion systems, including motor, propeller, and electronic speed controller combinations, requires simultaneous measurement of thrust and torque across a range of operating conditions. Commercial solutions capable of this are priced at several thousand USD, motivating a low-cost, open alternative [1]. This paper describes the development of such a rig at the MechatronicSystems.Group at the University of Cape Town and reports the findings from its characterisation.

2 Design approach

Development followed a deliberate iterative strategy enabled by FFF additive manufacturing. A simple thrust-only first design was completed within one week of CAD work, providing an early platform for testing data acquisition electronics and software while the more capable dual-load cell sensor design was developed in parallel. All printed parts were designed explicitly for FFF manufacturability; fastener holes oriented normal to the build plane, bridging cuts in captive bolt overhangs, and a minimum 3 mm wall thickness around fasteners [2]. Parts were printed in PLA and PETG; aluminium extrusion framing provided the structural backbone.

* Corresponding author: thmmic028@myuct.ac.za

3 Mechanical design

The central challenge is decoupling coaxial thrust and torque for independent measurement. The adopted approach mounts the motor on a shaft that is free to rotate; a thrust bearing transmits axial force to one load cell, enabling thrust measurement, while a lever arm transmits reaction torque to a second. The prototype is depicted in Figure 1. This bearing-based decoupling introduces friction and potential backlash into the torque path, and step-down throttle transients were found to cause the lever arm to briefly separate from the torque load cell, producing impulse artefacts. This limitation motivates investigation of solid-state decoupling in future work. The motor adapter plate is interchangeable, permitting different motor sizes and load cell beams without redesign.

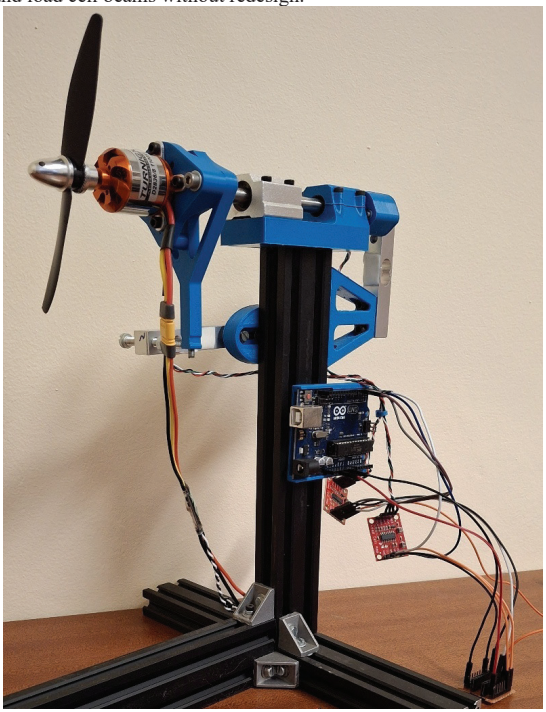


Fig. 1. The prototype thrust and torque measurement rig using HX711 ADCs.

4 Electronics and software

The initial acquisition system used two HX711 load cell analogue to digital converted (ADC) boards with an Arduino microcontroller, achieving a maximum sample rate of 80 Hz. This rate is adequate for quasi-static characterisation but insufficient for dynamic analysis. A custom Python-based GUI supports automated test profiles, real-time graphing, and CSV export. The second development cycle produced a custom printed circuit board (PCB) implementing two parallel signal paths: a high-resolution 24-bit ΣΔ ADC and a secondary

analogue path via an instrumentation amplifier, targeting 1 kHz output data rate. Electromagnetic interference (EMI) mitigation was incorporated at the board level through differential input filtering and power rail isolation.

5 Experimental results

PCB bench validation confirmed correct gain and filter behaviour. Static load testing with calibrated masses demonstrated high linearity on both acquisition paths, with measured forces agreeing with applied loads to within 1 % across the full test range. Dynamic testing with a motor and propeller, however, revealed a noise floor that increased with throttle, rendering the torque channel unreliable under power. Three noise sources are hypothesised but not individually confirmed: EMI coupled from the motor and ESC into the load cell wiring; mechanical resonance of the rig or bearing assembly, suggested by a spectral feature near 146 Hz but unconfirmable without RPM measurement; and resistor noise introduced by the PCB passive components, meaning the PCB itself cannot yet be excluded as a noise contributor. Digital post-processing techniques were evaluated in simulation, but none fully compensated for the throttle-correlated noise.

6 Conclusions and future work

A low-cost UAV propulsion thrust and torque measurement rig was developed using rapid prototyping techniques and validated against static loads. The iterative development approach, enabled by FFF printing, allowed fast design cycles at relatively low cost. The experimental campaign showed that noise from the mechanical and electromagnetic environment, not the acquisition electronics, is the binding constraint on dynamic measurement quality. The custom PCB achieved its 1 kHz target but could not be productively deployed until upstream noise sources are resolved; development reverts to the 80 Hz HX711 architecture in the interim.

Future work will operate the rig without a propeller to isolate electromagnetic noise from mechanically induced noise sources, thereby enabling independent characterisation of the PCB noise floor in the absence of motor-induced mechanical vibrations. Further work will improve load cell cable shielding and investigate solid-state torque decoupling. These findings will inform the full paper and guide subsequent hardware development.

References

1. FoxTech, Test Equipment (2025). https://www.foxtechfpv.com/others/test-equipment.html
2. M. Fernandez-vicente, M. Canyada, A. Conejero, Identifying limitations for design for manufacturing with desktop FFF 3D printers. Int. J. Rapid Manuf. **5** (2015). https://doi.org/10.1504/IJRAPIDM.2015.073551

The potential for additively manufactured triply periodic minimal surface components to improve the efficiency of reciprocating compressors

Annaléne Olwagen[1*] and *Gysbert* Jacobs

[1]Department of Mechanical and Mechatronic Engineering, Central University of Technology, Free State, Bloemfontein, 9300, South Africa

Abstract. Compressors account for a significant share in global energy consumption making efficiency improvements a key research priority. In reciprocating compressors, the compression process generates substantial heat, which reduces efficiency and limits the ability to approach ideal isothermal compression. Existing cooling methods still fall short to adequately control compression temperatures. Triply Periodic Minimal Surface (TPMS) structures, particularly gyroid geometries, offer high surface-area-to-volume ratios and interconnected flow channels that enhance heat transfer and fluid mixing. Advances in additive manufacturing enable the fabrication of these complex structures, which are difficult to produce using conventional methods. This study investigates the feasibility of integrating TPMS structures into reciprocating compressor components to enhance heat dissipation and improve overall compressor efficiency.

1 Introduction

Compressors account for approximately 15% of total energy consumption in developed countries [1–3] and contribute nearly 3,000 megatons of CO_2 emissions annually [4]. With the global shift toward greener and more sustainable energy technologies, improving compressor efficiency has become an increasingly important research focus.

Reciprocating compressors are widely used across numerous industrial sectors due to their relatively simple design, robustness, and reliability [5–7]. However, the compression process generates significant heat, which can negatively affect compressor efficiency, performance, and component durability. Conventional cooling approaches used in these systems are often insufficient to effectively manage the thermal loads, and continued research is therefore directed toward developing improved thermal management strategies [8].

Heat exchangers are widely used to transfer heat between a heat source and a working fluid, thereby maintaining the desired operating temperatures of a system [9]. Plate-and-frame and shell-and-tube designs is the most widely used heat exchanger configurations [7].

* Corresponding author: aolwagen@cut.ac.za

Increasing attention has recently been directed toward alternative geometries that can enhance heat transfer performance while reducing its size [9].

Among these, TPMS structures have recently been explored for heat exchanger applications [10]. TPMS structures boast with exceptionally high surface-to-volume ratios and improved heat dissipation [7] while maximizing strength [11]. As a result, TPMS structures are emerging as promising candidates for next-generation heat exchanger designs.

Despite their demonstrated potential in heat exchanger applications, the integration of TPMS structures directly into compressor components for improved thermal management has received limited attention. In this study, the feasibility of incorporating TPMS structures into reciprocating compressor components is investigated as a novel approach to enhance heat dissipation and improve overall compressor efficiency.

2 Efforts to improve the efficiency of compressors

It is generally believed that the best efficiency in compressors is obtained when isothermal compression is achieved. A typical isothermal compression process is represented in Fig. 1 by path 1–3 in the pressure-volume (P-V) diagram. This process requires less compression work compared to an isentropic compression (process 1–2) [12] .

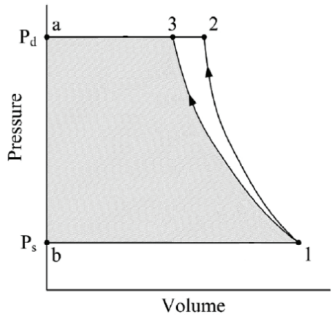


Fig. 1. PV-diagram in which typical polytropic and isothermal compression profiles are indicated (Adapted from [13]).

To reach isothermal compression, the actual temperature of the gas in the cylinder should be kept as close as possible to the initial suction temperature, and this is often done by cooling the compressor cylinder and cylinder head with air or water [14–16].

Innovative techniques are required to enhance heat transfer in compressors, as achieving isothermal or near-isothermal compression in practice remains challenging [17]. Several approaches have been investigated to reduce compression temperatures in reciprocating compressors. These include inter-stage cooling [18, 19], external cooling methods [14], [20, 21], the use of fins to increase heat transfer area [22], liquid piston concepts [23–25] and coolant injection during the compression process [23], [26–30]. While these approaches can improve thermal management, they often introduce additional system complexity or only provide limited improvements in heat transfer performance.

3 Triply periodic minimal surfaces for application in heat exchangers

TPMS structures are characterised by smooth, interconnected flow channels that can enhance heat transfer while maintaining relatively low pressure losses when applied in heat exchangers [31]. Gyroid structures, a common type of TPMS geometry, divide space into two continuous but non-overlapping networks of passages. This architecture provides a large heat transfer area per unit volume and has demonstrated superior cooling performance in heat exchanger applications compared with conventional lattice-frame structures [10], [32]. The interconnected flow channels promote enhanced fluid mixing and turbulence, increasing the Reynolds number and improving heat dissipation [10], while simultaneously maintaining structural strength and minimizing mass [16].

These characteristics make gyroid-based geometries promising candidates for improving heat exchanger compactness and overall thermal performance [31]. In addition, gyroid structures exhibit high mechanical robustness, enabling them to withstand shocks and vibrations in demanding applications [33]. An example of a typical TPMS structures are presented in Fig. 2 below.

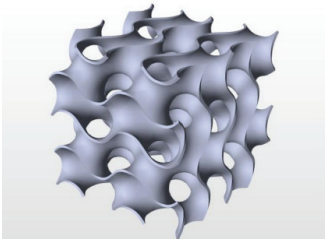


Fig. 2. An example of a gyroid structure [9].

4 Additive manufacturing and TPMS

One of the key advantages of additive manufacturing (AM) is its ability to produce complex geometries that are difficult or impossible to fabricate using conventional manufacturing methods. This capability enables the development of advanced geometries, such as computer aided design (CAD) lattice structures, tailored for specific functional applications [33]. Among these, gyroid structures offer advantages for thermal applications. In metal AM processes, gyroids are inherently self-supporting and can often be manufactured without the need for additional support material, even at relatively large scales [33].

5 Summary

This study explores the use of additive manufacturing to integrate TPMS structures into reciprocating compressor components as a novel approach to enhance heat dissipation and improve compressor efficiency.

References

1. Atlas Copco Compressed air can consume more than 40% of a plant's total electricity bill! https://www.atlascopco.com/en-za/compressors/News-and-stories/local-compressor-news/compressed-air-consumption. Accessed 15 May 2024
2. Friedenstein BM, Cilliers C, van Rensburg J (2018) Simulating operational improvements on mine compressed air systems. South African Journal of Industrial Engineering 29:69–81. https://doi.org/10.7166/29-3-2049
3. Schroeder FW (2009) Energy efficiency opportunities in mine compressed air systems. North-West University
4. Ritchie H, Roser M (2020) CO2 Emissions. Our World in Data
5. Mecholic (2024) Reciprocating Compressor Working, Applications, Advantages and Disadvantages
6. Mohammadi-Amin M, Jahangiri AR, Bustanchy M (2020) Thermodynamic modeling, CFD analysis and parametric study of a near-isothermal reciprocating compressor. Thermal Science and Engineering Progress 19:. https://doi.org/10.1016/j.tsep.2020.100624
7. Ita Ekong G (2020) Performance Analysis of a Single-acting Reciprocating Compressor Using Thermodynamic Concepts
8. Jacobs GG (2014) The influence of controlled coolant injection on quasi-isothermal compression. North-West University
9. Mezaki N (2023) Optimal Design of Heat Exchangers to Enhance Thermal Performance. WashU Scholarly Repository
10. Diegel O, Collins F (2021) Design for Additive Manufacturing: A workflow for a metal AM heat exchanger using nTopology. Metal Additive Manufacturing 7:185–189
11. Yan G, Sun M, Zhang Z, et al (2023) Experimental study on flow and heat transfer performance of triply periodic minimal surface structures and their hybrid form as disturbance structure. International Communications in Heat and Mass Transfer
12. Olwagen A, Jacobs GG (2026) Coolant Injection in Reciprocating Compressors: Current Status and Opportunities. In: Kovacevic A, Read M, Rane S, et al (eds) 14th International Conference on Compressors and Their Systems. Springer, Cham, pp 341–357
13. Cengel YA, Cimbala JM, Turner RH (2017) Fundamentals of Thermo-Fluid Sciences. Mc Graw Hill Education
14. Eastop TD, McConkey A (1993) Applied Thermodynamics for Engineering Technologists. Pearson Education Limited, Gosport
15. Shcherba VE, Shalai V V., Grigoryev A V., et al (2021) General Approach for Estimating the Energy Efficiency of Cooling in Positive Displacement Compressors. Chemical and Petroleum Engineering 57:567–575. https://doi.org/10.1007/s10556-021-00977-y
16. Govt. of India M of power Bureau of Energy Efficiency BEE Book, Volume 1, Chapter 3. Energy Audit and Management
17. Acharya P, Patil V, Ro P (2018) Experimental Investigation of Water Spray Cooling for Temperature Reduction in Liquid Piston Compressor. In: International Compressor Engineering Conference. Purdue E-Pubs
18. Jia G, Weiqing X, Maolin C, Yan S (2018) Micron-sized water spray-cooled quasi-isothermal compression for compressed air energy storage. Exp Therm Fluid Sci 96:470–481. https://doi.org/10.1016/j.expthermflusci.2018.03.032

19. Jiajun L, Hang L, Zheng C, Jianqiang D (2023) Study of the independent cooling performance of adiabatic compressed air energy storage system. International Journal of Refrigeration 152:155–170. https://doi.org/10.1016/j.ijrefrig.2023.05.006
20. Coker AK (2007) Ludwig'c Applied Process Design for Chemical and Petrochemical Plants, 4th ed
21. Qin C, Loth E (2014) Liquid piston compression efficiency with droplet heat transfer. Appl Energy 114:539–550. https://doi.org/10.1016/j.apenergy.2013.10.005
22. Heidari M, Mortazavi M, Rufer A (2017) Design, modeling and experimental validation of a novel finned reciprocating compressor for Isothermal Compressed Air Energy Storage applications. Energy 140:1252–1266. https://doi.org/10.1016/j.energy.2017.09.031
23. Schmitt J, Langebach R (2024) High-pressure liquid refrigerant injection for reciprocating compressors. International Journal of Refrigeration 164:29–37. https://doi.org/10.1016/j.ijrefrig.2024.04.017
24. Van de Ven JD, Li PY (2009) Liquid piston gas compression. Appl Energy 86:2183–2191. https://doi.org/10.1016/j.apenergy.2008.12.001
25. Weiqing X, Ziyue D, Xiaoshuang W, et al (2020) Isothermal piston gas compression for compressed air energy storage. Int J Heat Mass Transf 155:. https://doi.org/10.1016/j.ijheatmasstransfer.2020.119779
26. Valenti G, Murgia S, Contaldi G, Valenti A (2014) Experimental Evidence of thermal effect of lubricating oil spayed in sliding-vane air compressors. Case Studies in Thermal Engineering 113117
27. Bell IH, Lemort V, Groll EA, et al (2012) Liquid Flooded compression and expansion in scroll machines-Part II: Experimental testing and model validation. International Journal of Refrigiration 1890–1900
28. Xu X, Hwang Y, Radermacher R (2011) Refrigerant injection for heat pumping/air conditioning systems: Literature review and challenges discussions. International Journal of Refrigeration 34:402–415. https://doi.org/10.1016/j.ijrefrig.2010.09.015
29. Li J, Wu H, Wang B, et al (2009) Research on the performance of water-injection twin screw compressor. Appl Therm Eng 29:3401–3408. https://doi.org/10.1016/j.applthermaleng.2009.05.018
30. Yuanyang Z, Liansheng L, Pengcheng S (2006) Thermodynamic Simulation of Scroll Compressor/Expander Module in Automotive Fuel Cell Engine. Journal of Automobile Engineering 220:571–577
31. Volcheck K, Pfau S Revolutionizing heat exchangers with additively manufactured gyroids. In: Heat Exchanger World. https://heat-exchanger-world.com/revolutionizing-heat-exchangers-with-additively-manufactured-gyroids/. Accessed 28 Jul 2025
32. Yeranee K, Rao Y (2022) A Review of Recent Investigations on Flow and Heat Transfer Enhancement in Cooling Channels Embedded with Triply Periodic Minimal Surfaces (TPMS). Energies (Basel). 15
33. Fastway Engineering Gyroid Lattice Heat Exchanger - A Fluid Flow Study. https://blog.fastwayengineering.com/3d-printed-gyroid-heat-exchanger-cfd. Accessed 28 Jul 2025

Investigating a lattice structure for a 316L stainless steel injection mould cavity

Andile Ndlovu[1], and *Natasha* Sacks[1*]

[1]Department of Industrial Engineering, Stellenbosch University, South African

Abstract. This study investigated the potential of using a Kelvin cell lattice structure to redesign a 316L stainless steel injection mould cavity for fabrication via laser powder bed fusion with the aim of reducing material consumption and production costs. Finite element analysis was employed to simulate the static stress and thermal distribution of the lattice structures while benchmarking against the properties of the solid cavity. While a reduction in material usage and good static strength was achieved, the thermal distribution properties of both lattices are currently not on par with that of the solid cavity and require further investigation.

1 Introduction

Injection moulding is a leading manufacturing process for mass production of plastic components due to its precision and repeatability [1]. As industries seek to optimize production efficiency and reduce costs, advancements in mould design have become increasingly critical [2]. Traditional mould inserts, commonly made from steel, offer robust performance but often at the expense of weight and material efficiency. Heavy, solid moulds can lead to increased production costs and energy consumption, thereby prompting the exploration of innovative alternative mould designs [3]. Additive manufacturing, with its known advantage of design complexity as well as its potential for lean production has been investigated by several authors to redesign moulds for injection moulding. For example, Park et al [4] demonstrated that Ti-6Al-4V moulds designed with lattice structures can achieve a weight reduction of approximately 79% compared to the solid moulds, while maintaining mechanical integrity under industrial injection conditions. Similarly, Shen et al [5] showed that lattice structures integrated within conformal cooling channels significantly improve cooling performance compared to traditional straight or basic conformal cooling designs. In the current study a Kelvin cell lattice structure was investigated for potential redesign of a 316L stainless steel injection mould used in the production of plastic light switch covers. The lattice structures were tested against the static strength and thermal distribution properties of known operational conditions for the mould. The insights gained from this research provides a foundation for further investigation which can potentially lead to the development of a lightweight mould which can contribute to a more sustainable and efficient injection moulding process for the light switch covers.

* Corresponding author: natashasacks@sun.ac.za

2 Methodology and results

A solid cavity insert of a 316L stainless steel mould used for light switch covers was redesigned in Fusion 360 and is shown in Fig. 1(a). This cavity was shelled to create a hollow structure as shown in Fig. 1(b). The shelled cavity was filled with a uniform Kelvin cell lattice structure as shown in Fig. 1(c). The Kelvin cell design was selected for its ability to partition space into equal volumes with minimal surface area, which is essential for optimising thermal management in mould applications [6].

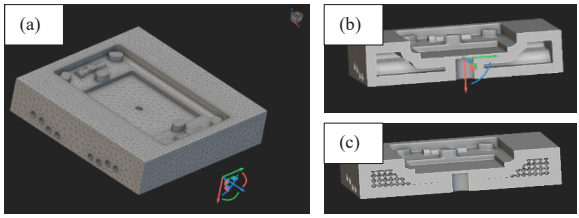


Fig. 1. Cavity insert: (a) meshed cavity, (b) shelled cavity and (c) uniform lattice filled cavity

Static strength and thermal distribution analyses were performed on the designs using finite element analysis (FEA), and injection mould data sourced from literature was used for benchmarking. From the static analyses of the uniform Kelvin cell lattice structure mould design, regions experiencing high stress were identified, which allowed for targeted modifications to the lattice thickness in these specific regions to enhance structural integrity. This led to a second shelled cavity being only partially filled with the Kelvin cell lattice structure and having variable thickness to attempt to reduce high stress regions. The static analysis results revealed stress values of 358 MPa for the uniform Kelvin cell lattice design and 346 MPa for the partial Kelvin cell lattice design. Both stress values are below the yield strength of 563 MPa for additively manufactured 316L stainless steel, which indicates that the two designs can potentially withstand the static mechanical loads encountered during the injection moulding process without experiencing structural failure.

The uniform Kelvin cell lattice design achieved a mass reduction of 5%, while the mould with the partial Kelvin cell lattice design achieved a mass reduction of 3.6%. The greater mass reduction in the uniform lattice structure can be attributed to its consistent geometric design, which optimally utilizes material while maintaining strength. The lower mass reduction for the variable lattice thickness in the partial Kelvin cell lattice design is due to the retained material in the identified critical areas of high stress.

Fig. 2 shows the thermal analyses of the solid cavity (Fig. 2(a)) and uniform Kelvin cell lattice design (Fig. 2(b)). The current thermal analyses was based on using the conventional cooling channels for the mould and hence there is an uneven distribution of the temperature for all designs. For both lattice designs an increase in temperature was observed due to the lower thermal mass in the lattice integrated moulds which cause the heat to be absorbed at a slower rate through the lattice structures compared to the solid cavity, which is consistent with the findings of Sakalys et al [3]. This reduced heat transfer in the lattice structures could be improved by optimizing the lattice cell size and incorporating conformal cooling channels, which could potentially enhance heat removal. However, this requires further investigation.

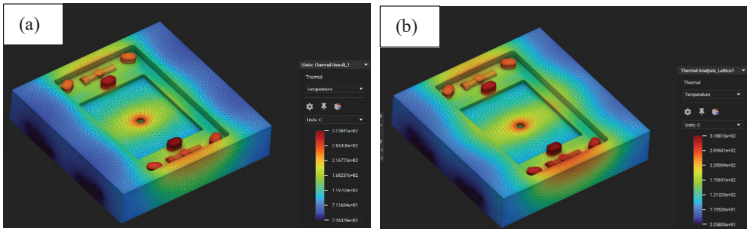


Fig. 2. Thermal analysis of (a) solid cavity and (b) uniform Kelvin cell lattice design

3 Conclusion

The numerical results from this study demonstrate the potential of incorporating Kelvin cell lattice configurations into 316L stainless steel injection mould cavities used in the production of plastic light switch covers. While a reduction in material usage and good static strength was achieved by both lattice designs, the thermal distribution properties of both lattices are currently not on par with that of the solid cavity and require further investigation.

The authors acknowledge the funding of the research study by the Collaborative Programme in Additive Manufacturing (CPAM) and the Council for Scientific and Industrial Research (CSIR) (Grant no. CPAM-25-PGS-09). The opinions expressed and the conclusions arrived at are those of the authors and are not necessarily to be attributed to the CPAM or the CSIR

References

1. C. Malca, C. Santos, M. Sena, A. Mateus, Development of SLM cellular structures for injection molds manufacturing. Sci. Technol. Mater. **30**, 13–22 (2018) https://doi.org/10.1016/j.stmat.2018.03.001
2. Z. Chval, K. Raz, J. da Silva, Integrating 3D printing with injection molding for improved manufacturing efficiency. Polymers **17**, (2025) https://doi.org/10.3390/polym17141935
3. R. Šakalys, C. O'Hara, M. Kariminejad, A. Weinert, M. Kadivar, B. Zluhan, K. Costello, M. McAfee, G. McGranaghan, R. Raghavendra, D. Tormey, Additively manufactured injection mould tooling incorporating gradient density lattice structures for mass and energy reduction. Int. J. Lightweight Mater. Manuf. **8**, 522–536 (2025) https://doi.org/10.1016/j.ijlmm.2025.03.007.
4. S. J. Park, S. M. Yeon, J. H. Lee, S. H. Kim, J. Yang, S. Hong, W. Heogh, Y. Son, J. Park, D. Kang, Lightweight injection mold using additively manufactured Ti-6Al-4V lattice structures. J. Manuf. Process. **79**, 759–766 (2022) https://doi.org/10.1016/j.jmapro.2022.05.022
5. S. Shen, B. B. Kanbur, C. Wu, F. Duan, Three-dimensional printing conformal cooling with structural lattices for plastic injection molding. Front. Heat Mass Transf. **22**, 397–415 (2024) https://doi.org/10.32604/fhmt.2024.048984
6. K.-M. Park, G.-O. Kim, J.-G. Kim, Y.-S. Roh, Mechanical properties of additive manufactured variable-density Kelvin lattice structures: A novel design method for Kelvin unit cells. J. Struct. Integr. Maint. 7, 34–45 (2022) https://doi.org/10.1080/24705314.2021.1971893

Optimum processing of cpTi using laser powder bed fusion

Nthabiseng Nhlapo[1*], *Thywill Cephas* Dzogbewu[1]

[1]Department of Mechanical and Mechatronics Engineering, Central University of Technology, Free State, South Africa

Abstract. Laser powder bed fusion (LPBF) is an additive manufacturing technique that is capable of fabricating customised parts from a variety of materials. Titanium (Ti) has favourable properties for numerous applications, and Ti parts produced using LPBF are at the forefront of several industry applications. This study aimed to optimise the process parameters of the commercially pure Ti (cpTi) using LPBF by following an established hierarchical approach. The process ensued by studying the LPBF single tracks to optimise the laser power and scanning speed, followed by evaluating the double layers to optimise the hatch distance and attain the final process parameters. The results showed that the LPBF technology may be effective in producing parts from elemental Ti powder. Future studies should focus on optimising the properties of cpTi for specific industrial applications.

1 Introduction

Additive manufacturing (AM) processes occupy well-established niches across branches such as aerospace, automotive, healthcare and the energy sector. Laser powder bed fusion (LPBF) is employed in these industries to fabricate lightweight and customised metal parts with complex geometries from computer-aided design (CAD) data [1]. LPBF is among the most widely recognised and versatile AM techniques, capable of manufacturing parts from a variety of materials [2]. Titanium (Ti) and its alloys have been widely adopted in numerous industrial applications due to their exceptional strength, lightweight properties, and high corrosion resistance [3]. Furthermore, the demand for rapid production of custom parts has resulted in the prominence of LPBF Ti-based components. The process parameters for LPBF require optimisation for a particular metallic powder feedstock since the quality and mechanical properties of the final LPBF products depend on the selected process parameters [4]. Of the numerous LPBF processing parameters, the four principal process parameters that influence the quality of LPBF manufactured parts are laser power, scanning speed, hatch distance and powder layer thickness [5]. The optimisation procedure generally involves these four variables as they determine the energy input during the manufacturing process and, hence, the mechanical properties of LPBF-manufactured parts [4]. For each type of metallic powder, there is a particular combination of these parameters that may yield optimum results.

* Corresponding author: nhlapo86@gmail.com

It is, therefore, obligatory to determine the optimum processing parameters that may be applied to produce aTi part using LPBF for industrial applications. The aim of this study was to optimise the process parameters of the commercially pure Ti (cpTi) using LPBF by following the hierarchical and systematic approach described Yadroitsev et al. [6].

2 Methodology

The Electro-Optical System (EOS M 280) Direct Metal Laser Sintering (DMLS) machine supplied by EOS GmbH was used for the optimisation process of commercially pure titanium (cpTi, Grade 2) powder. A uniform powder deposition thickness of 50 µm was applied on a Ti6Al4V substrate. Single tracks were sintered at laser powers of 100, 150, 170 and 300 W and at a scanning speed range of 0.08–1.2 m/s. The tracks were analysed from the top and the cross-sectional views to obtain the optimum sets of laser powers and scanning speeds. To determine the optimum hatch distance, double layers were produced using a pair of optimum laser power and scanning speed parameters determined from the single track analysis. The double layers were sintered at hatch distances of 80, 90 and 100 µm and analysed from the top and the cross-sectional views. The top and cross-sectional examination of the single tracks and double layers was conducted using the ZEISS Axio Scope.A1 Optical Microscope (OP). The samples were prepared for metallurgical analysis by mounting and etching with Kroll's reagent for OP examination as described by Dzogbewu [7]. The surface roughness was measured with a Mitutoyo Surftest SJ-210 profilometer.

3 Results and discussion

Single tracks produced during the LPBF process were analysed to observe their continuity along the lengths and for defects such as spatter particles (also known as satellites). Discontinuous tracks are presented in irregularly shaped or droplets of solidified molten metal known as a balling effect (formation of molten pool balls) [8,9]. The penetration depths and shapes, and the heights of the single tracks were also studied along with the effect of the laser energy. From the single-track analysis, the parameters of 150 W at 0.3 m/s and 170 W at 0.6 m/s were found to produce the most stable tracks. These parameters were employed to fabricate the double layer at hatch distances of 80, 90 and 100 µm using the single scan and rescan strategies. From the tops and cross-sections of the double layers were studied to investigate the occurrence of defects such as satellites, balling, microcracks and porosity. The surface roughness values were also presented to elucidate the defects. The selected optimum process parameters were a laser power of 170 W, scanning speed of 0.6 m/s, hatch distance of 80 µm and a powder layer thickness of 50 µm.

4 Conclusion

The top and cross-sectional analyses of single tracks and double layers of cpTi fabricated using the LPBF machinery were conducted to establish the optimum process parameters. The results illustrated that LPBF is an effective process in manufacturing stable, quality single tracks in the track-by-track and layer-by-layer building process. Moreover, the LPBF may be a dependable process to manufacture parts from elemental cpTi powders that can be applied widely in industry. Future research should explore the optimisation of various LPBF Ti properties for applicability in specialised industries.

Reference

1. S. Dehghan, S. Sattarpanah Karganroudi, S. Echchakoui, N. Barka, The Integration of additive manufacturing into Industry 4.0 and Industry 5.0: A Bibliometric analysis (trends, opportunities, and challenges). Machines. **13**, 1–37 (2025). https://doi.org/10.3390/machines13010062
2. F. Lupi, A. Pacini, M. Lanzetta, Laser powder bed additive manufacturing: A review on the four drivers for an online control. J. Manuf. Process. **103**, 413-429 (2023). https://doi.org/10.1016/j.jmapro.2023.08.022
3. P. Pushp, S.M. Dasharath, C. Arati, Classification and applications of titanium and its alloys. Mater. Today Proc. **54**, 537-542 (2022). https://doi.org/10.1016/j.matpr.2022.01.008
4. T.C. Dzogbewu, Laser powder bed fusion of Ti6Al4V-xCu: Process parameters. J. Met. Mater. Miner. 31, 62-70 (2021). https://doi.org/10.55713/jmmm.v31i2.1051
5. T.C. Dzogbewu, I. Yadroitsev, P. Krakhmalev, I. Yadroitsava, A. Du Plessis, Optimal process parameters for in-situ alloyed Ti15Mo structures by Direct Metal Laser Sintering, in Proceedings of the 28th Annual International Solid Freeform Fabrication Symposium – An Additive Manufacturing Conference, Austin, Texas August 7-9 (2017).
6. I. Yadroitsev, P. Krakhmalev, I. Yadroitsava, Hierarchical design principles of selective laser melting for high quality metallic objects. Addit. Manuf. **7**, 45–56 (2015). https://doi.org/10.1016/j.addma.2014.12.007
7. T. C. Dzogbewu, Laser powder bed fusion of Ti15Mo. Results Eng. **7**, 100155 (2020). https://doi.org/10.1016/j.rineng.2020.100155
8. C.L. Chan, J. Mazumder, M.M. Chen, Three-dimensional axisymmetric model for convection in laser-melted pools. Mater. Sci. Technol. (United Kingdom). **3**, (1987). https://doi.org/10.1179/mst.1987.3.4.306
9. I. Yadroitsev, Selective laser melting: Direct manufacturing of 3D-objects by selective laser melting of metal powders. Appl. Catal. B Environ. **75**, (2009).

Cylindrical window mounting design for a mirror-steered optical system

Andrew Baloyi[1*]

[1]Council for Scientific and Industrial Research (CSIR), Defence and Security, Optronic Sensor

Abstract. The design of window mounting brackets is a vital stage in developing optical systems. Window mounting brackets must be designed so that thermal stresses remain low enough to prevent damage or cracking of the window during operation. In this paper, we reviewed various window mounting methods to mount a cylindrical window of a Mirror Steered Optical System currently under development by Optronic Sensor Applications (OSA) group at the Council for Scientific and Industrial Research (CSIR). Cylindrical windows have various challenges from optics perspective because they possess power, however in this paper, we only focused on their mounting methods and mounting bracket design. The review considered the window material selection, mounting bracket design & mounting methods, mounting bracket material selection and cost. Firstly, window and bracket materials were paired according to their coefficient of thermal expansions (CTE's). Secondly, various window mounting methods were explored and reviewed to select the optimal window mounting solution. Lastly, cost on the window – bracket material combination pairs were analysed. It was established that the best window - bracket material combination pair that resulted in lower thermal stresses was the Fused Silica – Invar 35-5 combination pair. For window mounting bracket design, the U-shaped seal design; utilizing Ethylene Propylene Diene Monomer (EPDM) as the seal was found to be the most optimal due to easy of manufacturing and integration. Lastly, regarding cost, the PYREX 7740 BOROFLOAT– Invar 42 pairing was determined to be the least expensive among all the combinations evaluated. This analysis will provide valuable insight about the design and selection of window materials to optimise cost while ensuring reliability, durability and functionality of the optical systems.

1 Introduction

Window mounting bracket design plays a crucial role in the design and development of optical systems. Windows in an optical system does not only transmit crucial electromagnetic radiation, but also protect the optical system's critical electronic components from dust particles, moisture, rain etc. Apart from this, they also need to meet stringent requirements such as high mechanical strength, robustness and resilience to impact damages to preserve their optical properties [1]. The first aspect to consider when designing optical window

* Corresponding author: abaloyi3@csir.co.za

mountings is material selection. Window mountings often involve the pairing of two dissimilar materials, i.e., window and mounting bracket materials. Selecting materials with coefficient of thermal expansions (CTE's) that are close to each other is therefore crucial. The second aspect to consider is the window mounting techniques/ methods on the mounting bracket material. Different mounting methods have their advantages and disadvantages, and it is important to select the optical one taking into consideration the optical systems application. The last aspect is cost. The materials selected for both window and window mount bracket must be within the project's budget. In this paper, we present a comprehensive review on various window mounting methods to be employed on the bracket design, taking into consideration material selection and cost. The window in question is a cylindrical window used on the Mirror Steered Optical System currently under development by the OSA group. In the literature, window mounting methods have been designed for flat and dome windows, and none for cylindrical windows. This paper will review these methods to establish if they are suitable to mount cylindrical windows. This analysis will offer important insights into the design, best mounting methods, and material selection needed to minimise costs while maintaining the reliability, durability, and performance of optical systems.

2 Methodology

The objective of this study was to examine the different methods for mounting a cylindrical window employed in the Mirror Steered Optical System. The window mounting bracket design is shown in Figure 1 below. Firstly, commonly used window materials for optical systems were surveyed and summarized, as presented in Table 1. As illustrated in the Table, all the essential properties of the selected window materials are incorporated. Secondly, window mounting bracket materials were also reviewed and tabulated as shown in Table 2. Window bracket material's critical properties that are sought after during the selection process are those that influence shape and position, i.e., specific stiffness, density and coefficient of thermal expansion (CTE) [1]. Thirdly, the window and mounting bracket materials were paired according to their coefficient of thermal expansions (CTE's). This was done to establish a combination that would result in the lowest thermal expansion during operation. Lastly, cost on each window – bracket material combination was evaluated to establish the combination with the least cost implications.

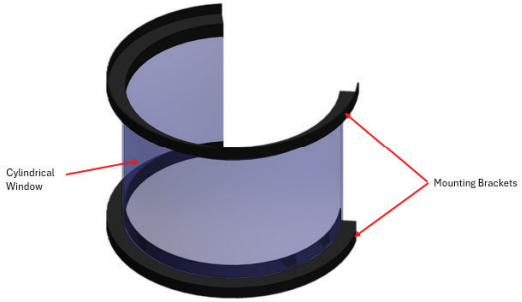


Fig. 1. Window mounting bracket sub-assembly.

Table 1. Window materials properties.

Material	**Fused Silica**	**Zerodur**	**N-BK7 borosilicate**	**BOROFLOAT borosilicate (PYREX 7740)**
Index of refraction (n)	1,458	1,542	1,517	1,472
Density [g/cm^3]	2,2	2,53	2,53	2,2
Coefficient of thermal expansion (CTE) [10^-6 /K]	0,56	0,05	7,1	3,25
Abbe number	67,8	56,2	64,2	65,7
Specific Stiffness [N*m/g]	33,2	35,7	32,7	28-32
Elastic Modulus [GPa]	73,2	91	80,7	65,5
Edmund cost (12,5mm uncoated) [rand]	1793	1312	1137	416

Table 2. Window mounting bracket material properties.

Material	**Invar 36**	**Invar 32-5**	**Kovar**	**Invar 42**
Density [g/cm^3]	8,11	8,15	8,36	8,11
Coefficient of Thermal Expansion (CTE) [10^-6 /K]	1,2	0,63	4,9-5,8 (5,35)	4-4,7 (4,35)
Specific Stiffness [N*m/g]	17,5	17,5	16,5-16,7	18,5
Elastic Modulus [GPa]	141	144	138	148
Cost per kilogram [Rands]	324-810	1350-2520	350-1100	340-680
Average cost per kilogram [Rands]	567	1935	725	510

3 Results and discussion

Table 3 shows comparative results of window - bracket material combination pairs. As stated, these combination pairs were conducted based the materials (window and bracket materials) coefficient of thermal expansions. As shown on the Table, the combination pair with the highest CTE percentage difference is Fused Silica – Invar 36 combination pair (53.5%). The combination pair with the least CTE percentage difference is Fused Silica – Invar 32-5 (12.5%). In terms of cost, the combination pair with highest cost is Fused Silica – Invar 32-5 (R3728), which is four times the cost of PYREXX 7740 BOROLFOAT – Invar 42 combination pair (the least costly combination pair).

Table 3. Window - mounting bracket combination pairs.

Combination Pairs	**Combination Pair 1**		**Combination Pair 2**		**Combination Pair 3**		**Combination Pair 4**	
Window and Bracket Materials	**PYREX 7740 BOROFLOAT**	**Invar 42**	**N-BK7**	**Kovar**	**Fused Silica**	**Invar 36**	**Fused Silica**	**Invar 32-5**
CTE values	3,25	4,35	7,1	5,35	0,56	1,2	0,56	0,63
CTE difference [%]	25.3		24.7		53.3		12.5	
Average Costs [Rands]	416	510	1137	725	1793	567	1793	1935
Total Cost [Rands]	926		1862		2360		3728	

As much as ma3terial selection is crucial in lowering the thermal stresses between dissimilar materials, the window mounting methods are equally important. Based on the design requirements, Table 4 shows the summary of the two selected methods that could be suitable to mount the cylindrical window. Figure 2 and Figure 3 show schematics of the two window mounting methods, the potted and U-shaped seal respectively. Both methods involve creating a groove, while the potted method additionally requires drilling holes through which silicone is poured to fill the groove. As illustrated in Table 4, the potted method requires silicone to cure before use, while the U-shaped seal does not.

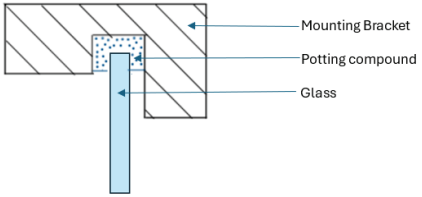


Fig. 3. Potted method.

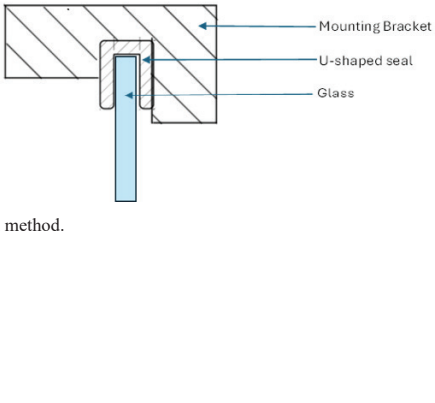


Fig. 4. U-shaped seal method.

Table 4. Window - mounting bracket combination pairs.

Design	**Potted Method**	**U-shaped Seal Design**
Material	Silicone - Dow 3145 RTV	EPDM (Ethylene Propylene Diene Monomer)
Manufacturing Requirements	Potting gap; holes for pouring the compound	Groove

4 Conclusions

This study conducted a review on window mounting bracket designs and mounting methods for Mirror Steered Optical System's cylindrical window. The objective of the study was to establish the best window – mounting bracket material combination pair, i.e., combination pair that resulted in lower thermal expansions, and therefore alleviate thermal stresses. The study also evaluated the costs associated with each combination pair. The combination pair with the highest CTE percentage difference was Fused Silica – Invar 36 combination pair (53.5%). The combination pair with the least CTE percentage difference was Fused Silica – Invar 32-5 (12.5%). In terms of cost, the combination pair with highest cost was Fused Silica – Invar 32-5 (R3728). The combination pair with the lowest cost factor was PYREX 7740 BOROFLOAT - Invar 42 (R926). Based on the requirements of the Mirror Steered System, PYREX 7740 BOROFLOAT - Invar 42 combination pair could be suitable, although the CTE percentage is 50% higher than that of Fused Silica – Invar 36.

References

1. D. Vukobratovich and P. Yoder, Fundamentals of Optomechanics, CRC Press, 2018.
2. A. Ahmad, Handbook of Optomechanical Engineering, CRC Press, 2017.
3. D. Vukobratovich, Optomechanical Design Principles, CRC Press, 1999.

08

ABSTRACTS

Process Development

Evaluation of thermal stability and phase transformation in β-type Ti-10Nb-1Ru alloy

Duduzile Nkomo[1,2*], *Roelf* Mostert[2], and *Maje* Phasha[1]

[1]Advanced Materials Division, Mintek, Johannesburg, Randburg 2125, South Africa
[2] Department of Materials Science and Metallurgical Engineering, University of Pretoria, Pretoria, Hatfield 0028, South Africa

Abstract. Phase stability of Ti-10Nb-1Ru alloy was investigated through integration of ab-initio calculations and experimental characterization. First-principles analysis of thermodynamic and mechanical properties identified the ω_{iso} phase as the most stable among all the configurations investigated. Conversely, experimental microstructural and thermal analyses revealed a multi-phase constituent at room temperature, predominantly comprised of β, α″ and ω_{ath} phases. Differential Scanning Calorimetry (DSC) identified α″→β and ω→β transformations at temperatures exceeding 100°C upon heating. Current results reveal that besides alloy's biocompatibility and potential shape-memory effect suitable for biomedical applications, this alloy demonstrates high-temperature phase transition, a characteristic required for high-temperature shape memory alloys.

1 Introduction

Ti-Nb alloys have been extensively researched for biomedical applications, owing to their superior biocompatibility, corrosion resistance, and inherent shape memory properties [1]. However, their functional performance is often constrained by low transformation strains. This limitation is largely attributed to the similar atomic radii of Ti and Nb; consequently, alloys exceeding 15 at. % Nb typically exhibit inadequate transformation strain [2-4].

To address this, several studies have attempted to reduce Nb content to enhance strain; however, decreasing Nb concentrations often compromises β phase stability at room or near body temperature, leading to poor superelastic (SE) properties in ternary systems [3,4].

Recent work by Wen et al. [5] demonstrated that adding Ru to Ti-20Nb-(0-1.5)Ru alloys effectively stabilised β phase and enhanced yield strength, suggesting that Ru is a highly desirable ternary addition.

Accordingly, the present study explores an alloy containing less than 15 at. % Nb with minor Ru addition (1 at. %) to optimise performance for both biomedical and high-temperature applications.

2 Methodology

* Corresponding author: dudunk@mintek.co.za

Theoretical investigations were conducted using density functional theory (DFT) based first-principles calculations, as implemented in the CASTEP code. The virtual crystal approximation (VCA) was employed to simulate the multicomponent system. VCA crystal models for the β, α″,α and the ω phases of the Ti-10Nb-1Ru (at.%) alloy were constructed to determine lattice parameters, thermodynamic stability, and elastic properties from the resulting geometry-optimised structures.
The microstructure and phase identification of homogenised and water-quenched samples were characterised using optical microscopy (OM) and X-ray diffraction (XRD), while phase transformation behaviour was determined via differential scanning calorimetry (DSC).

3 Results and discussions

First-principles calculations indicated that the ω phase is the most thermodynamically and mechanically stable phase for the Ti-10Nb-1Ru alloy. In contrast, experimental data at room temperature identified the β phase as the predominant constituent, as evidenced by prominent XRD peaks. Furthermore, DSC analysis revealed two distinct exothermic events at approximately 400 and 600°C, corresponding to the dissolution of the α″ and ω phases into the β matrix, respectively.

4 Conclusions

Theoretical and experimental investigations into the thermal stability and phase transformations of the Ti-10Nb-1Ru alloy demonstrated that, while the β phase was predominantly retained upon cooling to room temperature, subsequent transitions from ω or α″ phases at temperatures above 100°C during heating highlighted its versatility. These results confirmed the alloy's suitability for development in both biocompatible medical devices and high-temperature structural applications.

References

1. L.C. Zhang and L.Y. Chen, A review on biomedical titanium alloys: recent progress and prospect. Advanced engineering materials, **21**(4), p.1801215 (2019)
2. H.Y. Kim, Y. Ikehara, J.I. Kim, H. Hosoda, S. Miyazaki, Martensitic transformation, shape memory effect and superelasticity of Ti–Nb binary alloys. Acta materialia, **54**(9), pp.2419-2429 , (2006)
3. S. Miyazaki, H.Y. Kim, H. Hosoda, Development and characterization of Ni-free Ti-base shape memory and superelastic alloys. Materials Science and Engineering: A, **438**, pp.18-24 (2006)
4. D.C. Zhang, Y.F. Mao, Y.L. Li, J.J. Li, M. Yuan, J.G. Lin, Effect of ternary alloying elements on microstructure and superelasticity of Ti–Nb alloys. Materials Science and Engineering: A, **559**, pp.706-710 (2013)
5. A. Biesiekierski, J. Lin, Y. Li, D. Ping, Y. Yamabe-Mitarai, C. Wen, Impact of ruthenium on mechanical properties, biological response and thermal processing of β-type Ti–Nb–Ru alloys. Acta Biomaterialia, **48**, pp.461-467 (2017)

System dynamics-based modelling for remaining useful life estimation of bearings in rotating machinery

Themba Mashiyane[1,2*], *Lagouge* Tartibu[2] , *Mosa* Machesa[2]

[1]Specialised Testing & Sustainable Energy Research, Eskom, Research Testing & Development, Johannesburg, South Africa.
[2]Department of Mechanical & Industrial Engineering Technology, University of Johannesburg, Johannesburg, South Africa

Abstract. Unexpected failures of rotating machinery remain a major challenge in industrial equipment, particularly in energy and process plants where bearing faults contribute significantly to machinery downtime. This study presents a system dynamics-based modelling approach for estimation of the remaining useful life of bearings to support predictive maintenance planning. The model represents bearing degradation as a stock variable governed by a degradation rate influenced by key operating factors, including mechanical load, shaft misalignment, and operating temperature. Simulation results illustrate the nonlinear responses prescribed by the operating conditions on bearing life. An increase in operating temperature from 60°C to 80°C reduced the predicted bearing life from 50,000 hours to 27,400 hours. Similarly, increased shaft misalignment (0.8 relative to an allowable limit of 0.5) reduced the predicted life to 31,200 hours under nominal operating conditions. These conditional outputs highlight the sensitivity of bearing model to its thermal and alignment conditions. The proposed model provides a dynamic approach for capturing degradation behaviour and provides a framework for investigating maintenance scenarios to improved maintenance decision-making in rotating machineries.

1 Introduction

Rotating Rotating machinery is widely used in industrial systems such as power plants, manufacturing facilities, mining operations, and chemical processing industries. The reliable operation of these systems depends heavily on the condition of critical components such as rolling element bearings [1]. Bearings support rotating shafts and reduce friction between moving parts; however, they are also among the most failure-prone components in rotating machinery [2]. Bearing failures can lead to severe operational disruptions, unplanned downtime, and significant economic losses. As a result, predicting bearing degradation and

*Corresponding author : tmashiyane12@gmail.com

estimating remaining useful life (RUL) has become an important focus in reliability engineering and maintenance management.

Advances in sensing technologies, condition monitoring systems, and data analytics have accelerated the adoption of predictive maintenance strategies. Modern industrial systems generate large volumes of operational data, enabling the development of models capable of predicting equipment failure before it occurs [4]. Techniques such as vibration monitoring, temperature analysis, and lubricant condition monitoring are widely used to detect early signs of bearing faults and assess machinery health [5]. This study develops a system dynamic-based model that integrates key operational factors influencing bearing degradation to predict RUL and provide indicators such as the Bearing Health Index (BHI) to support improved maintenance planning and reliability.

2 Methodology

This study develops a system dynamics model for estimating the remaining useful life of bearings in rotating machinery. The modelling approach captures the interaction between operational conditions and bearing degradation mechanisms to estimate the progression of wear and predict maintenance in compliance with ISO 281 bearing life requirements [3]. The methodology consists of three main stages: model development, parameter definition, and simulation analysis, as shown in Figure 1.

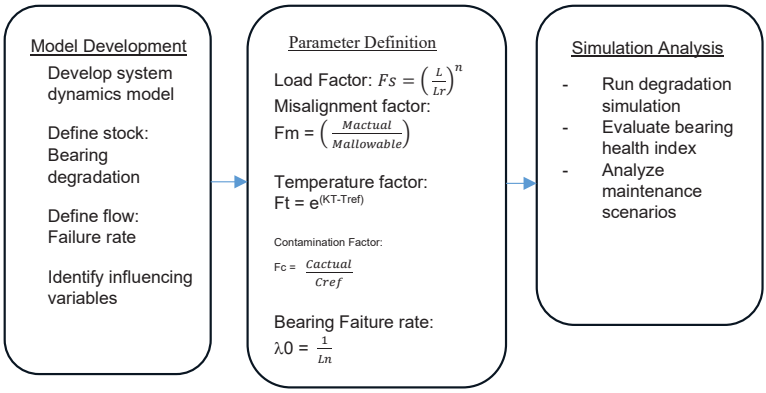


Fig. 1. System dynamics methodology for bearing useful life prediction

The model represents bearing degradation as a stock variable governed by a degradation rate influenced by operating conditions. Key factors such as mechanical load, misalignment, temperature, and contamination are incorporated through intermediate variables that determine the bearing failure factor. The parameter definition stage establishes mathematical relationships for these factors, while simulation analysis evaluates their impact on degradation progression. The model outputs key indicators, including the Bearing Health Index (BHI) and Remaining Useful Life (RUL), as shown in Figure 2

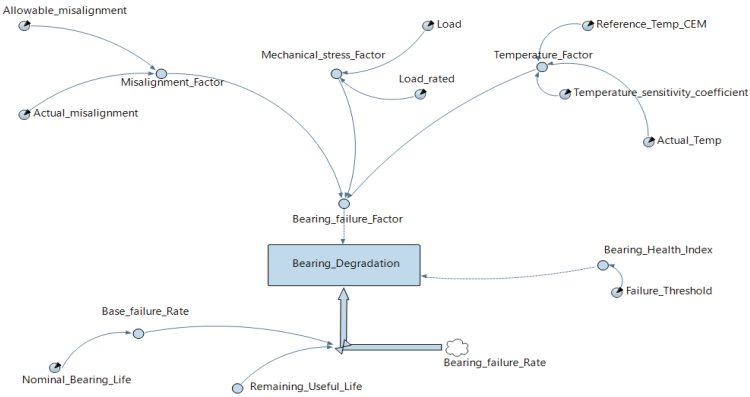


Fig. 2. Bearing degradation Stock-flow diagram

3 Conclusion

This study presented a system dynamics-based modelling approach for predicting the estimated remaining useful life (RUL) of rolling element bearings under varying thermo-mechanical operating conditions. The model represents bearing degradation as a dynamic stock variable governed by a degradation rate influenced by key factors, including operating temperature, shaft misalignment, and mechanical load. Simulation results illustrate that operating conditions have a significant and nonlinear impact on bearing degradation. An increase in temperature from 60°C to 90°C resulted in a substantial reduction in bearing life from approximately 50,000 hours to 20,322 hours, illustrating the thermal sensitivity. Similarly, increased shaft misalignment was shown to accelerate degradation and reduce bearing life, even under otherwise operating conditions. The combined analysis further reproduced that thermo-mechanical effects are nonlinear and non-additive. The interaction between temperature and misalignment leads to a multiplicative amplification of the failure rate, resulting in a more severe reduction in RUL than when considering individual factors independently. This behaviour reflects predicted industrial conditions, where multiple stressors act simultaneously on rotating machinery components. To capture these interactions, the study introduced theThermo-mechanical degradation model, which provides a unified formulation for estimating bearing remaining useful life based on coupled operating conditions. The model integrates exponential thermal effects, power-law mechanical loading, and proportional misalignment influence within a system dynamics approach, offering a physically interpretable approach to degradation modelling.The simulations illustrate conditional bearing-life responses under selected operating scenarios. The temperature response follows the prescribed exponential relationship, while the misalignment response follows the proportional modifier. Their combined influence reflects the multiplicative structure of the model. The framework provides an interpretable basis for investigating degradation scenarios; however, its predictive accuracy requires calibration and independent bearing-life validation in future research.

References

[1.] T. Mashiyane, D. Desai, L. Tartibu. Numerical simulation of the effect of angular misalignment on the dynamic behaviour of bearing. MATEC Web Conf. 370 09003 (2022). https://doi.org/10.1051/matecconf/202237009003

[2.] T. Mashiyane, D. Desai, & L. Tartibu. Finite Element Analysis of the Thermo-mechanical Behaviour of Defect-Free Cylindrical Roller Bearing in Operation. Arab J Sci Eng 47, 8577–8587 (2022). https://doi.org/10.1007/s13369-021-06412-4

[3.] International Organization for Standardization, ISO 281: Rolling Bearings - Dynamic Load Ratings and Rating Life, Geneva, Switzerland, 2007

[4.] J. Lee, H.A. Kao, and S. Yang, Service innovation and smart analytics for Industry 4.0 and big data environment, Procedia CIRP, vol. 16, pp. 3–8, (2014). https://doi.org/10.1016/j.procir.2014.02.001

[5.] R.B. Randall. Vibration-Based Condition Monitoring : Industrial, Aerospace and Automotive Applications, John Wiley & Sons, (2011). https://doi.org/10.1002/9780470977668

Evaluation of HHD62G medical-grade high-density polyethylene before use in material extrusion additive manufacturing for fabrication of craniomaxillofacial augmentation implants

Rebakakgosi Mohutsiwa[1*], *Jacobus* van der Walt[1], *and Hercules* van den Heever[1]

[1*]Central University of Technology, Department of Mechanical and Mechatronics Engineering, Private Bag X20539, Bloemfontein, Free State 9300, South Africa.

Abstract. High-density polyethylene (HDPE) is often used to cosmetically augment facial features such as cheekbones, cranium, and nasal bones when affected by deformities. This is made possible by its ability to bond with tissues. Material extrusion additive manufacturing (ME-AM) promises to enable the direct production of HDPE patient-specific porous facial implants. However, this approach is limited by the material's shrinkage behaviour and part warpage issues when processed through ME-AM technologies. This paper aims to evaluate HHD62G medical-grade HDPE and predict material performance before being used in ME-AM for fabricating facial augmentation implants.

1 Introduction

Material extrusion additive manufacturing (ME-AM) technologies have the potential to fabricate patient specific implants using medical-grade high-density polyethylene (HDPE) by enabling precise material placement, controlled internal geometry, and implant customisation through integration with medical imaging data [1-4]. Medical-grade materials often come with biological substances which improve their properties and enhance their biological performance at the cost of rendering these materials unsuitable for ME-AM. HDPE, in particular, has proven problematic when processed through ME-AM. Wampol [5] noted that extruded rasters of HDPE material exhibit poor adhesion to the build platform. This material behaviour was linked to significant thermal shrinkage and severe part warpage upon material cooling [5]. Hence, a comprehensive material evaluation is essential for evaluating the material and assessing its properties before use in ME-AM. This evaluation of the material will also help predict its processability in ME-AM and prevent future hurdles when medical-grade HDPE material is to be processed in ME-AM. Differential scanning calorimetry (DSC), melt flow index (MFI) testing, thermogravimetric analysis (TGA), Fourier transform infrared spectroscopy (FTIR), and x-ray diffraction (XRD) together aim to

* Corresponding author: MohutsiwaRR@gmail.com

screening, assess and evaluate the HDPE material predict its performance in ME-AM prior to the fabrication of porous implant structures.

2 Methodology and results

Medical-grade HDPE pellets (Repsol Healthcare® HHD62G) from Repsol Quima, S.A, supplied by Peak Performance Compounding, LLC, were chosen for this study. The MFI testing of these pellets was carried out in accordance with ASTM D1238-23a using a Davenport extrusion plastometer from AMETEK. Inc. DSC, TGA, FTIR and XRD of the pellets were conducted at the Department of Chemistry at the University of the Free State. DSC analysis of the HHD62G HDPE sample which weighed 12.24 mg was conducted under a nitrogen atmosphere with a flow of 50 ml/min using a TA DSC2500® instrument. TGA analysis was performed on one sample of the polymer using a Mattler Toledo (TGA/SDTA851®) apparatus. The sample weighed 12.2 mg and was heated up to a maximum temperature of 600 °C at a constant heating rate of 10 °C/min under a nitrogen atmosphere. Fourier-transform infrared spectroscopy was conducted using the medical-grade HDPE pellets on a Bruker Tensor 27® FTIR spectrometer. The infrared spectra were measured within a wavenumber range of 399 to 4000 cm^{-1} to identify the chemical nature and oxidation of the polymer and its additives. XRD analysis was performed on the medical-grade HDPE polymer using a Malvern Panalytical – Empyrean® diffractometer at Department of Geology at the University of the Free State. Using tube settings of 40 mA and 45kV, the HDPE sample was scanned between 3.5º and 70º 2θ angles. Following results of the material evaluation, filament was produced using a Precision Series 450 filament maker from 3devo. The filament batches which satisfied the quality control criteria were subjected to preliminary extrudability tests using a Creality CR-200B® 3D Printer from Creality 3D Technology Co., Ltd. The results from these tests are shown in Table 1 below.

Table 1. Material evaluation results

Property	**Results**
MFI (g/10 min)	0.299
Peak melting temperature (^{o}C)	Approximately 136
Degree of Crystallinity (%)	60 - 65
Onset degradation temperature (^{o}C)	398
FTIR spectra (cm^{-1})	2916 – 2848 and 1460 - 1470 (HDPE signature peaks) 720 – 730 (confirmation of material purity)
Major XRD peaks (º, 2θ)	21.7 and 24.1
Filament diameter (mm)	1.75 ± 0.05
Extrudability in ME-AM	Continuous and smooth extrusion with no material blockages.

3 Discussion of results

The MFI results showed that the HHD62G medical-grade HDPE pellets have high viscosity and controlled flow behaviour confirming its potential for the fabrication of high strength HDPE filaments for use in ME-AM. The DSC revealed reasonable peak melting temperatures and high degree of crystallinity further demonstrating that these HDPE pellets have high structural order and dimensional stability needed for the fabrication of dimensionally stable implants. TGA also added to this and indicated that the material was thermally stable with

onset degradation temperatures above typical extrusion temperatures often used for HDPE and related polymeric materials. The absorption bands observed under the FTIR spectroscopy confirming material purity and characteristic HDPE spectra and the presence of characteristic short-chain branching which enhanced the materials processability as a melt. XRD analysis also detected two prominent peaks which correspond with orthorhombic HDPE. Filament fabrication produced a consistent diameter which was successfully run through the ME-AM at different temperatures which ranged between 235 °C and 260 °C.

4 Conclusion

The overall results presented in this study have shown that Repsol Healthcare® HHD62G HDPE material is thermally robust and possesses the melt processing characteristics necessary for successful HDPE filament fabrication and basic extrusion in the ME-AM technology. The material's chemical purity, controlled branching, high crystallinity, and good thermal stability makes it suitable for producing mechanically stable, biocompatible and reliable components through the ME-AM process. These results lay a strong foundation for studies focusing on the evaluation of the material's suitability to exhibit good printing behaviour and produce dimensionally stable and accurate objects with good mechanical performance under controlled ME-AM processing conditions.

References

[1] S. Polo, A. García-Domínguez, E. M. Rubio, and J. Claver, Lattice Structures in Additive Manufacturing for Biomedical Applications: A Systematic Review. Polymer. **17**, 2285 (2025). https://doi.org/10.3390/polym17172285

[2] M. Samykano, R. Kumaresan, J. Kananathan, K. Kadirgama, and A. K. Pandey, An overview of fused filament fabrication technology and the advancement in PLA-biocomposites. Int. J. Adv. Manuf. Technol. **132**, 27–62 (2024). https://doi.org/10.1007/s00170-024-13394-1

[3] A. Das, E. L. Gilmer, S. Biria, and M. J. Bortner, Importance of Polymer Rheology on Material Extrusion Additive Manufacturing: Correlating Process Physics to Print Properties. ACS Appl. Polym. Mater. **3**, 1218–1249 (2021). https://doi.org/10.1021/acsapm.0c01228

[4] G. D. Goh, Y. L. Yap, H. K. J. Tan, S. L. Sing, G. L. Goh, and W. Y. Yeong, Process–Structure–Properties in Polymer Additive Manufacturing via Material Extrusion: A Review. Crit. Rev. Solid State Mater. Sci. **45**, 113–133 (2020). https://doi.org/10.1080/10408436.2018.1549977

[5] C. Wampol, Additive Manufacturing with High Density Polyethylene: Mechanical Properties Evaluation, Master Thesis, South Dakota University, Brookings, South Dakota (2018)

Performance evaluation of a polynomial regression based NUC for variable integration-time

Mathews Chirindo[1*] and *Mirriam* Molekoa[1]

[1]Council for Scientific and Industrial Research, Manufacturing Cluster, South Africa

Abstract. Non-Uniformity Correction (NUC) is essential for improving infrared image quality but is challenged by calibration-factor storage demands and performance variations under variable integration times and operating temperatures. This paper investigates a temperature-adaptive Polynomial Regression Model (PRM) for NUC under variable integration-time conditions. The proposed method employs temperature-interpolated polynomial coefficients to estimate corrected pixel values across varying operating conditions, validated using real detector data and compared against the two-point NUC (TPN) and a 2D calibration scheme. Results demonstrate that PRM reduces memory requirements by a factor of three compared with TPN while maintaining residual non-uniformity (RNU) below 1% across tested integration times.

1 Introduction

The pixel response in the Focal Plane Array (FPA) of an infrared camera is inherently not uniform owing to imperfections in the manufacturing process relating to detector material deposition, pixel microstructures, and readout electronics. The pixel-to-pixel variation manifests as fixed pattern noise or spatial non-uniformity. Several methods are proposed to correct for this non-uniformity with the intent to enhance image quality. However, most of these methods are challenged by increased storage demand and performance variations especially when the camera integration time is to be varied. In this case separate storage space is required for the gain and offset calibration factors at each integration time leading to critical hardware constraints.

The choice of the NUC method in a variable integration time use case is determined by the level of accuracy required in addition to the available storage space. In this paper, we propose to evaluate a temperature-adaptive polynomial regression framework for variable integration-time operation. The performance of this approach is compared with that of the traditional TPN [1] and a two-dimension calibration method proposed in [2].

2 Polynomial regression model

* Corresponding author: mchirindo@csir.co.za

The PRM NUC method estimates the corrected value at each pixel position in the FPA based on the raw pixel value at a certain integration-time and interpolated temperature within the calibration range. For each pixel, a polynomial regression model is fitted across the raw data taken at different integration-time points. The polynomial model learns from a dataset consisting of: 1) low temperature frames from a uniform blackbody scene captured at 8 integration-time points. 2) high temperature frames from a uniform blackbody scene captured at 8 integration-time points.

For each pixel, the low and high temperature models are given in (1) below.

$$D_{corr}^{L}(y) = a_0^L + a_1^L y + a_2^L y^2, \qquad D_{corr}^{H}(y) = a_0^H + a_1^H y + a_2^H y^2 \qquad (1)$$

where y is the raw pixel value, $a_0^L\ a_1^L\ a_2^L$ are the low temperature coefficients and $a_0^H\ a_1^H\ a_2^H$ are the high temperature coefficients. D_{corr} is the corrected digital number of the pixel after NUC. For any arbitrary temperature, T between the low and high temperatures (T_L, T_H) the interpolated polynomial coefficients are found from:

$$a_k(T) = \alpha a_k^L + (1-\alpha)a_k^H \qquad (2)$$

where $\alpha = \frac{T-T_H}{T_L-T_H}$, k is the polynomial order index.

The full correction polynomial regression model for each pixel position, i, j is shown in compact form as:

$$D_{corr,ij} = \sum_{k=0}^{n}[\alpha a_k^L + (1-\alpha)a_k^H]y_{i,j}^k \qquad (3)$$

where n is the polynomial degree.

Instead of storing all the gain and offset maps at each integration time in the traditional TPN, the PRM only stores the polynomial coefficients for each pixel, thereby significantly reducing the storage demand while presenting acceptable image quality. The performance is also compared with a two-dimensional calibration method proposed in [2].

In this extended abstract, the performance of the PRM is evaluated in terms of the Residual Non-Uniformity (RNU) percentage as follows:

$$RNU(\%) = \frac{\sigma}{\mu} \times 100 \qquad (4)$$

where σ and μ are the standard deviation and mean of the corrected image, respectively.

The memory budget is calculated per NUC method based on the amount of calibration coefficients and base images (if applicable) required.

In the full paper, metrics such as radiometric linearity and integration time drift are evaluated.

3 Test results

The RNU(%) performance evaluation of the PRM against the TPN and the 2D Calibration methods is shown in Fig. 1. It is seen that that the PRM performs better than the 2D Calibration method while the TPN performance is superior in this metric. The TPN is explicitly optimized to minimize fixed-pattern noise between exactly two temperatures /

radiance points while PRM spreads its fitting power across temperatures and integration times.

The memory budget for the three NUC methods is shown in Fig. 2. The PRM reduces memory requirements by a factor of three compared with TPN. The results are based on the second polynomial order which strikes a balance between accuracy and compute complexity.

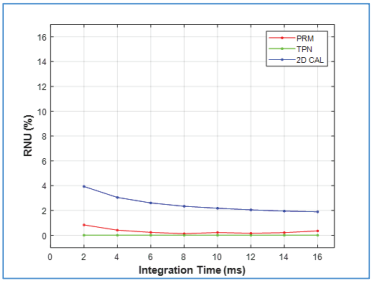


Fig. 1. Residual Non-Uniformity (RNU) performance evaluation of the proposed PRM against the TPN and the 2D Calibration methods.

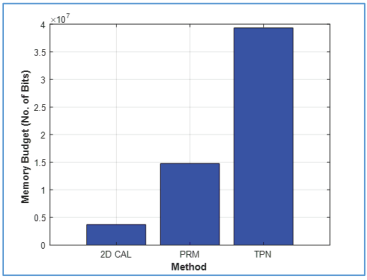


Fig. 2. Memory budget evaluation of the proposed PRM against the TPN and the 2D Calibration methods.

4 Conclusion

The PRM based NUC achieves a residual non-uniformity (RNU) of less than 1% across the evaluated integration-time while requiring three times less memory than the TPN. The results demonstrate that the PRM provides a practical and flexible correction framework for variable operating conditions while significantly reducing calibration storage requirements.

References

1. J. C. Njuguna, E. Alabay, A. Celebi, A. T. Celebi, M. K. Gullu, Field programmable gate arrays implementation of two-point non-uniformity correction and bad pixel replacement algorithms, in 2021 International Conference on INnovations in Intelligent SysTems and Applications (INISTA), Kocaeli, Turkey, Aug 25-27 (2021).
2. N. Chen, J. Zhang, S. Zhong, Z. Ji, L. Yao, Nonuniformity correction for variable-integration-time infrared camera, JPHOT, **10**, 2881393 (2018).

An initial dynamic resource-driven activity-based framework for identification of cost drivers within the laser powder bed fusion process chain

Tadiwanashe Zinzombe[1], *Natasha* Sacks[1*], and *Theuns* Dirkse van Schalkwyk[1]

[1]Department of Industrial Engineering, Stellenbosch University, South Africa

Abstract. Laser powder bed fusion costing often overlooks pre- and post-processing, which can distort economic evaluations by 50%. This paper proposes a structured framework using Time-Driven Activity-Based Costing to decompose the manufacturing process chain into measurable activities. By mapping resources and drivers across unit levels, the framework dynamically allocates expenditures. Crucially, it integrates sustainability indicators of carbon footprint and material recycling, thereby addressing a major literature gap. This approach quantifies the cost-sustainability nexus providing a robust tool that captures many economic and environmental cost drivers to support lifecycle costing.

1 Introduction

Laser powder bed fusion (LPBF) offers several manufacturing benefits such as design complexity, lean production, and short lead times, yet its industrial adoption is sometimes constrained by uncertainties regarding production and investment costs, and environmental impact. While the build phase is typically the primary focus in LPBF, the complete process is based on a complex workflow including digital preparation, powder feedstock preparation, thermal and/or mechanical finishing, and rigorous quality inspection [1-2]. Accurate cost estimation remains a challenge because many frameworks overlook soft costs such as iterative software workflows, machine cleaning, and manual support removal, which increases labour and overhead costs [3-4]. Prior research into LPBF economics has produced various design-to-cost tools, but these suffer from a build-centric perspective that omits critical downstream operations like heat treatment or indirect costs such as ancillary equipment [5]. A notable limitation is the treatment of material costs, where many frameworks assume near-infinite powder reuse, ignoring how degradation and complex sieving or mixing policies drive both quality risks and expenses [1], [5-6]. Furthermore, sustainability assessments often treat environmental metrics qualitatively or in isolation, despite evidence that electricity consumption, powder production, and energy-intensive post-processing (representing up to 25% of total energy) are key contributors to the carbon footprint [7-8].

* Corresponding author: natashasacks@sun.ac.za

Thus, there is a need for a framework which maps all activities in the LPBF process chain from pre-processing to post-processing and captures all relevant cost drivers including the main sustainability metrics. This study introduces a structured framework mapping the LPBF process chain using a Time-Driven Activity-Based Costing (TDABC) approach. By mapping costs to the time spent on each task, it captures the overlooked soft costs such as machine setup and gas purging. The framework also integrates sustainability indicators of carbon footprint and material recycling.

2 Methodology and results

The methodology centres on an Activity-Resource-Data Mapping strategy which systematically decomposes the LPBF process chain into sequential pillars. The framework first establishes a comprehensive process chain covering the pre-processing, processing, and post-processing stages. Once the chain is defined, each specific activity within it is identified along with its corresponding cost driver. By applying TDABC logic, the framework maps costs directly to the time-resolved consumption of resources, such as labour hours or machine run-time. This ensures that each unit of time spent by a resource is linked to a specific activity, thereby providing a granular view of cost accumulation from digital file preparation to final quality assurance.

The results demonstrate that this framework transitions from static estimates to a dynamic framework that accounts for operational variance. By identifying cost drivers for every activity and machine used, the framework can simultaneously calculate the carbon footprint associated with each activity based on power ratings and duration of use. Furthermore, it accounts for material collection, sieving, and recycling rates. By structuring the framework to recognize stochastic inputs, it allows for the mathematical propagation of uncertainty throughout the process chain. This is critical for capturing how fluctuations in material waste and manual post-processing impact both economic and environmental performance indicators.

3 Conclusion

This framework overcomes the limitations of a build-centric approach for LPBF costing by integrating Time-Driven Activity-Based Costing with a comprehensive LPBF manufacturing process chain analysis. By mapping all the manufacturing activities to their specific economic and environmental drivers, the framework captures hidden variables which contribute towards total manufacturing cost and performance. It also bridges the sustainability data gap through formal cost driver identification and a mathematical basis for material recycling and carbon footprint. Overall, the framework is a robust tool that captures many economic and environmental cost drivers which is currently missing in published literature.

The authors acknowledge the funding of the research study by the Collaborative Programme in Additive Manufacturing (CPAM) and the Council for Scientific and Industrial Research (CSIR) (Grant no. CPAM-25-PGS-09). The opinions expressed and the conclusions arrived at are those of the authors and are not necessarily to be attributed to the CPAM or the CSIR.

References

1. M.W. Barclift, Cost modeling and design tools for additive manufacturing with laser powder bed fusion, Master Thesis, Pennsylvania State University, USA, (2019) https://etda.libraries.psu.edu/catalog/14896mzb5747

2. S. Afazov et al., Metal powder bed fusion process chains: an overview of modelling techniques. Prog. Addit. Manuf. **7**, 289-314 (2022) https://doi.org/10.1007/s40964-021-00230-1
3. P. Parenti, D. Puccio, Q. Semeraro, B.M. Colosimo, A techno-economic approach for decision-making in metal additive manufacturing: metal extrusion versus single and multiple laser powder bed fusion. Prog. Addit. Manuf. **9**, 185-210 (2024) https://doi.org/10.1007/s40964-023-00442-7
4. B. Karaş, A. Shokrani, Activity-based costing of laser powder-bed additive manufacturing incorporating discrete event simulation. npj Adv. Manuf. **2**, 24 (2025) https://doi.org/10.1038/s44334-025-00036-x
5. Q. Jarrar, F. Belkadi, A. Bernard, An activity-based costing model for additive manufacturing, in Proceedings of the PLM2021 conference, Product Lifecycle Management: Green and Blue Technologies to Support Smart and Sustainable Organizations, Curitiba, Brazil, July 11-14, edited by O. Canciglieri Junior, F. Noël, L. Rivest, A. Bouras (IFIP Advances in Information and Communication Technology, **639**, Springer, Cham, 2022), 492-507 https://doi.org/10.1007/978-3-030-94335-6_35
6. R. Al-zqebah, M. Guertler, L. Clemon, Powder bed fusion factory productivity increases using discrete event simulation and genetic algorithm. Prod. Eng. **19**, 29-45 (2025) https://doi.org/10.1007/s11740-024-01286-y
7. G.M. Cappucci, M. Pini, P. Neri, M. Marassi, E. Bassoli, A.M. Ferrari, Environmental sustainability of orthopedic devices produced with powder bed fusion. J. Ind. Ecol. **24**, 681-694 (2020) https://doi.org/10.1111/jiec.12968
8. T. Anwar, A.C. Lopes, E.C. Silva, S.T. Mould, A.M. Sampaio, A.J. Pontes, Cradle-to-gate life cycle assessment: a comparison of polymer and metal-based powder bed fusion for the production of a robot end-effector with internal conformal channels. Prog. Addit. Manuf. **10**, 561-579 (2025) https://doi.org/10.1007/s40964-024-00640-x

Experimental investigation of process characteristics in a 5-axis composite additive manufacturing system

Daniel Kirkman[1*] and *Riaan* Stopforth[2]

[1]University of KwaZulu-Natal, Discipline of Mechanical Engineering, Durban, 4001, South Africa
[2]University of KwaZulu-Natal, Scientific Multidisciplinary Advanced Research Technologies (SMART) Lab, Durban, 4001, South Africa

Abstract. A 5-axis composite additive manufacturing system is under development to address strength limitations associated with conventional fused filament fabrication approaches. Glass fibre reinforcement is added to a photopolymer resin, while a cartesian 3D printer with tilting build platform executes toolpaths. Results of tests to evaluate the performance of the system under various conditions are reported. Pulling force on the fibres was measured for several angles of the nozzle relative to the toolpath. Alternative motion configurations were explored for curved toolpaths, and the effectiveness of different nozzle profiles was evaluated. Results inform parameter selection and machine configuration for improved part quality.

1 Introduction

Polymer additive manufacturing (AM) incorporating continuous fibre reinforcement is seeing increasing attention from both the academic and industrial sectors [1]. A key limitation of conventional layer-based methods of AM which incorporate continuous fibre reinforcement is that the reinforcement is constrained to layers which often do not coincide with load paths [2], [3]. The reinforcing effect of continuous fibres is thus limited. Several studies have investigated the deposition of reinforcement fibres along nonplanar toolpaths for the reinforcement of 3D printed parts [4]–[6]. Improved mechanical performance has been reported [6]. However, such approaches are accompanied by increased machine and toolpath complexity, as nonplanar deposition may require 4 or 5-axis motion of the deposition head.

A novel 5-axis AM system facilitating continuous glass fibre reinforcement of a UV-curable resin via an instant-curing pultrusion process has been developed. The system, pictured in Figure 1, is capable of executing freeform toolpaths. Two build platform configurations are available: the tilt-tilt configuration shown in Figure 1, and a tilt-rotate configuration. Parameters affecting the quality of depositions include nozzle shape, fibre content, deposition speed, the relative angle of the nozzle to the toolpath, and nature of the relative movement between the nozzle and the build platform when depositing curved

* Corresponding author: kirkmand@ukzn.ac.za

segments. This study presents the results of several experiments in which these parameters are varied in order to gain a better understanding of the system's behaviour.

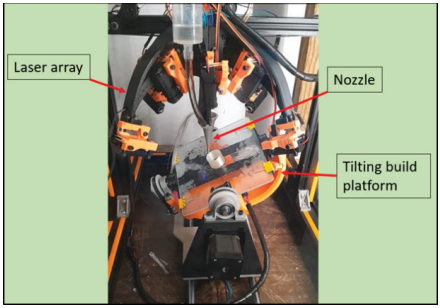


Fig. 1. Five-axis composite additive manufacturing apparatus

2 Methodology and results

2.1 Relative nozzle angle tests

Relative nozzle angle is defined as the angle between the nozzle centreline and the tangent to the toolpath where the toolpath and the nozzle exit intersect. In conventional "2.5D" printing processes, the relative nozzle angle is restricted to 90°. For a freeform deposition process, this angle can deviate from 90° for several reasons, including to avoid collisions of the nozzle with previously deposited segments, and to reduce flaring of the fibre yarns as they exit the nozzle. In the AM process under development, fibres are pulled through the nozzle by relative motion between the nozzle and the build platform. The force required to pull the fibres through the nozzle is dependent on the relative nozzle angle. Pulling force in turn determines the freeform deposition capabilities of the system, as a pulling force which is too large can restrict the ability of the system to deposit unsupported segments or segments along curved toolpaths. A series of tests was conducted to assess the effect of relative nozzle angles on pulling force, at various speed and fibre loading values. Pulling force was measured using a pulley system and a scale, allowing for reliable force measurements. Results indicated an exponential increase in pulling force as relative nozzle angle decreased. A minimum value of 80° for the relative nozzle angle is suggested to avoid excessively high pulling forces.

2.2 Relative nozzle motion tests

When executing planar or near-planar curved toolpaths with a 5-axis motion system, there are two possible ways to achieve the necessary motion between the nozzle and the build platform. The first method is to use predominantly linear motion of the axes, as in "2.5D" printing. When executing curved toolpaths, such as for spiralized cylindrical structures, this approach results in fibre twisting as there is rotation of the nozzle relative to the build platform. An alternative approach is to use build platform (C-axis) rotation to achieve curved toolpaths. Using this approach, the "inside edge" of the nozzle remains on the inside of the circular toolpath, and fibre twisting is diminished. Cylindrical test parts were fabricated using both approaches, and fibre twisting was assessed using microscope images. Results showed an improvement in surface quality and fibre placement for the second approach.

2.3 Alternative nozzle profile

Round nozzles are conventionally used for 3D printers. However, a limited number of studies have investigated alternative nozzle shapes [7]. The effects of a square nozzle on fibre placement was investigated by fabricating cylindrical test parts. Results indicated improved surface finish and fibre placement, as well as reduced fibre flaring when using a square nozzle in place of a circular nozzle. However, it was noted that, when using a square nozzle, relative rotation between the build platform and the nozzle must be eliminated. This requirement necessitates the addition of an extra rotational axis when executing more complex toolpaths.

3 Conclusion

A series of tests was conducted to assess the characteristics of a novel 5-axis composite AM system. Firstly, the pulling force required to pultrude yarns trough the deposition head was measured for various relative nozzle angles. Results indicated that relative nozzle angle should be kept above 80° to avoid excessive pulling forces, fibre flaring, and possible fibre damage. Next, alternative means of achieving circular toolpaths were assessed, with built platform rotation achieving the best results in terms of surface quality and fibre placement. Finally, the effectiveness of using a square nozzle in place of a round nozzle was investigated. Fibre placement and surface quality improved when using a square nozzle, although it was noted that using a non-circular nozzle profile increases toolpath complexity.

References

1. Y. Qiao, L. D. Fring, M. R. Pallaka, and K. L. Simmons, A review of the fabrication methods and mechanical behavior of continuous thermoplastic polymer fiber–thermoplastic polymer matrix composites. Polym. Compos. **44**, no. 2, pp. 694–733 (2023). doi: 10.1002/pc.27139
2. G. Lakshmi Srinivas, M. Pawel, L. Marius, and L. M. Faller, Supportless 5-axis 3D-printing and conformal slicing: a simulation-based approach. Proc. 24th Int. Conf. Therm. Mech. Multi-Physics Simul. Exp. Microelectron. Microsystems (EuroSimE). pp. 1–7 (2023). doi: 10.1109/EuroSimE56861.2023.10100840
3. G. Fang, S. Zhong, Z. Zhong, T. Zhang, X. Chen, and C. C. L. Wang, Reinforced FDM: multi-axis filament alignment with controlled anisotropic strength. ACM Trans. Graph. **39**, no. 6, p. 15 (2020). doi: 10.1145/3414685.3417834
4. P. Michalec, M. Laux, G. L. Srinivas, R. Weidner, and M. Brandstötter, Five-axis printing of continuous fibers on the mold. J. Manuf. Mater. Process. **9**, no. 1, pp. 1–19 (2025). doi: 10.3390/jmmp9010017
5. G. Fang, T. Zhang, Y. Huang, Z. Zhang, K. Masania, and C. C. L. Wang, Exceptional mechanical performance by spatial printing with continuous fiber: curved slicing, toolpath generation and physical verification. Addit. Manuf. **82**, 104048 (2024). doi: 10.1016/j.addma.2024.104048
6. K. Ruan, Y. Peng, Y. Weng, L. Zhou, and Y. Xiong, Rotatory additive manufacturing of grid-stiffened continuous fiber-reinforced polymer tubular structures. Compos. Part A Appl. Sci. Manuf. **194**, 108896 (2025). doi: 10.1016/j.compositesa.2025.108896
7. T. A. Himika, L. Olsen-Kettle, D. Ruan, and A. Daliri, Effects of nozzle geometry and fiber orientation on the tensile strength of 3D printed continuous fiber reinforced composites. Addit. Manuf. **94**, 104490 (2024). doi: 10.1016/j.addma.2024.104490

Use of ultrasonic atomisation in recycling of used powder and scrap from stainless steel

Donald Mhkonto[1*], *Kiyaasha* Dyal Ukabhai[1], *Ramogohlo* Diale-Boshielo[1], *Lebedike* Mampuru[1], *Maje* Phasha[1] *and Joseph* Moema[1]

[1] Advanced Materials Division, Mintek, 200 Malibongwe drive, Randburg, 2125, South Africa

Abstract. Additive manufacturing Methods and process is very crucial in metal products production. Importantly, metal powder feedstock, powder post processing handling and scrap print are crucial for cycle economy and waste minimisation. Used powder can only be recycled or reused for a limited number of times following re-sieving each time while scrap prints maybe difficult to recycle. We present recycled stainless steel scrap powder and print from Ultrasonic atomisation process. Produced powder is more spherical than commercial, and though high temperature melting is used in the process, metal alloy composition is kept. Produced powder is suitable for LPBF 3D printing systems.

1 Introduction

Metal powder production for additive manufacturing is an important aspect of this fast-growing technology. Particle size distribution suitable for 3D printing and specifically for laser powder bed fusion (LPBF) machines requires good techniques to produce. While the metal 3D printing can produce high volumes of intricate components and improve on lead time to production of parts, the reuse of metal powder and recycling of scrap material in general is very important. Recycling of metal powder plays a very crucial role in cycle economy and moreover, local metal powder production in countries that has abondance of minerals is crucial for mineral beneficiation at source like in South Africa.

Production of feedstock for additive manufacturing is an important aspect of powder metallurgy. And recycling metal powders and metal scrap back to useful powder is crucial. The most important feature in metal recycling also is thew maintenance of the alloy composition which is crucial for quality of the product with desired properties. The produced powders have to be in a particular form or shape and should be within a specific particle size distribution (PSD). In metal 3D printing, usually using laser powder bed fusion (LPBF) [Yap, *et al.,* 2015] machines, powder should be spherical and mainly have PSD of d50 = 60 µm and within a range of 20 µm to 60 µm depending on specific materials. Seungkyun *et al*. 2025, demonstrated that trimodal PSD is more suitable for selective laser melting or powder bed fusion additive manufacturing, because of its enhanced powder bed density and homogeneity [Seungkyun Yim, *et al*., 2025]. A mix of powders with large diameter flows readily compared to fine particles. However, larger particles sinter poorly, whereas particles

* Corresponding author: donaldm@mintek.co.za

with diameter less than 20 µm lead to more efficient sintering and higher density and also, nonspherical particles exhibiting low packing density than spherical particles ([Marczyk, *et al.*, 2023]. There is a need for proper and advanced methods of powder recycling and handling techniques or methods to maintain resulting powder quality, [Alex Lanzutti, *et al*, 2024] as well as effective strategies of powder management [Wu, *et al.*, 2018].

In this study results from ultrasonic atomisation of recycled stainless-steel powder and failed prints are presented. Starting with 304L steel wire, to a combination used 316L used powder, print supports and failed prints (all three from the same print batch), the spherical powder with particle size distribution suitable for metal 3D printing is produced. The wire is used as continuous feed and scrap was made into rods first that were used as feed stock for atomisation. This was achieved using the Amazemet rePowder machine [Żrodowski *et al.,* 2021].. For both feedstocks (rods and wire), the 20 and 40 kHz sonotrode on which arc melted material was dropped, has been used in an inert environment filled with argon gas to prevent oxidisation. Metallurgical analysis of produced powder was done to determine composition, particle shape or sphericity and particle size distribution.

2 Results

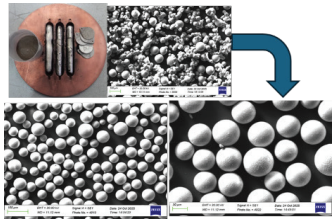


Fig. 1. On copper hearth is a container with used 316L steel powder and failed printed coins. These were melted into metal rods (three rods in the middle of the plate) to be used as feed stock for atomisation. The figure also shows SEM image of the used powder with irregular shape that was recycled into useful spherical clean powder. Furthermore, SEM images of spherical powder produced is shown with trimodal particle size distribution (PSD).

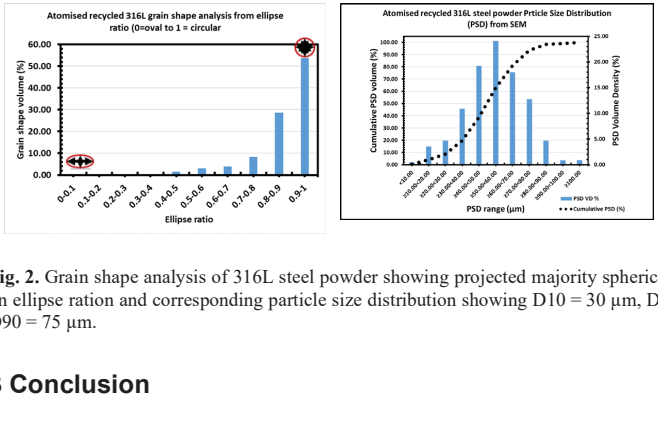


Fig. 2. Grain shape analysis of 316L steel powder showing projected majority spherical powder based on ellipse ration and corresponding particle size distribution showing D10 = 30 µm, D50 = 55 µm and D90 = 75 µm.

3 Conclusion

In this work, we have shown that used metal powders and failed prints or scrap metal can be recycled back to useful powder that can be used in additive manufacturing. The produced powders from the Amazemet rePowder system are more spherical compared to commercial powders, and in this case 316L steel. Though come out with PSD of D10 = 30 µm, D50 = 55 µm and D90 = 75 µm compared to commercial D10 = 15 µm D50 = 30 µm and D90 = 45 µm, the recycled powder due to its spherical nature will flow well and the trimodal PSD should have good packing density that is important for dense printing and quality product. The alloy composition of the steel material has not been fully explored for this study and shall be combined with other characterisation such as flowability, packing density and test prints. This work only focuses on capability demonstration. The results contribute immensely to circular economy where minimal waste is key and thus metals and alloys can be reused in additive manufacturing.

References

1. Yap, C.Y.; Chua, C.K.; Dong, Z.L.; Liu, Z.H.; Zhang, D.Q.; Loh, L.E.; Sing, S.L. Review of selective laser melting: Materials and applications. Appl. Phys. Rev. 2015, 2, 041101.
2. Yim Seungkyun, Koki Minowa, Kenta Yamanaka, Akihiko Chiba, Influence of particle size distribution on the powder bed quality in the powder bed fusion additive manufacturing process, Journal of Materials Research and Technology 37, 2025, p. 2038–2050.
3. Marczyk Joanna and Marek Hebda; Effect of the Particle Size Distribution of Irregular Al Powder on Properties of Parts for Electronics Fabricated by Binder Jetting, Electronics 2023, 12(12), p. 2733.
4. Lanzutti Alex, and Elia Marin; The Challenges and Advances in Recycling/Re-Using Powder for Metal 3D Printing: A Comprehensive Review; Metals 2024, 14, p. 886.
5. Wu, H.C.; Chen, T.C.T. Quality control issues in 3D-printing manufacturing: A review. Rapid Prototyp. J. 2018, 24, 607–614.
6. Żrodowski, L., Wróblewski, R., Choma, T., Morończyk, B., Ostrysz, M., Leonowicz, M., Łacisz, W., Błyskun, P., Wróbel, J.S., Cieślak, G., Wysocki, B., Żrodowski, C. and Pomian, K., Novel cold crucible ultrasonic atomization powder production method for 3D printing. *Materials,* 2021, 14, p. 2541.

09
ABSTRACTS
Rapid Casting

Influence of sand grain fineness and droplet spacing (DX) on the mechanical properties of additive binder jetting manufactured sand moulds

Jonathan Kabadjundi Kabasele[1*], *Kasongo Didier* Nyembwe[2,3]

[1]University of Johannesburg, Engineering Metallurgy, Johannesburg, South Africa
[2]Cape Peninsula University of Technology, Mechanical Engineering, Cape Town, South Africa
[3]Vaal University of Technology, Applied Research and Collaboration, Vaal, South Africa

Abstract. Binder jetting of sand moulds requires specific grain characteristics fineness, purity, and morphology for consistent layer deposition and strength. Prior research on local sands focused on matching imported sand properties, treating these attributes as fixed. However, grain fineness (AFS), chemical purity, and morphology directly affect mechanical performance and reliability of binder-jetted sand moulds. As industry seeks local sand to reduce costs, this study examines variations in fineness, purity, and morphology of local silica sands and compares their performance with imported sands to assess suitability for binder jetting applications.

1 Introduction

Rapid sand casting via binder jetting is increasingly being adopted as a key technology in modern foundries, particularly in South Africa, where improving sector competitiveness is a strategic priority. Efforts have focused on localising raw materials, especially silica sand, and a study by Oyombo Dady et al. showed that locally sourced South African sand could achieve mechanical properties comparable to imported alternatives. However, that study treated sand fineness as a fixed characteristic. Building on this, the present study systematically varies the AFS grain fineness of local silica sands, thereby altering grain size distribution, which critically affects powder flow, layer deposition, binder penetration, and strength development in the absence of mechanical compaction. The study quantifies the impact of sand fineness on key mechanical properties including friability, tensile strength, compressive strength, and flexural strength of binder jetted sand moulds [1, 2].

1.1 Problem statement

Previous studies have not sufficiently explored how AFS grain fineness and grain size distributions influence the mechanical properties of binder jetted sand moulds. The

* Corresponding author: kabasele.jonathan@yahoo.fr

connections between these sand characteristics and factors such as friability, tensile strength, compressive strength, and flexural strength remain inadequately investigated.

1.2 Importance of the study

This study is of significant relevance to the South African foundry industry as it seeks to optimise binder jetting processes through the utilisation of locally sourced silica sand, thereby addressing the high expenses and financial challenges linked to imported materials. By examining the influence of AFS grain fineness and grain size distribution on mechanical properties, the research offers valuable insights for improving mould quality, casting performance, and overall process efficiency. This work is aligned with the national strategy to advance additive manufacturing within the foundry sector, supporting efforts toward localisation, reducing production costs, fostering sustainable practices, and ultimately enhancing the global competitiveness of South African foundries.

2 Methodology

This work is divided into four main steps (see Fig. 1):

1. Sampling of local sand with different AFS values.
2. Printing of 3D sand moulds using the Voxeljet VX1000 printer.
3. Testing of 3D sand mould friability following the AFS 2248-11-S standard and mechanical properties including tensile, compressive, and flexural strength using standard procedures.
4. Establishing a correlation between grain size and mechanical properties.

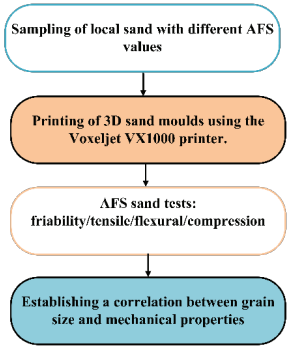


Fig. 1. Experimental procedure

3 Results

The preliminary results are listed in Table 1. The friability of the sand moulds ranges from 11% to 44%, indicating a wide variation in the ease with which the moulds break down. Flexural strength varies between 10.88 and 162.84 N/cm², compression strength ranges from 52.8 to 341.6 N/cm², and tensile strength ranges from 7.9 to 54.64 N/cm².

Table 1. Mechanical test results.

AFS	Friability %	Flexural strength N/cm^2	Compression strength N/cm^2	Tensile strength N/cm^2
55	11.49	162.84	106.16	31.64
	14.44	149.23	341.6	52.38
	17.81	122.3	254.4	52.98
	19.01	137.3	262.32	51.02
	15.35	140.98	273.04	54.64
58	31.11	62.07	144.48	10.56
	43.83	47.5	82.1	43.83
	43.77	53.6	104.96	14.44
	42.15	10.88	124.72	10.88
64.5	28.09	74.5	52.8	9.4
	40.71	55.15	76.88	9.4
	38.24	59.97	95.68	12.6
	36.42	48.76	72	7.9
65	38.26	53.92	82.88	11.78
	24.17	85.67	117.76	18.975
	28.41	73.67	98.72	17.64
	29.05	80.78	106.56	14.44

4 Conclusions

This study optimizes rapid sand-casting by examining how varying particle sizes in locally sourced silica sand affect binder jetting. The findings advance the technology's understanding and adoption in South African foundries, aligning with the national strategy to integrate additive manufacturing and strengthen industry competitiveness and local technical capabilities.

References

1. K. Nyembwe, D.D. Oyombo, D. de Beer, P. van Tonder, “Equitability of a South African silica sand for three-dimensional printing of foundry moulds and cores, SAJIE, 27, 3 (2016). http://dx.doi.org/10.7166/27-3-1662
2. M. Lehmann, H. Panzer, C.G. Kolb, M.F. Zaeh, “Influence of the pore radius on the penetration depth of inks in binder jetting: A modification of the Washburn equation, J. Man. Mat. Pro., 6, 5 (2022). https://doi.org/10.3390/jmmp6050101

Integrating the UNSDGs into South Africa's 3D sand printing industry

Neo Tshabalala[1*], and *Didier* Nyembwe[2,3]

[1]Department of Engineering Management, University of Johannesburg, South Africa.
[2]Mechanical and Mechatronics Engineering Department, Cape Peninsula University of Technology, South Africa.
[3]Department of Materials Science and Engineering, Vaal University of Technology, Vanderbijlpark, South Africa.

Abstract. United Nations Sustainable Development Goals (UNSDGs) have become the principal framework for guiding industrial practices internationally. However, despite broad corporate endorsement of the UNSDGs in principle, their integration remains limited, especially within mineral beneficiation supply chains supporting advanced manufacturing sectors. This study addresses this shortcoming by conducting a mixed-methods analysis of the South African chromite sand value chain, which provides refractory materials to both conventional foundries and innovative additive manufacturing (AM) platforms. The research synthesizes quantitative survey responses from 106 industry stakeholders with a structured, criteria-driven UNSDG alignment approach. The primary objective is to develop a sector-specific Quality Assurance Framework.

1 Introduction

Recent technical studies have demonstrated that locally sourced chromite sand can meet the stringent specifications required for three-dimensional sand printing (3DSP) opening a potential pathway for South African producers to transition from bulk commodity exports to high-value inputs for advanced manufacturing [1].

1.1 United Nations sustainable development goals (UNSDGs) alignment

Global customers, original equipment manufacturers, and increasingly stringent regulatory frameworks are demanding demonstrable evidence of responsible sourcing, environmental stewardship, and alignment with internationally recognised sustainability standards, most notably the UNSDGs [2].

Within the South African chromite sand value chain, there exists no empirically grounded framework to assess current sustainability practices, identify significantly relevant UNSDG targets or to formulate credible pathways through which technical process improvements contribute to measurable sustainability outcomes. The research endeavours to translate these

* Corresponding author: 201415703@student.uj.ac.za

aligned pathways into actionable provisions for a sector-specific Quality Assurance Framework.

In doing so, the paper provides the South African foundry and additive manufacturing sectors with a replicable, empirically grounded approach for integrating sustainability into quality management, transforming UNSDG alignment from a compliance burden into a strategic enabler of global competitiveness.

2 Methodology

This study employed a mixed-methods approach to assess industry perceptions of environmental sustainability in chromite sand for 3DSP. A structured questionnaire using 5-point Likert scales was distributed to 106 industry participants across chromite sand producers, foundries, and additive manufacturing specialists. Survey data were analysed using a criteria-based framework to assess alignment with relevant UNSDGs. Fig. 1 below shows the process.

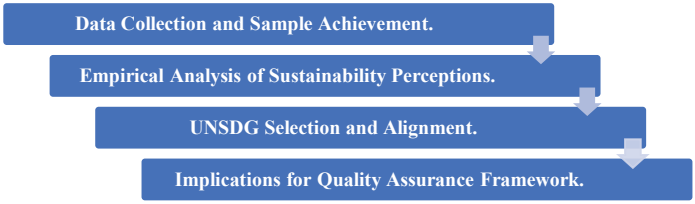


Fig. 1. Diagram depicting the process followed in this study.

The paper thereby provides a replicable approach for integrating sustainability into quality management transforming SDG alignment from compliance burden into strategic enabler.

3 Conclusion

The study finds that integrating UNSDGs into additive manufacturing supply chains is feasible with evidence-based methods. It also highlights a significant disconnect between companies stated commitment to sustainability and their actual practices in the South African chromite sand value chain.

References

1. M. Upadhyay, T. Sivarupan, M.E. Mansori, 3D printing for rapid sand casting. Int. J. Addit. Manuf. 29, (2017).
2. Romani, M Levi, V. Rognoli, Sustainable development goals enabled by additive manufacturing: A Design Perspective. In: Duarte, E., Di Roma, A. (eds) Developments in Design Research and Practice II. Senses 2021. Springer Series in Design and Innovation, **31**. Springer, Cham. pp. 382–397 (2023). https://doi.org/10.1007/978-3-031-32280-8_27

Smart supplier selection in metal casting processes: integrating MCDM and industry 4.0 – a critical review

Samson Dare Oguntuyi[1*], *Kasongo* Nyembwe[2] *Peter M.* Mashinini[3] and *Peter* Olubambi[1]

[1]Centre for Nanoengineering and Advanced Materials (CeNAM), School of Mining, Metallurgy and Chemical Engineering, University of Johannesburg, Johannesburg, 2092, South Africa
[2]Department of Mechanical and Mechatronic Engineering. Cape Peninsula University of Technology, Cape town, South Africa
[3]Department of Mechanical and Industrial Engineering, University of Johannesburg, Doornfontein Campus, Johannesburg 2028, South Africa

Abstract. In the metal casting industry, efficient manufacturing, delivery, and cost minimization require systematic prioritization of supply-chain parameters, including skilled labor, equipment selection, component durability, material costs, and product quality. Balancing these competing criteria remains a persistent challenge for decision-makers. Traditional experience-based and manual approaches are increasingly inadequate for managing the growing complexity and demand of modern casting supply chains. This review critically synthesizes advances in integrating Multi-Criteria Decision Making (MCDM) methods with Industry 4.0 technologies to optimize supplier selection in rapid sand casting and metal casting processes. Emphasis is placed on efficiency, quality, sustainability, and resilience, while identifying limitations.

1 Introduction

The metal casting industry operates within highly competitive and cost-sensitive environments where efficiency, timely delivery, and quality assurance are critical for sustainable performance [1, 2]. Achieving these objectives requires the systematic evaluation and prioritization of multiple supply-chain parameters, including skilled labor availability, equipment capability, component durability, raw material costs, and final product quality [3]. However, balancing these often-competing criteria presents significant challenges for decision-makers. Traditional experience-based and manual decision approaches are increasingly inadequate in addressing the complexity, uncertainty, and dynamic demands of modern casting supply chains. As production systems expand and customer expectations intensify, more structured and data-driven decision frameworks have become essential [4].

This review focuses on the integration of Multi-Criteria Decision Making (MCDM) methods with Industry 4.0 technologies to enhance supplier selection in rapid sand casting and broader metal casting processes. It critically synthesizes recent advances that combine

* Corresponding author: samsoniumdare@gmail.com

digital tools—such as data analytics, automation, and smart manufacturing systems—with systematic evaluation models to improve efficiency, product quality, sustainability, and supply-chain resilience. Furthermore, the review identifies current limitations, implementation challenges, and potential research directions for advancing intelligent decision-support systems in the casting industry.

2 Methodology

The methodology combines Multi-Criteria Decision-Making (MCDM) models with Industry 4.0 technologies to enable sustainable supplier selection, as graphically shown in Figure 1. MCDM provides a structured framework for evaluating key criteria such as cost, quality, delivery, risk, and sustainability, while Industry 4.0 tools—such as AI, IoT, big data analytics, and smart manufacturing—supply real-time data and predictive insights. This integration supports objective, data-driven, and resilient decision-making within the metal casting supply chain.

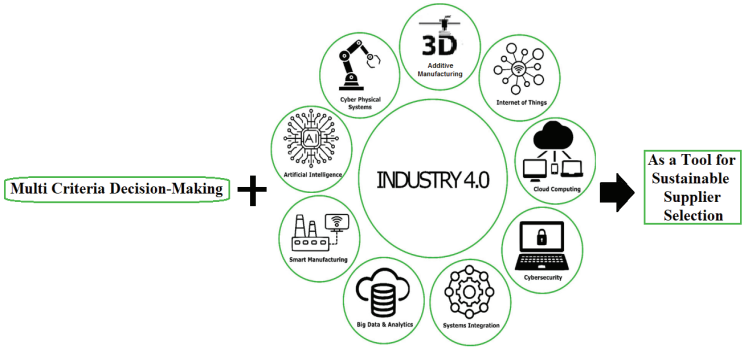


Fig. 1. The synergy of MCDM with Industry 4.0 for sustainable supplier selection

3 Conclusion

The integration of Multi-Criteria Decision-Making (MCDM) methods with Industry 4.0 technologies provides a robust and data-driven framework for optimizing supplier selection in the metal casting industry. By systematically evaluating competing supply-chain parameters and leveraging real-time digital insights, this approach enhances efficiency, product quality, sustainability, and resilience. The review highlights both the potential and current limitations of such integration, underscoring the need for further research and practical implementation strategies to fully realize intelligent, sustainable decision-support systems in modern casting supply chains.

References

1. S. K. Sahoo, S. S. Goswami, R. Halder, Supplier selection in the age of Industry 4.0: A review on MCDM applications and trends. *Decision Making Advances* **2**(1), 32–47 (2024).

2. C. H. L. Resende, C. A. S. Geraldes, F. R. L. Junior, Decision models for supplier selection in Industry 4.0 era: A systematic literature review. *Procedia Manufacturing* **55**, 492–499 (2021).
3. J. Chai, E. W. T. Ngai, Decision-making techniques in supplier selection: Recent accomplishments and what lies ahead. *Expert Systems with Applications* **140**, 112903 (2020).
4. T. E. Saputro, G. Figueira, B. Almada-Lobo, Hybrid MCDM and simulation-optimization for strategic supplier selection. *Expert Systems with Applications* **219**, 119624 (2023).

Effect of FeSi-based inoculants on microstructure, indentation size effect and strain gradient plasticity in grey cast iron

Pertunia Seema[1], *Desmond* Kleman[1], *Michael* Bodunrin[1], *Christo* Hattingh[1], *Joseph* Moema[2] and *Maje* Phasha[2]

[1]CHMT, University of the Witwatersrand, Johannesburg, South Africa
[2]Advanced Materials Division, Mintek, Randburg, South Africa

Abstract. This study explores the FeSi_Zr inoculant on the grey cast iron microstructure and hardness. The results reveal a progressive pearlite to ferrite transformation. Vickers testing shows a significant indentation size effect of grey cast iron from 100gf to 10kgf. Geometrically necessary dislocation density (GND) decreases when higher levels of inoculants are added, confirming strain gradient dominance. Optimal balance occurs at 0.2% addition, demonstrating the inoculant's dual role in refining castability while turning mechanical response through strain gradient effects.

1 Introduction

Grey cast iron remains a cornerstone for engineering materials, with its properties continually enhanced by advancement in materials science [1]. Grey cast iron has good properties such as machinability due to its refined flake-like microstructure; however, properties such as hardness are profoundly sensitive to microstructural variations [2]. Inoculation techniques that use FeSi-based inoculants are essential for refining graphite morphology and elevating mechanical performance. While silicon promotes graphitization and balances the ferrite-pearlite phases, FeSi inoculant with trace elements and their impact on microstructure and hardness remains limited [1].

The present study examines FeSi-based inoculants incorporating Zr to optimise grey cast iron properties. It emphasises their effects on microstructure and hardness, particularly the indentation size effect and strain gradient plasticity phenomena.

1 Corresponding author: pertuniaseema21@gmail.com

2 Methodology

Charge materials (steel iron, ferro-manganese, iron-sulphate and pure silicon) were melted in an induction furnace to 1354 °C, then cast into 19kg ingots. The first sample was uninoculated, and the remaining samples received FeSi_Zr inoculants at levels of 0.1%, 0.2% and 0.4%. The samples were then sectioned, hot-mounted in black Bakerlite resin, and optically examined for graphite morphology. The specimen was then etched to expose different phases for SEM analysis.

Vickers hardness testing employed multiple loads: 100 gf, 200 gf, 300 gf, 500 gf, 1 kgf, 3 kgf, 5 kgf and 10 kgf. The data obtained enabled indentation size effect and strain gradient plasticity calculations.

3 Results and discussion

Figure 1 presents scanning electron microscope (SEM) micrographs of the base and the inoculated samples. The uninoculated sample's surface has a high number of pearlitic phases, which are evenly distributed within the microstructure. Progressive inoculation of both FeSi_Zr reduces pearlite content while promoting ferrite formation, particularly at higher addition levels (0.2% to 0.4%). At 0.2% FeSi_Zr, results in ferrite around the graphite, becoming more pronounced at 0.4% addition. This Si driven phase shift aligns with established graphite effects, where silicon elevates the stable eutectic temperature and favours ferrite over pearlite [3].

This microstructural softening directly explains the observed hardness trends. Pearlite's characteristic lamellar structure creates internal barriers impeding dislocation motion, while ferrite enables unimpeded glide [4]. Consequently, increasing ferrite content results in an overall reduction of hardness.

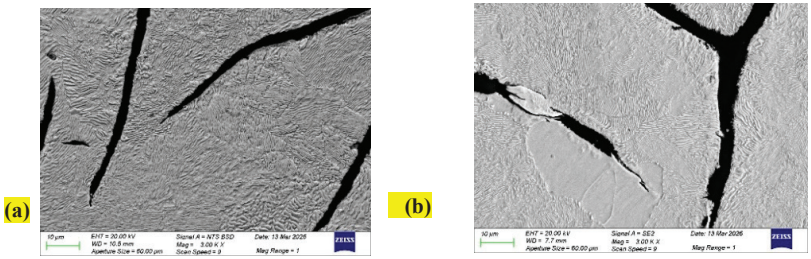


Fig. 1. SEM images of etched samples for grey cast iron at a magnification of 3.00 KX. (a) un-inoculated sample, (b) grey cast iron with 0.4%FeSi_Zr inoculation.

Vickers hardness testing reveals the indentation size effect in all conditions, as shown in Figure 2. Hardness decreases systematically with increasing indentation depths before stabilising in higher loads, a characteristic of heterogeneous material where small indents probe local microstructural variations while large indents average a representative volume due to the variety of phases it affects.

The base alloy maintains higher hardness across all depths. Increasing the FeSi_Zr from 0.1% to 0.4% progressively lowers the hardness curve. The 0.4% addition exhibits the strongest Indentation size effect, with a hardness drop at higher loads, indicating diminishing strain gradient strengthening capacity [5]. However, FeSi_Sr

have a subtle effect. The curves converge more rapidly at higher depth. This suggests that FeSi-Zr induces more pronounced matrix softening.

Dislocation density analysis confirms strain gradient dominance. Geometrically necessary dislocation (GND) density decreases systematically with indentation depth across all conditions, highest in the base alloy and progressively lower with inoculant content [5]. FeSi_Zr has a stronger influence, resulting in substantially reduced GND's at 0.4% addition.

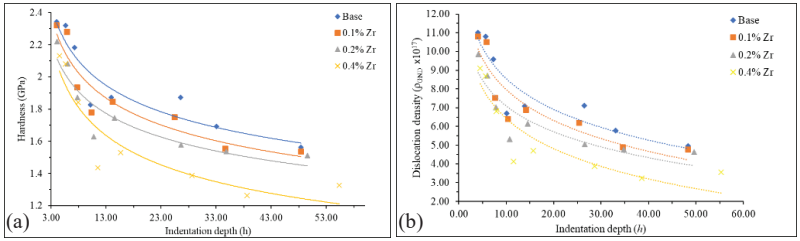


Fig. 2: (a) Micro and macro indentation showing hardness (GPa) against indentation depth (h) for un-inoculated grey cast iron and FeSi_Zr inoculated grey cast iron samples at different levels (0.1%, 0.2% and 0.4%). (b) Micro and macro indentation showing GND against indentation depth (h) for un-inoculated grey cast iron and FeSi_Zr inoculated grey cast iron samples at different levels (0.1%, 0.2% and 0.4%).

4 Conclusion

This study demonstrates that FeSi_Zr inoculation systematically transforms grey cast iron microstructure from pearlite-dominant to ferrite-rich, which results in lower hardness through enhanced dislocation mobility.

References

1. P. Singhal, K.K. Saxen, Effect of silicon addition on microstructure and mechanical properties of grey cast iron: An overview. Mater. Today: Proceedings. **26**,1393-1401 (2020).
2. S. Sahu, M.N. Bhat, A. Kumar, A. Pratik, A. Kumar, Effect of section thickness on the microstructure and hardness of gray cast iron (a simulation study), IJERT, **3**, 35 - 40 (2014).
3. G. Wang, X. Chen, Y. Li, Z. Liu, Effects of inoculation on the pearlitic gray cast iron with high thermal conductivity and tensile strength. Materials **11**, 1876 (2018).
4. S. Yin, Y. Zhang, Y. Zhang, L. Zhou, J. Zhou, Microstructural evolution mechanisms of nanolaminated pearlitic steels upon large-strain deformation. Int. J. Mech. Sci. **289**, 110076 (2025).
5. B. Addai, K.O. Gyimah, T.K. Anto, M. Klenam, W.O. Soboyejo, Strain gradient plasticity in AISI A36 plain carbon steel weldment: Comparison of butt and lap joint configurations. RINENG **22**, 102078 (2024).

10

ABSTRACTS

Industry presentations

Additive manufacturing: from material characterization to quality performance

Zwelihle Ndlovu and *Bomkazi* Sobuwa

Anton Paar Southern Africa (Pty) Ltd, Corporate Park South, Old Pretoria Road, Randjiesfontein, Midrand 1685, South Africa

Abstract

Additive manufacturing is rapidly evolving, but achieving consistent, high-quality printed components depends heavily on understanding and controlling the materials used throughout the process. The presentation explores how advanced analytical techniques can help manufacturers characterize polymers and metal powders; optimize processing conditions to improve the performance and reliability of finished components.

The presentations will highlight practical applications of rheology, particle size analysis, density, porosity measurements, surface characterization, tribology, and X-ray diffraction (XRD). Particular focus will be placed on understanding powder flowability, polymer melting and crystallinity, metal powder phase purity, particle characteristics, residual stresses, and the structural properties of printed components.

By connecting material properties to processing behavior and final product performance, participants will gain insight into how analytical characterization can support process optimization, quality control, material development, and more reliable additive manufacturing outcomes.

CTI: A computational tool for industrial investment readiness in Africa

Vince Mbanze, *Thabo* Pilusa, *Ofentse* Pholosi

Nexusnode, Gauteng, South Africa

Abstract

In many emerging economies, growth in financial depth does not consistently translate into productive fixed investment. This weak transmission matters for industrialisation, because manufacturers, technology ventures, and scaling firms depend not only on the availability of finance, but on finance reaching real capital formation. This presentation introduces the Credit-to-Investment Transmission Index (CTI), a computational analytics tool designed to assess how effectively private-sector credit is associated with productive investment over time.

CTI combines macro-financial and investment indicators into a structured, comparable signal that helps distinguish between environments where finance supports productive expansion and those where credit growth is decoupled from real capital formation. Built as a reproducible data-driven workflow, the framework uses interpretable metrics and scorecards to support cross-country and over-time analysis for decision-making.

For industry and innovation stakeholders, the relevance is practical. Industrial scale-up, manufacturing growth, and technology commercialisation all require an environment in which finance can be translated into machinery, infrastructure, productive capacity, and firm expansion. CTI offers a decision-support lens for industrial planners, researchers, development finance actors, and firms seeking to identify investment readiness and structural bottlenecks. The presentation will outline the conceptual basis of CTI, the data and modelling workflow, and how such a tool can support evidence-based discussion on moving from prototype activity to production at scale.

Keywords: computational analytics, industrial investment readiness, data-driven modelling, financial transmission

From print to performance: unlocking additive manufacturing potential through heat treatment and smart hardness verification

Wise Mukhola

Verder Scientific (Pty) Ltd, South Africa

Abstract

Additive manufacturing enables rapid production of complex components but achieving consistent and reliable mechanical performance requires more than successful printing. As-built parts may contain residual stresses, microstructural anisotropy and variations in hardness caused by build orientation, process parameters and material history. Controlled heat treatment is therefore an important step in transforming printed components into functional and production-ready parts.

This presentation explores an integrated approach that combines Carbolite heat-treatment systems with the Qness 60 EVO hardness tester to close the quality loop in additive manufacturing. Heat treatment is used to modify residual stress and microstructure, while hardness testing provides a practical and traceable method for evaluating the resulting mechanical condition of the component.

The presentation will outline a typical workflow, including sample preparation, selection and control of heat-treatment cycles, hardness measurement and comparison of as-built and heat-treated conditions. It will also discuss how hardness mapping can reveal variations across different locations, orientations or regions of an additively manufactured part.

By linking thermal processing with mechanical verification, manufacturers and research institutions can improve process understanding, support material qualification and increase confidence in the repeatability of AM components. The combined approach demonstrates how laboratory and production-quality tools can help move additive manufacturing from prototype capability toward validated industrial performance.

Microstructural characterisation of AM components using penetrative radiation techniques

Andrew Venter[1]*

[1]Research and Innovation Division, Necsa SOC Ltd. Pretoria, South Africa

Abstract

Integral to the development of advanced materials is the availability of advanced non-destructive characterisation techniques, not only during development phases, but in the form of manufactured components. During the AM process the powdered material is heated to its melting point from where it cools rapidly to form the solidified build layers towards establishing a solid part. This heating and cooling cause expansion and contraction which establish non-homogeneous plastic strain fields in the material surrounding the melt pool. This leads to the formation of porosity and chemical changes that are the primary mechanisms for residual stress buildup and complications such as cracking, distortions and delaminations.

At Necsa, neutron and complementary X-ray based instruments are available as User Facilities within the National System of Innovation in support of the South African research and industrial communities. More specific the superior penetration capabilities of neutrons into most materials allows for the analysis of bulk or localised depth-resolved properties. Materials that can be investigated include metals, alloys, composites, ceramics and coated systems. Especially, depth-resolved analyses using neutron diffraction complements the surface investigations of laboratory X-rays in many scientific and engineering topics.

Application of the techniques cut across many of the conference themes. The value addition prospects will be showcased with results from typical studies of additive manufactured components. As an example, Fig. 1 shows the measured residual stress distribution over a cross section of an additive manufactured Ti-6Al-4V sample.

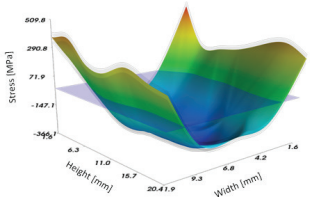


Fig. 1. Residual Stress along a cross section in an AM produced Ti-6Al-4V sample.

* Corresponding author: andrew.venter@necsa.co.za

11

ABSTRACTS

Poster Abstracts

Molecular dynamics simulations of TiO_2 nanomaterials as a future anode electrode material

Thamia Molefe[1*], Phuti Ngoepe[1], and Blessing Rikhotso[1]
[1]Materials Modelling Centre, University of Limpopo, Private Bag x1106, Sovenga 0727, South Africa.

Abstract. The growing global demand for sustainable and high-performance energy storage systems has directed significant research attention toward titanium dioxide (TiO_2) as a prospective anode material for lithium-ion batteries. In this study, the structural and thermodynamic behaviour of amorphous TiO_2 is systematically investigated using classical molecular dynamics (MD) simulations, with particular emphasis on its applicability in electrochemical energy storage. This study establishes a robust atomistic framework for the continued development and optimization of TiO_2-based anode materials, highlighting the critical role of computational modelling in advancing next-generation battery technologies.

1 Introduction

Lithium-ion batteries play an important role in energy storage for electronics and the energy is released when needed [1]. Soon the rechargeable batteries will need longer cyclic stability, high energy density and lower costs. For low-cost energy-devices, graphene nanostructures have been explored [2]. As seen that mobile electronics functionality is growing, this will demand improved battery performances, like lasting longer before recharging. TiO_2 is used in energy storage, catalysis and photocatalysis [3], but there is limited information on the amorphous TiO_2 materials than crystalline. This includes the structural behaviour of nanoporous TiO_2 at high temperatures specifically the amorphisation and recrystallisation processes, which are not well understood at the atomic scale. Experimental techniques have limitations in studying the atomic behaviour and recording the rapid changes that occur during amorphisation and recrystallisation [4]. Therefore, molecular dynamic simulations are needed to study the thermal stability, atomic interactions and structural changes that occur in the nanoporous TiO_2 which is important in optimizing its performance in battery applications.

2 Materials and methodology

Molecular Dynamics simulations were performed using DL_POLY software [5], which handles large systems containing millions of atoms. This simulation is used to study the structural behaviour of materials. Molecular Dynamics is based on classical mechanics

* Corresponding author: molefethamia@gmail.com

approach which is Newton's second law of motion, and it uses Buckingham potential indicated in the equation below:

$$\phi(r) = Aexp\left(-\frac{r}{\rho}\right) - \frac{C}{r^6}$$

A- repulsion strength constant
ρ - range parameter of the exponential repulsion
r- interatomic separation
C- dispersion (van der Waals) coefficient

3 Results and discussion

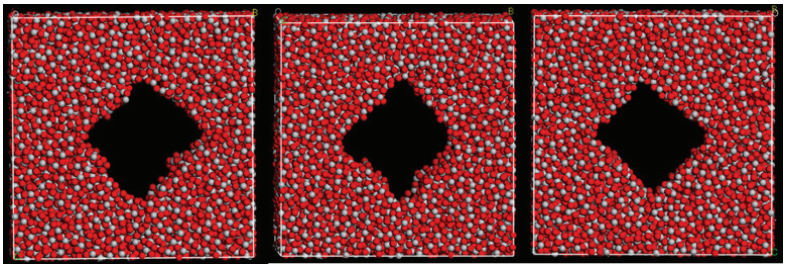


Fig. 1. Three-sided view of the amorphised nanoporous TiO_2 structure at 1000 K, showing a highly disordered atomic configuration.

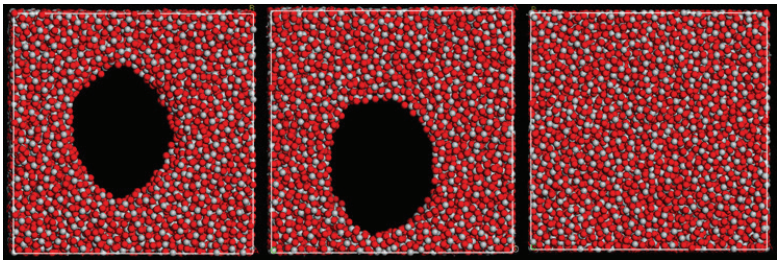


Fig. 2. Three-sided view of the recrystallised nanoporous TiO_2 structure at 2000 K, showing a highly disordered atomic configuration.

As the temperature was incrementally increased from 1000K to 2000K in steps of 100K, noticeable structural changes occurred as seen in figure 1 and 2. Between 1000K and 1700K, the material consistently exhibited varied pore sizes at increased temperature. These pore sizes suggest the material remained in an amorphous state, with atomic diffusion driven by increased kinetic energy at elevated temperatures. At 1900K and 2000K, the third side of the structure does not have a pore, which suggest that the structure was beginning to recrystallize.

4 Conclusion

In conclusion amorphization and recrystallization of the nanoporous TiO_2 was successfully completed through varying the temperature from 1000K to 2000K. This study aimed to investigate the structural behaviour and thermal stability of nanoporous TiO_2 for lithium-ion battery applications. Thereof voids were there on all sides of the structure at temperatures between 1000K-1800K but disappeared on one side at 1900K and 2000K, this indicates that the atoms were starting to be arranged in order which addresses one of the questions on atomic arrangement at high temperatures. RDF analysis clarified atomic arrangements, while diffusion coefficients demonstrated increasing atomic mobility with temperature. These findings suggest that the nanoporous TiO_2 can improve the thermal stability by withstanding high temperatures to work best as an anode electrode material in the lithium-ion batteries and thus contributing to longer battery span.

All calculations were performed at Materials Modelling Centre (MMC), University of Limpopo and the Centre for High Performance Computing (CHPC) in Cape Town, South Africa. This work is supported by the National Research Funding (NRF).

References

1. I. Zeydabadi-Nejad, N. Zolfaghari, M. Mousavi Mashhadi, M. Baghani, M. Baniassadi, Anatase TiO_2 nanotubes as Li-ion battery anodes : A molecular dynamics study of Li-ion adsorption on anatase nanotubes. *Sustain. Energy Technol. Assess.* **47**, (2021).
2. A. Kausar, I. Ahmad, Energy systems endorsing graphene nanocomposites—Next energy vision. *Next Energy*. **4**, (2024).
3. A. Bokare, F. Erogbogbo, Photocatalysis and Li-ion battery applications of 001-faceted anatase TiO_2-based composites. *J.* **4**, 500–530 (2021).
4. Y. Zhang, Q. Mao, H. Pitsch, Amorphous-to-crystalline transition during sintering of nascent TiO_2 nanoparticles in gas-phase synthesis: A molecular dynamics study. *J. Phys. Chem.* C **124**, 27763–27771 (2020).
5. W. Smith, I. T. Todorov, A short description of DL_POLY. *Mol. Simul.* **32**, 935–943 (2006).

Sulphur doping of $LiTi_2(PO_4)_3$ NaSICon: structural stability, and Li-ion transport

Gift Matleke*, *Donald* Hlungwani, *Cliffton* Masedi, *Phuti* Ngoepe, and *Sylvia* Ledwaba

Materials Modelling Centre, University of Limpopo, Private Bag x1106 Sovenga, 0727, Polokwane, South Africa

Abstract. Solid-state electrolytes have attracted considerable interest for energy storage applications, owing to their high energy density. However, the SSE performance remains insufficient for commercialisation, owing to the intrinsic low Li^+ conductivity. Here, sulphur incorporation in $LiTi_2(PO_4)_3$ (LTP) is achieved via partial substitution of oxygen (O^{2-}) with sulphide (S^{2-}) species to regulate the local anionic framework. DFT calculations investigated the effect of sulfur doping on LTP's local structure and mechanical properties. For 2% and 3% sulfur doping, the bulk, shear, and Young's moduli were found to be 83.68, 55.01, 135, and 83.22, 54.25, 133.69 GPa, for S1 and S2, respectively.

1 Introduction

Owing to the rapid development of electric vehicles and severe conditions arising from climate change, the next generation of lithium-ion batteries must be prioritised in this era [1]. The Li-ion batteries (LIBs) remain the preeminent energy storage technology, serving as a critical pillar for global transition towards carbon neutrality and the long-term mitigation of fossil fuel dependence. However, organic traditional liquid electrolytes have been facing severe hurdles due to their flammability, incompatibility with liquid electrolytes, interfacial instability, and operational limits [2, 3]. Solid electrolytes have been introduced in response to limitations due to their enhanced safety, good thermal stability, wide electrochemical window (4.5 V vs Li^+/Li), and exceptional air and moisture stability [3, 4]. Despite the promising attributes, the widespread commercialisation of solid-state lithium-ion batteries faces significant solid-solid interface hurdles between the electrode-electrolytes, creating high resistance, which scholars are currently exploring the framework regulation mechanisms and thin film coating to improve wetting and ion jumping pathway efficiency [5]. Compositional engineering through co-doping strategies has emerged as a common and effective technique of enhancing ionic transport by modifying the bottleneck dimensions within the crystal structure and optimising the local coordination environment for lithium-ion migration [6]. This study involves the optimisation of lithium-ion conductivity in LTP through doping, establishing a defined structural property correlation between lattice layer spacing and diffusion kinetics to design a high-performance electrolyte with enhanced structural stability.

* Corresponding author: molatelomatleke22@gmail.com

2 Computational approaches

Spin-polarized DFT calculations were executed using the VASP code [7] with the projected augmented wave (PAW) [8] pseudopotentials and the generalised gradient - Perdew, Burke, and Ernzerhof for solid system (GGA-PBEsol) exchange correction functional. Electronic wavefunctions were expanded with a 650 eV plane-wave cutoff, and the Brillouin zone was sampled using a 5x5x2 γ-centred k-point mesh. A Hubbard U correction of 0 eV was applied to Ti. Structural optimisation was performed with the electronic convergence of 10^{-6} eV, and the interatomic forces were relaxed below 10^{-2} eV/Å.

3 Results and discussion

The results outline that the Bulk modulus appears to decrease with increasing doping percentage, indicating potential risk of porosity-induced degradation, which could result in disruption of ion-conduction pathways. These can be mitigated during the synthesis of the material through sintering techniques. In contrast, the shear modulus exhibits only minor variations and remains within a satisfactory range, preserving its capacity to suppress the dendrite formation. Furthermore, the Young's modulus, along with Pugh's and Poisson's ratios, demonstrates favourable results, suggesting that the material is shifting towards the ductility threshold, reducing the interfacial resistance. Thus, it is behind literature to report that the compatibility between the electrode and electrolyte will be enhanced.

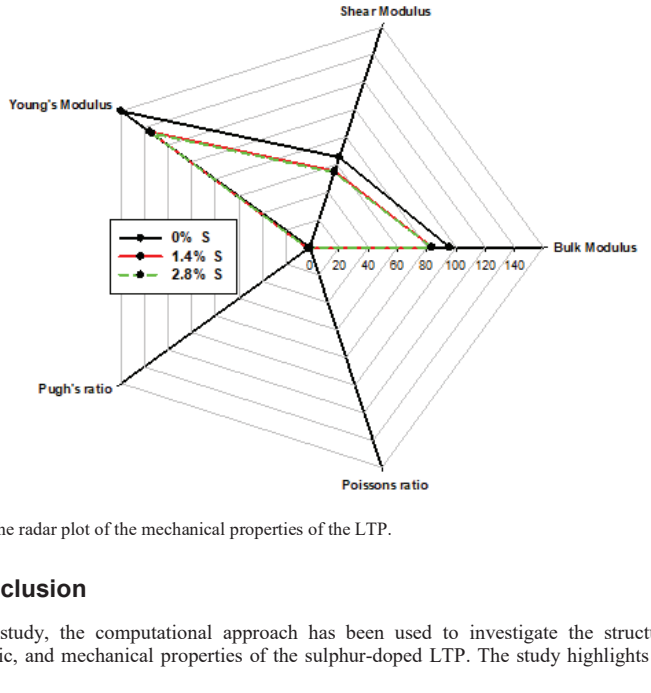


Fig. 1. The radar plot of the mechanical properties of the LTP.

4 Conclusion

In this study, the computational approach has been used to investigate the structural, electronic, and mechanical properties of the sulphur-doped LTP. The study highlights that

the incorporation of sulphur in the LTP improves the compatibility of the electrode-electrolyte interface. The shear modulus has displayed a convincing value, which is suitable for the dendrite suppression. Furthermore, the bulk modulus has decreased due to the asymmetric local structural distortion observed upon the introduction of sulphur in the LTP. Subsequently, the expansion of (O, S)-Ti framework reduces the rigidity in the Li diffusion pathways, which is beneficial to ionic conductivity.

The authors would like to acknowledge the Material Modelling Centre (MMC) at the University of Limpopo and the Centre for High-Performance Computing (CHPC) under the National Integrated Cyber Infrastructure System (NICIS) for high-performance computing facilities.

References

1. Y. He, Z. Zhang, G. Feng, H. Li, Two-dimensional LiTi2(PO4)3 flakes for enhanced lithium-ion battery anode, Heliyon. **10**, e23396 (2024).
2. A.K. Das, S. Kumar, In Situ Polymerization-Enabled Facile Electrode Interface in Solid-State Lithium–Metal Batteries, ACS pub electron. mater. **7**, 9994 (2025).
3. J. Shen, C. Cui, J. Zhao, H. Lin, Y. Zhang, W. Dai, C. Zhao, S. Huang, Advancing NASICON solid-state electrolytes for lithium metal batteries: interfacial challenges, engineering strategies, and future directions, Energy Storage Materials. **81**, 104471 (2025).
4. J. Kang, Z. Hu, M. Niu, J. Wang, Z. Qi, Z. Zheng, Y. Liu, C. Jia, X. Ken, T. Yang, S. Xu, T. Wu, Y. Liu, D. Wang, S. Yuan, X. Wei, Y. Liu, L. Liu, Recent Advances in NASICON-Type Electrolytes for Solid-State Metal Batteries, Carbon energy. **7**, 1 (2025).
5. J.-S. Kim, D. Han, J. Choe, Y. Kim, Y. Kim, H.-Y. Kim, S. Lee, J. Seo, S.-H. Ham, Y.Y. Song, C.-D. Lee, H. Kwak, J. Kim, Y.S. Jung, S.-K. Jung, K.-W. Nam, D.-H. Seo, Divalent anion-driven framework regulation in Zr-based halide solid electrolytes for all-solid-state batteries, Nat. Commun. **16**, 10678 (2025).
6. M. Gain, F. Tietz, O. Guillon, New promising NASICON material as solid electrolyte for sodium-ion batteries: Correlation between composition, crystal structure and ionic conductivity of Na3+xSc2SixP3-xO12, Solid state ionics. **293**, 18 (2016).
7. J. Hafner, Ab-Initio Simulations of Materials Using VASP: Density-Functional Theory and Beyond, J Comput. Chem. **29**, 2044 (2008).
8. J. Slater, An Augmented Plane Wave Method for the Periodic Potential Problem, Phys. Rev. **92**, 603 (1953).

Redox behaviour of the Co_3O_4 (001) surface for Li–air batteries: a DFT study

Pabalelo Malatjie*, *Tshegofatso* Phaahla, *Phuti* Ngoepe, *Khomotso* Maenetja
Materials Modelling Centre, School of Physical and Mineral Sciences, University of Limpopo, Private Bag x1106, Sovenga 0727, South Africa

Abstract. Over the years Co_3O_4 structure has gained more research interest as catalyst for various components. However, the catalytic behaviour of Co_3O_4 remains poorly understood, hence we employ computational modelling based on density functional theory (DFT) to the explore the redox properties of the $Co3O_4$ (001) surface in Li-air batteries application. The results indicated that adsorbing oxygens on the Co_3O_4 (001) surface stabilizes the surface, while removing oxygens destabilizes the surface. The work function Φ also increased with the increase in the number of oxygens, while the was slight increase in the work function Φ when oxygens are removed.

1 Introduction

Currently, electric energy demand and depleting raw materials which is increasing day by day calls for alternative, clean energy storage equipment and since conventional fossil fuels contribute to global warming, there is a high need for energy sources for our everyday needs as a household (especially with the limited power supply issue we are currently facing in South Africa) [1]. Several alternative energy sources were previously explored by many researchers and aside from the range of other energy sources (fossil fuels, nuclear energy etc.), lithium-air batteries are considered the most promising and least expensive batteries that can solve challenge of energy demand. Their environmental friendliness and low cost compensate for high carbon emissions, pollution of fossil fuels and high cost of nuclear energy respectively [2]. However, these metal-air batteries lose substantial capacity due to the generation of unstable discharge products, which causes excessive overpotential, poor electrochemical performance, and electrode deterioration [3]. Many catalysts and electrolyte mediators, including MnO_2, SnO_2, VCo_2O_4, Co_3O_4, etc., have been used in the past to address these problems by lowering the high over-potential [4]. Hence, we will be using Co_3O_4 as a catalyst to improve the performance of the lithium air battery by first understanding the redox properties of the most stable surface of our catalyst.

*Corresponding author: pabalelopabi1@gmail.com

2 Materials and methodology

This study employed the density functional theory (DFT) calculations with Vienna Ab-initio Simulation Package (VASP) [5] where all calculations were performed within the generalized gradient approximation (GGA) using Perdew, Burke, and Ernzerhof (PBE) exchange-correlation functional [6]. The cut-off energy of 600 eV and the *k*-points of 5x5x5 was used for Co_3O_4 the bulk structure, while the surface slabs were set at 5x5x1. We included the U-parameter of U = 3.0 eV to describe the 3*d* localized orbitals of Co.

3 Results and discussion

The investigation initially focused on the oxidation of the surface at different geometries, primarily on-site A-F as shown in figure 1b, followed by reduction on the same surface at sites 1-8. The results indicate that the surface its stabilised when oxygen is adsorbed on Co-D with the surface free energy of σ = 0.087 eV. Conversely, reduction makes the surface more reactive as the surface free energies increases when oxygen is removed. This is also reflected in the work function Φ, which increases with oxygen adsorption on the Co_3O_4 (001) surface, reaching a maximum of Φ = 6.66 eV. During reduction, the work function slightly increases as the number of oxygen atoms decreases from the surface.

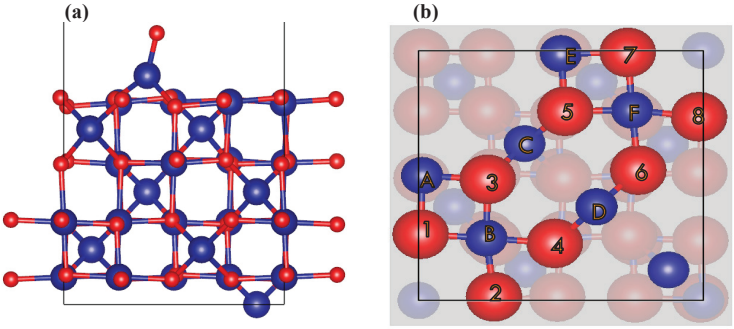


Fig. 1. (a) oxygen atom adsorbing on the (001) Co3O4 surface (b) different geometry sites for redox calculation.

4 Conclusion

The DFT approach was successfully utilized to investigate the redox properties on the Co_3O_4 (001) surface as a catalyst for Li_2O_2 batteries. Oxygen atom adsorption stabilises Co_3O_4 (001), whereas reduction increases surface free energies and destabilizes the system. The work function value increases with oxygen adsorption. The work function Φ is slightly increased by decreasing the number of oxygen atoms on the surface, while the surface's reactivity decreases when oxygen atoms adsorb onto it. The surface's reactivity increases after removing oxygen atoms, with no charge lost during oxygen oxidation and reduction.

References

1. R. Inglesi-Lotz, Load shedding in South Africa: Another nail in income inequality?. S. Afr. J. Sci., **10**, 119, (2023). https://doi.org/10.17159/sajs.2023/16597
2. F. Perera and K. Nadeau, Climate change, fossil-fuel pollution, and children's health. N. Eng. J. Med., **386**, 2303-2314, (2022).

   https://doi.org/10.1056/nejmra2117706
3. J. Ryu, M. Park, and J. Cho, Advanced technologies for high-energy aluminum–air batteries, Adv. Mater., **31**, 1804784, (2019).

   https://doi.org/10.1002/adma.201804784
4. S. Kang, Y. Mo, S. P. Ong, and G. Ceder, A facile mechanism for recharging Li2O2 in Li–O2 batteries. Chem. Mater., **25**, 3328–3336 (2013).

   https://doi.org/10.1021/cm401720n
5. F. Fuchs, J. Furthmüller, F. Bechstedt, M. Shishkin, and G. Kresse, Quasiparticle band structure based on a generalized Kohn-Sham scheme. Phys. Rev. B.,**76**, 115109 (2007). https://doi.org/10.1103/PhysRevB.76.115109
6. J. P. Perdew, K. Burke, and M. Ernzerhof, Generalized gradient approximation made simple. Phys. Rev. Lett., **77**, 38651996 (1996).

   https://doi.org/10.1103/PhysRevLett.77.3865

First-principles comparative study of $LiTi_2(PO_4)_3$ and $LiGe_2(PO_4)_3$: the role of Ti and Ge in structural and electronic properties

Leago Pitsa*, *Kemeridge* Malatji, *Phuti* Ngoape, and *Khomotso* Maenatja

Materials Modelling Centre, University of Limpopo, Private Bag x1106, Sovenga 0727, South Africa.

Abstract. NASICON-type solid-state electrolytes, such as $LiTi_2(PO_4)_3$ (LTP) and $LiGe_2(PO_4)_3$ (LGP), were investigated using first-principles density functional theory (DFT) calculations to evaluate the effects of Ti and Ge substitution on their structural, electronic, and mechanical properties. LGP exhibits a denser lattice and shorter bond lengths than LTP, indicating stronger bonding. LTP has a band gap of 2.676 eV and LGP shows a larger gap of 3.686 eV, classifying LTP as a semiconductor and LGP as an insulator.

1. Introduction

The rapid growth in portable electronic devices and electric vehicles has intensified the demand for safer and more efficient energy storage technologies [1-3]. Solid-state lithium-ion batteries have gained significant attention due to their enhanced safety, thermal stability, and electrochemical performance compared to conventional liquid electrolyte systems [4,5]. Among various solid electrolytes, NASICON-type materials are particularly attractive because of their three-dimensional lithium-ion conduction pathways, structural robustness, and favourable electrochemical stability [6]. Despite their promising characteristics, both materials exhibits low ionic conductivity and therefore require further optimization to enhance their ionic conductivity and structural performance[7]. This study aims to conduct a first principles (DFT) comparative analysis of LTP and LGP to evaluate how Ti and Ge affects their structural and electronic properties within the rhombohedral NASICON framework. The goal is to identify the most suitable composition for solid-state electrolyte applications and provide atomistic insights for the design of advanced lithium-ion battery materials.

2. Materials and methodology

Density Functional Theory (DFT) calculations were performed through the Vienna Ab initio Simulation Package (VASP) [8,9] using the Generalized gradient approximation (GGA). All calculations used Perdew, Burke, and Ernzerhof in solids (PBEsol) exchange–correlation

* Corresponding author: leagoheaven63@gmail.com

functional for examining the properties [10]. For the electronic properties Ti as a transition metal used a U parameter of 3.5 eV [11]. A plane-wave basis set with an energy cutoff of 500 eV was employed to ensure accurate total energy convergence. The Brillouin zone was sampled using a Monkhorst–Pack k-spacing of 0.219 $Å^{-1}$ for bulk calculations.

3. Results and discussion

Both $LiTi_2(PO_4)_3$ and $LiGe_2(PO_4)_3$ are stable in the rhombohedral NASICON phase, with LGP exhibiting a more compact lattice and shorter bond lengths. The structural contraction in LGP suggests stronger Ge-O bonding compared to Ti-O bonding in LTP. Electronic band structure analysis shows band gaps of 2.676 eV for LTP and 3.686 eV for LGP which indicades semiconductor and insulator, respectively. The larger band gap of LGP indicates superior electronic insulation, desirable for solid electrolyte applications. Density of states results reveal that O 2p orbitals dominate the valence band in both systems, while Ti 3d states significantly influence the conduction band in LTP.

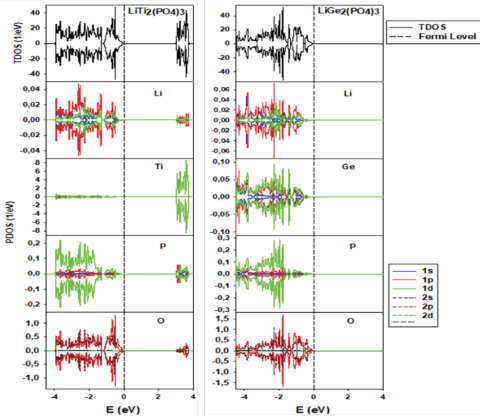


Fig. 1: Density of states for (a)LTP and (b)LGP

4. Conclusion

In this study, first-principles density functional theory (DFT) calculations were performed to investigate the structural and electronic properties of the materials. The results confirm that both compounds are structurally stable in the rhombohedral NASICON phase. Electronic structure analysis shows that LTP behaves as a semiconductor, whereas LGP exhibits a larger band gap, indicating stronger insulating behavior. The difference in band gap mainly arises from the presence of Ti 3d states near the conduction band in LTP, which reduce the band gap. In contrast, the Ge states in LGP lie higher in the conduction band and contribute less near the band edges. In both materials, the valence bands are primarily dominated by O 2p states. Overall, LGP demonstrates enhanced structural characteristics and stronger insulating properties, suggesting its potential as a promising solid-state electrolyte candidate.

We sincerely acknowledge the National Research Foundation (NRF) for their financial support. This study utilized the computational resources of the Materials Modelling Centre (MMC) at the University of Limpopo and the Centre for High Performance Computing (CHPC) in Cape Town, South Africa.

References

1. I. Hadjipaschalis, A. Poullikkas, V. Efthimiou, Overview of current and future energy storage technologies for electric power applications. Renew. Sustain. Energy Rev., **13**, 1513-1522 (2009) https://doi.org/10.1016/j.rser.2008.09.028
2. A. Azzuni, C. Breyer, Energy security and energy storage technologies. Energy Procedia, **155**, 237-258 (2018) https://doi.org/10.1016/j.egypro.2018.11.053
3. Y. Zou, Z. Lin, D. Li, Z. Liu, Advancements in Artificial Neural Networks for health management of energy storage lithium-ion batteries: A comprehensive review. J. Energy Storage., **73**, 109069 (2023) https://doi.org/10.1016/j.est.2023.109069
4. X. Yu, R. Chen, L. Gan, H. Li, L. Chen, Battery Safety: From Lithium-Ion to Solid-State Batteries Engineering, **21**, 9-14 (2023) https://doi.org/10.1016/j.eng.2022.06.022
5. B. Lang, B. Ziebarth, C. Elsässer, Lithium Ion Conduction in LiTi2(PO4)3 and Related Compounds Based on the NASICON Structure: A First-Principles Study Chem. Mater., **27**, 5040-5048 (2015). https://doi.org/10.1021/acs.chemmater.5b01582
6. L. Zhang, Y. Liu, Y. You, A. Vinu, L. Mai, NASICONs-type solid-state electrolytes: The history, physicochemical properties, and challenges. interd meter., **2**, 91-110 (2023) https://doi.org/10.1002/idm2.12046
7. X. Deng, Y. Wang, J. A. Chen, L. Zhang, T. Cao, G. Huang, Inorganic precipitation synthesis of Sn-doped LiTi2(PO4)3 as an anode material for high-performance aqueous lithium-ion batteries. J. Mater. Sci., **60**, 7653-7666, (2025) https://doi.org/10.1007/s10853-025-10887-6
8. N. Argaman, G. Makov, Density functional theory: An introduction. Am. J. Phys., **68**, 69-79 (2000) https://doi.org/10.1119/1.19375
9. X. Li, Y. Ma, W. Zhou, Z. Liu, Spin-polarized DFT calculations of elemental effects on hydrogen atom adsorption on FeCrAl (1 1 0) surface. Appl. Surf. Sci., **581**,152273 (2022) https://doi.org/10.1016/j.apsusc.2021.152273
10. A. M. De Andrade, J. Kullgren, P. Broqvist, Improving the transferability of density functional theory predictions through correlation analysis: Structural and energetic properties of NiX alloys (X = C, Si, Ge, and Sn). Phys. Rev. B, **105**, 085127 (2022) https://doi.org/10.1103/PhysRevB.105.085127
11. E. German, R. Faccio, A.W. Mombrú, A DFT + *U* study on structural, electronic, vibrational and thermodynamic properties of TiO_2 polymorphs and hydrogen titanate: tuning the Hubbard '*U*-term'. J.Phys. Commun., **1**, 055006 (2017) https://doi.org/10.1088/2399-6528/aa8573

Prelithiation of $LiMn_2O_4$@Li_2MnO_3 core-shell cathodes: molecular dynamics study

Mogau Kgasago[1]*, *Katlego* Phoshoko[2], *Donald* Hlungwani[1], *Phuti* Ngoepe[1], and *Raesibe* Ledwaba[1]

[1]Materials Modelling Centre, University of Limpopo, Private Bag x1106 Sovenga, 0727, South Africa
[2]Data Intensive Research Initiative of South Africa, Council for Scientific and Industrial Research, P.O. Box 395, Pretoria, 0001, South Africa

Abstract. Prelithiation is an effective strategy to compensate for the initial irreversible capacity loss that occurs during the first charge of lithium-ion battery cathodes. Molecular dynamics simulations were used to investigate the combined effects of prelithiation and core–shell engineering in a $Li_2Mn_2O_4$@Li_2MnO_3 system. The Li_2MnO_3 shell stabilized the spinel core during delithiation, maintaining structural integrity from $Li_{2.0}$ to $Li_{1.2}$ and up to 1200 K without interfacial degradation. Radial distribution analysis confirmed minimal Mn–O distortion, while lithium diffusion remained high (4.54×10^{-7} cm^2 s^{-1}). These results suggest that prelithiated core–shell designs could improve the stability of spinel cathodes.

1 Introduction

Spinel $LiMn_2O_4$ is a promising cathode material due to its low cost and three-dimensional lithium diffusion pathways, but its performance is limited by irreversible capacity loss and Mn migration during cycling [1]. Increasing the lithium content of pristine $LiMn_2O_4$ through prelithiation can compensate for lithium loss and improve the initial lithium inventory [2]. However, directly over-lithiating the pristine spinel destabilizes the structure and promotes Mn migration, limiting its long-term stability. Introducing a Li_2MnO_3 shell offers a strategy to stabilize the structure and suppress Mn migration while maintaining ionic conductivity and interfacial integrity [3]. This study therefore investigates the influence of prelithiation combined with a Li_2MnO_3 core–shell design on the structural stability and Li-ion mobility of $LiMn_2O_4$ during delithiation.

2 Materials and methodology

A $Li_2Mn_2O_4$ spinel core was constructed and coated with a Li_2MnO_3 shell to form a nano-spherical $Li_2Mn_2O_4$@ Li_2MnO_3 core-shell structure, using an optimized interface distance and shell thickness. Stepwise lithium removal from the core region was employed to simulate the charging process across compositions from $Li_{2.0}Mn_2O_4$@ Li_2MnO_3 to $Li_{1.2}Mn_2O_4$@

[1] Corresponding author: 201818190@myturf.ul.ac.za

Li_2MnO_3. Molecular dynamics simulations were performed using the DL_POLY code [4] in the NVT ensemble with the Nosé-Hoover thermostat, while long-range electrostatic interactions were treated using the Ewald summation method.

3 Results and discussion

The results indicate that the core-shell structure remained structurally intact across all lithium concentrations and temperatures investigated, with no evidence of interfacial separation. Coordination analysis confirmed the retention of MnO_6 octahedra, with only minor increases in MnO_5 units at lower lithium contents, suggesting controlled structural relaxation. Radial distribution function analysis showed stable Mn-O bond distances and preserved interfacial bonding. At 300 K, the core-shell system exhibited a diffusion coefficient of 4.54×10^{-7} cm^2 s^{-1}, slightly higher than the core-only structure (4.35×10^{-7} cm^2 s^{-1}), with diffusion increasing further at elevated temperatures and higher lithium concentrations.

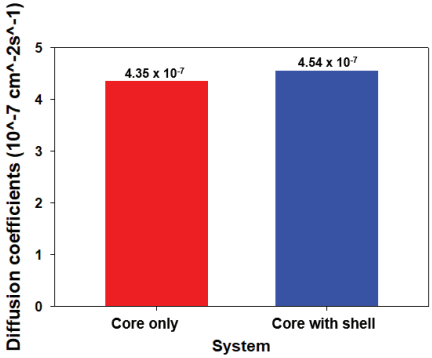


Fig. 1. Comparison of lithium diffusion coefficients for prelithiated core and core-shell systems at 300 K.

4 Conclusions

This study demonstrates that combining prelithiation with core–shell engineering enhances the structural stability of spinel $LiMn_2O_4$ without compromising lithium-ion mobility. The Li_2MnO_3 shell effectively suppresses manganese migration and preserves interfacial integrity during delithiation, maintaining a stable Mn-O framework even at elevated temperatures and reduced lithium contents. Coordination and radial distribution analyses confirmed that structural relaxation occurs without lattice collapse. Importantly, diffusion results show that the shell does not hinder lithium transport, with the core-shell system exhibiting slightly higher diffusion coefficients than the core-only structure. Overall, the integration of prelithiation and core-shell design provides a balanced approach to improving both structural reliability and ionic conductivity in spinel-based cathodes.

The authors acknowledge the financial support of the National Research Fund (NRF) and Materials Modelling Centre at the University of Limpopo, as well as the computational resources provided by the National Integrated Cyberinfrastructure System (NICIS).

References

1. N.M. Jobst, G. Gabrielli, P. Axmann, M. Hölzle, M. Wohlfahrt-Mehrens, Compensation of the Irreversible Loss of Si-Anodes via Prelithiated NMC/LMO Blend Cathode, J. Electrochem. Soc., **168**, 070550, (2021).
2. F. Holtstiege, P. Bärmann, R. Nölle, M. Winter, T. Placke, Pre-Lithiation Strategies for Rechargeable Energy Storage Technologies: Concepts, Promises and Challenges, Batteries, **4**, 1-39, (2018).
3. J. Xu, S. Zhu, Z. Xu, H. Zhu, The basic physical properties of Li_2MnO_3 and $LiMn_2O_4$ cathode materials, Comput. Mater. Sci., **229**, 1-7, (2023).
4. I.T. Todorov, W. Smith, The DL_POLY_4 user manualSTFC Daresbury Laboratory, Cheshire, United Kingdom, (2021).

The effect of F on $LiMn_2O_4$ cathode material: a DFT+U study

Mmeshi Hiine[1*], *Kemeridge Malatji*[1], *Phuti Ngoepe*[1], and *Khomotso Maenetja*[1]

[1]Materials Modelling Centre, University of Limpopo, Private Bag x1106, Sovenga 0727, South Africa.

Abstract. Density functional theory with the Hubbard parameter (DFT+U), implemented in the Vienna Ab initio Simulation Package (VASP) code, was used to investigate the structural properties of pristine and F-doped $LiMn_2O_4$. The cluster expansion technique was employed to generate possible fluorinated phases by partially substituting oxygen with fluorine in the $LiMn_2O_4$ lattice. The results show that $LiMn_2O_{3.75}F_{0.25}$ is the most thermodynamically stable among the predicted structures, as indicated by its lower heat of formation compared to the other compositions.

1 Introduction

Spinel $LiMn_2O_4$ has been widely considered a promising cathode material for lithium-ion batteries due to its low cost, environmental friendliness, and natural abundance of manganese. However, $LiMn_2O_4$ suffers from structural instability during cycling, mainly caused by Jahn–Teller distortions and oxygen loss, which lead to capacity fading and reduced performance [1]. Doping $LiMn_2O_4$ with other elements has been explored as an effective strategy to improve its structural stability and electrochemical performance [2]. Therefore, this study aims to investigate the effect of fluorine substitution on the structural and thermodynamic properties of $LiMn_2O_4$ using cluster expansion combined with density functional theory (DFT) calculations.

2 Materials and methodology

The search for the ground-state structures of $LiMn_2O_{4-x}F_x$ was carried out using the Universal Cluster Expansion code (UNCLE) [3]. The density functional theory (DFT) based Vienna ab initio simulation package (VASP) [4] code was used to compute the total energy, while the Perdew-Burke-Ernzerhof (PBE) generalized gradient approximation (GGA) was employed to assess the exchange-correlation interaction [5].

* Corresponding author: jassicon11@gmail.com

3 Results and discussion

Table 1 : Calculated space groups, lattice parameters, and formation energies of $LiMn_2O_{4-x}F_x$ structures.

System	Space Group	Lattice Parameters (Å)	Energy of formation (kJ/mol)
$LiMn_2F_4$	Fd-3m	a=8.474286 b=8.474286 c=8.474286	-894.28
$LiMn_2O_{1.5}F_{2.5}$	Cm	a=10.840158 b=6.2612727 c=10.847598	-3206.52
$LiMn_2OF_3$	P-4m2	a=6.229442 b=6.229442 c=8.872225	-1684.25
$LiMn_2O_2F_2$	I4_1md	a=6.166952 b=6.166952 c= 8.651814	-1511.96
$LiMn_2O_{2.25}F_{1.75}$	Cm	a=10.376875 b=6.061885 c=10.569789	-5841.16
$LiMn_2O_{2.5}F_{1.5}$	Cm	a=10.551176 b=6.034893 c=6.289867	-2861.47
$LiMn_2O_3F$	Ima2	a=6.172915 b=8.447713 c=5.843503	-1387.49
$LiMn_2O_{3.5}F_{0.5}$	Cm	a=10.329653 b=5.968640 c=10.306497	-2621.05
$LiMn_2O_{3.75}F_{0.25}$	Pm	a=8.544742 b=5.835656 c=5.857575	-5088.08
$LiMn_2O_4$	Fd-3m	a=8.336821	-674.24

Table 1 shows that the heat of formation for F-doped $LiMn_2O_4$ structures are lower than that of the pristine $LiMn_2O_4$, implying that fluorine incorporation enhances the thermodynamic stability of the spinel structure.

4 Conclusion

The stability of pristine and F-doped $LiMn_2O_4$ was investigated using DFT+U calculations. The results show that introducing fluorine improves the thermodynamic stability of $LiMn_2O_4$, as indicated by the lower heat of formation compared to the pristine material.

The authors gratefully acknowledge financial support from the National Research Foundation (NRF) of South Africa. Computational work was carried out using resources from the Materials Modelling

Center (MMC) at the University of Limpopo, the Centre for High Performance Computing (CHPC), and the National Integrated Cyberinfrastructure System (NICIS), based in Cape Town, South Africa.

References

[1] M.M. Thackeray, Prog. Solid State Chem. **25**, 1 (1997)
[2] J. Reed, G. Ceder, Chem. Rev. **104**, 4513 (2004)
[3] D. Lerch, O. Wieckhorst, G.L. Hart, R.W. Forcade, S. Müller, Model. Simul. Mater. Sci. Eng. **17**, 055003 (2009)
[4] G. Kresse, J. Furthmüller, Phys. Rev. B. **54**, 11169 (1996)
[5] J.P. Perdew, K. Burke, M. Ernzerhof, Phys. Rev. Lett. **77**, 3865 (1996)

Structural, thermodynamic and mechanical properties of TiNbMoCrW high-entropy alloy

Ramalebana Moeti*, *Tshegofatso Phaahla*, *Phuti Ngoepe* and *Hasani Chauke*

[1]Materials Modelling Centre, University of Limpopo, Private Bag X 1106, Sovenga, 0727, South Africa

Abstract. High-entropy alloys (HEAs) have gained significant attention for high-temperature applications due to their excellent thermal stability, mechanical strength, and resistance to structural degradation. However, identifying compositions that maintain phase stability and mechanical performance under extreme conditions remains challenging. In this study, density functional theory (DFT) was employed to investigate the structural, thermodynamic, and mechanical properties of the TiMoNbCrW HEA. The calculated structural parameters agree with experimental data within 5.26%. The alloy demonstrates thermodynamic favorability and mechanical stability, indicating strong structural integrity. These results highlight the potential of TiMoNbCrW as a stable single-phase HEA suitable for high-temperature applications.

1 Introduction

High-entropy alloys represent a new class of advanced materials that consist of five or more principal elements mixed in near-equiatomic compositions [1]. This concept was first introduced to overcome the limitations of conventional alloys and to explore new compositional spaces in materials design [2]. Due to their high configurational entropy, HEAs often form simple solid-solution phases such as body-centered cubic (BCC), face-centered cubic (FCC), or hexagonal close-packed (HCP) [3]. These alloys exhibit exceptional properties including high strength, good thermal stability, oxidation resistance, and excellent mechanical performance at elevated temperatures, making them promising materials for high-temperature applications in aerospace and energy systems [4]. However, designing stable HEAs with optimal performance remains challenging due to the complexity of multi-component systems [5]. Therefore, computational approaches such as Density Functional Theory (DFT) are widely used to predict and understand the structural, thermodynamic and mechanical properties of HEAs. In this study, DFT calculations are employed to investigate the TiMoNbCrW high-entropy alloy and evaluate its potential for high-temperature applications.

* Corresponding author: ramalebana19@gmail.com

2 Methodology

The calculations were carried out employing first-principles approach based on the DFT as implemented in the Vienna ab initio simulation package (VASP) code [6]. The exchange-correlation energy functional was described by the well-established by Perdew, Burke and Ernzerhof (PBE) [7] version of the generalized gradient approximation (GGA) [8]. The High-Entropy Alloys Predicting Software (HEAPS) [9] was used to determine thermodynamic properties of the TiNbMoCrW alloy. To ensure highly converged and accurate results, the Brillouin zone integration was performed using the Monkhorst-Pack k-point sampling scheme. A suitable k-point mesh of 6x3x3 and a kinetic energy cutoff of 325 eV were used to converge the total energy of the structure.

3 Results and discussion

Table 1: Calculated mixing enthalpy (ΔHmix) and entropy of mixing (ΔSmix), Gibbs energy of mixing(ΔG_mix), atomic size difference(δ), ratio of entropy and enthalpy of mixing(Ω) and valence electron concentration (VEC) of TiNbMoCrW alloy.

Parameter	Solid solution phase	TiNbMoCrW
ΔH_{mix}	$-10\frac{KJ}{mol} < \Delta H_{mix} < 5\frac{KJ}{mol}$	-4.64
ΔS_{mix}	$\Delta S_{mix} \geq 13{,}38\ \frac{J}{Kmol}$	13.38
ΔG_{mix}	ΔG_{mix} = negative	-18.02
δ	$\delta \leq 6{,}6\ \%$	5.3
Ω	$\Omega \geq 1{,}1$	7.56
VEC	$VEC < 6{,}8$ for BCC and $VEC > 8$ for FCC	5.40
Melting temperature	-	2692

The results indicate that the calculated lattice parameter (a = 3,3350 Å) and the experimental value (a = 3,1685Å [4]), are in good agreement. This structural consistency suggests that the material is stable and well-ordered. The results in Table: 1 indicated that the structure is a solid solution phase with a BCC configuration and thermodynamically stable. Additionally, the structure was found to be mechanically stable implying that the alloy is structurally reliable and capable of maintaining its integrity under mechanical loading.

4 Conclusion

The structural, thermodynamic, and mechanical properties of the TiMoNbCrW high-entropy alloy were examined using the density functional theory (DFT) approach. The calculated structural parameters closely align with available experimental data, with deviations of less than 5.26%, thereby confirming the reliability of the computational method. The findings demonstrate that the alloy is both thermodynamically and mechanically stable, which

indicates its capacity to maintain structural integrity under small mechanical deformations and varying thermodynamic conditions. Consequently, the TiMoNbCrW high-entropy alloy exhibits robust structural stability and favourable mechanical performance, making it a promising candidate for high-temperature applications.

This work was conducted at the Materials Modelling Centre, University of Limpopo and the Centre for High Performance Computing (CHPC) in Cape Town. The authors would like to acknowledge the financial support of the National Research Foundation (NRF).

References

1. Y. Jien-Wei, S.K. Chen, S.J. Lin. Adv. Eng. Mater, **6**, 299–303 (2004).
2. B. Cantor, I.T.H. Chang, P. Knight, A.J.B. Vincent, Mater. Sci. Eng., A, **375**, 213–218 (2004).
3. Y. Zhang, T.T. Zuo, Z. Tang, (2014). Prog. Mater. Sci**.**, **61**, 1–93 (2014).
4. N. Oleg, D. Senkov, G.B. Wilks, J.M. Scott, D.B. Miracle, IM, **19**, 698–706 (2011).
5. C. Michael, Y. Gao, J.W. Yeh, P.K. Liaw, P.K. (2016).
6. G. Kresse, J. Hafner, Phys. Rev. B, **47**, 558-561, (1993).
7. P.J. Perdew, K. Burke, M. Ernzerhof, Phys. Rev. Lett, **77**, 3865-3868 (1996)
8. D. Karlsson, G. Ek, J. Cedervall, C. Zlotea, K.T. Møller, T.C. Hansen, J. Bednarcik, M. Paskevicius, M.H. Sørby, T.R. Jensen, U. Jansson, Inorg. Chem., **57**,2103-2110 (2018).
9. P. Martin, C.E. Madrid-Cortes, C. Cáceres, N. Araya, C. Aguilar, J.M. Cabrera, Comput. Phys. Commun, **278**, 08398, (2022)

Transport properties of pristine, lithiated and Al-doped $LiTi_2(PO_4)_3$ solid electrolyte materials

Lisbon Maake[1*], *Beauty* Shibiri[1], *Phuti* Ngoepe[1] and *Raesibe* Ledwaba[1]

[1]Materials Modelling Centre, University of Limpopo, Private Bag x1106, Sovenga, 0727, South Africa

Abstract. The NASICON-type $LiTi_2(PO_4)_3$ (LTP) solid electrolyte is a promising candidate for solid-state batteries due to its broad electrochemical stability window and strong chemical durability. However, its low ionic conductivity remains a challenge. In this study, molecular dynamics simulations were utilised to generate and compare pristine, lithiated ($Li_3Ti_2(PO_4)_3$) and Al-doped ($Li_{1.3}Al_{0.3}Ti_{1.7}(PO_4)_3$) LTP, with the focus on evaluating how these compositional modifications influence Li^+ transport properties. Lithium mobility was quantified using diffusion analysis, and the results showed improved activation energy and Li^+ diffusion in the lithiated and doped LTP systems relative to pristine LTP, indicating enhanced ionic conductivity through compositional tuning.

1 Introduction

NASICON-type lithium titanium phosphate (LTP) solid electrolytes have attracted significant attention for their potential application in solid-state batteries due to their stability and relatively high ionic conductivity compared to other solid electrolytes. However, despite these advantages, their ionic conductivity remains insufficient for large-scale application, limiting their practical use in battery technologies [1, 2].

To better understand and address this limitation, it is imperative to study the lithium-ion transport mechanisms in rhombohedral NASICON-structured $LiTi_2(PO_4)_3$ and $Li_3Ti_2(PO_4)_3$. In $LiTi_2(PO_4)_3$, Li ions primarily occupy node sites and migrate along separated chains, whereas in $Li_3Ti_2(PO_4)_3$, Li ions at transition sites experience repulsion from surrounding Li ions, leading to concerted motion along multiple 3D pathways [2, 3]. Theoretical calculations indicate that the larger diffusion bottleneck in $Li_3Ti_2(PO_4)_3$ reduces the hopping energy compared to $LiTi_2(PO_4)_3$, contributing to its enhanced transport properties [1]. Another way to improve the transport performance of LTP is through aliovalent Al doping, which introduces additional Li ions for charge compensation and modifies the local NASICON framework, thereby lowering the migration barrier and enhancing Li ions diffusion and ionic conductivity [3, 4].

To further explore the impact of structural modifications on ionic conductivity and diffusion, this study employs molecular dynamics simulations to generate NASICON-type LTP solid electrolytes through the amorphisation and recrystallisation technique. Through the analysis

* Corresponding author: lisbonmaake8@outlook.com

of transport properties across different NASICON-type LTP structures, the research provides valuable insights into the structure, activation energy, conductivity, and diffusion relationship of the LTPs, aiding in its optimisation for next-generation solid-state battery applications.

2 Methodology and results

In this study, all molecular dynamics simulations were performed using the DL_POLY code [5]. The canonical (NVT) ensemble was employed to maintain a constant temperature during the simulations, making it suitable for evaluating temperature-dependent diffusion behaviour. Using this setup, the diffusion coefficients were calculated over a range of temperatures for pristine, lithiated, and doped LTP. Activation energies were then obtained from Arrhenius plots constructed using the lithium diffusion coefficients across the simulated temperature range. The room-temperature (RT) ionic conductivities were calculated using the Nernst-Einstein relation.

Table 1: Comparison of the activation energies of the bulk $LiTi_2(PO_4)_3$, $Li_3Ti_2(PO_4)_3$ and $Li_{1.3}Al_{0.3}Ti_{1.7}(PO_4)_3$ with their corresponding slopes for the regime < 1000 K.

Structures	Slope (K)	Activation energy (eV)	
		This work	Experimental
$LiTi_2(PO)_3$	-4002.70	0.34	0.16 - 0.40 [3, 4]
$Li_3Ti_2(PO)_3$	-3063.59	0.26	
$Li_{1.3}Al_{0.3}Ti_{1.7}(PO_4)_3$	-1812.86	0.16	

The $Li_{1.3}Al_{0.3}Ti_{1.7}(PO_4)_3$ exhibits the lowest activation energy (0.16 eV), followed by $Li_3Ti_2(PO_4)_3$ (0.26 eV) and $LiTi_2(PO_4)_3$ (0.34 eV), as presented in Table 1. This indicates that Li^+ migration is energetically most favourable in the Al-doped system, requires more energy in the lithiated system, and is least favourable in the pristine material. At room temperature, the diffusion coefficients are 2.23×10^{-8} cm^2/s for pristine LTP, 1.37×10^{-7} cm^2/s for lithiated LTP and 4.76×10^{-7} cm^2/s for the Al-doped LTP. The corresponding RT ionic conductivities are 4.79×10^{-4} S/cm, 1.067×10^{-2} S/cm and 1.13×10^{-2} S/cm for the pristine, lithiated and Al-doped LTP systems, respectively. These indicate enhanced transport properties with lithiation and more advanced with Al doping.

3 Conclusion

Temperature-dependent diffusion simulations were successfully performed for pristine $LiTi_2(PO_4)_3$, lithiated $Li_3Ti_2(PO_4)_3$, and Al-doped The $Li_{1.3}Al_{0.3}Ti_{1.7}(PO_4)_3$ to compare their Li^+ transport behaviour. The results show a clear improvement in lithium mobility with compositional modification, with the The $Li_{1.3}Al_{0.3}Ti_{1.7}(PO_4)_3$ system exhibiting the lowest activation energy, the highest diffusion coefficients and ionic conductivity at RT. This confirms that Al-doping delivers the most favourable transport performance in this work, outperforming both the pristine and lithiated LTP structures and indicating stronger potential for solid-state electrolyte applications.

We thank the National Research Foundation (NRF) for financial support and acknowledge the computational resources of the MMC, University of Limpopo, and CHPC, Cape Town.

References

1. K. Takada, M. Tominaga, I. Yamada, T. Ichikawa, A. Kato, M. Kondo, S. Kondo, M. Watanabe, Lithium-ion conduction in $LiTi_2(PO_4)_3$. Solid State Ion. **139**, 241 (2001).
2. M. Giarola, A. Sanson, F. Tietz, S. Pristat, E. Dashjav, D. Rettenwander, G.J. Redhammer, G. Mariotto, Structure and vibrational dynamics of NASICON-Type $LiTi_2(PO_4)_3$. J. Phys. Chem. C. **121**, 3697 (2017).
3. M. Monchak, T. Hupfer, A. Senyshyn, H. Boysen, D. Chernyshov, T. Hansen, K.G. Schell, E.C. Bucharsky, M.J. Hoffmann, H. Ehrenberg, Lithium Diffusion Pathway in $Li_{1.3}Al_{0.3}Ti_{1.7}(PO_4)_3$ (LATP) Superionic Conductor. Inorg. Chem. **55**, 2941 (2016).
4. V. Epp, Q. Ma, E.M. Hammer, F. Tietz, M. Wilkening, Very fast bulk Li ion diffusivity in crystalline $Li_{1.5}Al_{0.5}Ti_{1.5}(PO_4)_3$ as seen using NMR relaxometry. Phys. Chem. Chem. Phys. **17**, 32115 (2015).
5. W. Smith, T.R. Forester, DL_POLY_2. 0: A general-purpose parallel molecular dynamics simulation package. J. Mol. Graph. **14**, 136 (1996).

Atomistic simulation studies of Mooihoekite ($Cu_9Fe_{16}S_{16}$)

Kagiso Mashishi[1*], *Phuti* Ngoepe[1], *Peace* Mkhonto[1], and *Mofuti* Mehlape[1]

[1] Department of Physics, Material Modelling Centre, University of Limpopo, South Africa

Abstract. Molecular dynamics (MD) simulations were performed to investigate the thermodynamic behaviour of bulk mooihoekite. Interatomic potentials based on the Born model were parameterised by fitting to structural and elastic properties and subsequently employed in used in MD simulations. The developed potential model was validated through calculated lattice parameters, bond lengths and elastic constants, which showed good agreement with available electronic structure calculations and experimental data. Structural analyses based on radial distribution functions revealed increasing atomic disorder at elevated temperatures. In addition, diffusion coefficients increased significantly, indicating enhanced atomic mobility at elevated temperatures. Variations in the total system energy further suggested the occurrence of a phase transition, consistent with experimental observations.

1 Introduction

Transition metal sulphides constitute a critically important class of geologically abundant minerals and serve as major sources of copper, iron, nickel, and other technologically important metals [1]. Their complex crystal structures govern how they behave during processing, making it essential to understand their properties under varying thermodynamic conditions. This is especially important for improving flotation recoveries, which remains the dominant technique for sulphide mineral beneficiation. Among these sulphides, Mooihoekite ($Cu_9Fe_9S_{16}$) emerges as a particularly noteworthy copper-bearing phase. Experimental studies of Mooihoekite are complicated by its scarcity as a pure phase and its frequent association with other sulphides. Molecular dynamics (MD) simulations provide an alternative way to model the mineral's response to temperature, capturing both structural dynamics and long-range interactions. This study aims to derive novel interatomic potentials which will be subsequently used for molecular dynamics (MD) to study the bulk properties of mooihoekite under varying geological conditions like temperature.

2 Methodology

The GULP code [2] was used to fit and modify interatomic potentials originally developed by Blesgen [3]. These modified potentials were then applied in molecular dynamics

* Corresponding author: 201914374@myturf.ul.ac.za

simulations using the DL_POLY code [4]. Simulations were carried out in the canonical (NVT) ensemble on a tetragonal 3×3×3 supercell containing 918 atoms, with an equilibration time of 100 ps followed by a 200 ps production run. Temperature was controlled using the Nosé–Hoover thermostat to minimize energy drift caused by cumulative numerical errors during the simulations.

3 Results and discussion

Table 1. Fitted lattice parameters, bond lengths and elastic moduli of $Cu_9Fe_9S_{16}$

Parameters	a (Å)	b (Å)	c (Å)	Vol (Å^3)	Density(g.cm^{-3})
GULP (This work)	10.547	10.547	5.201	578.443	4.558
Experimental [5,6]	10.580	10.580	5.370	603.200	4.380 [4.40]
Bond distances (Å)					
Bond	Fe-S	Cu-S	Fe-Fe	Fe-Cu	
GULP (present work)	2.283	2.323	2.695	2.756	
Experimental [7]	2.280	2.330	2.692	2.731	
Elastic moduli (GPa)					
	Bulk modulus		Young's modulus		
GULP(This work)	78.79		87.89		
Experimental [5]	67.1		58.3		

Table 1 illustrates the fitted lattice parameters, bond lengths and elastic moduli of Mooihoekite. It is observed that the fitted lattice parameters, bond lengths and elastic moduli correlate reasonably well with the experimental results.

4 Conclusion

The interatomic potentials for mooihoekite were successfully derived using the GULP code. The potential model was able to reproduce the experimental lattice parameters, bond lengths and elastic moduli validating the potential model.

The authors acknowledge with gratitude the Materials Modelling Centre at the University of Limpopo and the computational resources provided by the Centre for High Performance Computing (CHPC) in Cape Town.

References

[1] M.E Schlesinger, K.C. Sole, W.G. Davenport, Extractive metallurgy of Copper (Elsevier, Oxford, 2011)
[2] J.D. Gale, A computer program for the symmetry-adapted simulation of solids, J. Chem. Soc, Faraday Trans, **94**, 3527-3536 (1997)

[3] T. Blesgen, A multiscale approach for quantitative simulations of diffusion induced segregation, Model. Simul. Mater. Sci. Eng, **14**, 389–408, (2006)
[4] W. Smith and T.R. Frester. A general-purpose parallel molecular dynamics simulation package J. Mol. Graph, **14**, 136-341(1996)

[5] L. Cabri and S. Hall, Mooihoekite and haycockite, two new copper-iron sulfides and their relationship to chalcopyrite and talnakhite, Am Mineral, **57**, 689-708, (1972)
[6] Q. Xianxiu, Q. Pengfei, D. Tingting, H. Hui, D. Xiaolong, S. Xun and C. Lidong, Thermoelectric Properties of Nano-grained Mooihoekite $Cu_9Fe_9S_{16}$, *Z. Anorg. Allg. Chem.* **646**, 1116–1121, (2020)
[7] S.R. Hall, Crystal structures of the chalcopyrite series, *Can. Mineral,* **13**, 168–172, (1975)

A computational investigation of niobium doping in $LiMn_{1.5}Ni_{0.5}O_4$ cathode materials

Shaney Mulaudzi*, *Gratitude* Mphahlele, *Phuti* Ngoepe, and *Kemeridge* Malatji

Materials Modelling Centre, University of Limpopo, Private Bag x1106, Sovenga 0727, South Africa.

Abstract. $LiMn_{1.5}Ni_{0.5}O_4$ cathode materials are promising for high-voltage lithium-ion batteries because of their high thermal stability and low cost. However, reducing production costs and improving long-term durability remain key challenges. This paper reviews recent advances in lithium nickel manganese oxide, focusing on dual doping to enhance electrochemical performance. The objective was to understand how niobium incorporation influences challenges such as Jahn–Teller distortion, Mn dissolution, limited Li+ diffusion, oxygen loss, poor intrinsic electronic conductivity, structural degradation, and poor conductivity. Density Functional Theory and Cluster Expansion methods were used to investigate structural, thermodynamic, mechanical, and electronic properties of pristine and Nb-doped.

1 Introduction

High-voltage $LiMn_{1.5}Ni_{0.5}O_4$ spinel cathodes provide a promising cobalt-free solution for next-generation lithium batteries but are traditionally hampered by bad electrical conductivity and structural instability during cycling [1]. To overcome these limitations, dual-doping strategies using Niobium specifically have emerged as a superior modification technique compared to single-element doping [1, 2]. The introduction of Nb ions into the crystal grid stabilizes the host structure by suppressing the Jahn-Teller distortion and minimizing mechanical stress during and after the lithiation. This synergistic change not only strengthens the stability of bulk crystals but also protects electrode surfaces from high voltage degradation and facilitates the rapid spread of lithium ions [3, 4]. Consequently, the Nb-doped $LiMn_{1.5}Ni_{0.5}O_4$ system exhibits significant improvements in capacity retention, high-rate performance, and thermal tolerance, positioning it as a highly robust candidate for high-performance energy storage applications [3, 5].

2 Materials and methodology

Density functional theory (DFT) calculations were performed within the Vienna ab initio simulation package (VASP) to calculate the structural, electronic, and mechanical properties. Using the default k-point mesh settings in the Perdew-Burke-Ernzerhof Generalized Gradient

* Corresponding author : thandishaney@gmail.com

Approximation (GGA-PBE), the plane wave cut-off energy was varied from 100-900 eV at intervals of 100 eV to determine the convergence point of the cut-off energy of $LiMn_{1.5}Ni_{0.5}O_4$. The total energy calculations were carried out at a fixed cut-off energy of 500eV while the k-points mesh was varied from 1x1x1 to 9x9x9. The Universal Cluster-Expansion (UNCLE) [6] code was used to generate phases $LiMn_{1.5}Ni_{0.5}O_4$ doped with Nb.

3 Results and discussion

The binary ground state diagram (Fig. 1.**)** shows the results of the cluster expansion. The cluster expansion method was succesfully used to generate 37 new phases of Nb-doped $LiMn_{1.5}Ni_{0.5}O_4$. The system exhibits a miscibility gap and miscible constituents, with six strucures lying on the ground state line, indicating their thermodynamic stability. Among these six structures, the most stable configuration occurs at the niobium site. The negative heats of formation suggest that the resulting phases are thermodynamically stable. The cluster expansion analysis shows that it favours the Nb site.

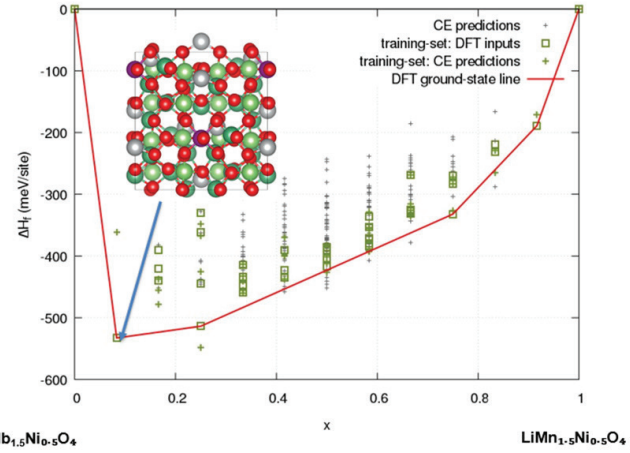


Fig. 1. Binary ground state diagram of Nb-doped $LiMn_{1.5}Ni_{0.5}O_4$.

4 Conclusion

The cluster expansion method was succesfully used to generate new phases of Nb doped $LiMn_{1.5}Ni_{0.5}O_4$, with some of the predicted structures being thermodynamically stable. $LiMn_{0.125}Nb_{1.375}Ni_{0.5}O_4$ was the most thermodynamically stable structure.

Study utilized the computational resources of the Materials Modelling Centre (MMC) at the University of Limpopo and the Centre for High Performance Computing (CHPC) in Cape Town, South Africa.

References

1. S. Choi, W. Feng, Z. Liu and Y. Xia, A novel morphology of high voltage LiMn1.5Ni0.5O4 cathode material with niobium-doping. Chem. Eng. J. **495**, 153447 (2024).
2. J. Cen, B. Zhu, S.R. Kavanagh, A.G. Squires and D.O. Scanlon, Cation disorder dominates the defect chemistry of high-voltage LiMn1.5Ni0.5O4 (LMNO) spinel cathodes. J. Mater. Chem. **11**, 13353-13370 (2023).
3. L. Ming, B. Zhang, Y. Cao, J.F. Zhang, C.H. Wang, X.W. Wang and H. Li, Effect of Nb and F co-doping on Li1.2Ni0.13Co0.13Mn0.54O2 cathode material for high-performance lithium-ion batteries. Front. Chem. **6**, 76 (2018).
4. H.G. Kim and Y.J. Park, Synergy effect of K doping and Nb oxide coating on Li1.2Ni0.13Co0.13Mn0.54O2 cathodes. J. Electrochem. Sci. Technol. **12**, 377-386 (2021).
5. A. Wei, J. Mu, R. He, X. Bai, X. Li, L. Zhang, Y. Wang, Z. Liu and S. Wang, Enhanced electrochemical performance of LiMn1.5Ni0.5O4 composite cathodes for lithium-ion batteries by selective doping of K+/Cl− and K+/F−. Nanomaterials. **9**, 2323 (2021).
6. D. Lerch, O. Wieckhorst, G.L. Hart, R.W. Forcade and S. Müller, UNCLE: a code for constructing cluster expansions for arbitrary lattices with minimal user-input. Model. Simul. Mater. Sci. Eng. **17**, 055003 (2009).

DFT study of palladium (Pd) as a catalyst in lithium-air batteries

Bornwise Mugwena*[1],*Percy* Ngobeni[2], *Phuti* Ngoepe[2] and *Khomotso* Maenetja[1]

Materials Modelling Centre, University of Limpopo, Private Bag x1106, Sovenga 0727, South Africa.

Abstract. Lithium-air batteries are promising for future energy storage due to their high energy density and environmental friendliness. Their performance, however, is limited by slow oxygen reduction and evolution reactions (ORR and OER) at the cathode. Palladium (Pd) can enhance these reactions due to its excellent catalytic properties. In this study, Density Functional Theory (DFT) was used to examine the cubic structural, electronic, vibrational, and surface properties of the metal. Vibrational analysis confirmed structural stability, and electronic properties showed metallic behaviour. These results offer insights for the design of more efficient lithium-air battery catalysts.

1 Introduction

The demand for cleaner and more efficient energy storage is growing faster than ever. Among the many options being explored, lithium-air batteries stand out for their ability to store far more energy than standard lithium-ion batteries [1], all at a lower production cost. At the heart of their operation are two key reactions the oxygen reduction reaction (ORR) during discharge and the oxygen evolution reaction (OER) during charging. However, both reactions are slow, limiting the battery's performance [2]. To overcome this challenge, our study focuses on Palladium (Pd) as surface catalyst to speed up these reactions [3]. The metal was chosen because of its stability, high corrosion resistance, and strong catalytic activity compared to conventional materials [4]. Using Density Functional Theory (DFT), the cubic structural, electronic, vibrational, and surface properties of the material are investigated to explore its role in improving the efficiency and lifespan of lithium-air batteries. The findings offer early guidance for the development of advanced catalysts in lithium-air batteries.

2 Materials and methodology

The study employed Density Functional Theory (DFT) with the GGA-PBE functional [5] and a cut-off energy of 400 eV for palladium (Pd) bulk structure. The k-points for Pd were set to 6×6×6, For surface calculations, the k-points were 6×6×1, as the systems are periodic in two directions. Bulk structural, electronic, and vibrational properties were determined

[1] Corresponding author: Bornwisemugwena02@gmail.com

using the Vienna Ab initio Simulation Package (VASP) code [6]. For surface modelling, the optimized bulk Pd structures were cleaved using the METADISE code to generate surface slabs, preserving both stoichiometry and symmetry system.

3 Results and discussion

The electronic properties of palladium (Pd) were evaluated using Density Functional Theory (DFT). The band structure shows the absence of a band gap at the Fermi level due to orbital overlaps, indicating metallic behavior. This metallic nature observed in the band structure is further confirmed by the density of states (DOS). Vibrational properties were also analyzed, and the absence of negative frequencies confirms that the system is vibrationally stable. In addition, the (111), (011), and (001) surfaces were investigated to examine how different crystallographic orientations influence the stability of the system. Surface energy calculations reveal that the (001) surface has the lowest surface energy, indicating that it is the most stable surface.

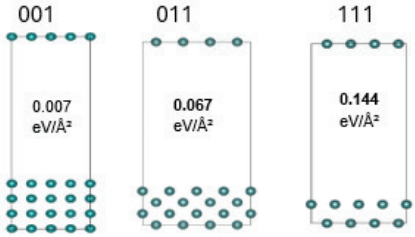


Fig. 1. Surface of Pd.

4 Conclusion

The density functional theory (DFT) was successfully employed to investigate the electronic and vibrational properties of palladium (Pd). The electronic analysis confirmed the metallic behavior of Pd, as indicated by the absence of a band gap at the Fermi level. Vibrational analysis further demonstrated that the system is stable, as no negative frequencies were observed. Using the METADISE code, different Pd surfaces were modelled, and the results show that the Pd (001) surface is the most stable. This is further supported by surface morphology, where the (001) surface occupies the largest surface area. These findings provide preliminary insights that contribute to the understanding of palladium surfaces for lithium-air battery catalyst applications.

We sincerely acknowledge the National Research Foundation (NRF) for its financial support. This study utilized the computational resources of the Materials Modelling Centre (MMC) at the University of Limpopo and the Centre for High Performance Computing (CHPC) in Cape Town, South Africa.

References

1. X. Wang, Q. Weng, Y. Yang, Y. Bando, D. Golberg. Hybrid two-dimensional materials in rechargeable battery applications and their microscopic mechanisms. Chemical Society Reviews, **45**, pp.4042-4073 (2016). https://doi.org/10.1039/C5CS00937E

2. R. Zhan, X. Wang, Z. Chen, Z.-W. Seh. Promises and Challenges of the Practical Implementation of Prelithiation in Lithium-Ion Batteries. Adv. Energy Mater., 11, 2101565 (2021). https://doi.o rg/10.1002/aenm.202101565
3. C.-C. Hsieh, W.-R. Liu. Effects of nitrogen doping on Si/carbon composite anode derived from Si wastes as potential active materials for Li ion batteries. J. Alloys Compd., 790, 829-836 (2019). https://doi.org/10.1016/j.jallcom.2019.03.242
4. L. Sun, L. Wang, Y. Liu, H. Wang, Z. Jin. Synergistic engineering of micron-sized porous silicon anodes via Ge doping and liquid metal alloy modification for high-energy-density lithium-ion batteries. J. Mater. Chem. A, 13, 14346-14352 (2025). https://doi.org/10.1039/D5TA00298B
5. Q. Wu, B. He, T. Song, J. Gao, S. Shi. Cluster expansion method and its application in computational materials science Comput. Mater. Sci., 125, 243–254 (2016). https://doi.org/10.1016/j.commatsci.2016.08.034
6. J. Hafner. Ab-initio simulations of materials using VASP: Density-functional theory and beyond. J. Comput. Chem., 29, 2044–2078 (2008). https://doi.org/10.1002/jcc.21057

First-principles study on sulphur-doped $Li_{1.2}Mn_{0.8}O_2$ cathode material for lithium-ion batteries

Bridget Mokgabudi*, *Kemeridge* Malatji, *Noko* Ngoepe, and *Phuti* Ngoepe

Materials Modelling Centre, University of Limpopo, Private Bag x1106, Sovenga 0727, South Africa.

Abstract. Lithium-ion batteries (LIBs) are widely used in applications like laptops, smartphones, and electric vehicles due to their high energy density, light weight, and compact size. However, they face challenges, including high cost, limited lifespan, safety risks, environmental concerns, and temperature sensitivity. Introducing Sulphur (S) as a dopant in $Li_{1.2}Mn_{0.8}O_2$ can improve electrochemical performance, electrical conductivity, and structural stability. Using Cluster Expansion (CE) and density functional theory (DFT), 165 new S-doped $Li_{1.2}Mn_{0.8}O_2$ structures were generated. One of the generated structures was found to be thermodynamically stable due to its negative heat of formation. These findings contribute to the development of more stable and high-performance cathode materials for lithium-ion batteries, enhancing their overall efficiency and life span.

1 Introduction

The rapid advancement of modern technologies, including digital infrastructure, electric transportation, and portable electronics, has significantly increased the demand for efficient, reliable, and safe energy storage systems, especially as renewable energy becomes vital for a sustainable future [1]. Lithium-ion batteries (LIBs) are widely regarded as the leading energy storage technology due to their high energy density of around 265-280 $WhKg^{-1}$, long cycle life, and relatively low cost [2, 3]. However, their performance is still limited by challenges such as degradation, safety concerns, and material and sustainability constraints [2]. Among potential cathode materials ($LiNiO_2$, $LiMnO_2$, $LiCoO_2$), $LiMnO_2$ has attracted attention because of its low cost, abundance of manganese, environmental friendliness, and high theoretical capacity of about 286 mAh g^{-1} [4]. Since the cathode plays a crucial role in determining battery performance and energy density, developing materials with higher specific capacity is essential [5]. These challenges reduce battery lifespan and limit large-scale commercialization. Various approaches, including elemental doping, surface modification, and coating, have been explored to address these limitations, although

* Corresponding author: bridgetmokgabudi02@gmail.com

developing stable and high-performance cathode materials remains an ongoing challenge [6, 7].

2 Materials and methodology

Density functional theory (DFT) [8] calculations were performed within the Vienna ab initio simulation package (VASP) [9] to calculate the structural, electronic and mechanical properties. Using the default k-point mesh settings in the Perdew-Burke-Ernzerhof Generalized Gradient Approximation (GGA-PBE) [10, 11], the plane wave cut-off energy was varied from (100-900) eV at intervals of 100 eV to determine the convergence point of the cut-off energy of $Li_{1.2}Mn_{0.8}O_2$. The total energy calculations were carried out at a fixed cut-off energy of 500eV while the k-points mesh were varied from 1x1x1 to 9x9x9. The Universal Cluster-Expansion (UNCLE) [1 2] code was used to generate phases $Li_{1.2}Mn_{0.8}O_2$ doped with Sulphur.

3 Results and discussion

The binary ground state diagram (figure 1) shows the results of the cluster expansion which was successfully used to generate 165 new phases of S-doped $Li_{1.2}Mn_{0.8}O_2$. The system exhibits a miscibility gap and miscible constituents, with one of these phases aligning with the ground state line, indicating its stability. The negative heats of formation suggest that the resulting phase is thermodynamically stable, except for those located within the miscibility gap.

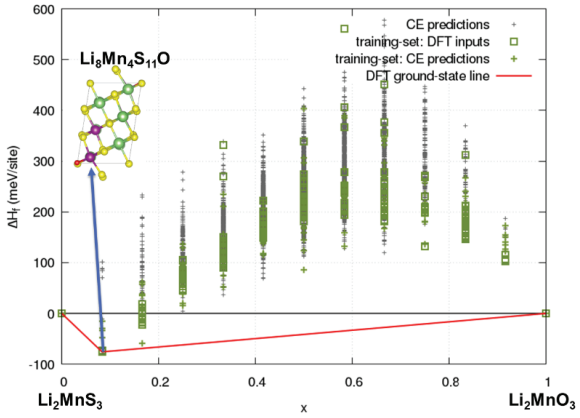


Fig. 1. Binary ground state diagram of S-doped $Li_{1.2}Mn_{0.8}O_2$.

4 Conclusion

CE was successfully used to generate new phases of S-doped $Li_{1.2}Mn_{0.8}O_2$. Among the new generated phases $Li_4MnSn_3O_8$ was found to be the most thermodynamically stable due to its negative formation energy.

The study utilized the computational resources of the Materials Modelling Centre (MMC) at the University of Limpopo and the Centre for High Performance Computing (CHPC) in Cape Town, South Africa.

References

1. M.Y. Shabalov, Y.L. Zhukovskiy, A.D. Buldysko, B. Gil, V.V. Starshaia, Energy Rep, **7**, 2664-2680 (2021).
2. K.R.Ngoy, V.T.Lukong, K.O.Yoro ,J.B.Makambo, N.C.Chukwuati, C.Ibegbulam, O.Eterigho-Ikelegbe, K.Ukoba, T.C.Jen, Renew Sust Energ Rev, **223**, 115971 (2025).
3. F.N.U. Khan, M.G. Rasul, A.S.M. Sayem N. Mandal, Energy Reports, **9**, 11-21, (2023).
4. S. Choi, W. Feng,Y. Xia, ACS omega, **9**, 18688-18708 (2024).
5. W. Fu, D. Kim, F. Wang, G. Yushin, J. Power Sources, **561**, 232738 (2023).
6. H. Zheng, X. Han, W. Guo, L. Lin, Q. Xie, P.Liu, W. He, L. Wang, D.L. Peng, Mater. Today Energy, **18**, 100518 (2020)
7. C.I. Azambou, F.H.K. Djioko, O.O. Obiukwu, P.K. Tsobnang, E.E. Kalu, I.T. Kenfack, E.E.l Oguzie, Mater. Today Commun, **35**, 105738 (2023).
8. S. Kurth, M.A.L. Marques, E.K.U. Gross, Encycl. Condens. Matter. Phys, **9**, 395-405 (2005).
9. W. Yi, G. Tang, X. Chen, B. Yang, X. Liu, Comput Phys Commun, **257**, 107525 (2020).
10. A.D. Becke, Phys. Rev. A, **38**, 3098-3100 (1988).
11. J.P. Perdew, K. Burke, M. Ernzerhof, Phys. Rev. Lett, **77**, 3865 (1996).
12. D. Lerch, O. Wiekhorst, G. L. W. Hart, R. W. Forcade, and S. Muller, Model Simul. Mater. Sci. Eng, **17**, 055003, (2009).

Effect of temperature on the predicted $Fe_{1-x}Ag_xAl$ stable phases for component coating

Christine Mkhonto[1*], *Ndanduleni* Lethole[2], *Hasani* Chauke[1], *and Phuti* Ngoepe[1]

[1] Materials Modelling Centre, University of Limpopo, Sovenga 0727, South Africa.
[2]Sefako-Makgatho-Health-Sciences-University, Gauteng, Medunsa 0204, South Africa.

Abstract. Fe-Al alloys are significant due to their excellent corrosion resistance and favorable mechanical qualities in industrial sectors. Thermodynamic properties were determined for FeAl system doped with Ag. Temperature effect on the ternary $Fe_{1-x}Ag_xAl$ systems was investigated using LAMMPS code to determine lattice expansion and Gibbs free energies. Considered stable phases ranging between 100 – 3000 K. The $FeAgAl_2$ denoted expansion at 1100 K. The $FeAgAl_2$ phase showed spontaneity with negative ΔG = -231.082 eV signifying thermodynamic stability. The $FeAgAl_2$ system showed decrease in c/a, indicating greater expansion along a-axis relative to c-axis. These systems form protective layer for component coating.

1 Introduction

The iron-Aluminides have remarkably become the most applied coating method in protective coatings for they possess excellent high-temperature corrosion resistance making it suitable for applications in the aerospace and energy sectors [1]. The favorable aluminium content and adhesion of the scale to the substrate is a protective barrier, guaranteeing intermetallic alloys that are corrosion resistant [2]. Suppose a metallic substance does not generate a protective oxide layer on its surface at high temperatures. In that case, it loses too much base mass, which is a damaging deterioration mechanism for metallic objects.

FeAl alloy has a good specific modulus, strength-to-weight ratio, and corrosion resistance to oxidation, sulfidation, and other forms of corrosion [3]. These capabilities allow for significant solubility for third-element additions and the possibility of alloying, producing an acceptable material. Various alloying elements have different effects on the oxidation resistance of FeAl alloy [4].

In this study, a combination methodology based on density functional theory (DFT) are used for alloy design and phase stability prediction. Cluster Expansion (CE) is used to examine ternary $Fe_{1-x}Ag_xAl$ phases, which are crucial for identifying novel alloy compositions with specific qualities. The DMol3 and LAMMPS algorithms were used to investigate the effects of temperature on the anticipated systems. These methodologies provide insights into the applications of automobile parts and turbines in the steel sector.

* Corresponding author: chresimkhonto@gmail.com

2 Methodology

Density functional theory (DFT) is a quantum mechanical method for calculating the ground state energy of many-body systems that was first suggested by Hohenberg-Kohn [5] to lay the groundwork for accurate calculation. This is the most effective method for calculating electronic structures for various materials. The Perdew-Berke-Ernzerhof (PBE) function was utilized. The plane-wave cut-off energy is 270 eV, with an 8x8x8 K-point and k-spacing of 0.5 1/Ang was found to be adequate to successfully reduce the internal energy to within 0.001 eV. The Universal Cluster Expansion (UNCLE) [6] code was used to anticipate new thermodynamically stable phases and to investigate the mechanical stability of doped $Fe_{1-}xAgxAl$ ternary phases. It outlines unstable, meta-stable, and stable systems by determining the enthalpies of formation using the precision of DFT + CE prediction. Molecular Dynamics (MD) [7] simulations were employed to improve energy efficiency via algorithmic optimization, specific LAMMPS code [8], and the DMol3 [9] approach.

3 Results and discussions

3.1 Lattice Expansion

Lattice expansion is investigated to identify a change or increase in the interplanar spacing of the structure of the material. In this section, the thermal expansion of $Fe_{1-X}Ag$=Al systems was evaluated as the temperature increases. A 6x6x6 supercell was used, and atomic phases of $Fe_{1-X}AgxAl$ were evaluated. Lattice expansion calculations were performed from 100 K to 3000 K to determine the possible transition when temperature is introduced and the effect on the ternary $Fe_{1-X}Ag_XAl$ systems. The number of atoms and volume remained constant across the temperature range. The intermolecular force (IMF) was determined considering the strength or bonding between the particles, showing how molecules arrange themselves within the structure.

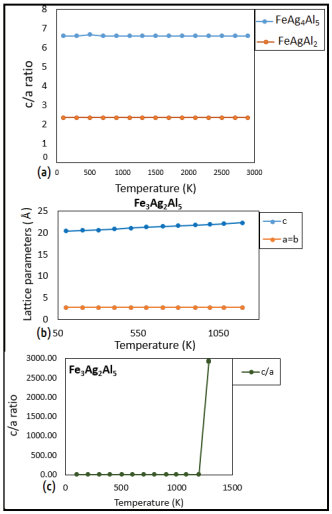


Fig. 1. Graph of c/a, ratio against temperature for (a) $FeAgAl_2$, (b) $FeAg_4Al_5$ and (c) $Fe_3Ag_2Al_5$ systems.

References

1. G. Fu, Z. Qi, Y. Su, Q. Liu and X. Guo, Effect of Different Treatment on Corrosion High Temp. Mater. **33**, 489 - 493 (2014). DOI 10.1515/htmp-2013-0110
2. Y. N. Mansurov and J. U. Rakhmonov, Analysis of the phase composition and the structure of aluminum alloys with increased content of impurities, Mater. Sci. **2**, 37 - 42 (2018). DOI: 10.17580/nfm.2018.02.07
3. D. G. Morris, M. A. Munoz and J. Chao, Development of high strength, high ductility and high creep resistant iron aluminide, Intermetallics **12**, 821 - 826 (2004). doi: 10.1016/j.intermet.2004.02.032
4. B. B. Karki, G. J. Ackland and J. Crain, Elastic instabilities in crystals from ab initio stress-strain relations J. Phys.: Condens. Matter. **9**, 8579 - 8589 (1997). **DOI** 10.1088/0953-8984/9/41/005
5. P. Hohenberg and W. Kohn, Introduction to density functional theory Phys. Rev. **137**, 864 - 871 (1964).
6. D. Lerch, O. Wiekhorst, G. L. W. Hart, R. W. Forcade, and S. Muller, UNCLE: a code for constructing cluster expansions for arbitrary lattices with minimal user-input, *Model. Simul. Mater. Sci. Eng.* **17**, 330 - 339 (2009). http://dx.doi.org/10.1088/0965-0393/17/5/055003
7. X. W. Zhou, H. N. G. Wadley, J. S. Filhol and M. N. Neurock, Modified charge transfer–embedded atom method potential for metal Õ metal oxide systems, Phys. Rev. B, **69**, 03540 (2004). DOI: https://doi.org/10.1103/PhysRevB.69.035402
8. B. Delley, From molecules to solids with the DMol3 approach J. chem. phys. **113**, 7756-7764 (2000). https://doi.org/10.1063/1.1316015.
9. D. Lerch, Wieckhorst O., Hart, G.L.W., Forcade R.W., and Muller S., A code for constructing cluster expansion for arbitrary lattices with minimal user-input modelling Simul. Mater. Sci. Eng. 17, 1-9 (2009). http://dx.doi.org/10.1088/0965-0393/17/5/055003

From anatase to rutile: the combined effect of Cu/Fe doping and temperature on the phase transformation of TiO_2 nanoparticles

Lesiba Malebo Mokonyane[1] and *Olatunbosun Owolabi* Nubi[1*]

[1]Department of Physics, University of Limpopo, South Africa

Abstract. Lowering the anatase-to-rutile phase transformation temperature of TiO_2 is essential for heat-sensitive applications. Cu/Fe-doped TiO_2 nanoparticles were synthesised via sol–gel method. XRD and Raman spectroscopy show that Cu doping reduces the phase transformation temperature, promoting rutile formation. In contrast, Fe incorporation increases the transformation temperature. Further calcination tests reveal that Cu/Fe co-doping counteracts Cu-induced reduction, producing XRD patterns closely resembling those of undoped TiO_2 across the investigated temperature range. UV–Vis analysis indicates that doping narrows the band gap through the introduction of d-orbital energy levels. These findings demonstrate a dual-doping strategy for controlling TiO_2 phase composition and properties.

1 Introduction

Titanium dioxide (TiO_2) is a cornerstone material in photovoltaics, photocatalysis, and self-cleaning surfaces, with its performance intrinsically linked to crystal structure. Anatase is prized for high photocatalytic activity, while rutile offers superior chemical stability, a high refractive index, and a narrower bandgap for visible-light absorption [1]. A primary barrier to its versatile application is the high temperature (>900°C) conventionally required for the complete anatase-to-rutile phase transformation. This not only restricts TiO_2 integration with heat-sensitive substrates and inflates energy costs, but also causes severe particle sintering, degrading the high surface area essential for nanomaterial performance [2].

Doping is a proven strategy to lower this transformation temperature by introducing lattice strain and oxygen vacancies that accelerate structural rearrangement [3, 4]. Yet, precisely controlling the transformation while tuning functional properties remains challenging. This study explores multi-ion doping to overcome this hurdle. We investigate the synergistic effect of copper (Cu) and iron (Fe) co-doping on the phase stability of sol-gel synthesised TiO_2 nanoparticles. By systematically analysing undoped, mono-doped (Cu), and co-doped (Cu/Fe) samples across a wide temperature range (100°C–1100°C), we demonstrate that this dual-doping approach drastically accelerates the transformation kinetics, reducing the threshold by approximately 300°C compared to pristine TiO_2. This

* Corresponding author: olatunbosun.nubi@ul.ac.za

strategy enables precise phase composition control at lower thermal budgets, facilitating the engineering of phase-dependent optical and electronic properties for advanced applications.

2 Methodology

Three TiO_2 nanoparticle variants were synthesised via a modified sol-gel route: (i) undoped, (ii) Cu-doped (5 wt%), and (iii) Cu/Fe co-doped (5 wt% each). Resulting gels were aged, dried, and calcined in a muffle furnace at 100–1100°C (2 h steps, ambient atmosphere) to track phase evolution.

Phase composition was determined by X-ray diffraction (XRD), with anatase (101) and rutile (110) peak intensities used to calculate phase fractions. Complementary Raman spectroscopy (532 nm excitation) probed structural symmetry and local vibrational modes. Optical properties and defect structures were assessed via UV-Vis diffuse reflectance spectroscopy (DRS)—converted to Tauc plots for bandgap estimation. Surface morphology and particle size distribution were examined using scanning electron microscopy (SEM).

3 Results and discussion

XRD analysis confirmed that undoped TiO_2 nanoparticles exhibit high anatase phase stability, with significant transformation to rutile occurring only above 900°C (Fig. 1). Cu-doping markedly destabilised the anatase structure, shifting the transformation kinetics to lower temperatures. Raman spectroscopy corroborated these findings, revealing a strong correlation between the suppression of the characteristic E_g anatase band (144 cm^{-1}) and the emergence of rutile Eg and A_{1g} modes in doped samples at reduced temperatures.

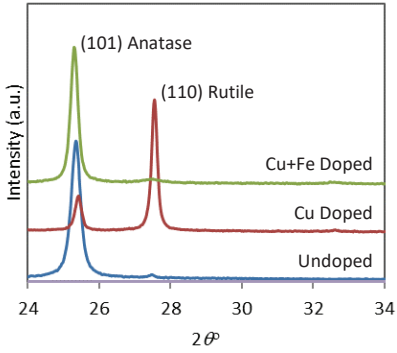


Fig. 1. XRD spectra of undoped and doped annealed at 600°C TiO_2.

While doping with 5 wt% Cu alone proved effective at lowering the transformation temperature, Cu/Fe co-doping was found to counteract this Cu-induced reduction. The co-doped samples produced XRD patterns that closely resembled those of pristine TiO_2 across the entire temperature range investigated. This neutralising effect is primarily attributed to a charge compensation mechanism, whereby Fe^{3+} ions offset the charge imbalance created by Cu^{2+} substitution, thereby eliminating the oxygen vacancies responsible for the lattice destabilisation.

Cu alone: Creates vacancies → Destabilises anatase → Lowers transformation temperature.

Cu + Fe: Fe compensates the charge → Quenches vacancies → Restores structural stability → Transformation temperature rises.

As a result, the crystal structure becomes less defective, and the phase composition (anatase/rutile ratio) at a given calcination temperature reverts to that of the undoped sample, explaining the similarity in their XRD patterns. Analysis of crystallite size revealed distinct trends: in their anatase form, the co-doped samples exhibited crystallite sizes similar to their Cu-doped counterparts, whereas the opposite trend was observed for the rutile phase. Generally, anatase samples consisted of smaller particles than the rutile samples.

These structural modifications directly influenced the optical characteristics of the materials. UV-Vis analysis revealed a distinct red shift in the absorption onset for the Cu-doped systems, irrespective of the TiO_2 phase. For the Cu/Fe co-doped sample, a bandgap narrowing from 3.20 eV (undoped anatase) to 2.85 eV was observed. This reduction is facilitated by the introduction of localised d-orbital states from the Cu and Fe ions within the TiO_2 bandgap.

4 Conclusion

This study demonstrates that the anatase-to-rutile phase transformation in TiO_2 nanoparticles can be strategically modulated through tailored doping. Cu doping (5 wt%) significantly lowered the transformation temperature by introducing oxygen vacancies that destabilise the anatase lattice. However, Cu/Fe co-doping counteracted this effect, with charge compensation from Fe^{3+} ions quenching vacancy formation and restoring structural stability comparable to undoped TiO_2. This mechanism was reflected in XRD patterns of co-doped samples, which closely resembled those of pristine TiO_2 across all temperatures.

Crystallite size analysis revealed phase-dependent behavior, with anatase samples consistently exhibiting smaller crystallites than their rutile counterparts. Optically, Cu doping induced a distinct red shift in absorption, while Cu/Fe co-doping resulted in a narrowed bandgap (from 3.20 eV to 2.85 eV), attributed to localised d-orbital states introduced within the TiO_2 bandgap. These findings highlight the potential of strategic co-doping to decouple phase stability from optical tuning, offering a route to design TiO_2-based materials with tailored properties for photocatalytic and optoelectronic applications.

References

1. D. A. H. Hanaor, C. C. Sorrell, Review of the anatase to rutile phase transformation. J. Mater. Sci. **46**, 855–874 (2011). https://doi.org/10.1007/s10853-010-5113-0
2. N. Khatun, S. Tiwari, C. P. Vinod, C. M. Tseng, S. W. Liu, S. Biring, S. Sen, Role of oxygen vacancies and interstitials on structural phase transition, grain growth, and optical properties of Ga doped TiO_2. J. Appl. Phys. **123**, 245702 (2018). https://doi.org/10.1063/1.5027672
3. A. Raj, S. K. Jha, Hyperdoping: doping TiO_2 beyond thermodynamic limits using Flash sintering. J. Eur. Ceram. Soc. **44**, 116720 (2024). https://doi.org/10.1016/j.jeurceramsoc.2024.116720
4. L. Kernazhitsky, V. Shymanovska, T. Gavrilko, V. Naumov, V. Kshnyakin, T. Khalyavka, A comparative study of optical absorption and photocatalytic properties of nanocrystalline single-phase anatase and rutile TiO_2 doped with transition metal cations. J. Mol. Model. **198**, 511-519 (2013). https://doi.org/10.1016/j.jssc.2012.11.015

Cluster expansion investigation of Ti and F doping effects on the structural stability of $Li_{1.2}Mn_{0.8}O_2$ cathode materials

Emmanuel Kgoedi[1][1], *Raesibe* Ledwaba[1], *Noko* Ngoepe[1], *Mallang* Masedi[1], and *Phuti* Ngoepe[1]

[1]Materials Modelling Centre, University of Limpopo, Private Bag x1106, Sovenga 0727, South Africa.

Abstract. Lithium-rich manganese oxide cathodes, particularly $Li_{1.2}Mn_{0.8}O_2$, have attracted significant interest due to their high capacity and energy density. However, their practical application is limited by voltage fade, poor cycling stability, and oxygen release during electrochemical operation. Doping strategies involving transition metals such as Ti and anion substitution with F have been proposed to address these limitations. In this study, cluster expansion, a statistical mechanics-based framework for modelling configurational disorder, is applied to investigate Ti- and F-doped systems and their co-doped configurations. The results indicate that rational doping improves structural stability and suppresses oxygen vacancy formation, thereby mitigating voltage decay and enhancing long-term cycling performance.

1 Introduction

The accelerating growth of portable electronics, electric mobility, and large-scale energy storage systems has driven an increasing global demand for advanced lithium-ion batteries (LIBs) that offer higher capacity, longer lifespan, and improved safety [1]. Lithium-rich layered oxides, especially $Li_{1.2}Mn_{0.8}O_2$, are regarded as attractive cathode materials owing to their high specific capacity and the earth-abundant nature of manganese, offering a cost-effective and sustainable pathway for large-scale energy storage applications [2]. Despite their advantages, these materials face persistent challenges such as voltage decay, oxygen release, and structural instability during electrochemical cycling, which significantly impede their commercial viability [3].

Despite these advancements, understanding the mechanisms behind dopant-induced stabilization and precisely controlling dopant distribution at the atomic level remains highly challenging. This is primarily due to the immense configurational complexity and the coupled multivalent cation-anion redox processes, which cannot be fully captured through experimental methods or conventional first-principles simulations alone [4]. As a result, the

[1] Corresponding author: 201829960@myturf.ul.ac.za

cluster expansion (CE) method has become a pivotal computational tool in this domain. CE enables the efficient representation of substitutional disorder within a generalized Hamiltonian, allowing high-throughput exploration of extensive dopant configurations while dramatically reducing the computational cost compared to exhaustive density functional theory (DFT) calculations [5]. By facilitating the assessment of energetics, structural stability, and defect formation across broad dopant concentration ranges, CE models provide a powerful framework to accelerate the rational design of next-generation cathode materials [6].

2 Materials and methodology

The cluster expansion computations presented in this study were carried out using the Universal Cluster Expansion (UNCLE) code developed by Müller et al. [7]. The code can perform a comprehensive cluster expansion (CE) fit through the application of a genetic algorithm, enabling the prediction of ground states in systems comprising three or more constituent elements. UNCLE systematically increases the number of clusters incorporated into the expansion until the specified level of accuracy is attained [8]. This approach was employed to determine the ground-state configuration and thermodynamic properties of $Li_{1.2}Mn_{0.8-x}Ti_xO_{2-y}F_y$, and $Li_{1.2}Mn_{0.8-x}Ti_xO_2$.

The present computational investigations were conducted using the projector-augmented wave (PAW) formalism within the framework of density functional theory (DFT), as implemented in the Vienna Ab initio Simulation Package (VASP) [9]. The exchange–correlation energy was described within the framework of the spin-polarized generalized gradient approximation (GGA) and parameterized using the Perdew Burke Ernzerhof (PBE) functional [10, 11]. The localization effects associated with the d electrons of the transition metal ions were incorporated using the GGA + U formalism proposed by Dudarev et al [12].

3 Results and discussion

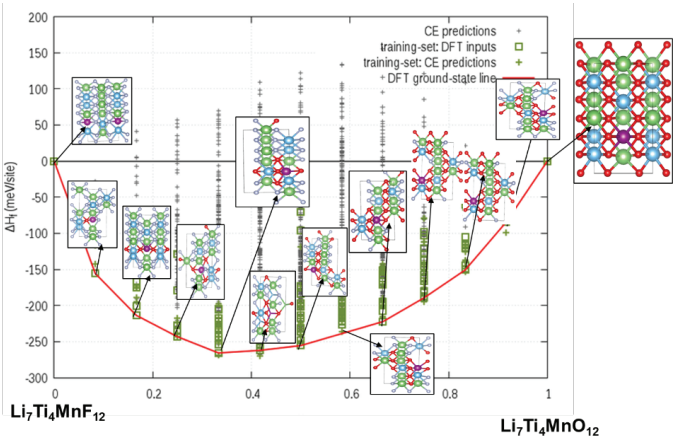


Fig. 1. CE formation enthalpy convex hull for Ti substitution in $Li_{1.2}Mn_{0.8}O_2$.

The results show that fluorine substitution induces composition-dependent stabilization, with intermediate concentrations exhibiting the lowest formation energies and several configurations lying on the convex hull. This indicates that moderate fluorine doping enhances structural stability, whereas higher concentrations lead to increased formation energies. The good agreement between DFT calculations and CE predictions confirms the reliability of the model in describing the configurational energetics of the fluorine-doped system.

4 Conclusion

The cluster expansion analysis demonstrates that fluorine substitution significantly influences the thermodynamic stability of the system. The formation enthalpy landscape reveals that intermediate fluorine concentrations yield the lowest energies and stable ground-state configurations along the convex hull, indicating optimal stabilization of the crystal lattice. In contrast, both low and excessive fluorine contents show relatively higher formation energies, suggesting reduced stability. The strong agreement between the DFT calculations and CE predictions confirms the reliability of the model in capturing the configurational energetics. Overall, the results indicate that moderate fluorine doping is thermodynamically favourable and may enhance structural stability in the material system.

We sincerely acknowledge the Council for Scientific and Industrial Research (CSIR) for financial support. This work utilized the computational resources of the Materials Modelling Centre (MMC) at the University of Limpopo and the Centre for High Performance Computing (CHPC), Cape Town, South Africa.

References

[1] N. Nitta, F. Wu, J.T. Lee, G. Yushin, Mater. Today 18, 252 (2015)
[2] M.E. Kgoedi, R.S. Ledwaba, M.C. Masedi, N. Ngoepe, P. Ngoepe, MATEC Web Conf. 388, 07005 (2023)
[3] N. Kunanusont, T. Sesuk, P. Eiamlamai, S. Buakeaw, P. Tammawat, P. Limthongkul, Electrochem. Soc. Meet. Abstr. 244, 451 (2023)
[4] K. Koester, P. Kaghazchi, Electrochem. Soc. Meet. Abstr. prime2024, 1395 (2024)
[5] J.H. Chang, D. Kleiven, M. Melander, J. Akola, J.M. Garcia-Lastra, T. Vegge, J. Phys.: Condens. Matter 31, 325901 (2019)
[6] P. Zhong, F. Xie, L. Barroso-Luque, L. Huang, G. Ceder, PRX Energy 2, 043005 (2023)
[7] R. Hill, Proc. Phys. Soc. A 65, 349 (1952)
[8] M. Mphahlele, M. Masedi, K. Malatji, P. Ngoepe, R. Ledwaba, MATEC Web Conf. 388, 07005 (2023)
[9] G. Kresse, D. Joubert, Phys. Rev. B 59, 1758 (1999)
[10] B. Liu et al., Phys. Rev. B 49, 16223 (1994)
[11] G. Kresse, J. Furthmüller, Comput. Mater. Sci. 6, 15 (1996)
[12] J.P. Perdew, K. Burke, M. Ernzerhof, Phys. Rev. Lett. 77, 3865 (1996)

First-principles investigation of structural, magnetic and mechanical properties of $L1_0$ MnPt-Ir alloys

Thabang Kombesi[1*], *Mordecai* Mashamaite[1], *Ramogohlo* Diale-Boshielo[1, 2], and *Hasani* Chauke[1]

[1]Materials Modelling Centre, University of Limpopo, Private Bag X 1106, Sovenga, 0727, South Africa
[2]Advanced Materials Division, MINTEK, Private bag X 3015, Randburg, 2125, South Africa

Abstract. The $L1_0$ MnPt alloy is a promising antiferromagnetic material for spintronic applications due to its strong magnetic stability and favorable mechanical properties. In this work, the influence of Ir substitution on the structural, thermodynamic, electronic, magnetic, and mechanical properties of $L1_0$ $Mn_{50}Pt_{50-x}Ir_x$ is investigated using density functional theory. The calculated lattice parameters agree well with available data, and formation energies confirm thermodynamic stability. Elastic properties indicate good mechanical stability with Ir incorporation, while magnetic calculations preserve antiferromagnetic ordering. Electronic structure analysis shows that Ir modifies states near the Fermi level, influencing electronic stability and spin polarization.

1 Introduction

The rapid advancement of artificial intelligence, cloud computing, and the Internet of Things (IoT) has driven a growing need for high-density, energy-efficient data storage and spintronic technologies [1,2]. Traditional charge-based memory devices suffer from drawbacks such as high power usage, data volatility, and scaling constraints, which have spurred the search for alternative materials with enhanced magnetic and electronic characteristics [3]. Antiferromagnetic (AFM) materials integrated into spintronic components, such as magnetic random-access memory (MRAM), giant magnetoresistance (GMR) sensors, and magnetic tunnel junctions (MTJs), provide benefits including rapid switching speeds, low energy consumption, and non-volatile data retention [3]. Within this class of materials, the $L1_0$-ordered MnPt alloy has garnered considerable interest due to its large magnetocrystalline anisotropy, outstanding thermal stability, and stable AFM ordering [3, 4]. In this study, first-principles density functional theory (DFT) calculations are used to examine the structural, magnetic, and mechanical characteristics of $L1_0$ MnPt-Ir alloys for prospective spintronic applications.

2 Methodology

First-principles calculations were performed within the framework of density functional theory (DFT) using the Vienna Ab-initio Simulation Package (VASP) [5]. The projector

* Corresponding author: 202005520@myturf.ul.ac.za

augmented-wave (PAW) [6] method was employed to describe the electron-ion interactions, while the generalized gradient approximation (GGA) in the Perdew-Burke-Ernzerhof (PBE) [7] formulation was used to account for exchange-correlation effects. For these simulations, a 2×2×2 supercell was used containing 32 atoms. Brillouin zone integrations were performed using a 14 × 14 × 11 Monkhorst-Pack k-point mesh, and a plane-wave cutoff energy of 500 eV was used to ensure reliable convergence of the total energy.

3 Results and discussion

Figure 1(a) presents the calculated bulk modulus (B), shear modulus (G), and Young's modulus (E) of the $L1_0$ $Mn_{50}Pt_{50-x}Ir_x$ alloys as a function of Ir concentration (at. %). These mechanical moduli provide important insight into the stiffness and bonding strength of the alloys as alloying elements are introduced. As shown in Fig. 1(a), the moduli exhibit systematic variations with Ir substitution. In particular, the incorporation of Ir generally increases the values of B, G, and E, indicating stronger interatomic bonding and enhanced rigidity of the alloy system. This behavior suggests that Ir substitution improves the mechanical stiffness and structural robustness of $L1_0$ $Mn_{50}Pt_{50-x}Ir_x$ alloys. Figure 1(b) shows the calculated Pugh's ratio (k = B/G) and Poisson's ratio (v) for $L1_0$ MnPt and Ir-doped $L1_0$ MnPt alloys. According to the ductility criteria (k > 1.75 and v > 0.26), all compositions remain ductile. However, both k and v gradually decrease with increasing Ir concentration, indicating a slight reduction in ductility. This trend suggests that Ir addition increases resistance to plastic deformation, making the alloy relatively less ductile, although the overall ductile nature of the structure is preserved across the studied composition range.

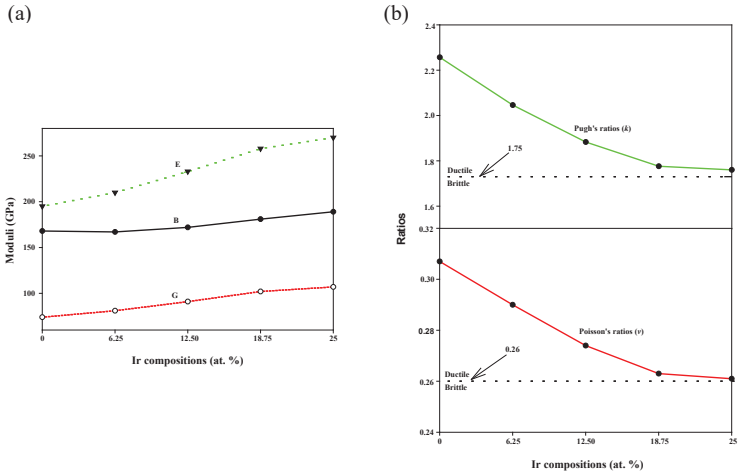


Fig. 1. (a) Moduli (GPa) and (b) Pugh's ratio (k) and Poisson's ratio (v) for $L1_0$ $Mn_{50}Pt_{50-x}Ir_x$ alloys ($0 \leq x \leq 25$ at. %).

4 Conclusion

First-principles calculations were performed to investigate the structural, thermodynamic, electronic, magnetic, and mechanical properties of Ir-doped $L1_0$ MnPt alloys. The results show that Ir incorporation enhances the bulk and shear moduli while maintaining ductile behavior, indicating improved mechanical reliability suitable for spintronic device integration. The antiferromagnetic ground state of $L1_0$ MnPt is largely preserved at low Ir concentrations, whereas higher Ir content introduces a weak ferromagnetic contribution due to modifications in magnetic exchange interactions. Overall, these findings demonstrate that Ir substitution enables effective tuning of the mechanical stability and magnetic behavior of MnPt-based alloys, highlighting their potential for antiferromagnetic spintronic and high-density magnetic memory applications.

References

1. M. U. Farooq, M. Waseem, S. Mazhar, A. Khairi, T. Kamal, A review on Internet of Things (IoT), *International Journal of Computer Applications*, **113**(1), 1–7 (2015).
2. F. Mouhat, F. X. Coudert, Necessary and sufficient elastic stability conditions in various crystal systems, *Physical Review B*, **90**(22), 224104 (2014).
3. V. Baltz, A. Manchon, M. Tsoi, T. Moriyama, T. Ono, Y. Tserkovnyak, Antiferromagnetic spintronics, *Reviews of Modern Physics*, **90**(1), 015005 (2018).
4. Z. Lu, R. V. Chepulskii, W. H. Butler, First-principles study of magnetic properties of $L1_0$-ordered MnPt and FePt alloys, *Physical Review B*, **81**(9), 094437 (2010).
5. J. Hafner, Ab-initio simulations of materials using VASP: Density-functional theory and beyond, *Journal of Computational Chemistry*, **29**, 2044–2078 (2008).
6. P. E. Blöchl, Projector augmented-wave method, *Physical Review B*, **50**, 17953–17979 (1994).
7. J. P. Perdew, K. Burke, M. Ernzerhof, Generalized gradient approximation made simple, *Physical Review Letters*, **77**, 3865–3868 (1996).

Exploration of new phases of Ti-Al-V alloys using universal cluster expansion

Mordecai Mashamaite[1*], *Phuti* Ngoepe[1], and *Hasani* Chauke[1]

[1]Materials Modelling Centre, University of Limpopo, South Africa

Abstract. The effects of V on TiAl alloys were investigated using cluster expansion techniques. It was observed that, the clusters fitting was considered reliable since the CVS score was less than 5 meV/position, indicating a high fitting accuracy of the cluster expansion. Furthermore, the cluster expansion method yielded 40 novel structures. Among these, 6 distinct configurations were identified as thermodynamically stable. The outcome of this study is intended to inform and direct the rational design and discovery of novel Ti–Al–V alloys specifically optimized for aerospace applications, thereby contributing to the advancement of lightweight, mechanically robust, and durable structural components.

1 Introduction

TiAl alloys have been extensively used in aerospace, chemical industries and biomedical applications, due to their excellent properties, including high specific strength, exceptional corrosion resistance, and good biocompatibility [1,2]. The addition of vanadium (V) to TiAl is expected to act as a β-phase stabilizer, enhancing mechanical strength and manufacturability, as well as improving ductility, while simultaneously mitigating the brittleness typically observed in binary TiAl alloys [3]. In this study, we employ cluster expansion and density functional theory to explore new unreported Ti-Al-V phases and to investigate the thermodynamic stability of the alloys.

2 Methodology

2.1 Cluster expansion

The cluster expansion calculations were computed using the module UNCLE [4]. The code can perform a complete cluster expansion fit using a genetic algorithm (GA) and predict the ground states of systems containing three elements. This method was used to determine the ground-state structure and thermodynamic properties of Ti-Pt-V. The fitness of every figure set was evaluated using the cross-validation score (CVS), which quantifies the predictive accuracy of the figure set for an unknown structure [5]. The cluster has a total of 9 iterations.

* Corresponding author: mordecai.mashamaite@ul.ac.za

The clusters were considered reliable since the CVS score was < 5 meV/position indicating fitting accuracy of the method.

2.2 Geometry optimization

Within the UNCLE code [4], the total energy calculations of Ti-Pt-V alloys were performed using the Vienna Ab-initio Simulation Package (VASP) [6]. The generalized gradient approximation (GGA) function of Perdew-Burke-Ernzerhof (PBE) was introduced to describe the exchange-correlation energy [7]. An energy cut-off of 500 eV was used for the plane-wave expansion of wave functions. The k-spacing of 0.2 was used, according to the Monkhorst and Pack grid, for specified k-point sampling [8]. The SCF convergence threshold for the total energy was set at 10^{-6} eV/atom. Full geometry optimization was performed on the ground-state structures between TiV ↔ TiAl.

3 Results

Figure 1 shows all predicted structures of Ti-Al-V on the Al site. The predicted structures are denoted by grey cross. In addition, the cluster expansion generated a total of 40 new structures, and six (6) stable structures were found on the ground-state line. The $(Ti_3AlV_2)_2$ alloy is the most thermodynamically stable structure on the ground state line.

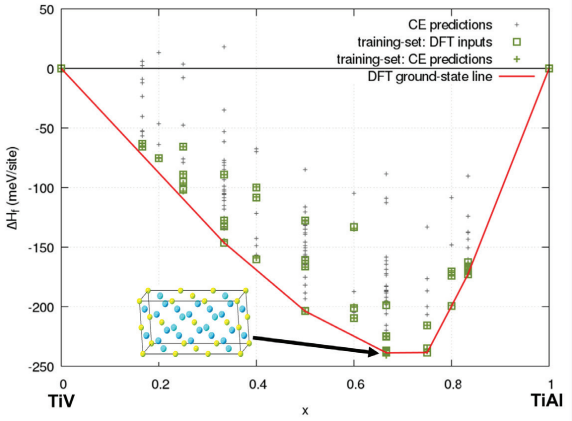


Fig. 1. The ground-state diagram of Ti-Al-V alloys.

4 Conclusion

The cluster expansion method enabled the systematic prediction of 40 novel Ti–Al–V structures. This approach was subsequently employed to identify the ground-state configurations and to construct the phase diagram of the Ti–Al–V alloy on the Al sublattice. Among the predicted compositions, the $Ti_6Al_4V_2$ alloy was selected as the most stable configuration along the ground-state line, exhibiting a formation energy of −0.239 eV/atom. These results indicate that V is an effective alloying addition to TiAl-based alloys.

References

1. X. Wu, Review of alloy and process development of TiAl alloys. Intermetallics. **14**, 1114, (2006)
2. H. Zhang, N. Yan, H. Liang, Y. Liu, Phase transformation and microstructure control of Ti2AlNb-based alloys: A review. J. Mater. Sci. Technol., **80**, 203 (2021)
3. W. Zhou, C. Shen, X. Hua, L. Wang, Y. Zhang, F. Li, J. Xin, Y. Ding, The effect of vanadium on the microstructure and mechanical properties of TiAl alloy fabricated by twin-wire directed energy deposition-arc. Addit. Manuf. **62**, 103282, (2023)
4. D. Lerch, O. Wieckhorst, G.L. W. Hart, R.W. Forcade, S. Müller, UNCLE: UNCLE: A Code for Constructing Cluster Expansions For Arbitrary Lattices With Minimal User-Input. Mater. Sci. Eng. **1**, 55003 (2009)
5. A. van de Walle, M. Asta, G. Ceder, The Alloy Theoretic Automated Toolkit: A User Guide. Calphad, **26**, 539 (2002)
6. G. Kresse, J. Hafner, Ab initio Molecular Dynamics for Liquid Metals. Phys. Rev. B., **47**, 558 (1993)
7. J.P. Perdew, K. Burke, M. Ernzerhof, Generalized Gradient Approximation Made Simple. Phys. Rev. Lett. **77**, 3865 (1996)
8. G.W. Fernando, R.E. Watson, M. Weinert, Heats of Formation of Transition-Metal Alloys: Full-Potential Approach and the Pt-Ti System. Phys. Rev. B. **45**, 15, 8233 (1992)

NOTES

NOTES

NOTES

NOTES

RAPDASA

RAPID PRODUCT DEVELOPMENT ASSOCIATION OF SOUTH AFRICA

CONFERENCE BOOKLET

The 27th Annual International RAPDASA Conference joined by AMI

Co-hosted by MINTEK and the University of Limpopo



www.rapdasas.org

From Prototype to Production: Translating Research in to Reality